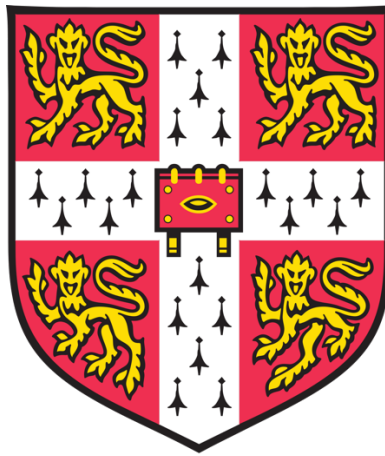


Activation of lipid kinase VPS34 by Rab GTPases



Shirley Tremel

MRC Laboratory of Molecular Biology
University of Cambridge

This thesis is submitted for the degree of Doctor of Philosophy

Queens' College

April 2020

Declaration

This thesis is the result of my own work and includes nothing which is the outcome of work done in collaboration except as declared in the Preface and specified in the text. It is not substantially the same as any that I have submitted, or, is being concurrently submitted for a degree or diploma or other qualification at the University of Cambridge or any other University or similar institution except as declared in the Preface and specified in the text. I further state that no substantial part of my thesis has already been submitted, or, is being concurrently submitted for any such degree, diploma or other qualification at the University of Cambridge or any other University or similar institution except as declared in the Preface and specified in the text. It does not exceed the prescribed word limit for the relevant Degree Committee.

Shirley Tremel

April 2020

Activation of lipid kinase VPS34 by Rab GTPases

Shirley Tremel

VPS34 is a lipid kinase that uses phosphatidylinositol (PI) as a substrate to produce the signalling lipid phosphatidylinositol-3-phosphate (PI(3)P). In the cell, VPS34 has to team up with other proteins in order to increase its enzymatic activity. It forms primarily two hetero-tetrameric complexes, complexes I and II, which act as key regulators of autophagy and endocytic trafficking, respectively. Complex I consists of VPS34, VPS15, Beclin 1 and ATG14L, whereas complex II contains UVRAG instead of ATG14L. VPS34 complex activity is regulated by membrane properties and by members of the Rab family of small G proteins, which are important for orchestrating intracellular vesicle sorting and transport. However, their detailed activation mechanisms have been poorly understood.

Firstly, we found that high curvature, negative charge, lipid unsaturation and specific phosphoinositides activate both VPS34 complexes. While the autophagic complex I relies on an amphipathic helix in ATG14L for membrane association, the endocytic complex II uses mainly three aromatic loops in the Beclin 1 subunit to engage with membranes. I have found that Rab GTPases act as specific regulators for each complex. While Rab5 is a strong activator for endocytic complex II, Rab1 specifically activates the autophagic complex I. To gain insight into the activation mechanism, I obtained a 9.8 Å resolution structure of complex II bound to Rab5 on membranes, using electron cryo-tomography and subtomogram averaging. Complex II is dynamic on membranes with only the UVRAG/Beclin 1 “adaptor arm” permanently contacting the outer leaflet of the lipid bilayer. In contrast, the VPS15/VPS34 “catalytic arm” hovers over the membrane and is able to tilt up and down. Rab5 binds on the “adaptor arm” of the complex to a tripartite motif made of VPS34 C2, VPS15 WD40 and FF domain. These interactions increase membrane recruitment and PI(3)P production of complex II specifically on early endosomes.

Acknowledgements

I would like to take the opportunity to thank all the people who have contributed to this thesis in many different ways and made the last four years an unforgettable experience to me.

First and foremost, I would like to thank my supervisor Roger Williams for given me the opportunity to join Yohei Ohashi on the VPS34 project and giving me the freedom to explore cryo-electron tomography and subtomogram averaging. Roger has been tremendously helpful over the years and his never-subsiding curiosity is truly remarkable and makes him an inspiring scientist.

Yohei Ohashi has provided me with the greatest support and kindness in the lab. He is an incredibly smart scientist, always showed patience and was nothing but helpful to me. This thesis was built on a lot of effort that Yohei has worked for for several years. I have also never met a person, who could remember so many papers in such detail!

Dustin Morado was instrumental in helping me with the subtomogram averaging. Dustin was incredibly patient and has sacrificed many hours at sitting at the microscope, answering my numerous and often annoying questions and was even reachable 24/7 over WhatsApp for any tomography question. Without him, this thesis wouldn't have been possible.

Glenn Masson is one of the sharpest and funniest brains I have ever met. He has made my stay in the Williams lab incredibly enjoyable and taught me that British stamps are a valid means of payment at an unforgettable dinner at Downing College with Alison Inglis. He is truly a master of HDX-MS and I hope he will soon get the PI position he truly deserves!

I would also like to thank Olga Perisic, who keeps the lab running and has always been helpful with advice she has acquired over the years. She has also been so kind to clone numerous plasmids to keep me from endlessly trouble shooting primers.

I would also like to thank the rest of the lab for tea times and gossip to lighten the mood after a failed protein prep or an unsuccessful microscope session. I would also like to thank the many people and fellow students within the LMB who have helped me at every stage of my work. I am especially grateful to the electron and light microscopy facilities, who keep everything running so smoothly and provided dedicated training and support. Furthermore, Mark Skehel and Sarah Maslen were helpful in acquiring the HDX-MS data and our collaborators Kathrin Lang, Marie-Kristin von Wrisberg, Juri Rappsilber and Zhuo Chen were essential for the UAA crosslinking. Jessi Bertram and Sean Munro have also contributed to this project by suggesting that Rab1 is an additional puzzle piece of the VPS34 complex recruitment.

Lastly, I would like to thank my family and friends, who had to endure another move to the UK from me for this PhD. I promise this will be the last time! They have provided support whenever I wasn't sure I was capable. Lastly, I would like to thank Patrick, who has been very patient and supportive over the years and laughed at all the late night "catastrophy hours".

Abbreviations

ADP	adenosine diphosphate
AF	aromatic finger
AF647-PX	Alexa Fluor 647-PX label
ALPS	amphipathic lipid packing sensor
ALS	amyotrophic lateral sclerosis
AMP	adenosine monophosphate
Atg	Autophagy-related
ATP	adenosine triphosphate
BATS	Barkor/ATG14L autophagosome targeting sequence
C2HH	C2 helical hairpin insertion
CC	cross correlation/coiled coil
CORVET	class C core vacuole/endosome tethering
Cryo-EM	cryo-electron microscopy
Cryo-ET	cryo-electron tomography
CTF	contrast transfer function
DFCP1	double FYVE domain-containing protein 1
DO	18:1-18:1/1,2-dioleoyl lipid
EEA1	early endosome autoantigen 1
ER	endoplasmic reticulum
ERES	ER-exit sites
ERGIC	ER-Golgi intermediate compartment
FYCO1	FYVE and coiled-coil domain-containing 1
FTD	frontotemporal dementia
GAP	GTPase-activating protein
GDF	GDI dissociation factor
GDI	guanine nucleotide dissociation inhibitor
GDP	guanosine diphosphate
GEF	guanine nucleotide exchange factor
GPCR	G protein-coupled receptor
GTP	guanosine triphosphate
GUVs	giant unilamellar vesicles
HDX-MS	hydrogen deuterium exchange mass spectrometry
HELICAT	helical and kinase domains
HL	hydrophobic loop
HOPS	homotypic fusion and protein sorting
HVD	hypervariable domain

ITO	indium tin oxide
Liss-Rhod	Lissamine™ rhodamine B-DOPE
LUVs	large unilamellar vesicles
MAO	monoamine oxidase
mTORC1	mechanistic target of rapamycin complex 1
PA	phosphatidic acid
PAS	pre-autophagosomal structure
PC	phosphatidylcholine
PCA	principal component analysis
PE	phosphatidylethanolamine
PEG	polyethylene glycol
PEI	polyethylenimine
PI	phosphatidylinositol
PI3K	phosphatidylinositol-3-kinase
PI(3)P	phosphatidylinositol-3-phosphate
PI(3,4)P2	phosphatidylinositol-3,4-bisphosphate
PI(3,4,5)P2	phosphatidylinositol-3,4,5-trisphosphate
PI(3,5)P2	phosphatidylinositol-3,5-bisphosphate
PI(4)P	phosphatidylinositol-4-phosphate
PI(3,4)P2	phosphatidylinositol-4,5-bisphosphate
PI(5)P	phosphatidylinositol-5-phosphate
PIP	phosphoinositide species
PKC	protein kinase C
PS	phosphatidylserine
Rab	Ras-related in brain
REP	Rab escort protein
RabGGTase	Rab geranylgeranyltransferase
SM	sphingomyelin
SNR	signal-to-noise ratio
SNXs	sorting nexins
SO	18:0-18:1/1-stearoyl-2-oleoyl lipid
SPA	single particle analysis
SUVs	small unilamellar vesicles
UAA	unnatural amino acid
ULK1	UNC51-like Ser/Thr kinase
VPS	vacuolar protein sorting
WIPI	WD-repeat domain phosphoinositide-interacting proteins

Table of content

1	Introduction	- 1 -
1.1	The Rab GTPase family.....	- 1 -
1.1.1	Rab GTPases in the cell.....	- 1 -
1.1.2	Rab regulators and effectors	- 4 -
1.1.3	Endosome maturation orchestrated by Rab GTPases.....	- 6 -
1.2	Autophagy	- 10 -
1.2.1	Autophagy initiation.....	- 11 -
1.2.2	Autophagosome expansion and maturation.....	- 14 -
1.2.3	Autophagosome-lysosome fusion and degradation.....	- 15 -
1.3	Membrane lipids.....	- 16 -
1.4	VPS34 and its complexes.....	- 21 -
1.4.1	Complex I	- 25 -
1.4.2	Complex II.....	- 27 -
1.5	Hydrogen deuterium exchange mass spectrometry (HDX-MS)	- 29 -
1.6	Cryo-electron tomography (cryo-ET) and subtomogram averaging.....	- 33 -
2	Aims	- 40 -
3	Materials and methods	- 42 -
3.1	Protein expression and purification	- 42 -
3.1.1	Purification of human VPS34 complexes I and II	- 43 -
3.1.2	Purification of human VPS34	- 44 -
3.1.3	Purification and labelling of p40-PX domain.....	- 46 -

3.1.4	Purification of human Rab1a.....	- 47 -
3.1.5	Purification of human Rab5a.....	- 49 -
3.2	GUV assay.....	- 50 -
3.2.1	GUV generation and immobilisation.....	- 52 -
3.2.2	Rab labelling of GUVs.....	- 52 -
3.2.3	Time series acquisition by confocal microscopy.....	- 53 -
3.2.4	Image analysis.....	- 54 -
3.3	Liposome preparation.....	- 55 -
3.3.1	LUV and SUV preparation.....	- 55 -
3.3.2	Rab labelling of SUVs/LUVs.....	- 56 -
3.4	Flotation assay.....	- 56 -
3.5	Hydrogen deuterium mass spectrometry (HDX-MS).....	- 57 -
3.5.1	Sample preparation of CI and CII incubated with liposomes.....	- 57 -
3.5.2	Sample preparation of CII incubated with Rab5a.....	- 58 -
3.5.3	Hydrogen deuterium mass spectrometry (HDX-MS).....	- 59 -
3.6	Unnatural amino acid (UAA) crosslinking.....	- 60 -
3.6.1	Purification of Rab5a S84→BrCO6K.....	- 60 -
3.6.2	Crosslinking of Rab5a S84→BrCO6K and VPS34/ complex II.....	- 61 -
3.7	Cryo-ET and subtomogram averaging.....	- 62 -
3.7.1	Sample preparation.....	- 62 -
3.7.2	BSA coating of gold fiducial.....	- 62 -
3.7.3	Cryo-ET acquisition.....	- 63 -
3.7.4	Raw image processing and tomogram reconstruction.....	- 63 -
3.7.5	Subtomogram averaging.....	- 64 -

4	Increasing VPS34 activity by protein domains and membrane composition.....	- 68 -
4.1	Results.....	- 68 -
4.1.1	Measuring PI3K lipid kinase activity.....	- 68 -
4.1.2	ATG14L BATS is essential for complex I activity.....	- 71 -
4.1.3	HDX-MS reveals crucial membrane binding motifs in Beclin 1.....	- 77 -
4.1.4	Phosphatidylserine activates complex I, complex II, and VPS34.....	- 83 -
4.1.5	Phosphoinositides activate complexes I and II.....	- 85 -
4.1.6	Membrane curvature can counteract lipid packing.....	- 87 -
4.1.7	The level of saturation in PI affects kinase activity.....	- 89 -
4.2	Discussion.....	- 91 -
5	Activation of VPS34 complexes by Rab GTPases.....	- 98 -
5.1	Results.....	- 98 -
5.1.1	Immobilisation of Rab GTPases on membranes.....	- 98 -
5.1.2	Rab5a is a strong activator of complex II.....	- 100 -
5.1.3	Rab7a does not activate either complexes I or II.....	- 102 -
5.1.4	Rab7a is a strong activator of complex II Rubicon.....	- 104 -
5.1.5	Rab1a is a complex I specific activator.....	- 106 -
5.2	Discussion.....	- 110 -
6	Studying VPS34 complex II on Rab5a coated membranes by MS and cryo-ET	- 114 -
6.1	Results.....	- 114 -

6.1.1	Mapping Rab5a binding to complex II by HDX-MS	114 -
6.1.2	Mapping Rab5a binding to complex II by UAA crosslinking	116 -
6.1.3	Rab5a uses a tripartite binding site made of VPS34 and VPS15	118 -
6.1.4	Cryo-ET to study membrane bound VPS34 complex.....	120 -
6.1.5	Sample preparation strategy for subtomogram averaging.....	120 -
6.1.6	Particle extraction and identification in subtomogram averaging-	123 -
6.1.7	Analysing structural heterogeneity by 3D classification.....	128 -
6.1.8	Subtomogram averaging of complex II UVRAG Δ C+BATS on Rab5a decorated membranes at 9.8 Å.....	131 -
6.1.9	Cryo-ET confirms Rab5a tripartite binding site	133 -
6.1.10	Capturing VPS34 in its activated state	135 -
6.1.11	Beclin-1 BARA is the main membrane binding site	136 -
6.1.12	Analysing flexibility of membrane binding by 3D classification	138 -
6.2	Discussion	141 -
7	Conclusion.....	156 -
8	References	161 -

List of figures

Figure 1–1: Cellular localisation of Rab GTPases	- 2 -
Figure 1–2: Rab GTPases as molecular switches.....	- 3 -
Figure 1–3: Cellular distribution of Rab GTPases is driven by the GTPase Cycle.....	- 5 -
Figure 1–4: Endosome maturation by Rab5-Rab7 conversion.....	- 7 -
Figure 1–5: Overview of the autophagy pathway	- 13 -
Figure 1–6: Structures of glycerophospholipid species	- 17 -
Figure 1–7: Physicochemical parameters for membrane-protein interaction	- 19 -
Figure 1–8: Class III PI3-kinase VPS34 produces PI(3)P.....	- 22 -
Figure 1–9: Structural organisation of the class III PI3K complexes.....	- 24 -
Figure 1–10: Workflow of HDX-MS to study protein-protein interactions	- 30 -
Figure 1–11: Workflow of cryo-ET and subtomogram averaging.....	- 34 -
Figure 1–12: Missing wedge bias in Fourier space.....	- 38 -
Figure 4–1: Design of GUV PI3 kinase assay	- 71 -
Figure 4–2: Human complex I is more active than complex II on DO base lipids...-	73 -
Figure 4–3: Complex I has a higher affinity for membranes than complex II.....-	74 -
Figure 4–4: The ATG14L BATS domain is crucial for the activity of complex I on DO base membranes	- 75 -
Figure 4–5: BATS domain activates complex II UVRAG fusion constructs	- 76 -
Figure 4–6: Analysis of membrane binding of human complex I using HDX-MS....-	78 -
Figure 4–7: Analysis of membrane binding of human complex II using HDX-MS..-	79 -
Figure 4–8: Complex dependent membrane binding of the BARA domain.....-	80 -
Figure 4–9: Complex II relies more on Beclin 1 BARA domain for membrane binding than complex I.....	- 82 -
Figure 4–10: Increasing PS levels activate VPS34, complexes I and II.....	- 84 -

Figure 4–11: Phosphoinositides activate complexes I and II.....	86 -
Figure 4–12: Packing defects increase the activity of complexes I and II.....	88 -
Figure 4–13: AF647-PX binds to PI(3)P regardless of lipid saturation.....	89 -
Figure 4–14: Saturation level of the substrate PI influences kinase activity.....	90 -
Figure 4–15: Factors that increase activity of complexes I and II	97 -
Figure 5–1: Immobilisation of Rab GTPases on membranes	99 -
Figure 5–2: Membrane bound Rab5a activates complex II in a GTP dependent manner	100 -
Figure 5–3: Rab5a recruits complex II to membranes.....	101 -
Figure 5–4: Complex I is less activated by Rab5a-GTP than complex II.....	102 -
Figure 5–5: Rab7a does not activate complex I or II.....	103 -
Figure 5–6: Rab7a does not recruit complex II to membranes.....	104 -
Figure 5–7: Membrane bound Rab7a is an activator for complex II Rubicon.....	105 -
Figure 5–8: Rab7a recruits complex II Rubicon to the membrane	105 -
Figure 5–9: MitoID results show Rab1a interacts only with complex I subunits	107 -
Figure 5–10: Membrane bound Rab1a activates complex I.....	108 -
Figure 5–11: Rab1a recruits complex I to membranes.....	109 -
Figure 5–12: Rab1a does not activate complex II.....	109 -
Figure 6–1: Mapping the binding of Rab5a to complex II by HDX-MS.....	115 -
Figure 6–2: UAA crosslinking of Rab5a to VPS34 in complex II	117 -
Figure 6–3: Summary of HDX and UAA crosslinking of Rab5a and complex II....	119 -
Figure 6–4: Comparison of acquired cryo-electron tomography data sets and their subtomogram averaging results	121 -
Figure 6–5: Membrane bound Rab5a can activate complex II UVRAG Δ C+BATS	122 -
Figure 6–6: Rab5a coated vesicles decorated with complex II UVRAG Δ C+BATS	124 -

Figure 6–7: Particle picking along vesicle membranes	126 -
Figure 6–8: Structure determination progress of complex II by subtomogram averaging.....	127 -
Figure 6–9: Analysis of heterogeneity by 3D classification.....	129 -
Figure 6–10: Wedge bias in 3D classification.....	130 -
Figure 6–11: 9.8 Å reconstruction of complex II UVRAG Δ C+BATS on Rab5a decorated membranes	131 -
Figure 6–12: Model of Rab5a bound to human complex II UVRAG Δ C+BATS.....	132 -
Figure 6–13: Rab5a binds to three regions in VPS34 and VPS15 in complex II-	134 -
Figure 6–14: Cryo-ET catches VPS34 kinase domain in its active state.....	136 -
Figure 6–15: Cryo-ET structure of membrane-associated human complex II UVRAG Δ C+BATS.....	137 -
Figure 6–16: Complex II UVRAG Δ C+BATS is highly flexible on membranes.....	139 -
Figure 6–17: Rab5a effector binding surface	142 -
Figure 6–18: VPS34 HELCAT dynamics.....	146 -
Figure 6–19: Beclin 1 BARA domain membrane contacts	149 -
Figure 6–20: Comparison of Rab5 and Rab1 amino acid sequence and tertiary structure.....	152 -
Figure 6–21: Comparison of complexes I and II architecture	154 -
Figure 7–1: Differential membrane recruitment of VPS34 complexes I and II to omegasomes and early endosomes.....	157 -

List of tables

Table 1: Plasmid table.....	42 -
-----------------------------	------

Table 2: Lipid species	- 50 -
Table 3: GUV lipid mixtures.....	- 51 -
Table 4: SUV/LUV lipid mixtures.....	- 55 -
Table 5: Subtomogram averaging angular search runs	- 66 -

1 Introduction

1.1 The Rab GTPase family

Eukaryotic cells contain a wealth of intracellular organelles surrounded by membranes. The membranes provide a barrier to create compartments with distinct properties and thereby separate different cellular functions. However, organelles still need to exchange substrates among each other. Thus, eukaryotic cells have evolved an intricate and tightly controlled vesicular trafficking system. On the one hand, vesicles have to be able to identify their target membrane in order to faithfully deliver their cargo. On the other hand, organelles have to maintain their identity and function, despite vesicles constantly budding and fusing in this network. The Rab family of GTPases are key players in this process.

1.1.1 Rab GTPases in the cell

The superfamily of small GTPases encompasses the Rab, Ras, Rho, Ran and Arf families (Colicelli, 2004; Touchot et al., 1987). With over 70 members, Rab GTPases ('Ras-related in brain') constitute the largest of these families. All small GTPases possess a conserved fold called the G-domain, which contains sequence motifs for GTP and GDP binding and GTP hydrolysis (Vetter, 2014). The sheer number of different Rab GTPases reflects the complexity of membrane transport among organelles. Rab GTPases are localised to distinct membranes in the cell and thereby help to confer organelle identity (Pfeffer, 2013). Some Rabs also share an

evolutionary ancestor and have overlapping functions and interaction partners (Klöpffer et al., 2012). Rab GTPases are involved in all stages of vesicular transport and mediate vesicle budding, transport, tethering and fusion (Stenmark, 2009).

Figure 1-1 depicts the localisation of some Rab GTPase family members.

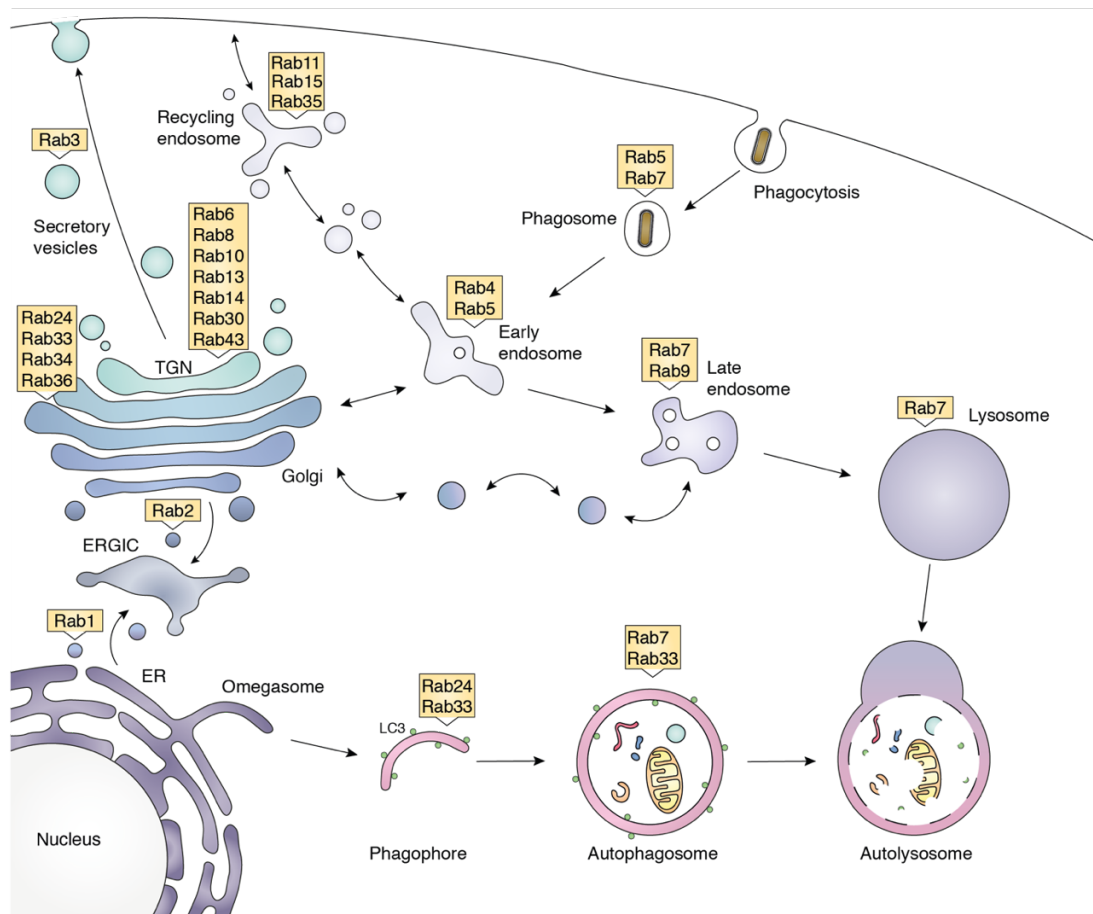


Figure 1-1: Cellular localisation of Rab GTPases

Overview of Rab GTPases in the cellular trafficking pathways. Figure adapted from Stenmark, 2009.

Rab GTPases act out these functions because of their switch-like nature. The first crystal structure of a small GTPase was solved in 1995, with the G-domain of the Ras GTPase Rap1A bound to the Ras-binding domain of the protein kinase c-Raf (Nassar et al., 1995). Since then, structures of other small GTPases have been determined, including a plethora of Rab GTPase structures.

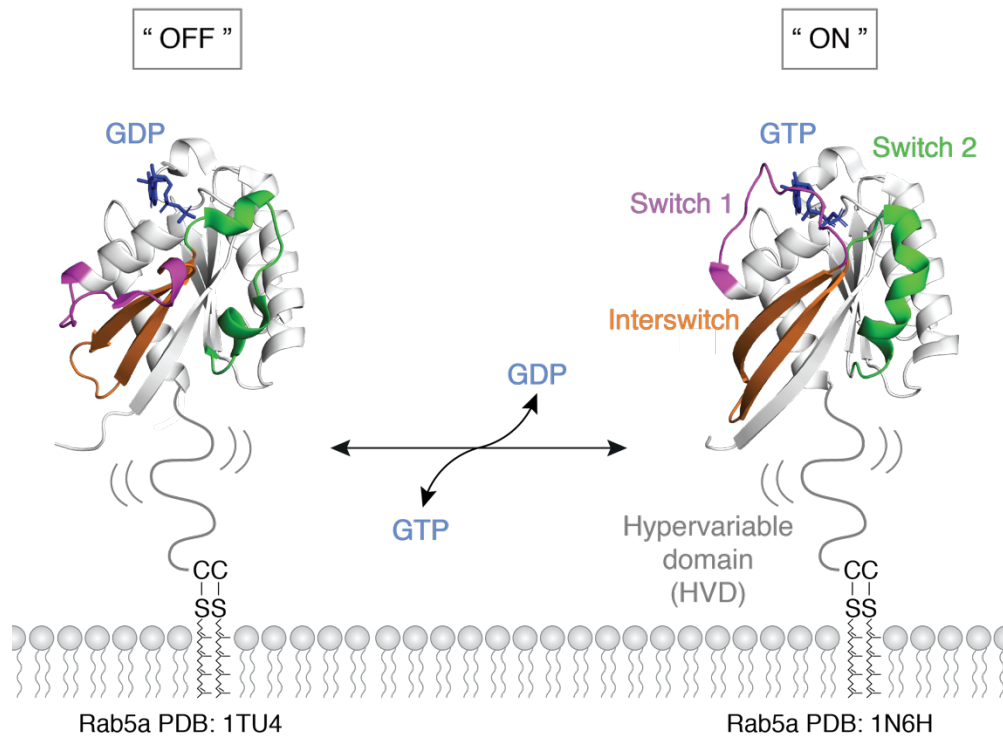


Figure 1-2: Rab GTPases as molecular switches

Crystal structures of human Rab5 in its “on”/GTP (PDB: 1N6H) and “off”/GDP-bound forms (PDB: 1TU4). The conserved switch 1, interswitch and switch 2 regions are shown in purple, orange and green, respectively. The Mg^{2+} ion was omitted so that the nucleotide is clearly visible. The unstructured hypervariable region is located at the C-terminus and contains the C-X-C or C-C motif, which is prenylated for membrane insertion.

The switch-like nature is conveyed by the conformations of three contiguous regions within the G-domain: the switch 1/interswitch/switch 2 interface. This interface has conserved residues for binding the guanine base, the γ -phosphate and the Mg^{2+} ion. When GTP is bound, switches 1 and 2 are stabilised. Upon GTP hydrolysis to GDP and Pi, the fold of the switch regions becomes increasingly unstructured (Pylypenko et al., 2017). Thus, Rabs are considered to be “on” if they are bound to GTP and “off” when bound to GDP. Figure 1-2 shows the GTP- and GDP-bound structures of Rab5a. Rab5a undergoes a dramatic conformational change upon GTP hydrolysis. The switch 1 loop dislocates by ~ 20 Å and the switch 2 helix becomes flexible and unstructured (Zhu et al., 2004). Comparing the GDP- and GTP-bound conformations of several Rab GTPases, different degrees of

conformational changes are apparent. However, compared to the GTP-bound conformations, all GDP-bound structures share a high degree of flexibility and disorder in the switch regions (Pylypenko et al., 2017). Thus, only the stabilised “on”/GTP form specifically recruits Rab effector proteins. Rab effectors can have a variety of functions and can act as tethers, motors, sorting adaptors, kinases and phosphatases (Gillingham et al., 2014). Rab GTPases also have an unstructured C-terminus called the hypervariable domain (HVD) that ends in a C-X-C or C-C motif (where C denotes a cysteine and X denotes another amino acid) (Figure 1–2). These cysteine residues are both geranylgeranylated by the Rab geranylgeranyltransferase II (RabGGTase II) and the lipid acyl chains are then used for membrane association (Shen and Seabra, 1996).

1.1.2 Rab regulators and effectors

Rab GTPases do have an intrinsic GTPase activity but it is on average very slow (Bergbrede et al., 2005). Instead, auxiliary proteins called GEFs (guanine nucleotide exchange factor) and GAPs (GTPase-activating protein) support the conversion between the “on”/GTP and “off”/GDP state. Whereas GEFs exchange GDP for GTP to activate the Rabs, GAPs stimulate the intrinsic Rab GTPase activity thereby generating the inactive GDP form (Barr and Lambright, 2010). Both GEFs and GAPs are specific for individual Rab isoforms or subfamilies. Furthermore, the nucleotide binding/hydrolysis cycle is highly dependent on the state of membrane association.

Figure 1–3 shows how Rabs are thought to cycle between membranes in the cell (Goody et al., 2017; Seixas et al., 2013). After ribosomal synthesis, unprenylated

Rabs are initially recognised by the Rab escort protein (REP), which in turn presents it to the RabGGTase II for prenylation. After prenylation, the prenylated Rab is delivered to the membrane by REP where it is activated to its GTP state by its specific GEF.

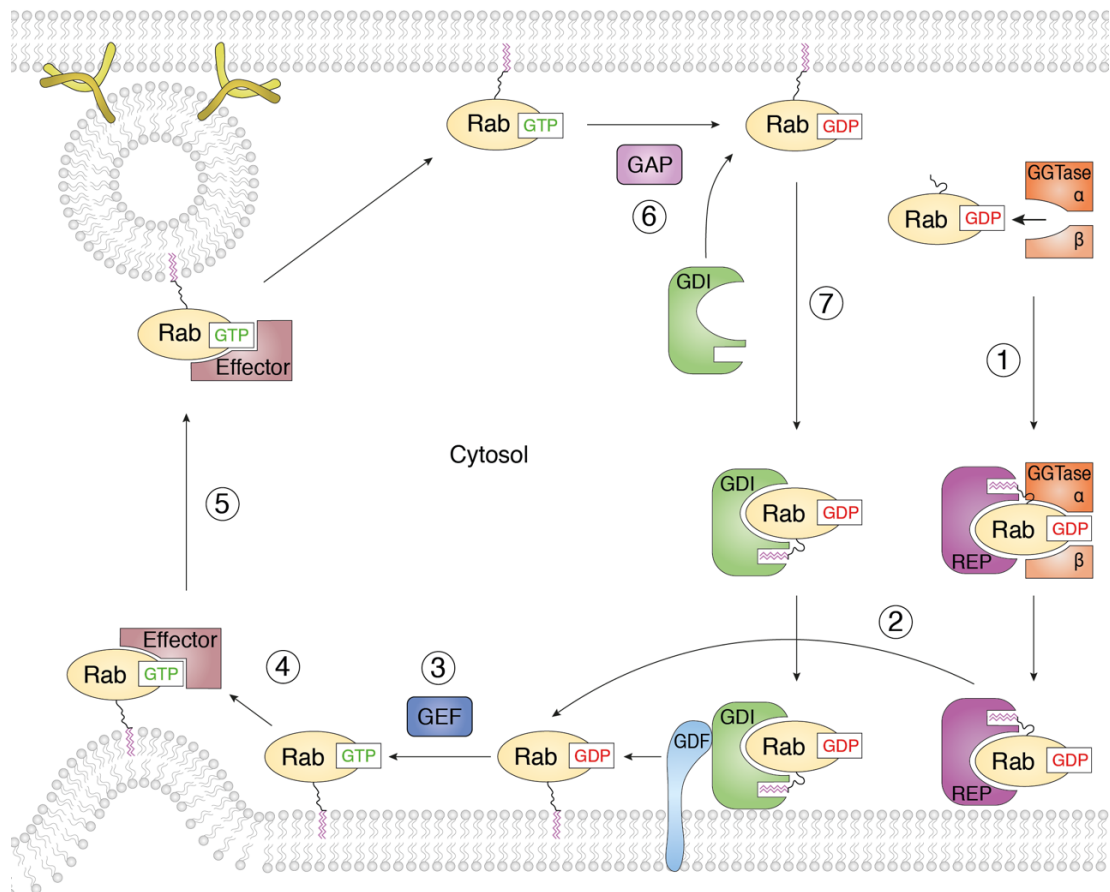


Figure 1-3: Cellular distribution of Rab GTPases is driven by the GTPase Cycle

(1) Rabs are prenylated by RabGGTase II (Rab geranylgeranyltransferase II) and (2) delivered to membranes by REP (Rab escort protein). (3) Rabs are activated by GEFs (guanine nucleotide exchange factor) and (4) subsequently attract effector proteins for vesicle trafficking (5). (6) Rabs are deactivated by GAPs (GTPase-activating protein) and (7) extracted from membranes by GDI (Rab guanine-nucleotide dissociation inhibitor). Figure adapted from Goody et al. 2017 and Seixas et al. 2013.

Once Rab is activated, it can recruit effector proteins to the membrane to regulate downstream events such as membrane tethering. Finally, Rab is deactivated by its specific GAP. Rab guanine-nucleotide dissociation inhibitor (GDI) then recognises the GDP state and Rab is removed from the membrane and kept soluble in the

cytosol. The membrane re-insertion is mediated by the GDI dissociation factor (GDF), which releases Rab from GDI. The cycle can then start over again. The question of how Rabs are targeted to specific membranes was initially thought to be solved in 1991 (Chavrier et al., 1991). Chavrier et al. claimed that the HVD was solely responsible for the specificity of membrane targeting. However, several studies since then have shown this picture is much more complex. Whereas Rab7 and Rab35 require their C-termini, Rab1 and Rab5 can be targeted to their membranes even if they have a polyethylene glycol (PEG) stretch instead of their HVD (Li et al., 2014). Current thinking is that the interplay of several components, such as the HVD, effectors and GEFs, determine Rab GTPase targeting to specific membranes (Goody et al., 2017).

1.1.3 Endosome maturation orchestrated by Rab GTPases

The endocytic trafficking network is in charge of sorting the endocytosed cargo to their final destination. Typically, endocytosed vesicles are initially delivered to early endosomes that are scattered in the cell periphery near the plasma membrane. Due to their slightly acidic pH (~pH 6), ligands dissociate from their receptors so that receptors can be directly recycled back to the plasma membrane (Cullen and Steinberg, 2018). Ligands and cargos, which are destined for degradation, are then further directed to the lysosome through the endocytic network. This happens by the maturation of early endosomes into late endosomes, which then finally fuse with lysosomes (Huotari and Helenius, 2011). The maturation process of early to late endosomes includes a change of two key markers of the compartments. Firstly, Rab5 is specifically located on early endosomes (Bucci et al., 1992). When early

endosomes mature into late endosomes, Rab5 is replaced with Rab7 (Zerial and McBride, 2001). Secondly, early endosomes have a high concentration of the phosphoinositide phosphatidylinositol 3-phosphate (PI(3)P), which is converted to phosphatidylinositol 3,5-bisphosphate (PI(3,5)P₂) during maturation (Wallroth and Haucke, 2017). The maturation of endosomes is highly conserved throughout evolution and controls the directionality of membrane trafficking. Figure 1–4 shows key steps in the maturation process and Rab5-Rab7 conversion.

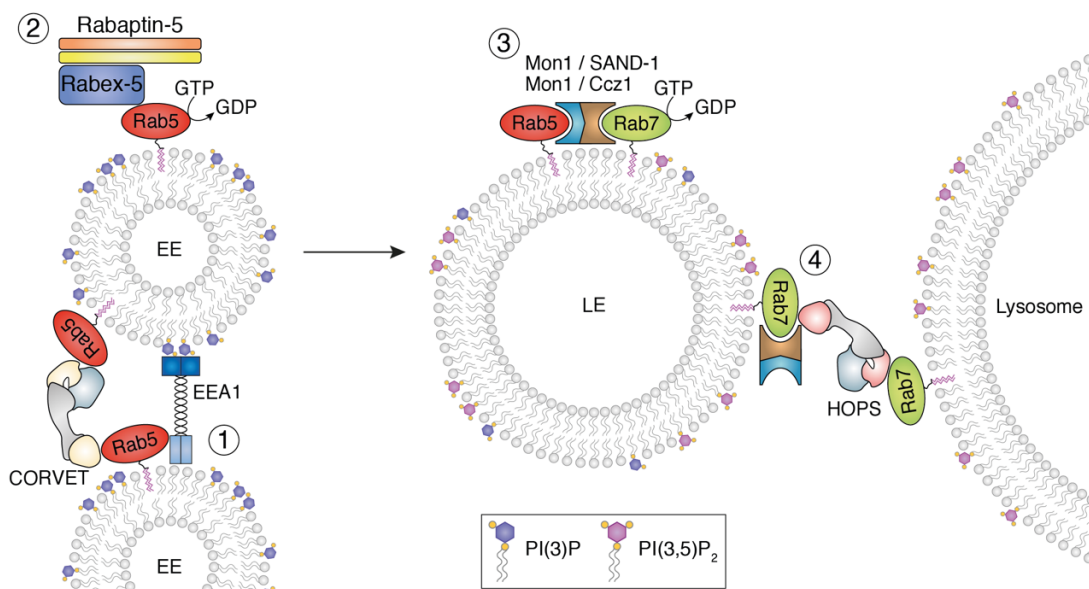


Figure 1–4: Endosome maturation by Rab5-Rab7 conversion

(1) Rab5 gets activated by the Rabaptin-5/Rabex-5 complex. Activated Rab5 recruits phosphatidylinositol 3-kinase (PI3K) VPS34, which produces PI(3)P. (2) PI(3)P and Rab5 recruit endosomal tethering factors EEA1 (early endosome autoantigen 1) and CORVET (class C core vacuole/endosome tethering). (3) Maturation of early to late endosomes goes along with a change in phosphoinositides and Rab GTPases. PI(3)P recruits phosphatidylinositol 3-phosphate 5-kinase PIKFYVE for the production of PI(3,5)P₂. The Rab5-Rab7 conversion is orchestrated by Mon1/SAND-1 and Mon1/Ccz1. (4) Finally, late endosomes fuse with lysosomes by the tethering complex HOPS (homotypic fusion and protein sorting).

Rab5 gets activated in a feedback loop by the effector Rabaptin-5 and the GEF Rabex-5 (Horiuchi et al., 1997; Zhang et al., 2014). Rabex-5 and Rabaptin-5 form a tight complex in which Rabaptin-5 localises the complex to membranes through the interaction with Rab5-GTP. Subsequently, Rabaptin-5 also causes a conformational

change in the autoinhibited Rabex-5 in order to activate its GEF activity to produce more Rab5-GTP (Zhang et al., 2014). Rab5-GTP in turn recruits more Rabex-5/Rabaptin-5 to membranes, which leads to the production of more activated Rab5 (Lippé et al., 2001). This loop generates an abundance of Rab5-GTP that then recruits other effectors. Phosphatidylinositol 3-kinase (PI3K) VPS34, which is the primary producer of endosomal PI(3)P, is recruited by Rab5 through the interaction with the regulatory protein VPS15 (Christoforidis et al., 1999). VPS34 will be discussed in detail in chapter 1.4. The endosomal tether EEA1 (early endosome autoantigen 1) binds to both Rab5 and PI(3)P and leads to the homotypic fusion of early endosomes (McBride et al., 1999). The CORVET (class C core vacuole/endosome tethering) protein complex also acts as a tether of early endosomes by interacting with Rab5 (Balderhaar et al., 2013). During the maturation process, PI(3)P recruits the phosphatidylinositol 3-phosphate 5-kinase PIKFYVE for the production of PI(3,5)P₂ (Rutherford et al., 2006). The conversion of Rab5 to Rab7 is regulated by two complexes Mon1/SAND-1 and Mon1/Ccz1 (Cabrera and Ungermann, 2010). Mon1/SAND-1 replaces Rabex-5 and thereby disrupts the Rab5 feedback activation loop (Poteryaev et al., 2010). Mon1/Ccz1 is recruited by PI(3)P and Rab5 and acts as a GEF for Rab7 activation (Cabrera et al., 2014; Kinchen et al., 2008; Yasuda et al., 2015). Additionally, Mon1/SAND-1 interacts with the tethering complex HOPS (homotypic fusion and protein sorting) (Poteryaev et al., 2010). The HOPS and CORVET complex share the same core subunits (Vps11, Vps16, Vps18, Vps33), but have unique subunits to either interact with Rab5 for CORVET (Vps3 and Vps8) or Rab7 for HOPS (Vps39 and Vps41) (Balderhaar and Ungermann, 2013). As a final step, the HOPS complex mediates late endosome-lysosome fusion by binding to Rab7 (Pols et al., 2012).

To conclude, a cascade of effectors and GEFs orchestrate the conversion of Rab5 to Rab7 containing endomembranes. However, “Rab cascades” are a general mechanism and can also be found with other Rabs in the endocytic network and secretory pathway (Mizuno-Yamasaki et al., 2012).

1.2 Autophagy

Autophagy (Greek, “self-eating”) describes all mechanisms by which parts of the cell, such as organelles or proteins, are delivered to the lysosome and degraded. The term “autophagy” was coined by Christian de Duve in 1963, who was awarded the Nobel Prize for Physiology and Medicine in 1974 for the discovery of the lysosome and peroxisome (Sabatini and Adesnik, 2013). He and other colleagues were puzzled by the discovery of double membrane bound vesicles containing cellular fragments of mitochondria, endoplasmic reticulum (ER) and lysosomal enzymes. Sixty years later, we have come closer to unravelling the mystery of autophagy. Autophagy is a highly conserved pathway from yeast to plants and animals. Although autophagy was initially discovered in mammalian cells, it was yeast genetics, which really shed light on the broad spectrum of proteins involved. These screens were carried out in the laboratories of Ohsumi and Thumm (Thumm et al., 1994; Tsukada and Ohsumi, 1993). To date, 42 AuTophagy-related (Atg) genes have been identified, with 15 “core” Atg genes (Atg 1-10, 12-14, 16 and 18) (Parzych et al., 2018; Suzuki and Ohsumi, 2007; Xie and Klionsky, 2007). These core gene products are essential for autophagosome formation and have homologues in mammals (Ktistakis and Tooze, 2016). In general, there are three different types of autophagy: chaperone-mediated autophagy, microautophagy and macroautophagy (Parzych and Klionsky, 2013). Chaperone-mediated autophagy is the direct lysosomal degradation of soluble cytosolic proteins through chaperones into lysosomes. During microautophagy, lysosomal compartments, which are called vacuoles in yeast, form direct invaginations that close around cytosolic cargo. In macroautophagy, a crescent double membrane structure is formed, termed phagophore, which expands and eventually forms a double-membrane vesicle – the

autophagosome. The autophagosome subsequently fuses with lysosomes to form autolysosomes and the engulfed content is degraded. Here, I will focus on macroautophagy (hereafter called autophagy). Autophagy can be separated into four steps, which can be seen in Figure 1–5: (1) Phagophore initiation, (2) autophagosome expansion and maturation, (3) autophagosome-lysosome fusion and (4) degradation.

1.2.1 Autophagy initiation

The initiation of autophagy is determined by the energy state of the cell, which is dependent on amino acid availability, glucose metabolism and presence of growth factors. The multi subunit protein complex mTORC1 (mechanistic target of rapamycin complex 1) is known to be the master regulator of cell growth and metabolism (Saxton and Sabatini, 2017). Under normal growth conditions, mTORC1 is active and suppresses autophagy by phosphorylating and thereby inactivating the UNC51-like Ser/Thr kinase (ULK1) complex (Kim et al., 2011; Puente et al., 2016). The ULK1 complex consists of ULK1, FIP200, ATG13, and ATG101. ULK1 is the only kinase in the hetero-tetrameric complex and is critical for autophagy initiation (Chan et al., 2008; Hara et al., 2008). Once mTORC1 becomes inactivated by starvation, the ULK1 complex is released and localises to subdomains of the ER to initiate the formation of the omegasome (Itakura and Mizushima, 2010; Karanasios et al., 2013). Although it is still debated where phagophores are formed, the ER is the most frequent proximal membrane to new autophagosomes and clearly plays a critical role in autophagy initiation (Axe et al., 2008; Itakura and Mizushima, 2010). However, it has been reported that autophagosomes are formed at ER-mitochondria

or ER-plasma membrane contact sites (Hailey et al., 2010; Hamasaki et al., 2013; Nascimbeni et al., 2017). The mechanism by which ULK1 is recruited to these sites is still under investigation (Mercer et al., 2018; Zachari and Ganley, 2017). The only transmembrane Atg protein is ATG9, which is required for the initiation of autophagy (Mari et al., 2010; Orsi et al., 2012). ATG9 has been located to various compartments such as the Golgi and endosomes and has been shown to be proximal to forming phagophores but not stably associated with them (Orsi et al., 2012; Yamamoto et al., 2012; Young et al., 2006). Immediately downstream, the PI3K VPS34 complex I (VPS34, VPS15, Beclin 1, ATG14L) is recruited to the ULK1 assembly site and produces PI(3)P, which is essential for the following steps of autophagy (Axe et al., 2008; Itakura and Mizushima, 2010). VPS34 complex I will be discussed in detail in chapter 1.4.1. ULK1 phosphorylates VPS34, ATG14L and Beclin 1 to increase the PI(3)P production (Egan et al., 2015; Park et al., 2018, 2016; Russell et al., 2013a; Wold et al., 2016). The production of PI(3)P provides a platform for DFCP1 (double FYVE domain-containing protein 1) and WIPI (WD-repeat domain phosphoinositide-interacting proteins) isoforms to bind. DFCP1 contains two FYVE domains, which bind to PI(3)P (Ridley et al., 2001). DFCP1 is not essential for autophagy but has gained attention for its ability to promptly localise to the VPS34 complex I derived PI(3)P in the ER membrane and thereby function as an omegasome marker (Axe et al., 2008). There are four members of the WIPI family (WIPI1-4) and all fold into a seven-bladed β -propeller that binds to PI(3)P (Proikas-Cezanne et al., 2015). WIPI2B in turn recruits the ATG12-5-16L complex by binding to ATG16L (Dooley et al., 2014).

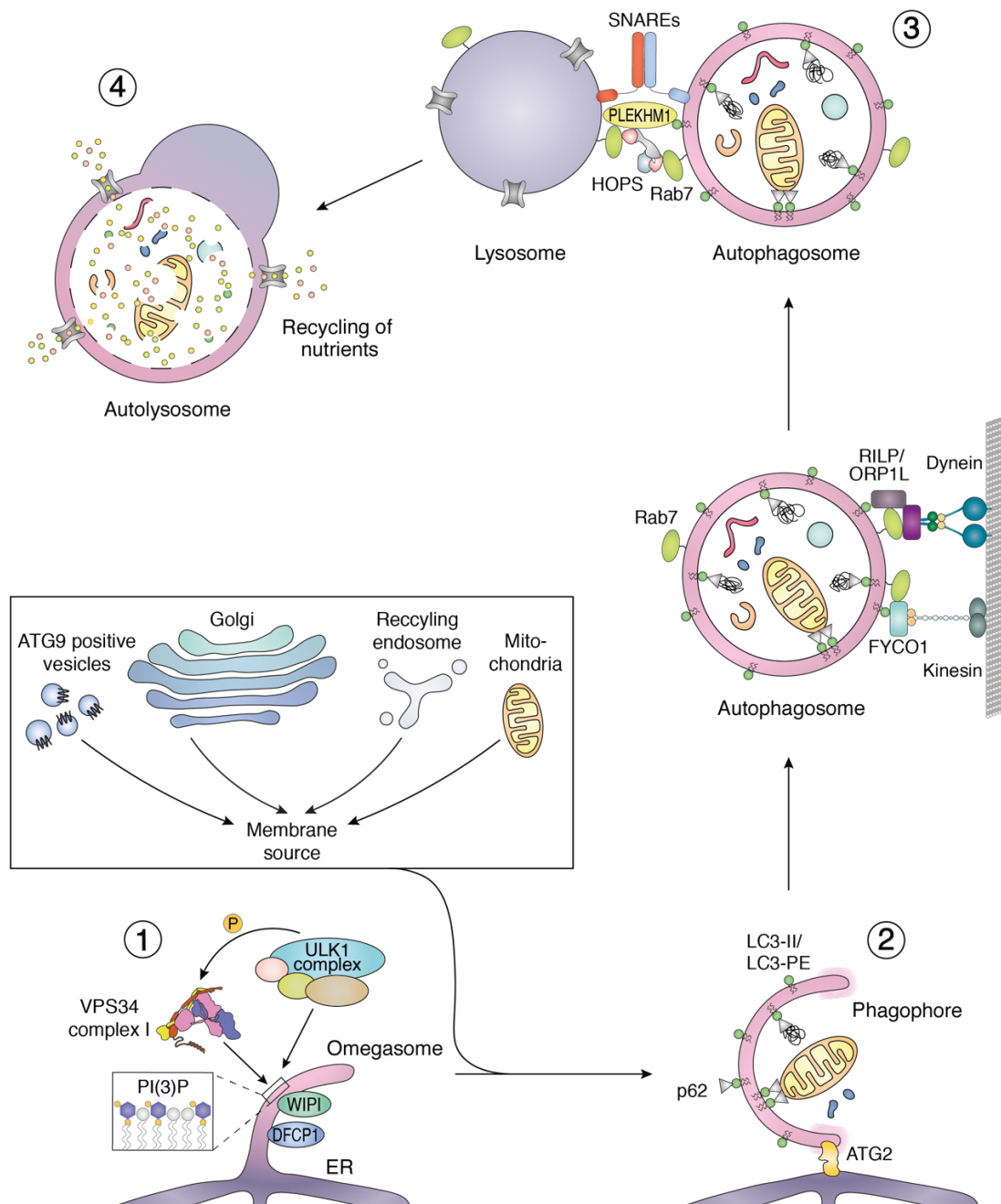


Figure 1-5: Overview of the autophagy pathway

(1) Autophagosome biogenesis was shown to occur at the ER. One of the first steps, is the recruitment of the ULK complex (ULK1, FIP200, ATG13, and ATG101), which phosphorylates and activates the VPS34 complex (VPS34, VPS15, Beclin 1, ATG14L) to produce PI(3)P. PI3P attracts DFCP1 and WIPIs for autophagosome progression. (2) WIPI recruits the conjugation machinery to produce lipidated LC3 (LC3-II/ LC3-PE). LC3 mediates cargo recruitment and phagophore expansion. ATG2 acts as a vesicle tether and lipid transporter. Other membrane sources such as ER-exit sites (ERES), ER-Golgi intermediate compartment (ERGIC), ATG9 positive vesicles, Golgi, recycling endosomes and mitochondria contribute to autophagosome formation. (3) Autophagosomes are transported by motor proteins dynein and kinesin towards lysosomes. The fusion of autophagosomes and lysosomes is mediated by the HOPS tethering complex and SNAREs. Additionally, Rab7 and PLEKHM1 are required for the efficient fusion. (4) Acid hydrolases in the lumen break down the content and lysosomal transporters export the nutrients to the cytosol for reuse. Figure adapted from (Dikic and Elazar, 2018).

1.2.2 Autophagosome expansion and maturation

The ATG12-5-16L complex and other members of the Atg family act in an autophagy-specific ubiquitin-like protein cascade to mediate the lipidation of the LC3 family (LC3A, LC3B, LC3C, GABARAP, GABARAPL1, and GABARAPL2). LC3 proteins are cytosolic in fed conditions but are conjugated to phosphatidylethanolamine (PE) (LC3-II/ LC3-PE) upon nutrient depletion and recruited to the autophagosomal membrane (Ichimura et al., 2000; Kabeya et al., 2000; Klionsky and Schulman, 2014). Membrane anchored LC3 and autophagy cargo adaptors like p62 are responsible for the selective degradation of substrates. p62 simultaneously binds to membrane bound LC3 and ubiquitinated proteins and organelles and thereby destines them for degradation (Bjørkøy et al., 2005). The Atg protein cascade and LC3 family members also contribute to the expansion of the phagophore as LC3B and GABARAPL2 have been suggested to promote tethering and membrane fusion (Weidberg et al., 2011). An unresolved question in the field is the source of the membrane for the autophagosome expansion and closure. ATG9 positive vesicles, ER-exit sites (ERES), the ER-Golgi intermediate compartment (ERGIC), the Golgi, mitochondria and (recycling) endosomes have all been suggested to function as membrane sources (Wei et al., 2018). Furthermore, the ER-resident ATG2 has the ability to tether liposomes and to transfer lipids and thereby mediate phagophore expansion (Li et al., 2020; Valverde et al., 2019, Maeda et al., 2019). Recently, several groups have used electron microscopy to solve the structure of ATG2, which forms a 20 nm long rod-shaped tunnel and was shown to bind to WIPI4 on one end (Chowdhury et al., 2018; Li et al., 2020; Valverde et al., 2019; Zheng et al., 2017, Maeda et al., 2019).

1.2.3 Autophagosome-lysosome fusion and degradation

Once the phagophore is closed, the double-membraned autophagosome is moved along microtubules to lysosomes for fusion and the formation of autolysosomes (Nakamura and Yoshimori, 2017). Lysosomes are both in the cell periphery and in the perinuclear region depending on their pH and Rab7 density (Johnson et al., 2016). Transport of autophagosomes has been shown to occur via kinesin and dynein. On the one hand, kinesin binds through FYCO1 (FYVE and coiled-coil domain-containing 1) to Rab7 and LC3 on autophagosomes and moves them towards the cell periphery (Pankiv et al., 2010). On the other hand, dynein mediates autophagosome transport toward the perinuclear region through an interaction network of Rab7, the lysosomal protein RILP and the cholesterol-sensing protein ORP1L (Johansson et al., 2007; Wijdeven et al., 2016). The fusion of autophagosomes with lysosomes has not been fully elucidated but requires the collective action of SNARE proteins, Rab GTPases and tethering factors. For example, the HOPS complex promotes autophagosome-lysosome fusion through its interaction with Rab7 and the SNARE STX17 (Itakura et al., 2012; Jiang et al., 2014; Stroupe et al., 2006). Furthermore, the protein PLEKHM1 (Pleckstrin homology domain containing protein family member 1) interacts with Rab7, HOPS complex and LC3 (McEwan et al., 2015; Tabata et al., 2010). Deletion of PLEKHM1 leads to an increase in the number of stalled autophagosomes indicating that it is involved in autophagosome-lysosome fusion (McEwan et al., 2015). After fusion, the acid hydrolases in the lysosomal lumen break down the autophagosomal membrane and the engulfed content of the autophagosome. Specific lysosomal transporters then export nucleotides, amino acids, lipids, sugars and other lysosomal degradation products to the cytosol for the cell to reuse (Ballabio and Bonifacino, 2019).

1.3 Membrane lipids

Lipids are amphipathic molecules, which have a polar end and a hydrophobic end. Their amphipathic character enables them to form compartments in the cell to segregate chemical reactions and biological processes. However, lipids can also form and fuse vesicles and tubules in order to enable contact between compartments. Eukaryotic organelles are composed of a variety of different lipids (Meer et al., 2008). At one extreme, the ER contains an abundance of loosely packed unsaturated lipids with little negatively charged phospholipids, in order to support the folding of nascent transmembrane proteins and protein secretion. At the other extreme, the plasma membrane consists of rigid saturated lipids, cholesterol and negatively charged phospholipids to protect the cell and serve as a barrier that reduces permeability (Vanni et al., 2014). The composition of lipids critically influences the function of membrane-embedded and -associated proteins as many essential signalling processes take place on membrane surfaces (Bogdanov et al., 2008). The most common lipids in eukaryotic cells are glycerophospholipids: phosphatidylcholine (PC), phosphatidylethanolamine (PE), phosphatidic acid, (PA) phosphatidylserine (PS) and phosphatidylinositol (PI) (Figure 1-6A and B) (Vance, 2015). PC is especially abundant and accounts for ~50% of the total phospholipids. Glycerophospholipids consist of two hydrophobic fatty acids, which are esterified to a glycerol backbone (Figure 1-6A). Additionally, the glycerol backbone is esterified to a phosphate group, which serves as a link to variable headgroups (Figure 1-6B). The headgroups can either be zwitterionic or anionic. While PC and PE are zwitterionic, PA, PS and PI are anionic. Furthermore, the inositol ring of PI can be reversibly phosphorylated at the 3rd, 4th and 5th position, generating a total of seven different phosphoinositide species (PIPs) (Figure 1-6C).

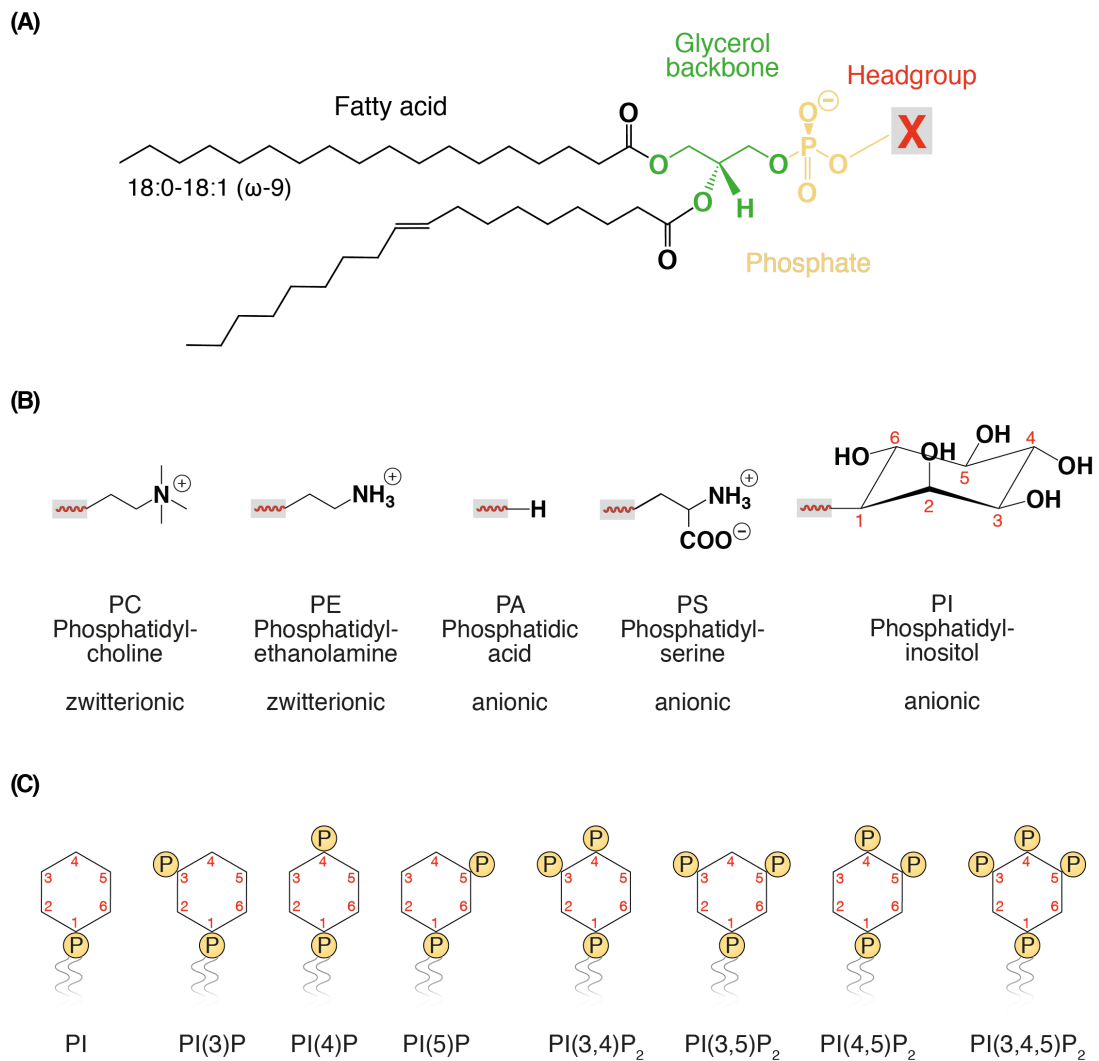


Figure 1-6: Structures of glycerophospholipid species

(A) Glycerophospholipids are made of two fatty acid esters, a glycerol backbone, a phosphate group and a variable headgroup. **(B)** Depiction of the headgroups of the most common glycerophospholipids: Phosphatidylcholine (PC), phosphatidylethanolamine (PE), phosphatidic acid, (PA) phosphatidylserine (PS) and phosphatidylinositol (PI). **(C)** PI can be further phosphorylated at the 3rd, 4th and 5th positions, generating a total of seven different phosphoinositide (PIP) species.

PIPs adopt a unique role among lipids. Although these lipids comprise less than 1% of the total cell lipids, they are crucial for fundamental processes such as membrane trafficking, cytoskeletal dynamics and cell growth (Lemmon, 2008). PIPs are also not uniformly distributed over all membranes, but each organelle is enriched in one or several PIPs that can further be organised in microdomains (Aoyagi et al., 2005; Gillyooly et al., 2003; Yoshida et al., 2017). The production of PIPs is highly regulated

in time and space by a family of phosphoinositide kinases and phosphatases (Sasaki et al., 2009). Examples of PIPs on specific organelles are: PI(4,5)P₂ at the plasma membrane, PI(3)P on early endosomes, PI(3,5)P₂ on late endosomes and PI(4)P at the Golgi (Vicinanza et al., 2008).

Membranes are ubiquitous in the cell, which requires proteins to be selective to which membranes they bind to. Three physicochemical parameters can be used to describe membranes: lipid packing, curvature and electrostatic charge (Bigay and Antonny, 2012) (Figure 1-7A). Lipid packing is influenced by the amount of saturated and unsaturated acyl chains in the membrane bilayer. Unsaturated lipids have one or several double bonds in their acyl chains, which create “kinks” and lead to geometrical packing defects (Bigay and Antonny, 2012). These defects are gaps in the membrane surface into which hydrophobic amino acid chains of peripheral membrane proteins can insert (Vanni et al., 2014). The extent of these gaps is dependent on the level of saturation in the acyl chains. While polyunsaturated acyl chains promote the formation of shallow defects, monounsaturated acyl chains caused deep defects (Pinot et al., 2014). The formation of packing defects by curvature usually goes hand in hand with the lipid composition. Increasing the membrane curvature alters the arrangement of the lipids and increases the space between headgroups and thereby create packing defects (Antonny, 2011; Vanni et al., 2014). Often, peripheral proteins do not actually recognise the actual curvature of a membrane but the increase in lipid packing defects in the curved region (Antonny, 2011). The electrostatic charge of a membrane can also attract peripheral membrane proteins by interaction with the lipid headgroups (Bigay and Antonny, 2012). PS and PIPs make up the main acidic phospholipids in the cell. The

interactions with charged membrane can either be mediated by non-specific amino acid residues or by specific structural domains, which is often the case for PIPs (Lemmon, 2008).

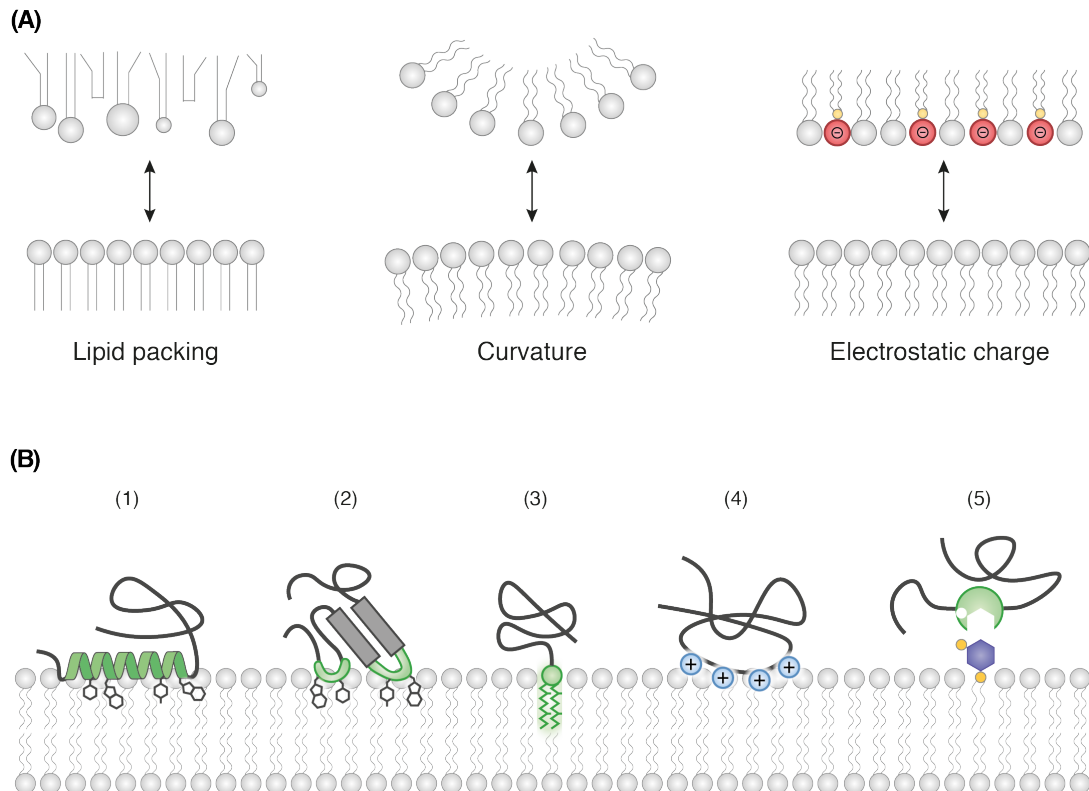


Figure 1-7: Physicochemical parameters for membrane-protein interaction

(A) Membranes can be described by three physicochemical parameters: Lipid packing, curvature and electrostatic charge. Lipid packing is influenced by acyl chain saturation. Unsaturated lipids have a looser packing than saturated lipids and have packing defects (left). The electrostatic charge of the membrane depends on anionic lipids like PS or PIPs (right). Figure adapted from Bigay and Antonny 2012. **(B)** Peripheral membrane proteins bind to lipid bilayers transiently and only bind to the outer leaflet of the lipid bilayer. They can interact with membranes via an (1) amphipathic helix, (2) hydrophobic loop, (3) lipid anchor, (4) non-specific basic amino acids or (5) stereo specific lipid binding domains.

Figure 1-7B shows how some types of peripheral membrane proteins detect and bind specific membranes. Peripheral membrane proteins bind transiently to the outer leaflet of the lipid bilayer, but otherwise behave like soluble proteins (Whited and Johs, 2015). Bulky hydrophobic amino acids often insert into packing defects and lead to a partitioning of the membrane (Vanni et al., 2014). These aromatic

residues can be in an amphipathic helix or in a flexible loop (Figure 1-7B, (1) and (2)). Furthermore, proteins can be post-translationally modified by prenylation, myristoylation or palmitoylation with a lipid anchor, which facilitate insertion into the membrane (Figure 1-7B, (3)). Charged lipids like PS or PIPs can be recognised by non-specific basic amino acids or by a stereospecific arrangement of amino acids in protein domains (Figure 1-7B, (4) and (5)).

1.4 VPS34 and its complexes

VPS34 was discovered in the early 1990's by a yeast screen for genes of the vacuolar protein sorting (Vps) pathway (Herman and Emr, 1990). VPS34 belongs to the family of phosphoinositide 3-kinases (PI3Ks), which phosphorylate the 3rd position of the inositol headgroup to generate specific phosphoinositide species (Bilanges et al., 2019). There are three classes of PI3Ks, which have been classified by structural features and substrate specificity. In general, all PI3Ks share a core structure with a C2, helical and kinase domain (Vanhaesebroeck et al., 2010). Class I PI3Ks are subdivided into class IA catalytic subunits (p110 α , p110 β and p110 δ), which bind to the regulatory subunit p85, and the class IB catalytic subunit (p110 γ), which binds to the regulatory subunits p101 and p87 (Vadas et al., 2011). Both subclasses are recruited to the plasma membrane by different signalling pathways. Whereas class IA is recruited and activated by the phosphorylated pYXXM motif of receptor tyrosine kinases, class IB is recruited and activated by the G $\beta\gamma$ subunit following GPCR activation (Engelman et al., 2006). Once recruited, both classes IA and IB use PI(4,5)P₂ to produce PI(3,4,5)P₃ or PIP₃ at the plasma membrane. PIP₃ is an important docking site for protein kinases like AKT, which then trigger a broad spectrum of signalling events to promote cell metabolism, proliferation, survival and growth (Burke and Williams, 2015). Class II PI3Ks only have a catalytic subunit (PI3K-C2 α , PI3K-C2 β , PI3K-C2 γ) and do not associate with a additional regulatory subunit. Although the functions of class II PI3Ks are poorly understood, they are involved in cell growth, clathrin-mediated endocytosis, and insulin signalling by producing mainly PI(3,4)P₂ and to a lesser extent PI(3)P (Burke, 2018). Compared to classes I and II, which possess several isoforms of the catalytic subunit, VPS34 is the only class III PI3K. VPS34 is present in all eukaryotes and is the only PI3K in

yeast (Vanhaesebroeck et al., 2010). VPS34 uses PI as a substrate to produce PI(3)P (Figure 1–8). VPS34 associates with the regulatory subunit VPS15. VPS15 is homologous to serine/threonine protein kinases but is thought to be a pseudokinase as it does not have a GxGxG canonical protein kinase motif and no credible substrate, besides potentially itself, has ever been demonstrated (Ohashi et al., 2018; Rostislavleva et al., 2015). VPS15 stabilises VPS34 and promotes its recruitment to membranes as well as its activation (Stack and Emr, 1994). The VPS34-VPS15 heterodimer can further associate with additional subunits to form two specific complexes: Complex I consists of VPS34, VPS15, Beclin 1 and ATG14L, whereas complex II contains UVRAG instead of ATG14L (Backer, 2016). As already mentioned in chapter 1.2.1, complex I is involved in the initiation of autophagy by producing PI(3)P at the ER for omegasome formation (Axe et al., 2008; Itakura et al., 2008; Itakura and Mizushima, 2010). The role of complex II has been less well defined but it has been implicated in endosome maturation and the late stages of autophagy (Itakura et al., 2008; Kim et al., 2015). The specific functions of complex I and complex II will be discussed further below.

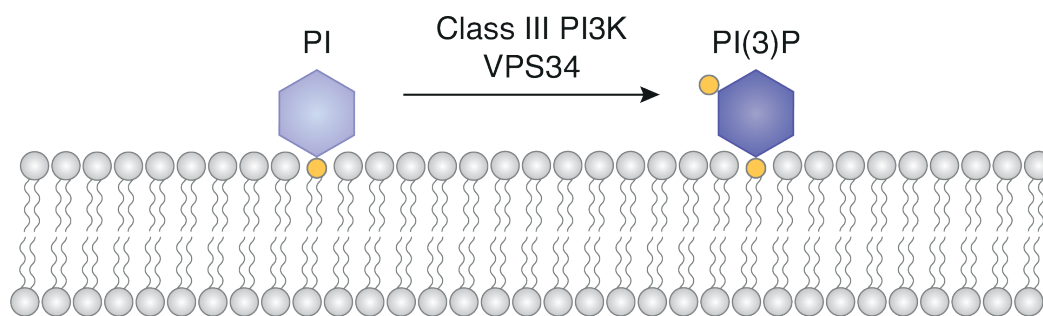


Figure 1–8: Class III PI3-kinase VPS34 produces PI(3)P

VPS34 is the only class III PI3K, which uses phosphatidylinositol (PI) as substrate to produce phosphatidylinositol 3-phosphate (PI(3)P).

Two crystal structures of VPS34 have been solved by the Williams group. In 2010, the lab reported the crystal structure of the catalytic and helical domains of Vps34 from *Drosophila melanogaster* (Miller et al., 2010). In 2015, the crystal structure of complex II from *Saccharomyces cerevisiae* (Vps34, Vps15, Vps30, Vps38) was solved (Rostislavleva et al., 2015) (Figure 1–9B). These structures represented a breakthrough in the understanding of VPS34 function. Yeast complex II was crystallised with a stabilising nanobody bound to the Vps34 kinase domain. Complex II adopts a V-shaped organisation in which one arm of the V conveys specificity in localisation and the other arm possesses the catalytic activity. The catalytic arm consists of the helical and kinase domains of Vps15/VPS15 and Vps34/VPS34. The other arm is made of a coiled coil heterodimer of Vps30/Beclin 1 and either Vps38/UVRAG for complex II or Atg14/ATG14L for complex I. The membrane-binding interface was mapped to the ends of both arms by hydrogen deuterium exchange mass spectrometry (HDX-MS) (Rostislavleva et al., 2015). The coiled-coil arm can be described as the adaptor arm, which gives the complex its unique identity and is responsible for the functional specificity of the membrane binding. The VPS34 C2 domain is at the heart of the complex and makes extensive protein-protein interactions with all subunits of the complex. (Figure 1–9B). Furthermore, the C2 domain has two unusual helical insertions. The CBR1 and the helical hairpin insertion (C2HH) were found to be important in yeast, as mutants demonstrated a temperature sensitive growth phenotype (Rostislavleva et al., 2015).

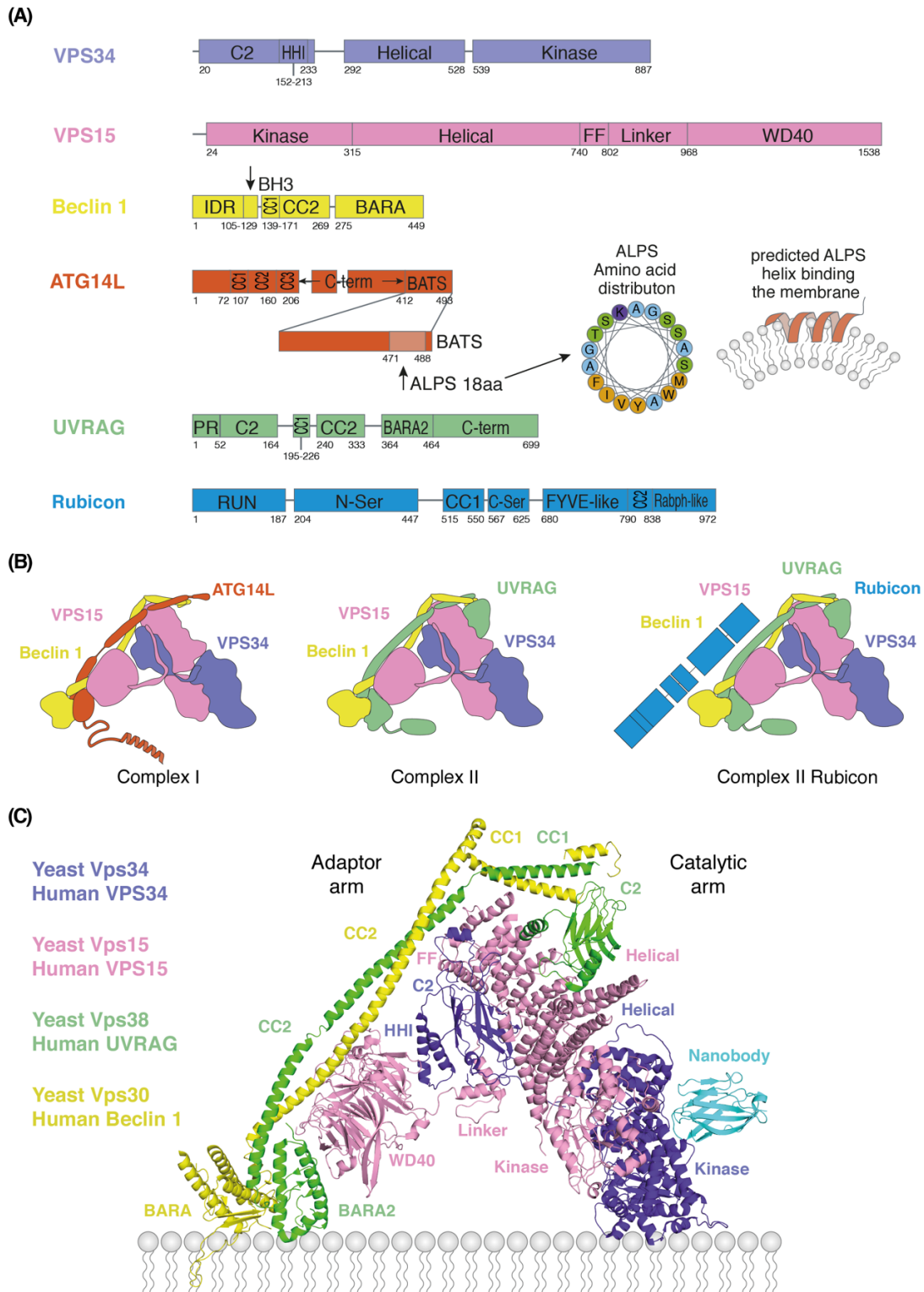


Figure 1-9: Structural organisation of the class III PI3K complexes

(A) Schematic representations of the VPS34 complex subunits. Complex I is made of VPS34, VPS15, Beclin 1 (Vps30 in yeast) and ATG14L (Atg14 in yeast) whereas complex II contains UVRAG (Vps38 in yeast) instead of ATG14L. Complex II can associate with Rubicon as a fifth subunit. **(B)** Structural models of complexes I, II and complex II Rubicon. **(C)** Structure of the yeast complex II (PDB: 5DFZ) (Rostislavleva et al., 2015). Complex II adopts a V-shape with membrane binding domains at the end of each arm. Complex II was crystallised with a stabilising nanobody at the kinase domain.

VPS30/Beclin 1 is found in both complexes I and II and was found to be essential for membrane recruitment in yeast complex II (Rostislavleva et al., 2015). The BARA domain at the C-terminus of both Vps30 and Beclin 1 was found to adopt a fold consisting of three β -sheet- α -helix repeats, which contains a loop with three consecutive aromatic amino acids (Phe359, Phe360, and Trp361 in Beclin 1) (Huang et al., 2012; Noda et al., 2012). Strikingly, the activity of yeast complex II was completely abolished when these three residues were mutated (Rostislavleva et al., 2015). Interestingly, the Beclin 1 coiled coil has a stronger affinity for the UVRAG coiled coil than for the ATG14L coiled coil (Li et al., 2012). This might influence the biochemical equilibrium of the two complexes and shift the balance according to the relative abundance of ATG14L and UVRAG.

ATG14L and UVRAG are the subunits that are specific for complexes I and II, respectively (Figure 1-9C). Their original functions were established in yeast, where complex I recruitment to the pre-autophagosomal structure was essential for autophagy initiation. In contrast, complex II was shown to be important for sorting of the vacuolar protease carboxypeptidase Y (Kihara et al., 2001). Although the mammalian complexes resemble their yeast counterparts, it is still not clear how their division in function arises.

1.4.1 Complex I

While the composition of the yeast complexes I and II was determined in 2001, the mammalian homologues remained unknown for a while. However, ATG4L was then identified by three groups in 2008 and 2009 (Itakura et al., 2008; Matsunaga et al.,

2009; Sun et al., 2008). ATG14L consists of an N-terminal domain, a short α -helix (CC1), two longer α -helices (CC2 and CC3), a C-terminal domain and the BATS domain (Figure 1–9A). Human complex I is involved in the initiation of autophagy (Itakura et al., 2008; Matsunaga et al., 2009; Sun et al., 2008). ATG14L is very important for the progression of autophagy, and knockout and knockdown experiments with ATG14L showed a dramatic decrease in LC3 puncta, indicating that ATG14L is crucial for autophagosome formation (Matsunaga et al., 2009; Sun et al., 2008). Fan et al. have discovered that the 80 C-terminal amino acids of ATG14L are necessary for complex I to locate to the ER. This domain was named the BATS domain (Barkor/ATG14L autophagosome targeting sequence) (Fan et al., 2011). An 18 residue amphiphilic helix was identified in the BATS domain, which has the same characteristics as the amphipathic lipid packing sensor (ALPS) motif (Drin et al., 2007; Nguyen et al., 2017; Vanni et al., 2013). ALPS motifs have been shown to be unstructured in solution but to fold into an α -helix upon incubation with membranes (Bigay et al., 2005). The ATG14L ALPS helix is enriched in serines and threonines on its polar side but has essential bulky hydrophobic residues on the apolar side (Figure 1–9A). Truncation or point mutations of three essential hydrophobic residues to arginine is enough to disturb the phagosomal localisation of ATG14L (Fan et al., 2011). The binding of the ALPS motifs to membranes was found to be independent of lipid charge (Drin et al., 2007). Instead, they only recognise packing defects in the lipid bilayer (Vanni et al., 2013).

1.4.2 Complex II

In contrast to ATG14L, UVRAG was not initially identified as an autophagy or endosome-trafficking related protein. UVRAG was first identified in a genetic screen in 1997 in which it was shown to partially rescue UV sensitivity in xeroderma pigmentosum cells (Perelman et al., 1997). Xeroderma pigmentosum is a genetic condition in which UV-light-induced DNA damage repair is impaired. UVRAG was rediscovered as a Beclin 1 binding protein in 2006 and was determined to be the mammalian homologue of Vps38 in 2008 and 2009 (Itakura et al., 2008; Itakura and Mizushima, 2009; Liang et al., 2006). UVRAG consists of six distinct regions: a proline-rich domain, a C2 domain, a short α -helix (CC1), a longer α -helix (CC2), a BARA2 domain and an unstructured C-terminal domain (Figure 1–9A). In general, the roles of UVRAG and complex II are less understood than the roles of ATG14L and complex I. It was first proposed that UVRAG was also involved in the autophagy pathway (Liang et al., 2008, 2006). However, several studies since have not found any defects in autophagy upon UVRAG knockdowns or knockouts (Farre et al., 2010; Jiang et al., 2014; Knævelsrud et al., 2010; Lórinicz et al., 2014; Takáts et al., 2014). Instead, it was shown that UVRAG was needed for intact endocytic trafficking and endolysosomal degradation. Interestingly, UVRAG did not colocalise with LC3 puncta, but was instead found on Rab5, Rab7 and Rab9 positive membranes (Itakura et al., 2008). In 1999, it was suggested that VPS15 binds to Rab5 and thereby recruits VPS34 to early endosomes to produce PI(3)P as mentioned in chapter 1.1.3 (Christoforidis et al., 1999). Stein et al has also suggested that Rab7 binds to VPS15 in pull down experiments (Stein et al., 2003). As the mammalian homologues of Atg14 and VPS38 were not known then, no involvements or dependencies of other subunits were tested. However, since then it has been

suggested by several studies that VPS34 interacts with Rab5 (Behrends et al., 2010; Gillingham et al., 2014; Murray et al., 2002; Ravikumar et al., 2008; Stein et al., 2003). In contrast to ATG14L, no membrane binding motif has yet been found in UVRAG. In contrast to Vps38, the mammalian homologue UVRAG has a longer and unstructured C-terminal region (residues 465-699). Interestingly, there are numerous sites in this region that are phosphorylated by mTORC1 (Kim et al., 2015; Munson et al., 2015; Oppermann et al., 2009). Since the C terminus would be positioned at the membrane interface, it is tempting to speculate that the additional charges of the phosphate groups could alter membrane binding and VPS34 activity (McLaughlin and Aderem, 1995). Munson et al. discovered that S550 and S571 are phosphorylated by mTORC1 and that these phosphorylations activate complex II at the lysosome (Munson et al., 2015). Mutating these residues leads to a decrease in a newly identified pool of PI(3)P at the lysosome and to an increase in lysosomal tubules that are needed for autophagosome-lysosome reformation. In contrast, Kim et al. showed that UVRAG is phosphorylated at S498 by mTORC1, which increases the association with the negative regulator Rubicon (Kim et al., 2015) (Figure 1-9A). Rubicon has been shown to interact exclusively with complex II via Beclin 1 and to negatively regulate the late stages of autophagy (Kim et al., 2015; Matsunaga et al., 2009; Nakamura et al., 2019; Zhong et al., 2009). However, Rubicon is also active in the non-canonical phagocytosis pathway termed as LC3-associated phagocytosis (Martinez et al., 2015). Paradoxically, Rubicon is necessary here for the activity of complex II on the LC3-associated phagosomes. It remains to be determined what effect Rubicon has on VPS34 activity. Moreover, Rubicon has also been shown to interact with Rab7 (Sun et al., 2010; Tabata et al., 2010).

1.5 Hydrogen deuterium exchange mass spectrometry (HDX-MS)

Hydrogen deuterium exchange mass spectrometry (HDX-MS) is a technique to study protein structure dynamics and protein interaction interfaces. Hydrogens on the peptide backbone and side chains are constantly exchanging with the hydrogen atoms of the solvent (Englander et al., 1996). There are three locations where hydrogen atoms can be exchanged on the protein: those in hydrogen-C α carbon bonds, those in amino acid side chains and those in amide groups. However, only the hydrogens in amide groups are capable of providing useful information for HDX experiments carried out in a time frame of seconds to hours. In contrast, hydrogens in amino acid side chains typically exchange far too rapidly to be retained for measurement and hydrogens in hydrogen-carbon bonds exchange far too slowly (Hamuro et al., 2003). The exchange of these backbone hydrogens depends mainly on the presence of intramolecular interactions or hydrogen bonds, but also on solvent accessibility (Fioramonte et al., 2017). On the one hand, hydrogens involved in secondary structure elements or in the hydrophobic protein core display a slower exchange rate. On the other hand, backbone amide group hydrogens found in intrinsically disordered regions, or to a lesser extent, amide groups on the protein surface will exchange at a faster rate. Additionally, pH and temperature substantially regulate the exchange kinetics (Engen and Wales, 2015). The hydrogen exchange reaction can be both acid- and base-catalysed and therefore produces a V-shaped curve with a minimum exchange rate between pH 2-3 (Matthew and Richards, 1983). The exchange rate has also been shown to be sensitive to temperature as a rise of 10°C increases the exchange rate by a factor of three (Englander et al., 1972).

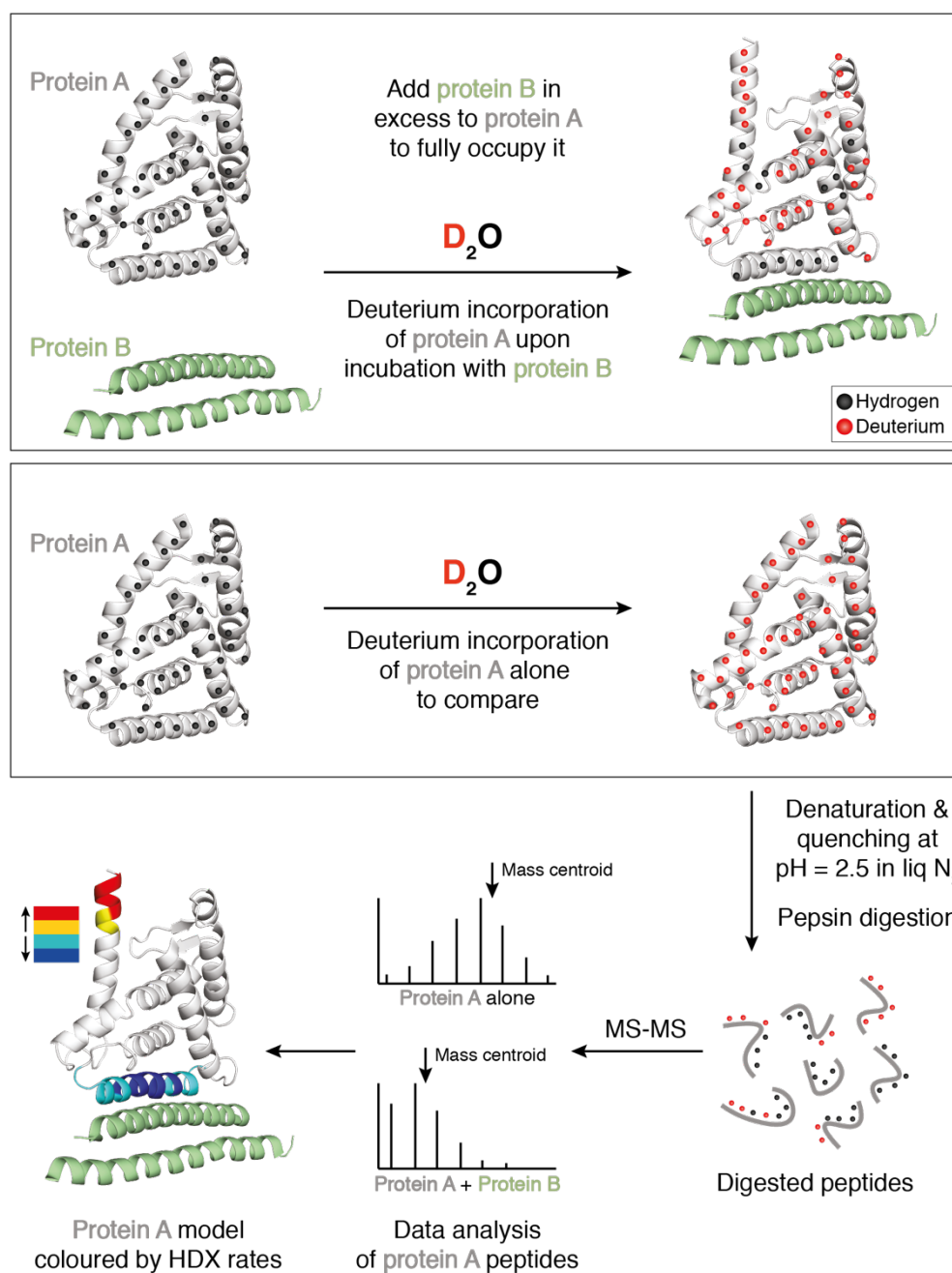


Figure 1-10: Workflow of HDX-MS to study protein-protein interactions

Deuterated buffer is added to protein A + protein B and protein A alone. The samples are incubated for a range of times in which hydrogens exchange with deuteriums depending on solvent accessibility and the presence of hydrogen bonds. The exchange reaction is quenched by dropping the pH to 2.5 and flash-freezing in liquid nitrogen. The proteins are denatured, and subsequently digested and then analysed by mass spectrometry. By mapping the differences in exchange rates between the complex and the free protein A onto the structure, the region of interaction of protein A with protein B can be visualised.

By changing the surrounding solvent from H_2O to D_2O , deuterium will be incorporated into the amide groups instead of hydrogens (Woodward et al., 1982).

With the help of mass spectrometry, the change of mass due to differential deuterium incorporation between a treated sample and an untreated control can be measured and compared. As HDX-MS is a very versatile technique it can be used to probe interactions with a variety of ligands, such as another protein (Ohashi et al., 2016), a lipid membrane (Rostislavleva et al., 2015) or a drug (Masson et al., 2017).

Figure 1–10 shows the workflow of an HDX-MS experiment to study protein-protein interactions (Masson et al., 2019). Usually, one is interested where protein A binds to protein B (or vice versa). In order to conduct an HDX-MS experiment of this nature, protein B has to be added in sufficient amounts to ensure complete binding to protein A. Otherwise, a mixed population of bound and unbound protein A is produced, resulting in a heterogeneous mixture of peptides with varying exchange kinetics. Firstly, deuterated buffer is either added to protein A mixed with protein B or protein A alone. The samples are then incubated for a range of labelling times such as 3 sec, 30 sec, 5 min and 50 min to capture a full range of exchange rates. To stop the exchange reaction and minimize back-exchange, samples are quenched by changing the pH to 2.5 and to temperatures lower than 0°C with liquid nitrogen. Furthermore, urea or guanidinium chloride is added to unfold the protein chains to enable subsequent proteolytic digestion. Then, the protein mixture is injected into an immobilised pepsin column for digestion and the peptides are separated using reverse-phase chromatography. The peptides' mass to charge (m/z) ratio is measured by electro-spray ionisation mass spectrometry and the degree of deuterium incorporation is analysed. By calculating differences in the exchange rates of the same peptide in protein A, both in a bound and unbound state, conclusions about interactions and conformational changes upon protein B binding

can be drawn. For example, the interaction between protein A and B might be mediated by the formation of new hydrogen bonds and this results in a decreased HDX rate in the particular region. Furthermore, a conformational change in the protein could cause localised protein unfolding, exposing amino acid residues to solvent and thereby causing an increased HDX rate. The HDX exchange rates can then be displayed on a structural model in a colour range from blue (decrease in HDX) to red (increase in HDX) (Figure 1-10).

1.6 Cryo-electron tomography (cryo-ET) and subtomogram averaging

The field of cryo-electron microscopy (cryo-EM) image analysis has flourished since the resolution revolution in the early 2010s when direct-electron detectors became widely available (Kühlbrandt, 2014). There are two major techniques in the cryo-EM imaging field: single particle analysis (SPA) and cryo-electron tomography (cryo-ET) combined with subtomogram averaging. For both techniques, samples are frozen in a thin layer of vitreous ice and are then imaged at liquid nitrogen temperatures. The vitrification of water leads to an amorphous and non-crystalline state in which weakly scattering objects like proteins can be imaged by phase contrast in electron microscopes (Dubochet et al., 1988). In SPA, 2D projections are taken from purified proteins in random orientations. From the collected 2D information, a 3D reconstruction can be computed with image processing softwares such as Relion (Scheres, 2012). In contrast, in cryo-ET often more complex and thicker specimens such as cells, non-uniform virus structures or protein coated vesicles are studied (Schur, 2019). For those, SPA cannot be used due to sample complexity and heterogeneity. The principle of electron tomography was developed in the 1970 by three groups independently (Hart, 1968; Hoppe, 1974; Hoppe et al., 1968; Rosier and Klug, 1968). However, due to technical challenges, it would take 20 years before tomography could be automated and therefore become accessible to a wider audience (Dierksen et al., 1992; Koster et al., 1992). In tomography, so-called tilt series are collected where 2D projections of the same area are taken at tilts ranging from $+60^\circ$ to -60° (Figure 1-11A) (Wan and Briggs, 2016). Most commonly, the tilt series is then reconstructed into its 3D volume called tomogram with the weighted back-projection algorithm (Radermacher, 2006). From each

tomogram, volumes can be picked in 3D and extracted as so called subtomograms (Figure 1-11A).

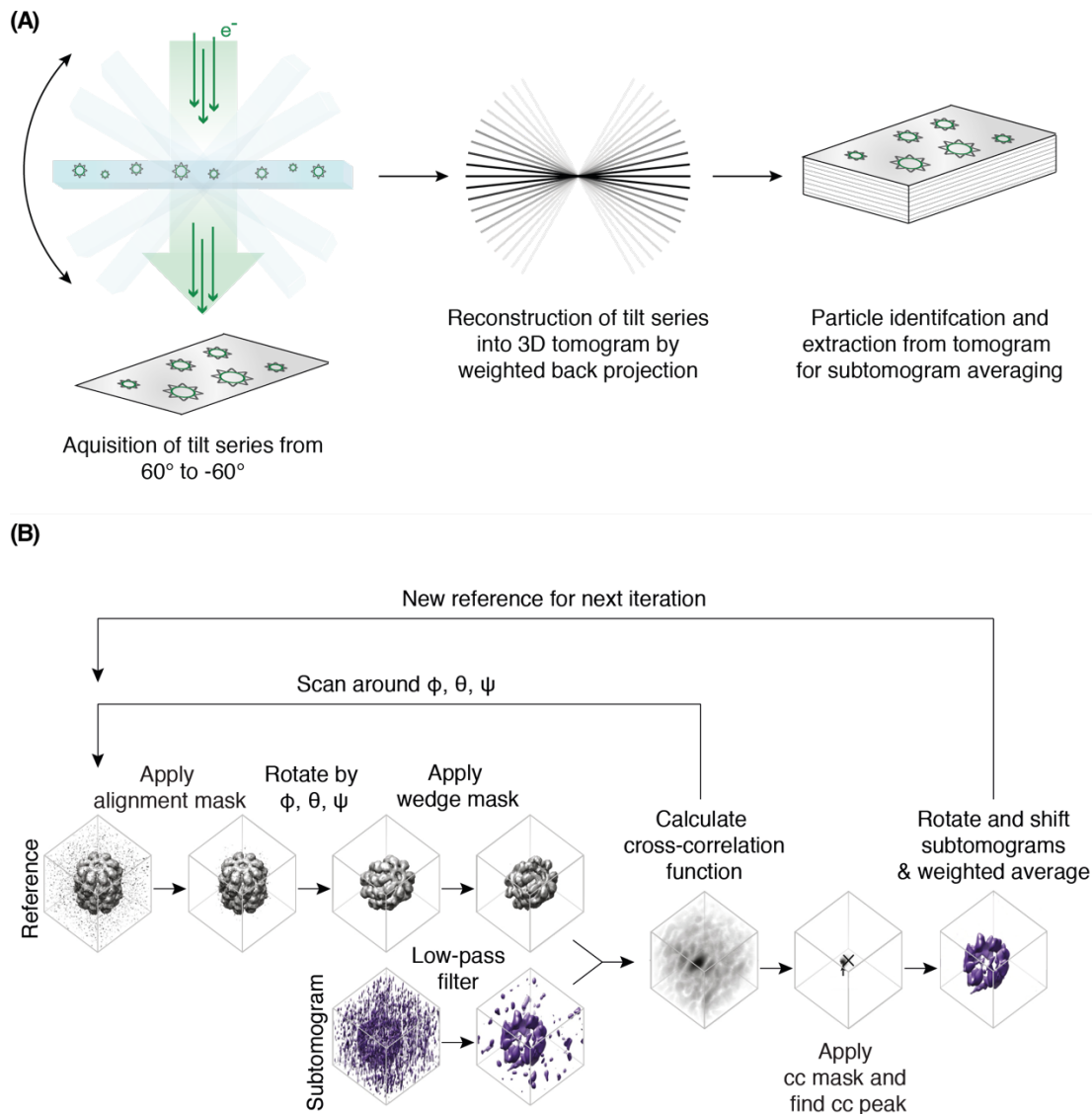


Figure 1-11: Workflow of cryo-ET and subtomogram averaging

(A) In cryo-electron tomography (cryo-ET) uses specimen vitrified in ice. Projections are taken from +60° to -60° to create a tilt series (left). The tilt-series can be computationally reconstructed into a 3D volume called tomogram (middle). Subtomograms of particles of interest can be extracted from the tomogram for subtomogram averaging (right). Figure adapted from Galaz-Montoya and Ludtke 2017. **(B)** Subtomograms can be aligned by angular search. A reference is chosen and masked and rotated by ϕ, θ, ψ for angular sampling. A wedge mask is additionally applied and a cross correlation (CC) function against a low pass filtered subtomogram in x/y/z is calculated. The peak CC score and associated position is identified and the subtomogram is moved. An average of the improved subtomogram orientations and positions is created and used as a reference for the next iteration. Figure adapted from Wan and Briggs 2016.

When multiple copies of the same protein can be found in the tomogram, subtomogram averaging can be used to obtain a structure (Walz et al., 1997). Figure 1-11B describes the workflow of subtomogram averaging by angular search (Wan and Briggs, 2016). Firstly, a reference structure is chosen as a method for identifying the target protein in the subtomograms. The reference structure is then masked to focus on a specific area and rotated by the Euler angles φ , θ , ψ to sample the angular environment. With the help of the Euler angles, any orientation of a particle in 3D space can be described. Specifically, θ and ψ describe the out-of-plane rotation while φ denotes the in-plane rotation. Lastly, a wedge weight is applied to the reference in order to reach similar sampling in Fourier space. The effect of the wedge will be discussed in detail further below. Subsequently, the subtomogram is low pass filtered to increase the signal-to-noise ratio (SNR) and to prevent overfitting to noise. The low pass filtered subtomogram is then compared to the reference by a cross correlation (CC) function. For the CC function, a cross correlation score is calculated for each possible x/y/z shift and Euler angles and displayed in real space. A calculated high CC score means that this particular shift and rotation improved the alignment of the subtomogram against the reference. As the edge of subtomograms can often cause artefacts in the CC calculation, a mask is used to restrain the range of permissible shifts. The highest CC score and affiliated shift and rotation is identified and the subtomogram is oriented and positioned to these coordinates. Lastly, an average of all subtomograms with improved orientations and positions is created and used as a reference for the next angular search. This workflow is a continually self-improving process as the alignment and the produced average should advance during each iteration. Furthermore, by averaging numerous subtomograms, which on their own have low signal, the SNR

is improved and higher resolution details can be obtained with each iteration. By using information out of a 3D volume instead of a 2D projection, combined with subtomogram averaging, structures can be determined that otherwise might have been obscured by other objects in the electron beam path.

Although the average resolution of subtomogram averaging has improved over the years with an average of $\sim 27 \text{ \AA}$, it is still far below the average resolution in SPA of $\sim 5 \text{ \AA}$ (Resolution Trends in the Electron Microscopy Data Bank EMDB). There are still limitations and challenges in cryo-ET and subtomogram averaging that need to be addressed in order to improve sample acquisition and processing. A limit that has been acknowledged from early on is the limitation of the total electron dose (Koster et al., 1997). In cryo-EM, the contrast in the acquired projection stems from electrons interacting with the sample. However, too high electron doses cause radiation damage, which limits the achievable resolution (Glaeser, 2008; Henderson, 1995). Whereas in SPA only a single image per area is taken, in cryo-ET ~ 40 - 60 images are taken for one tilt series. Thus, each image of the tilt series can receive an up to 10 times smaller dose than in SPA ($2.5 \text{ e}^-/\text{\AA}^2$ vs $30 \text{ e}^-/\text{\AA}^2$) (Kudryashev et al., 2012). In contrast, full tilt series are often imaged with a total dose of up to ~ 100 - $150 \text{ e}^-/\text{\AA}^2$. This means that cryo-ET images have more electron-induced damage and have a much lower SNR, which complicates particle identification and subtomogram alignment. Another problem is the ice thickness of samples. This might not be a problem for *in vitro* reactions of vesicles or viruses, but frozen cells can often be much thicker than 500 nm . Yet, the mean free path of an electron accelerated at 300 kV is $\sim 300 \text{ nm}$ (Rice et al., 2018). In thicker samples, more charging, blurring, and inelastic scattering of electrons lead to poor image

quality. Even for *in vitro* samples, ice thickness can become a problem at high tilts. As the path of the electron is extended two-fold at 60°, three-fold at 70° and almost six-fold at 80°, even thin samples experience deterioration in image quality (Nicastro, 2009). In order to look at thick cells under the electron beam, methods like vitreous sectioning or Focused ion beam (FIB) milling have been used to reduce the thickness of ice layers to ~100-300 nm (Marko et al., 2007; McDowall et al., 1983). On average, the number of particles per data set in cryo-ET is much smaller than in SPA. Whereas final SPA structures are often made of 100,000 particles or more, cryo-ET data sets are of variable size, but can contain anything from ~20,000 down to less than 500 particles (Kovtun et al., 2018; Weiss et al., 2019). This is due to the low abundance of some cryo-ET targets and the time consuming nature of collecting high-quality tilt-series (Nicastro, 2009). Another problem is the contrast transfer function (CTF) correction in cryo-ET. The signal in electron micrographs is modulated by a sinusoidal function of spatial frequency called the CTF, which depends on microscope parameters and the acquired defocus (Erickson and Klug, 1971). Due to the sinusoidal nature of the function, there is a periodic contrast inversion and signal loss at zero-crossings. If the microscopy data is not corrected for the CTF, then the attainable resolution is restricted to the first zero-crossing, which might be lower than 30 Å (Wade, 1992). As the CTF estimation is strongly dependent on an accurate defocus determination, tomograms can create several challenges. Not only is there a defocus gradient when the sample is tilted but also samples have a defocus gradient along their thickness (Turoňová et al., 2017). Consequently, accurate defocus estimation and 3D-CTF correction should be used as errors of 250 nm in defocus estimation have been shown to already limit the resolution to no better than 10 Å (Kudryashev, 2017). Unfortunately, CTF correction

is not yet a routine process in cryo-ET (Kudryashev et al., 2012). One of the biggest problems in subtomogram averaging is the effect of the missing wedge (Schmid and Booth, 2007). Due to mechanical and conceptual limitations, tilt series can only be acquired to a maximum tilt range of 50-70°. This incomplete sampling leads to missing information in Fourier space in the reconstructed tomograms (Radermacher, 1988) (Figure 1-12A).

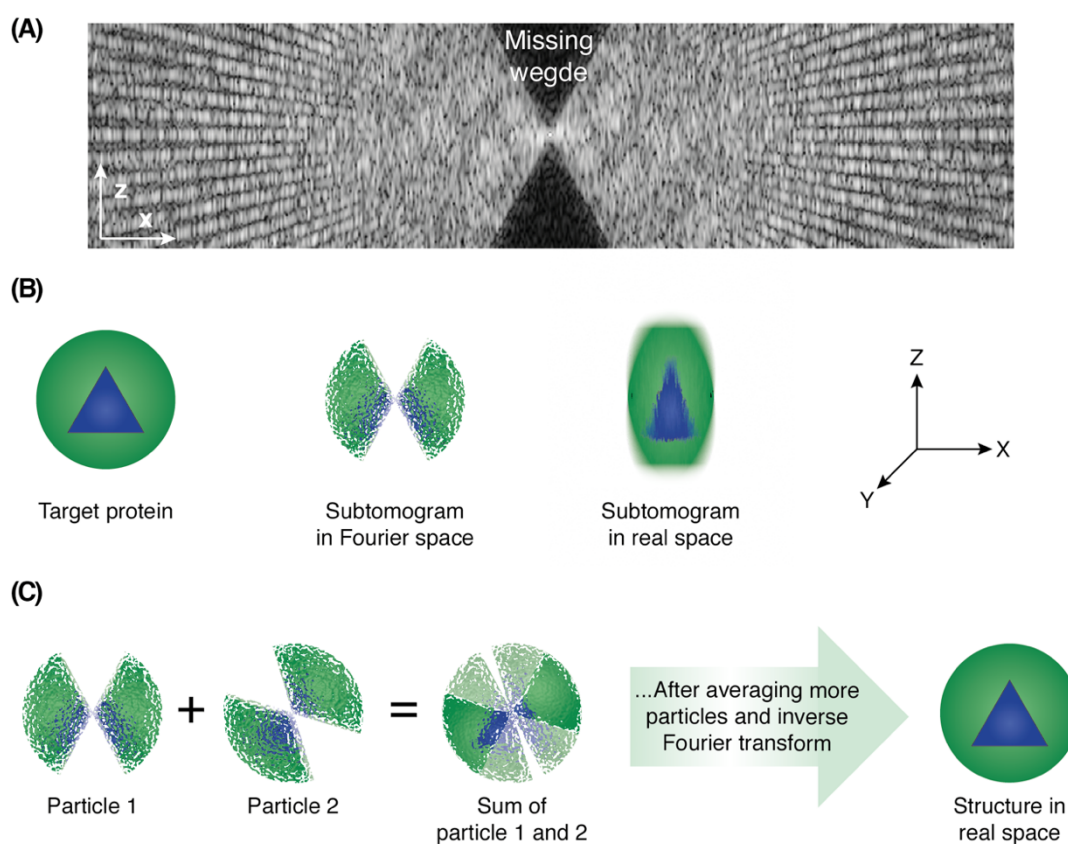


Figure 1-12: Missing wedge bias in Fourier space

(A) The Fourier transform of an acquired tomogram shows the missing information in Fourier space called the missing wedge. (B) A cartoon representation of a protein target (left). After capturing the target proteins in tomograms, the subtomogram has a missing wedge in Fourier space (middle) and wedge artefacts like elongation and loss of horizontal features in real space (right). (C) The missing information in Fourier space due to the wedge can be “filled in” by subtomogram averaging. Particles with different wedge orientations can be added in Fourier space for averaging and the Fourier space can be recovered. Figure adapted from (Galaz-Montoya and Ludtke, 2017).

Consequently, the extracted subtomograms also display a missing wedge in Fourier space and contain wedge artefacts in real space (Figure 1-12B). These real space

artefacts cause features that run horizontally in x to almost disappear and structures that run parallel to z to become stretched and blurred (Palmer and Löwe, 2013). As the CC function between reference and subtomograms is calculated in Fourier space, the missing wedge can become an overpowering feature. Thus, a method to compensate is to apply a binary wedge mask in the same orientation to the reference (Figure 1-11B) (Wan and Briggs, 2016). However, the missing wedge can also be “filled in”. When subtomograms with different missing wedge orientations are aligned to structural features and summed in Fourier space, as a part of the averaging procedure, then the missing information can be recovered (Galaz-Montoya and Ludtke, 2017) (Figure 1-12C).

2 Aims

The phosphatidylinositol kinase VPS34 and its product PI(3)P orchestrate diverse processes, including autophagy, endocytic sorting, phagocytosis and cell division. The lipid composition of the organelles involved in these processes varies dramatically and thereby influences membrane association and kinase activity. When I started my PhD, most kinase activity studies of VPS34 complexes had been carried out with immunoprecipitated proteins and non-physiological lipid mixtures that did not reflect intracellular conditions. Thus, only limited conclusions could be drawn from these experiments. To better understand the physiological function of VPS34, a system in which the activity of the human VPS34 complexes I and II could be reconstituted *in vitro* with clearly defined lipid compositions, mimicking cellular membranes, would be very valuable to the field. Furthermore, the small GTPase Rab5a had been suggested to interact with VPS15 over 20 years ago. However, no study has followed up on the specific interaction of Rab5 with either complex I or II. In order to map the Rab5 binding site on complex II, a complementary approach of hydrogen deuterium mass spectrometry (HDX-MS) and unnatural amino acid crosslinking was chosen. The second aim of this project was to use cryo-electron tomography and subtomogram averaging to visualise human VPS34 complex II directly on membranes. Several cryo-EM structures of the human VPS34 complexes have been solved, but no one has succeeded so far in solving the membrane bound structure. Studying the interaction of proteins with membranes has been very challenging for structural techniques, however, the recent advances in cryo-electron microscopy such as more sensitive direct electron detectors and advances

Aims

in cryo-electron tomography image processing provided the opportunity to pursue this challenging project.

The goal of my PhD was to shed light on the recruitment and activation mechanism of the VPS34 complexes *in vitro* and thereby infer why complex II is recruited to the endocytic pathway whereas complex I is active during the initiation of autophagy.

3 Materials and methods

3.1 Protein expression and purification

Table 1: Plasmid table

ID	Construct	Backbone	Used in
pYO1006	HsBeclin 1, untagged	pCAG	GUV assays, flotation, cryo-ET
pYO1017	ZZ-3X-TEV-HsATG14L	pCAG	GUV assays
pYO1018	ZZ-3X-TEV-HsUVRAG	pCAG	GUV assays
pYO1023	HsBeclin 1 + ZZ-3XTEV-HsUVRAG	pCAG	GUV assays
pYO1025	HsVPS34 + HsVPS15-3xTEV-ZZ	pCAG	HDX-MS, GUV assays, flotation, cryo-ET
pYO1031	HsBeclin 1 + HsUVRAG, both untagged	pCAG	HDX-MS, GUV assays, flotation
pYO1051	HsBeclin 1 AFM1 (FFW/DDD at 359-361) untagged + ZZ-3xTEV-HsATG14L	pCAG	GUV assays
pYO1052	HsBeclin 1 AFM1 (FFW/DDD at 359-361), untagged + ZZ-3xTEV-HsUVRAG	pCAG	GUV assays
pYO1067	ZZ-HsRubicon	pCAG	GUV assays, flotation
pYO1077	ZZ_3xTEV-HsATG14L delta ALPS (1-470)	pCAG	GUV assays
pYO1101	HsBeclin 1 + HsATG14L, both untagged	pCAG	HDX-MS, GUV assays, flotation
pYO1113	hsVPS15+hsVPS34 untagged	pCAG	GUV assays, flotation
pYO1118	HsBeclin 1 AFM2 (Q418D F419D), untagged + ZZ-3xTEV-HsATG14L	pCAG	GUV assays
pYO1120	HsBeclin 1 AFM2 (Q418D F419D), untagged + ZZ-3xTEV-HsUVRAG	pCAG	GUV assays
pYO1123	HsUVRAG fused to HsATG14L BATS domain (413-492), untagged	pCAG	GUV assays
pYO1124	HsUVRAG delta Cter (1-464) fused to HsATG14L BATS domain (413-492), untagged	pCAG	GUV assays, flotation, cryo-ET
pYO1125	GST-TEV-ATG-(Cys)-PX (2-149)	pOP	GUV assays

pYO1134	HsBeclin 1 AFM1(FFW/DDD at 359-361) + HLM (L293A V296A), untagged + ZZ-HsATG14L	pCAG	GUV assays
pYO1190	HsBeclin1 HLM (L293A V296A) + AFM2 (Q418D F419D)	pcDNA4/TO	GUV assays
pYO1262	His6-TEV-HsRab5A_Q79L_1-211	pOP	HDX-MS
pSM41	His6-TEV-hsVPS34	pOP	GUV assays
pJB78	GST-TEV-HsRab1a-(1-204)_Q70L_C26S_C126S	pOP	GUV assays, flotation
pOP823	His6-SUMO-HsRab5A_(1-212)_Q79L_C19S_C63S	pOPIN-S	GUV assays, flotation, cryo-ET
STp6	HsRab5a_Q79L_1-212_C19S_C63S_S84TAG	pBAD	UAA crosslink
STp12	TEMPOH-1_PylT_Mm (RNA/aminoacyl-tRNA synthetase)	pEVOL	UAA crosslink

3.1.1 Purification of human VPS34 complexes I and II

Expi293 suspension cells (ThermoFisher A14527) were grown at 37°C, 8% CO₂ in Expi293 Expression Medium (ThermoFisher A1435102) and at 125 rpm shaking. Cells were transfected with one or several plasmids at a cell density of $\sim 2.0 \times 10^6$ per mL. The plasmid concentration was 1.1 mg/L culture, using 3 mg/L of polyethylenimine (PEI) “MAX” dissolved in PBS (Polysciences 24765, 1 mg/mL). 2-4 L cells were grown for 48 h, then harvested at 3,000 g for 20 min. Harvested cells were frozen in liquid nitrogen and stored at -80°C. The purification of complexes I and II (+/- Rubicon) only differs in the concentration of NaCl in all buffers. While for complex I 150 mM NaCl was used, 300 mM NaCl was used for complex II (+/- Rubicon). The frozen cell pellet was resuspended in 70-150 mL lysis buffer (50 mM HEPES pH 8, 150 or 300 mM NaCl, 1% Triton X-100 (Sigma, X100), 10% glycerol, 1 mM TCEP (tris(2-carboxyethyl)phosphine), Soltec Ventures, M115), 2 mM MgCl₂, 1x EDTA-free inhibitor tablet (Roche, 05056489001)) and incubated on ice for 30 min. The insoluble fraction was removed by centrifugation at 18,000 g for 30 min. The supernatant fraction was incubated with 2 mL bed volume of IgG beads (GE

Healthcare, 17096902) for 3.5 h. The bead/supernatant mixture were centrifuged at 1,000 g, and $\frac{3}{4}$ of the supernatant was removed so that the beads were left in a thick slurry. The IgG beads were then transferred to a gravity flow column and washed with 150 mL of wash buffer (50 mM HEPES pH 8, 150 or 300 mM NaCl, 0.1 % Triton X-100, 1 mM TCEP, 5 mM ATP (Sigma, A2383), 50 mM MgCl₂, 5 µg/mL RNaseA (Sigma, 83834)) and 150 mL of TEV buffer (50 mM HEPES pH 8, 150 or 300 mM NaCl, 1 mM TCEP). TEV protease was added to 10 mL of TEV buffer and the solution was added to the gravity column for overnight incubation. The next day, the protein was eluted from the beads in 6 elution fractions of 10 mL and analysed by SDS-PAGE gel electrophoresis. The elution fractions were combined and concentrated using a 100 kDa molecular weight cut-off (MWCO) centrifugal concentrator (Millipore, UFC910096) for gel filtration. A S200 10/30 gel filtration column was equilibrated with gel filtration buffer (25 mM HEPES pH 8, 150 or 300 mM NaCl, 1 mM TCEP). The main peak fractions were analysed by SDS-PAGE gel electrophoresis and pooled. The fractions were then concentrated to 10-30 µM. The proteins were frozen in liquid nitrogen and stored at -80°C.

3.1.2 Purification of human VPS34

E. coli C41 (DE3) RIPL cells were transformed with the plasmid pSM41. The transformed bacteria were cultured in 2XTY medium with 0.1 mg/mL ampicillin at 37°C to OD₆₀₀ 0.8 and induced with 0.3 mM IPTG at 12°C for ~15 h. A culture volume of 4 L of cells was pelleted by 20 min centrifugation at 4,000 g and resuspended in ~100 mL of lysis buffer (10 mM Tris-HCl pH 8, 100 mM NaCl, 10 ml imidazole, 1 Complete EDTA-free Protease Inhibitor Cocktail Tablet (Roche, 11873580001), 0.1

mg/ml DNaseI, and 50 ml BugBuster (Novogen 70584) and sonicated on ice 3 times for 3 min. The sonicated lysates were centrifuged at 100,000 g for 40 min at 4°C and the supernatant was subsequently filtered through a 0.45 µm filter (Millipore, SE2M230I04). The filtered supernatant was loaded on two connected 5 mL Ni-NTA FF columns (GE Healthcare 17-5255-01). The columns were washed with 100 mL Ni A1 buffer (20 mM Tris pH 8, 300 mM NaCl, 10 mM imidazole, 2 mM β-mercaptoethanol), 100 ml Ni A2 buffer (20 mM Tris pH 8, 100 mM NaCl, 10 mM imidazole, 2 mM β-mercaptoethanol), and eluted in an imidazole gradient to about Ni B1 buffer (20 mM Tris pH 8, 100 mM NaCl, 300 mM imidazole, 2 mM β-mercaptoethanol). The eluted fractions were analysed by SDS-PAGE gel electrophoresis and combined. The N-terminal His6 tag was cleaved with TEV protease and incubated overnight with gentle rocking at 4°C. On the next day, the protein was loaded on a 5 mL Heparin HP column (GE Healthcare 17040701) by first washing with 20 mL HA buffer (20 mM Tris pH 8, 100 mM NaCl, 2 mM DTT) and then eluted with 100 mL HB buffer (20 mM Tris pH 8, 2 mM DTT, 1 M NaCl). The peak fractions were pooled and brought to 100 mM NaNO₃ to prevent precipitation during concentration in a 10 kDa MWCO centrifugal filter (Amicon Ultra15 concentrator, Millipore UFC901024). The concentrated protein was loaded on a Superdex 200 16/60 gel filtration column that was pre-equilibrated with running buffer (20 mM Tris HCl pH 8, 100 mM NaCl, 2 mM DTT). The peak fractions were analysed by SDS-PAGE gel electrophoresis and concentrated to ~50 µM. The proteins were frozen in liquid nitrogen and stored at -80°C.

3.1.3 Purification and labelling of p40-PX domain

E. coli C41 (DE3) RIPL cells were transformed with the plasmid pYO1125. The transformed bacteria were cultured in 2xTY medium containing 0.1 mg/ml ampicillin at 37°C to an OD₆₀₀ 0.6 and induced with 0.3 mM IPTG at 30°C for ~16 h. A culture of 2-6 L of cells was pelleted by 20 min centrifugation at 4,000 g and the pellets were resuspended in ~150 mL lysis buffer (20 mM HEPES pH 8, 200 mM NaCl, 1 mM TCEP, 0.05 μL/mL universal nuclease (ThermoFisher, 88702), 0.5 mg/mL lysozyme (MP Biomedicals, 195303)). The cells were sonicated 6 min on ice (10 s on/10 s off, 60% amplitude) and the lysates were spun at 30,000 g for 45 min at 4°C and the supernatant was filtered through a 0.45 μm filter (Millipore, SE2M230I04). An aliquot of 2.5 mL of washed Glutathione Sepharose beads was added (Glutathione Sepharose 4B, GE Healthcare 17-0756-05). The lysate was incubated on the beads for ~45 min with gentle rolling at 4°C. The beads were then transferred to a gravity flow column (Bio-Rad, 731-1550) and washed with 100 mL lysis buffer, 100 mL wash buffer (20 mM HEPES pH 8, 300 mM NaCl, 1mM TCEP) and 100 mL TEV buffer (20 mM HEPES pH 8, 200 mM NaCl, 1mM TCEP). The N-terminal GST tag was cleaved with TEV protease by incubation overnight with gentle rocking at 4°C. The next day, elution fractions were collected and concentrated in a 10 kDa MWCO centrifugal filter (Amicon Ultra15 concentrator Millipore, UFC901024). The concentrated protein was loaded on a Superdex 75 16/60 gel filtration column equilibrated with running buffer (20 mM HEPES pH 8, 200 mM KCl, 1mM TCEP). The peak fractions were analysed by SDS-PAGE gel electrophoresis and concentrated to ~1.3 mM. The proteins were frozen in liquid nitrogen and stored at -80°C.

For the labelling of the p40 PX domain, 1 mg of AF647 C2 Maleimide kit (Life Technologies, A20347) was dissolved in 100 μ L DMSO (ThermoFischer, Catalog No. BP231-100) to a final concentration of 7.7 mM. Then, 250 μ M p40 PX, 2.5 mM TCEP, 385 μ M AF647 dye was mixed in labelling buffer (50 mM HEPES pH 7, 200 mM KCl) to a total volume of 1 mL. The reaction tube was wrapped in aluminium foil, and was left at room temperature for 2 h with gentle rocking. After the incubation, DTT was added to a final concentration of 1 mM and the protein was loaded on a 5 mL Heparin HP column (GE Healthcare 17040701). The column was first washed with HA buffer (50 mM HEPES PH 8, 100 mM KCl, 1 mM TCEP) and then p40 PX was eluted with HB buffer (50 mM HEPES PH 8, 1 M KCl, 1 mM TCEP). The peak fractions were pooled and concentrated to \sim 380 μ M with \sim 20-30% labelling efficiency. The proteins were frozen in liquid nitrogen and stored at -80°C .

3.1.4 Purification of human Rab1a

As the Rab1a construct was used for maleimide labelling, Rab1a (1-204) was mutated to be in the “active” conformation (Q70L) and surface cysteines were mutated to serines (C26S, C126S). *E. coli* C41 (DE3) RIPL cells were transformed with the plasmid pJB78. The transformed bacteria were cultured in 2xTY medium containing 0.1 mg/ml ampicillin at 37°C to an OD_{600} 0.6 and induced with 0.3 mM IPTG at 18°C for \sim 16 h. A culture volume of 2-6 L of cells was pelleted by 20 min centrifugation at 4,000 g and the pellets were resuspended in \sim 150 mL lysis buffer (20 mM HEPES pH 8, 200 mM NaCl, 1 mM TCEP, 0.05 μ L/mL universal nuclease (ThermoFisher, 88702), 0.5 mg/mL lysozyme (MP Biomedicals, 195303). The cells were sonicated for 6 min on ice (10 s on/10 s off, 60% amplitude), and the lysates

were spun at 30,000 g for 45 min at 4°C and the supernatant was filtered through a 0.45 µm filter (Millipore, SE2M230I04). An aliquot of 2.5 mL of washed Glutathione Sepharose beads was added (Glutathione Sepharose 4B, GE Healthcare 17-0756-05). The lysate was incubated on the beads for ~45 min with gentle rolling at 4°C. The beads were then transferred to a gravity flow column (Bio-Rad, 731-1550) and washed with 100 mL lysis buffer, 100 mL wash buffer (20 mM HEPES pH 8, 300 mM NaCl, 5% glycerol, 1mM TCEP) and 100 mL TEV buffer (20 mM HEPES pH 8, 200 mM NaCl, 1mM TCEP). The N-terminal GST tag was cleaved with TEV protease by incubation overnight with gentle rocking at 4°C. Next day, elution fractions were combined, and diluted ¼ in dilution buffer (20 mM HEPES 8.0 and 1 mM TCEP). The diluted protein solution was loaded on a 5 mL Q column (GE Healthcare, 17505301), then the flow through fraction was loaded on a 5 mL heparin column (GE Healthcare, 17040601) to remove unbound GST and TEV protease, respectively. The heparin flowthrough fraction was concentrated in a 10 kDa MWCO MWCO centrifugal filter (Amicon Ultra15 concentrator Millipore, UFC901024) to ~1 mL and the protein concentration was measured. In a total volume of 2 mL, Rab1a is mixed with 11 molar excess of GTP (Jena bioscience NU-1012) or GDP (Jena bioscience NU-1172), 18 molar excess of EDTA for 90 min at room temperature. The solution was then brought to a 36 molar excess of MgCl₂ and incubated for another 30 min. The 2 mL mixture was loaded on a Superdex 75 16/6 gel filtration column that was pre-equilibrated with running buffer (25 mM HEPES pH 7, 150 mM NaCl, 0.5 mM TCEP). The peak fractions were analysed by SDS-PAGE gel electrophoresis and concentrated to ~0.5-1 mM. The proteins were frozen in liquid nitrogen and stored at -80°C.

3.1.5 Purification of human Rab5a

As this Rab5a construct was used for maleimide labelling, Rab5a (1-212) was mutated to be in the “active” conformation (Q79L) and surface cysteines were mutated to serines (C19S, C63S). *E. coli* C41 (DE3) RIPL cells were transformed with the plasmid pOP823. The transformed bacteria were cultured in 2XTY medium with 0.05 mg/ml kanamycin at 37°C to OD₆₀₀ 0.8 and induced with 0.3 mM IPTG at 37°C for ~3-5 h. 2-6 L of cells were pelleted by 20 min centrifugation at 4,000 g and resuspended in ~100 mL of lysis buffer (25 mM HEPES pH 8, 200 mM NaCl, 10 mM imidazole, 0.05 μL/mL universal nuclease (ThermoFisher, 88702), 0.5 mg/mL lysozyme (MP Biomedicals, 195303)) and sonicated 6 min on ice (10 s on/10 s off, 60% amplitude) The lysates were spun at 30,000 g for 45 min at 4°C, filtered through a 0.45 μm filter (Millipore, SE2M230I04) and loaded on two connected 5 mL Ni-NTA FF columns (GE Healthcare 17-5255-01). The columns were washed with 100 mL wash buffer (20 mM Tris pH 8, 300 mM NaCl, 10 mM imidazole, 2 mM β-mercaptoethanol, 5% glycerol) and 100 mL Ni A buffer (20 mM Tris pH 8, 100 mM NaCl, 10 mM imidazole, 2 mM β-mercaptoethanol, 5% glycerol). The protein was eluted with an imidazole gradient to Ni B buffer (20 mM Tris pH 8, 100 mM NaCl, 200 mM imidazole, 2 mM β-mercaptoethanol, 5% glycerol). The eluted fractions were analysed by SDS-PAGE gel electrophoresis, combined and concentrated with 10 kDa MWCO centrifugal filter (Amicon Ultra15 concentrator Millipore, UFC901024) to ~7-15 mL. The concentrated fractions were mixed with SUMO-protease, transferred to a dialysis bag (Dialysis tubing, 10K MWCO, SnakeSkin™ Thermo Fischer) and dialysed against 4 L of dialysis buffer overnight at 4°C (20 mM Tris pH 8, 150 mM NaCl, 1 mM TCEP, 5% glycerol). The next day, the protein was loaded on two connected 5 mL Ni-NTA FF columns and washed with ~50 mL

dialysis buffer. The flow-through was collected, concentrated to ~1 mL and the protein concentration was measured. In a total volume of 2 mL, Rab5 was mixed with 11 molar excess of GTP (Jena bioscience NU-1012) or GDP (Jena bioscience NU-1172) and 18 molar excess of EDTA for 90 min at room temperature. The solution was then brought to 36 molar excess of MgCl₂ and incubated for another 30 min. The 2 mL solution was loaded on a Superdex 75 16/6 gel filtration column that was pre-equilibrated with running buffer (25 mM HEPES pH 7, 150 mM NaCl, 0.5 mM TCEP). The peak fractions were analysed by SDS-PAGE gel electrophoresis and concentrated to ~0.5-1 mM. The proteins were frozen in liquid nitrogen and stored at -80°C.

For HXD-MS, a Rab5a construct was designed without C-terminal cysteine and mutated surface cysteines. This construct (Q79L, 1-211, plasmid pYO1261) was purified as above.

3.2 GUV assay

Table 2: Lipid species

Lipid species	Company	Catalogue number	Additional comments
DOPC	Avanti Polar Lipids, Inc	850375C	Dissolved in chloroform
DOPE	Avanti Polar Lipids, Inc	850725C	Dissolved in chloroform
DOPS	Avanti Polar Lipids, Inc	840035C	Dissolved in chloroform
Brain PC	Avanti Polar Lipids, Inc	840053C	Dissolved in chloroform
Brain PE	Avanti Polar Lipids, Inc	840022C	Dissolved in chloroform
Brain PS	Avanti Polar Lipids, Inc	840032C	Dissolved in chloroform
Liver PI (mixed chain PI)	Avanti Polar Lipids, Inc	840042C	Dissolved in chloroform

Materials and methods

DSPE-PEG(2000) Biotin	Avanti Polar Lipids, Inc	880129C	Dissolved in chloroform
DO Liss Rhod PE	Avanti Polar Lipids, Inc	810150P	Dissolved in chloroform
SOPC	Avanti Polar Lipids, Inc	850467C	Dissolved in chloroform
SOPE	Avanti Polar Lipids, Inc	850758C	Dissolved in chloroform
SOPS	Avanti Polar Lipids, Inc	840039C	Dissolved in chloroform
DSPI	Avanti Polar Lipids, Inc	850143P	Dissolved in chloroform:methanol:H2O =20:9:1
SAPI	Avanti Polar Lipids, Inc	850144P	Dissolved in chloroform:methanol:H2O =20:9:1
DOPI	Avanti Polar Lipids, Inc	850149P	Dissolved in chloroform:methanol:H2O =20:9:1
DO PI(3)P	Avanti Polar Lipids, Inc	850150P	Dissolved in chloroform
DO PI(4)P	Avanti Polar Lipids, Inc	850151P	Dissolved in chloroform
DO PI(4,5)P2	Avanti Polar Lipids, Inc	850155P	Dissolved in chloroform
18:1 PE MCC	Avanti Polar Lipids, Inc	780201C	Dissolved in chloroform

Table 3: GUV lipid mixtures

ID	Composition (% in mg/mL)	Description in figures
YOGUV3 / STGUV2	18% liver PI, 10% DOPS, 17% DOPE, 55% DOPC, 0.03% DSPE-PEG-Biotinyl, 0.017% Liss-Rhodamine	DO Base, 82% DO, 18% mixed PI chain, or 10% PS
YOGUV5 / STGUV1	18% liver PI, 25% DOPS, 17% DOPE, 40% DOPC, 0.03% DSPE-PEG-Biotinyl, 0.017% Liss-Rhodamine	DO high PS
YOGUV16	18% liver PI, 10% SOPS, 17% SOPE, 55% SOPC, 0.03% DSPE-PEG-Biotinyl, 0.017% Liss-Rhodamine	82% SO
YOGUV18	18% liver PI, 10% DOPS, 17% DOPE, 55% SOPC, 0.03% DSPE-PEG-Biotinyl, 0.017% Liss-Rhodamine	55% SO + 27% DO
YOGUV28 / STGUV7	18% liver PI, 10% DOPS, 17% DOPE, 50% DOPC, 5% DO PI(4,5)P2, 0.03% DSPE-PEG-Biotinyl, 0.017% Liss-Rhodamine	DO PI(4,5)P2
YOGUV34	15% liver PI, 10% DOPS, 17% DOPE, 55% DOPC, 3% DO PI(3)P, 0.03% DSPE-PEG-Biotinyl, 0.017% Liss-Rhodamine	DO base + 3% PI(3)
YOGUV36	15% liver PI, 10% SOPS, 17% SOPE, 55% SOPC, 3% DO PI(3)P, 0.03% DSPE-PEG-Biotinyl, 0.017% Liss-Rhodamine	SO base + 3% PI(3)
STGUV3	18% liver PI, 10% DOPS, 17% DOPE, 50% DOPC, 5% PI(4)P, 0.03% Lisamine Rhodamine-PE, 0.03% DSPE-PEG-Biotinyl	DO PI(4)P
YOGUV29	18% DOPI, 10% DOPS, 17% DOPE, 55% DOPC, 0.03% DSPE-PEG-Biotinyl, 0.017% Liss-Rhodamine	18% DOPI
YOGUV30	18% SAPI, 10% DOPS, 17% DOPE, 55% DOPC, 0.03% DSPE-PEG-Biotinyl, 0.017% Liss-Rhodamine	18% SAPI

YOGUV11	18% DSPI, 10% DOPS, 17% DOPE, 55% DOPC, 0.03% DSPE-PEG-Biotinyl, 0.017% Liss-Rhodamine	18% DSPI
STGUV11	18% liver PI, 10% DOPS, 7% DOPE, 55% DOPC, 10% PE-MCC, 0.03% Lisamine Rhodamine-PE, 0.03% DSPE-PEG-Biotinyl	DO Base + 10% PE-MCC

3.2.1 GUV generation and immobilisation

A 1 mg/mL GUV lipid mixture was assembled from the different lipid species. 15 μ L of this mixture was pipetted onto the indium-tin-oxide (ITO)-coated slides (Nanion) and then dried in a desiccator for 1 h. A rubber ring was mounted on top after drying and 220 μ L of swelling solution (0.5 M glucose or sucrose) was added into the rubber ring. Then, the second ITO slide was positioned on top of the O-ring. The Vesicle Prep Pro device (Nanion) was programmed for: 10 Hz, 60°C, 1 Amp, 3 min rise, 68 min fall. After the GUVs were generated, they were immediately removed from the ITO slide and transferred to a 1.5 mL tube.

The wells of an 8 well glass bottom chamber (Ibidi 80827) were treated with 100 μ L of avidin solution (0.1 mg/mL avidin egg white, Life Technologies A2667 dissolved in PBS and 1 mg/mL BSA) for 15 min and then washed 3 times with observation buffer (25 mM HEPES pH 8, 271.4 mM NaCl). 84 μ L observation buffer was added to the wells, followed by 48 μ L GUVs. GUV immobilization was inspected on the confocal microscope (Zeiss LSM780) and then 20 μ L of 10x buffer (250 mM HEPES pH 8, 10 mM EGTA, 20 mM MnCl₂, 10 mM TCEP, 1 mM ATP pH 8) was added.

3.2.2 Rab labelling of GUVs

GUVs were made as described above. The wells of an 8 well glass bottom chamber (Ibidi 80827) were treated with 100 μ L of avidin solution (0.1 mg/mL avidin egg white, Life Technologies A2667 dissolved in PBS, and 1 mg/mL BSA) for 15 min and

then washed 3 times with observation buffer (25 mM HEPES pH 7, 271.4 mM NaCl). 64 μ L observation buffer was added to the wells, followed by 48 μ L GUVs and 20 μ L Rab solution. The Rab solution contained 4x excess Rab over PE-MCC lipid. The well chambers were incubated overnight at 4°C. On the next day, the wells were washed by carefully adding and taking off 360 μ L of wash buffer (31.8 mM HEPEPS pH 8, 172.7 mM NaCl, 181.8 mM sucrose, 5 mM β -mercaptoethanol) 6-8 times. GUV immobilization was inspected on the confocal microscope (Zeiss LSM780) and then 20 μ L of 10x buffer (250 mM HEPES pH 8, 10 mM EGTA, 20 mM MnCl₂, 10 mM TCEP, 1 mM ATP pH 8) was added.

3.2.3 Time series acquisition by confocal microscopy

GUVs were observed with a 63x oil immersion objective (Plan-Apochromat 63x/1.40 Oil DIC, Zeiss) on an inverted confocal microscope (Zeiss 780), using ZEN software (Zeiss). The observation chamber was immobilized on a microscope stage holder using an adhesive (Blu-Tack, Bostik). In the ZEN software, Time Series and Positions were selected. The Lissamine-rhodamine channel for GUVs was observed with a 566-629 nm band and exited with a diode-pumped solid-state (DPSS) 561 nm laser. The AF647 channel for the p40 PX domain was observed with a 638-756 nm band and exited using a HeNe 633 nm laser. Six areas per well were selected randomly so that at least 20 GUVs were statistically be analysed. After area selection, an aliquot of 48 μ L containing VPS34 complex (50-100 nM final concentration in 200 μ L) and AF647-PX (15.2 μ M final concentration in 200 μ L) in protein dilution buffer (25 mM HEPES pH8.0, 150 mM NaCl, 1 mM TCEP, and 0.5 mg/mL BSA) was added to each well. The final concentrations are described in the figures and their legends. The Zen software took images every 2 min for 60-120 min.

For the Z-stack analysis, the Z-stack option in the Zen software was used and 10 slices of various thickness were acquired per stack.

3.2.4 Image analysis

Images were opened with Fiji software using Bio-Formats importer plugin. In order to analyse the collected time course, partial areas or whole GUVs from were selected using the ROI (region of interest) function tool and added to ROI manager. Fluorescence intensities were analysed using a macro called GUV_intensity.ijm. which was written by Jerome Boulanger. Background noise from unbound PX domain on the AF647 channel was subtracted from all each time frame by selecting ten random areas per image without GUVs. Then, the average AF647 values of the selected areas were obtained with the command: Image>Stacks>Plot Z -axis Profile. The mean values were subsequently subtracted from the fluorescence intensities of the reacted GUVs. For kinases with little or no activities (*e.g.*, for the BATS domain mutant and for VPS34 alone), the signal from the background noise can be stronger than the actual signal of the GUVs, which generates negative values. The increase of AF647-PX was plotted against the time with GraphPad Prism7 (GraphPad Software).

In order plot the correlation of GUV radii versus kinase activity (Figure 4-12), whole GUVs were selected with the oval selection tool and added to ROI manager. The regions were then analysed using a macro called GUV_intensity1dimension.ijm, which was written by Jerome Boulanger. 3-5 random areas were selected for background subtraction using the ROI selection tool and the mean values were

subtracted from the AF647 signal. Results were plotted with Microsoft Excel (Microsoft) and GraphPad Prism7 (GraphPad Software). The initial rates of the kinase reactions were analysed by approximating a linear function through the initial increase of AF647-PX of at least 20 GUVs areas with GraphPad Prism7 (GraphPad Software). The mean value and standard deviation were then plotted with bar graphs and their statistical difference was verified by t-test.

3.3 Liposome preparation

Table 4: SUV/LUV lipid mixtures

ID	Composition (% in mmol/L)	Used in
STSUV2	16% liver PI, 10% Brain PS, 18% Brain PE, 56% Brain PC, 0.1% Liss-Rhodamine	Flotation CI vs CII
STSUV19	16% liver PI, 10% Brain PS, 12% Brain PE, 56% Brain PC, 5% DOPE-MCC, 0.1% Liss-Rhodamine	Flotation +/- Rab GTPases
STSUV32	16% liver PI, 12% DOPE, 66% DOPC, 6% DOPE-MCC	Cryo-ET
STSUV22	17% liver PI, 78% DOPS, 5% DOPE-MCC	Cryo-ET
STSUV21	16% liver PI, 10% DOPS, 12% DOPE 57% DOPC, 5% DOPE-MCC	Cryo-ET

3.3.1 LUV and SUV preparation

A lipid mixture was assembled according to Table 4 and dried under a nitrogen gas. The tube was rotated so that a thin film was formed on the glass wall. The remaining solvent was evaporated by a vacuum treatment in desiccator for 1 h. The lipids were dissolved in lipid buffer (25 mM HEPES pH 8, 150 mM NaCl, 1 mM TCEP or for maleimide reactions 25 mM Hepes pH 7, 150 mM NaCl) and vortexed for 2 min. The solution was transferred to a 1.5 mL Eppendorf Tube and sonicated for 2 min in a

bath sonicator. Then 10 cycles of freeze/thaw in liquid nitrogen and a 43°C water bath were carried out. The lipid mixture was extruded at least 20 times through a 100 nm filter for LUVs (Whatman® Anotop® 10 syringe filter 0.1 µm diameter, 10 mm Cat No 6809-1112) or 50 nm filter for SUVs (NanoSizer™ MINI Liposome Extruder, Part Code: TT-001-0010). The lipid solution was then used fresh.

3.3.2 Rab labelling of SUVs/LUVs

The SUV were prepared as described above. SUV concentration was measured by Lissamine Rhodamine emission (ex 560/ em 583) by plate reader (PHERAstar BMG LABTECH) to have a fluorescence value proportional to the SUV concentration. Rab was added in 0.3-0.6x molar ratio to PE-MCC lipid in 25 mM Hepes pH 7, 150 mM NaCl. The reaction was left overnight in the fridge. The next day, the reaction was spun 5 min at 5,000 g and the supernatant was taken off to separate any precipitate. Then, SUVs were pelleted for 30 min at 60,000g at 4°C in a TLA 100 rotor (Beckman Coulter). After the spin, a pellet can be seen and the supernatant, which has still unreacted Rab in it, was taken off. SUVs were re-dissolved in buffer (25 mM Hepes pH 8, 150 mM NaCl, 1 mM TCEP) and the final SUV concentration was determined by Lissamine Rhodamine emission.

3.4 Flotation assay

An aliquot of total 20 µL of sample was prepared containing: 1.8 mM or 1.5 mg/mL LUVs, 2 µM VPS34 complex in buffer containing 25 mM HEPES pH 8, 150 mM NaCl and 1mM TCEP. While the LUVs and proteins were incubated on ice for 30 min, a sucrose gradient was prepared. For the gradient, several sucrose solutions were

layered from the bottom to the top in a Beckman centrifuge tube (343775 Thickwall Polycarbonate Tube, Beckman Coulter): 40 μL 30% sucrose solution, 52 μL 25% sucrose solution, 52 μL 20% sucrose solution. Then 16 μL of the LUV/protein sample was carefully pipetted on top of the gradient without disturbing the layers. From the remaining LUV/protein sample, 2.5 μL were kept as an input sample for the SDS-PAGE gel. The gradient was then centrifuged for 3 h in a TLS-55 rotor (Beckman Coulter) at 55,000 rpm and 4°C. Afterwards, 6 fractions of 26 μL were carefully collected from the top of the gradient. The input and gradient fractions were then loaded on an SDS-PAGE gel.

3.5 Hydrogen deuterium mass spectrometry (HDX-MS)

3.5.1 Sample preparation of CI and CII incubated with liposomes

Yohei Ohashi and Glenn Masson prepared the protein samples, acquired the HDX-MS dataset and analysed the peptides.

A protein/lipid stock solution consisting of 7.5 μM complex I or II with 2.2 mg/mL LUVs (55% DOPC, 18% Liver PI, 17% DOPE, 10% DOPS) was incubated for 10 minutes at room temperature. 5 μL of this stock solution was either exposed to 45 μL of D_2O Buffer+ lipids (20 mM HEPES pH 8, 300 mM NaCl, 0.5 mM TCEP, 1 mg/mL LUV in D_2O) or D_2O Buffer only (20 mM HEPES pH 8, 300 mM NaCl, 0.5 mM TCEP in D_2O). The final D_2O concentration was 74.6% (99.8% D_2O , Acros Organics 351430075). The reactions were incubated for 0.3/3/30/300/3000 s at room temperature (besides 0.3 s, see below). Then the reaction was quickly quenched

with 20 μL of ice cold 5 M guanidium chloride and 8.4% formic acid pH 1 (final pH 2.2). Each sample was then immediately flash frozen in liquid nitrogen and subsequently stored at -80°C until analysis. Five time points were produced, with each exchange reaction executed in triplicate. The 0.3 s time point was obtained by carrying out the exchange for 3 s at 4°C .

3.5.2 Sample preparation of CII incubated with Rab5a

I prepared the protein samples, Sarah Maslen and I acquired the HDX-MS dataset and Yohei Ohashi and I analysed the peptides.

A Rab5a/complex II stock solution consisting of 5 μM complex II with 30 μM Rab5a-GTP was incubated for 30 minutes at room temperature. An aliquot of 5 μL of complex II alone was exposed to 45 μL of D_2O Buffer only (25 mM HEPES pH 8.0, 50 mM NaCl, 1 mM TCEP and D_2O at 94.2% final concentration (D_2O , Acros Organics 351430075) for 3/30/300/3000 s at room temperature. Furthermore, an aliquot of 5 μL complex II (5 μM) with 30 μM Rab5a-Q79L-GTP exposed to 45 μL D_2O Buffer + Rab5 (25 mM HEPES pH 8.0, 50 mM NaCl, 1 mM TCEP, 30 μM Rab5a-GTP and D_2O at 94.2% final concentration) for 3/30/300/3000 s at room temperature. The final D_2O sample concentration was 84.8% D_2O . Each exchange reaction executed in triplicate. Then the reaction was quickly quenched with 20 μL of ice cold 5 M guanidium chloride and 8.4% formic acid pH 1 (final pH 2.2). Each sample was then immediately flash frozen in liquid nitrogen and subsequently stored at -80°C until analysis. Four time points were produced, with each exchange reaction executed in triplicate.

3.5.3 Hydrogen deuterium mass spectrometry (HDX-MS)

Samples were quickly thawed and manually injected in to the M-Class Acquity UPLC with HDX technology (Waters), which was kept at a constant temperature of 0.1 °C. Protein samples were digested using an Enzymate Pepsin “Trap” Column (Waters) at 15 °C for two minutes and eluted from the “Trap” and onto an Acquity 1.7 µm particle, 100 mm × 1 mm C18 UPLC column (Waters), which had already been equilibrated with Pepsin-A buffer (0.1 % formic acid). The digested peptides were eluted using a 5-36 % gradient of Pepsin-B buffer (0.1 % formic acid, 99.9 % acetonitrile) over 20 minutes. Peptide Data were collected using a Waters Synapt G2 Si (Waters) over a 50 to 2000 m/z range using the High-Definition MSe data acquisition mode fitted with an ESI source.

Peptide identification was conducted using the ProteinLynx Global Server (PLGS, Waters, U.K.). Peptides were identified from three non-deuterated samples for the VPS34 complexes and analysed using DynamX 3.0 software (Waters, U.K.). Peptide inclusion criteria were: minimum intensity of 5000, minimum sequence length of 5 amino acids, minimum of 0.1 products per amino acid, maximum MH⁺ error of 5 ppm, and a positive identification meeting these criteria in at least 2 of the 3 non-deuterated files. An initial automated spectral processing step was conducted by DynamX followed by a manual inspection of individual peptides for sufficient quality. The HDX analysis in this manuscript complies with the community agreed guidelines (Masson et al., 2019).

3.6 Unnatural amino acid (UAA) crosslinking

BrCO6K was synthesized by Marie-Kristin von Wrisberg in Kathrin Lang's group (Cigler et al., 2017). The protein purification and crosslinking were carried out by me. The crosslinking analysis by mass spectrometry was done Zhuo Chen in Juri Rappsilber's group.

3.6.1 Purification of Rab5a S84→BrCO6K

Electromax DH10B cells (Invitrogen Catalog number: 18290015) were transformed with two plasmids (STp6_pBAD_Rab5a_Q79L_1-212_C19S_C63S_S84TAG and STp12_Kathrin_Lang_pEVOL_TEMPOH-1_PylT_Mm tRNA + aminoacyl - tRNA synthetase) and plated on LB plates (100 µg/mL ampicillin and 50 µg/mL chloramphenicol). The transformed bacteria were cultured in LB medium with 100 µg/mL ampicillin, 50 µg/mL chloramphenicol and 4 mM nicotinamide at 37°C. When the OD₆₀₀ reached 0.2, BrCO6K was added to a final concentration of 1.5 mM. Cells were left to grow until OD₆₀₀ 0.6 and then induced with 0.02 % arabinose. After 6h at 37°C, cells were pelleted by 20 min centrifugation at 4,000 g and resuspended in ~100 mL of lysis buffer (25 mM HEPES pH 8, 200 mM NaCl, 10 ml imidazole, 0.05 µL/mL universal nuclease (ThermoFisher, 88702), 0.5 mg/mL lysozyme (MP Biomedicals, 195303)) and sonicated 6 min on ice (10 s on/10 s off, 60% amplitude). The lysates were spun at 30,000 g for 45 min at 4°C. The supernatant was filtered through a 0.45 µm filter (Millipore, SE2M230I04) and loaded on two connected 5 mL Ni-NTA FF columns (GE Healthcare 17-5255-01). The columns were washed with 100 mL wash buffer (20 mM Tris pH 8, 300 mM NaCl, 10 mM imidazole, 2 mM β-mercaptoethanol, 5% glycerol) and 100 ml Ni A buffer (20 mM

Tris pH 8, 100 mM NaCl, 10 mM imidazole, 2 mM β -mercaptoethanol, 5% glycerol). The protein was eluted with an imidazole gradient with ~100 mL of Ni B buffer (20 mM Tris pH 8, 100 mM NaCl, 200 mM imidazole, 2 mM β -mercaptoethanol, 5% glycerol). The eluted fractions were analysed by SDS-PAGE gel electrophoresis and combined, concentrated with 10,000 kDa MWCO centrifugal filter (Amicon Ultra15 concentrator Millipore, UFC901024) to ~1 mL and the protein concentration was measured. In a total volume of 2 mL, Rab5a was mixed with 11 molar excess of GTP (Jena bioscience NU-1012) or GDP (Jena bioscience NU-1172), 18 molar excess of EDTA for 90 min at room temperature. The solution was then brought to 36 molar excess of $MgCl_2$ and incubated another 30 min. The 2 mL mixture was loaded on a Superdex 75 16/6 gel filtration column that was pre-equilibrated with running buffer (25 mM HEPES pH 8, 150 mM NaCl, 0.5 mM TCEP). The peak fractions were analysed by SDS-PAGE gel electrophoresis and concentrated to ~0.5-1 mM.

3.6.2 Crosslinking of Rab5a S84→BrCO6K and VPS34/ complex II

Complex II was mixed with 50-100 molar excess of Rab5a S84→BrCO6K in 5-15 μ L reaction volume. VPS34 was mixed with 100-200 molar excess of Rab5a S84→BrCO6K in 5-15 μ L reaction volume. Both samples were incubated overnight at 4°C. Crosslinks were then analysed by SDS-PAGE gel electrophoresis. The bands were cut out and send to our collaborators Juri Rappsilber and Zhuo Chen for mass spectrometry analysis.

3.7 Cryo-ET and subtomogram averaging

Dustin Morado helped in the acquisition of the tilt series and provided guidance during the subtomogram averaging.

3.7.1 Sample preparation

SUVs were labelled with Rab5a-GTP as described above. For grid preparation, in a final volume of 3 μ L, 3-10 mmol/L of SUVs were incubated with at least 8 μ M of VPS34 complex and incubated on ice for 30-45 min. Then BSA-coated gold fiducials (Gold nanoparticles 10 nm, BBI Solutions EM.GC10) were then added up to the final volume and mixed. The 3 μ L samples were applied immediately to multi hole grids (Multi A (various hole sizes, carbon film), Grid: Au, Mesh: 300, QUANTIFOIL®) and plunge-frozen in liquid ethane cooled by liquid nitrogen inside a Vitrobot (FEI, ThermoFisher). Blotting papers were left at least for 30 min in 100% humidity and 18 °C. The Vitrobot blot force was 20, with a blot time of 6 s. The grids were glow discharged for 30 sec with the Quorum SC7620 glow discharger prior to use.

3.7.2 BSA coating of gold fiducial

A 25 μ L aliquot of 200 mM sodium phosphate buffer (pH 5) was added to 975 μ L of gold fiducials (Gold nanoparticles 10 nm, BBI Solutions EM.GC10). Then, 50 μ L of 5 mg/mL BSA in 5 mM sodium phosphate buffer (pH 5) was added as well and incubated for ~1-4 h at 4°C. The reaction was centrifuged in a table top centrifuge at maximum speed (~20.000 g) for 1 h at 4°C. Then, ~900 μ L supernatant was taken off without disturbing the pellet and 900 μ L of buffer (25 mM HEPES pH8, 100 mM NaCl, 1mM TCEP) was added and mixed. The pellet was centrifuged again and as

much supernatant was taken off as possible after the spin. The pellet was dissolved in the desired volume of buffer. For four reactions (4x 975 μL of gold fiducials), 30-50 μL was used.

3.7.3 Cryo-ET acquisition

Tomogram acquisition for complex II UVRAG Δ C+BATS on Rab5a decorated membranes was performed on a FEI Titan Krios operated at 300 kV with a Gatan Quantum energy filter (slit width of 20 eV) and a K3 direct detector operated in counting mode. Serial-EM software was used to acquire tilt series using a dose-symmetric scheme with a tilt range $\pm 60^\circ / 3^\circ$ angular increment and defoci between -2.5 to -5 μm (Hagen et al., 2016; Mastronarde, 2005). 41 tilt images were recorded as 10-frame movies in counting mode with a pixel size of 2.133 $\text{\AA}/\text{px}$ at dose rate $\sim 5.5 \text{ e}/\text{A}^2/\text{s}$ and a total dose per tomogram of $\sim 123 \text{ e}/\text{A}^2$. Data collection parameters are summarized in Figure 6-4.

3.7.4 Raw image processing and tomogram reconstruction

The raw movies were corrected for detector gain pixel defects and aligned using “alignframes” from the IMOD package (Kremer et al., 1996). Tilt series with unsatisfactory error during gold fiducial alignment or contamination such as dirt or ice were discarded. Tilt-series were low pass filtered according to the cumulative radiation dose and aligned using gold fiducial markers in the IMOD package (Grant and Grigorieff, 2015). Bin8 (pixel size 17.064 $\text{\AA}/\text{px}$) and bin4 (pixel size 8.532 $\text{\AA}/\text{px}$) non-contrast-transfer-function (CTF) corrected tomograms were reconstructed by weighted back-projection in IMOD. 3D CTF-correction for bin2 (pixel size 4.266

Å/px) and bin1 (pixel size 2.133 Å/px) tomograms were performed using NovaCTF phaseflip with defocus estimation by “ctfplotter” from the IMOD package (Turoňová et al., 2017).

3.7.5 Subtomogram averaging

Subtomogram alignment and averaging was done using a processing pipeline comprised of BASH scripts that organise and call a collection of compiled MATLAB functions built using the TOM toolbox (Förster et al., 2005). These scripts were written and assembled by Dustin Morado and termed the subTOM pipeline. Each script organises a routine operation, many of which rely on multiple functions, in a unified manner, simplifying access and modification to the function parameters. This additionally allows for functions to be called in a distributed manner using a batch-queuing system for parallel processing. Scripts also improve the ease of using compiled MATLAB functions, allowing the pipeline to be run using only the freely available MATLAB Compiler Runtime as opposed to requiring a MATLAB license. Additionally, instead of a binary wedge mask, a modified wedge mask was used (Wan et al., 2017). The modified wedge mask was generated specifically for each tomogram by averaging the amplitude spectra of 500 random positions in ice-only areas. Therefore, the noise amplitude spectrum in these areas is only modulated by CTF correction, dose filtering and weighted back-projection. The modified wedge mask was then rotated to the angular orientation (or Euler angles φ , θ , ψ) of each subtomogram and an average wedge was calculated in Fourier space. The average wedge was then inverted ($1/\text{average wedge}$) and multiplied with the Fourier transform of the subtomogram average. Lastly, the product of the multiplication is

inverse Fourier transformed and now represents the weighted subtomogram average. This approach is called weighted averaging (Walz et al., 1997). The average wedge can then also be used to assess the amount of missing wedge in Fourier space as done Figure 6–10. All relevant alignment runs and search parameters in order to yield the 9.8 Å map of complex II UVRAGΔC+BATS are summarised in Table 5. The alignment and CC masks were created with the `subtom_shape.sh` script and the value for each parameter in the script was kept in the name (*e.g.* `m28r10h6.em` = box size 28, radius 10, height 6).

To define the initial subtomogram positions, a plugin for Chimera, which was written by Kun Qu, was used (Qu et al., 2018). With the help of the plugin, the centres and radii of vesicles were manually set in bin8 tomograms. The subtomogram coordinates (x/y/z) and rotations (θ and ψ but random ϕ (in-plane) rotation) were defined by the sphere surface with a uniform sampling of 8 px (~ 136 Å). As vesicles are not perfectly spherical, subtomograms were first aligned to the vesicle lipid bilayer with a reference containing a membrane bilayer (Table 5, run_1). The vesicle diameters were determined by calculating the vesicle centroid by the average position of the subtomograms around each vesicle after membrane alignment. Then an average diameter was calculated by measuring the distance of each subtomogram to the calculated centroid and multiplied by two. The distance between the protein complex and membrane (~ 6 nm) was subtracted from the calculated diameter. Then, subtomograms were aligned to a V-shape to identify particles (Figure 6–7, Table 5, run_11). After 4 iterations, some subtomograms converged and formed clusters, which indicated the presence of a particle. The subtomogram coordinates were cleaned by a minimal distance threshold so that

191,169 particles remained. Subtomograms were split into even/odd halves in bin4 and further aligned separately until the resolution did not improve (Table 5, run_30 and run_31). Subsequently, principal component analysis (PCA) classification on wedge-masked difference maps was used to classify the subtomograms (Heumann et al., 2011). For the PCA, the same alignment mask was used as in run_31, which does not include membrane density. The first 5 eigencomponents were used to sort the data into 20 classes. Classes 1-6 were combined with a total of 31,307 particles and further aligned in bin4 (Table 5, run_36). The alignment was then continued in bin2, where the subtomograms were shifted to the centre of the box, and bin1 until no improvement in resolution could be achieved. The final resolution was 9.8Å (FSC 0.143 cutoff). The final maps were sharpened with local low-pass filtering using relion_postprocess from the Relion 3.0 package (Zivanov et al., 2018). Additionally, the LAFTER algorithm was used for local de-noising (Ramlaul et al., 2018).

Table 5: Subtomogram averaging angular search runs

Angular search run	Subtomogram coordinate file	Used reference	No of particles	Alignment mask	CC mask	Psi/theta search range	Phi (in-plane rotation) search range	Subtomogram low_pass filtered to
Bin8 - non-CTF corrected, pixel size 17.064 Å/px								
Run_1	Coordinates after seeding 8px	Membrane shape Box size 28 px	774,798	m28r9h12z-3sigma2.em Cylinder enclosing membrane	m28r1h24.em	/	10° steps, total range	60 Å
Run_11	Run_1 iter 6 CC cleaned 0.08	V shape Box size 28 px	640,787	m28r6h7x1y1z5phi270psi15theta15sigma1.em Cylinder above membrane	m28r10h6.em	5° steps, total range 20°	10° steps, total range 180°	60 Å
Bin4 - 3D CTF corrected (data set split in half → even/odd), pixel size 8.532 Å/px Duplicates cleaned by distance cut off 8px, cluster size 2, cluster distance 2px								

Materials and methods

Run_30 Even/odd	Run_11 iter 4	Ref of run_11 iter 4 Box size 56 px	191,169	m56r8h24x2y8p hi20psi20theta8 0sigma1.em Cylinder above membrane	m56r4h 2.em	5° steps, total range 15°	5° steps, total range 60°	Iter 1-4 40 Å Iter 4-7 26 Å
Run_31 Even/odd	Run_30 iter 7	Ref of run_30 iter 7 Box size 56 px	191,169	m56rx8ry18rz11 y2z6phi20sigma 05.em Elliptic cylinder above membrane	m56r4h 2.em	5° steps, total range 15°	5° steps, total range 60°	26 Å
Run_36 Even/odd	Run_31 iter 10 CC cleaned 0.2 3D classification output: Class 1-6 combined	Ref of un_31 iter 10 Box size 56 px CC cleaned 0.2 3D classification output: Class 1-6 combined	31,307	m56rx8ry18rz11 y2z6phi20sigma 05.em Elliptic cylinder above membrane	m56r2h 1.em	2° steps, total range 4°	2° steps, total range 8°	21 Å
Bin2 - 3D CTF corrected, pixel size 4.266 Å/px								
Run_42 Even/odd	Run_36 iter 2 Shifted position to box centre	Ref run_36 iter 2 Box size 80 px Shifted position to box centre	31,307	m80r30h30z8 phi-70theta 20psi20sigma2.e m Cylinder above membrane	m80r6h 3.em	1° steps, total range 5°	1° steps, total range 10°	16 Å
Bin1 - 3D CTF corrected, pixel size 2.133 Å/px								
Run_44 Even/odd	Run_42 iter 3	Ref run_42 iter 3 Box size 160 px	31,307	m160r60h60z10 phi280psi20thet a20sigma2.em Cylinder above membrane	m160r6 h6.em	1° steps, total range 6°	1° steps, total range 6°	16 Å
Final subtomogram coordinates: Run_44 iter 7, final resolution 9.8 Å (FSC 0.143 cutoff)								

4 Increasing VPS34 activity by protein domains and membrane composition

4.1 Results

4.1.1 Measuring PI3K lipid kinase activity

In previous research studies, the activity of VPS34 has been measured in various ways. Most commonly, VPS34 or other subunits were immunoprecipitated and immobilised on beads to measure kinase activity. It is important to check the composition of the desired complex on the beads by Western blotting, Coomassie staining or silver staining. This has not always been done and consequently effects from additional binding proteins cannot be excluded (Kim et al., 2013; Russell et al., 2013; Yuan et al., 2013).

Furthermore, the production of PI(3)P can be measured in different ways. The levels of PI(3)P in cells can be measured by using fluorescently labelled PI(3)P-protein binding domain such as PX or FYVE and measuring the total fluorescence. However, this does not account for which specific protein complex produced the PI(3)P or whether it was actually produced by dephosphorylating other phosphoinositides (Su et al., 2017). The amount of PI(3)P produced during *in vitro* reactions can be measured by using chemical extraction and thin layer chromatography (Kim et al., 2013; Munson et al., 2015; Stjepanovic et al., 2017; Yuan et al., 2013) or a kit for

measuring ADP generation from ATP by Promega (ADP-Glo Kinase assay kit) (Brier et al., 2019; Chang et al., 2019; Stjepanovic et al., 2017). Chemical extraction and thin layer chromatography can be an imprecise method and PI(3)P could be lost during extraction steps. When using the ADP-Glo kinase assay kit, one has to be careful about the purity of the VPS34 complex. Other proteins with ATPase activities such as chaperones are frequently co-purified and can cause a high background signal. Conducting negative controls, such as the inclusion of PI3K-specific inhibitors or the exclusion of PI are required in order to make sure that the ADP produced is by VPS34 due to phosphorylating PI to PI(3)P. However, the largest drawback is that these assays are all end point measurements, with enzyme kinetics inferred through varying enzyme concentration and incubation times. In order to accurately measure enzyme activity, a high enough enzyme concentration and a time course is necessary to ensure that the enzyme is within the linear range of its activity.

Another difficulty with estimating VPS34 activity is that it depends on the manner in which the substrate lipids are presented to the enzyme. Organelle membranes are lipid bilayers consisting of a variety of lipid species (Meer and Kroon, 2011). Yet, often liposomes consisting of 50% PI and 50% PS (Brier et al., 2019; Chang et al., 2019; Stjepanovic et al., 2017) or even a pure soluble PI lipid, not in vesicle form (Kim et al., 2013; Lu et al., 2014; Yuan et al., 2013; Zhong et al., 2009), are used to assess VPS34 activity. These mixtures are not physiological and do not reflect the intracellular conditions, limiting their use in inferring true-to-life enzyme characteristics.

In order to assess how protein domains and membrane composition alter VPS34 activity, we have developed an *in vitro* PI3K assay using purified protein complexes and giant unilamellar vesicles (GUVs) with a defined and physiological lipid composition. Giant unilamellar vesicles have a radius of ~1-30 μm and can be made by a process called electrosweeling (Angelova and Dimitrov, 1986). For this, lipids dissolved in an organic solvent are dried on ITO (indium tin oxide)-coated glass cover slides. Then a glucose or sucrose solution is added, and an alternating electric potential is applied that causes the swelling of the hydrated lipid layer to form GUVs. As the base lipid composition called “DO base”, a mix of 55% DOPC, 17% DOPE, 10% DOPS, 18% mixed chain PI and 0.3% fluorescent Lissamine™ rhodamine B-DOPE (Liss-Rhod) was chosen. This mix of phospholipids mimics the ER membrane where complex I was found to be active (Fan et al., 2011). We determined that the majority of lipid species would have acyl chains that are di-oleic acid (18:1-18:1, omega-9) in order to create a relatively loose membrane composition that is not permeable to the surrounding liquid (Manni et al., 2018). For PI, we chose a species that was purified from bovine liver with a mixed acyl chain composition (18:0, 20:4, 20:3, 18:1 and 18:2, hereafter called mixed chain PI). The influence of PI will be further discussed in chapter 4.1.7.

For the assay, a p40-PX domain is used as it was shown to selectively bind to PI(3)P (Ellson et al., 2001). The assay worked as follows: VPS34 complex, ATP and PX, which was labelled with Alexa Fluor 647 (AF647-PX), were added to a solution of PI-containing GUVs. Then, VPS34 phosphorylated PI to PI(3)P and subsequently the red fluorescent AF647-PX bound to the produced PI(3)P. Hence, PI(3)P production was measured by the increase of the AF647 signal around the GUVs over time

(Figure 4–1). Images were taken every 2 minutes on a confocal microscope for 60-90 minutes.

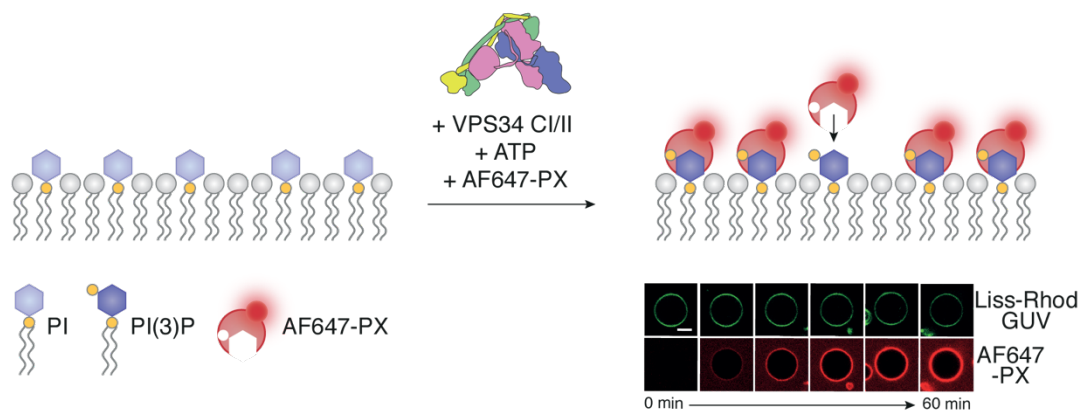


Figure 4–1: Design of GUV PI3 kinase assay

Complex I/II, ATP and Alexa Fluor-647 labelled p40-PX domain (AF647-PX) is added to GUVs containing PI. GUVs are labelled with Lissamine-Rhodamine (Liss-Rhod GUV), whose fluorescence delineates the membrane. As PI(3)P is produced, AF647-PX accumulates at the GUV surface. The amount of AF647-PX is indicative of VPS34 activity. Scale bars: 5 μm

For the following chapter 4, the experiments were conducted by both Yohei Ohashi and myself. We wished to juxtapose the activities of human VPS34 complexes I and II, with Yohei Ohashi examining complex I whereas I focused on complex II in the following GUV PI3 kinase assays.

4.1.2 ATG14L BATS is essential for complex I activity

In Rostislavleva et al., yeast complex I (Vps34, Vps15, Vps30, Atg14) and yeast complex II (Vps34, Vps15, Vps30, Vps38) activities were compared on GUVs made of a relatively rigid mixture of lipids purified from porcine brains with 18:1, 16:0, 18:0, and 20:4 acyl chains (Rostislavleva et al., 2015). Surprisingly, yeast complex II showed robust activity, while yeast complex I was inactive on this stiff lipid composition. With this intriguing observation, I wanted to explore the activity of human complex I (VPS34, VPS15, Beclin 1, ATG14L) and complex II (VPS34, VPS15,

Beclin 1, UVRAG) using the GUV PI3K assay. From here on, only the human protein subunits are discussed.

Human complexes I and II were purified with only VPS15 being C-terminally tagged with a ZZ-tag that was cleaved off during purification by cleavage with TEV protease (Chen et al., 2006). Using this method of purification ensured that no tags are left on the protein complexes that could interfere with the kinase activity, as they might be situated at a membrane interface. In contrast, in other studies, all protein subunits were N-terminally tagged with a non-cleavable 2x Strep tag (Chang et al., 2019; Stjepanovic et al., 2017). In fact, Itakura et al. have shown that human VPS34 N-terminally tagged with GFP was diffuse in the cytosol during starvation whereas VPS34 C-terminally tagged with GFP was able to form the characteristic punctate structures that represent forming autophagosomes (Itakura et al., 2008).

The activity of human complexes I and II were assayed at 100 nM on DO base lipids (Figure 4–2A). When the AF647-PX fluorescence values were plotted over a time course of 60 min, it is obvious that human complex I was substantially more active than complex II. Initial rates were estimated by fitting a line to the initial part of the curve. Comparing these initial rates, it became evident that complex I is 7-fold more active than complex II (Figure 4–2B). In Figure 4–2C, confocal images of GUVs at 60 min in AF647-PX and Liss-Rhod channels are shown. If the difference would have been taken from these end points, there would have been significant substrate depletion and complex I would have appeared to be only 3-fold more active. By making measurements over time, the linear portions of the curves before significant substrate depletion could be easily recognised.

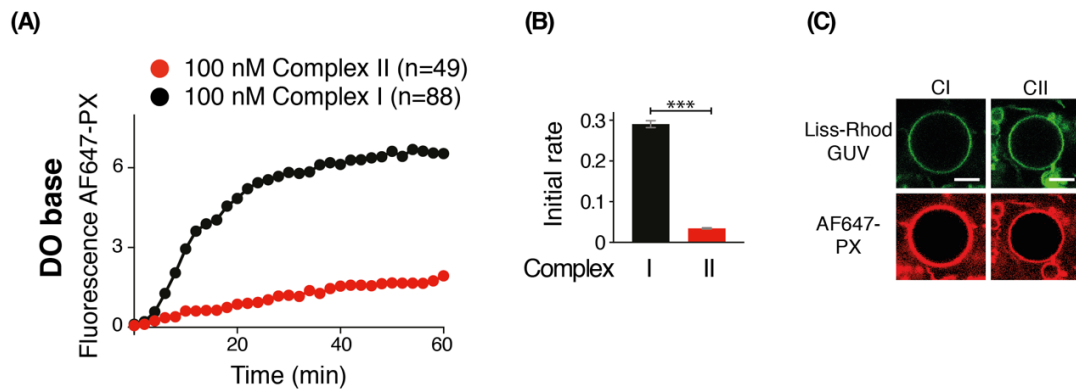


Figure 4-2: Human complex I is more active than complex II on DO base lipids

(A) On DO base lipids (18% mixed chain PI, 55% DOPC, 10% DOPS and 17% DOPE), complex I was more active than complex II. The signal of AF647-PX was plotted over time for complexes I and II. **(B)** A linear function was modelled in the beginning of the curves. Here, complex I was about 7-times more active than complex II. **(C)** Confocal images of representative GUVs are shown at 60 min. Scale bars: 5 μm . Significance level: *** $p < 0.001$; ** $p < 0.01$; * $p < 0.05$; n.s. = not significant. The number of GUVs for analysis is indicated by (n).

I also wanted to compare the ability of human complexes I and II to bind to membranes. Therefore, LUVs (large unilamellar vesicles) with a diameter of 100 nm were made and a flotation assay was carried out as follows. VPS34 complex and LUVs were mixed and pipetted onto a sucrose gradient. Then, the gradient was centrifuged and afterwards six fractions were carefully collected from the top of the gradient. The gradient fractions were then loaded on to a SDS-PAGE gel (Figure 4-3A). Fractions 1-3 contained floating liposomes and bound protein, while fractions 4-6 held the residual pelleted protein. If one compared the amount of complexes I and II bound to liposomes, it is clear that there was more complex I in fractions 1-3 (Figure 4-3B and C). Thus, complex I had a much higher affinity for membranes than complex II. It should be noted that for all flotation assays, LUVs were made out of the rigid lipid composition purified from brain with 18:1, 16:0, 18:0, and 20:4 acyl chains as in Rostislavleva et al., since DO Base lipids are too loose to see a difference between complexes I and II (Rostislavleva et al., 2015).

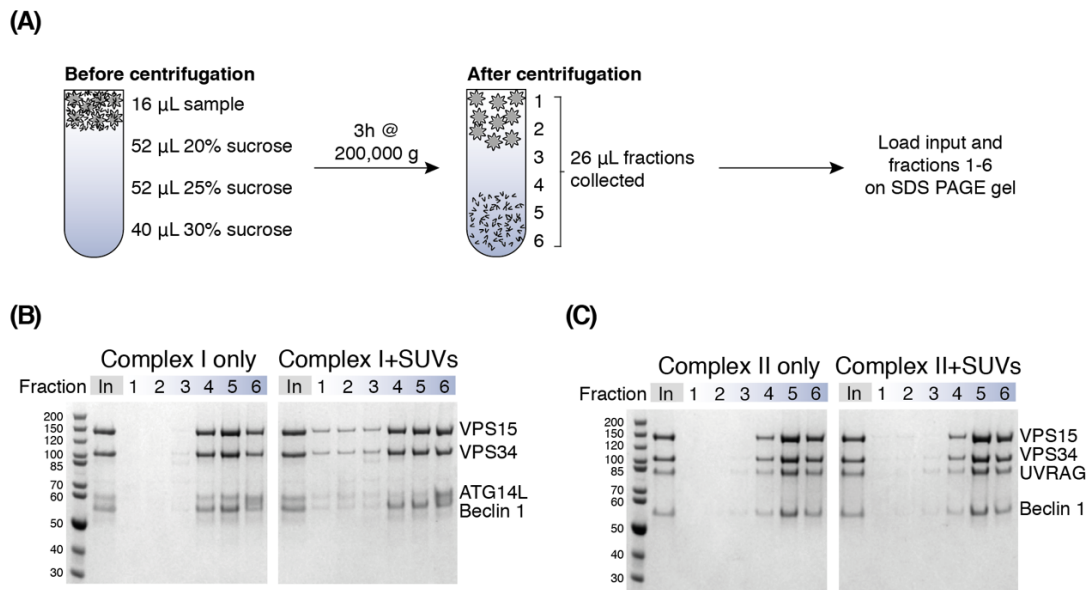


Figure 4-3: Complex I has a higher affinity for membranes than complex II

(A) Membrane binding of complexes I and II was tested by lipid flotation assay. Large unilamellar vesicles (LUVs, 100 nm) and proteins were incubated and then pipetted on to a sucrose gradient. The gradient was centrifuged, fractionated and loaded on to SDS-PAGE gels. Coomassie stained fractions 1-3 (numbering from the top of the gradient) contained floating vesicles and membrane-bound proteins whereas fractions 4-6 held pelleted proteins. **(B)** and **(C)** Complexes I and II without LUVs pelleted to the bottom. When LUVs were added, complex I showed a higher affinity for membranes than complex II.

The residues 471-488 of the complex I specific subunit ATG14L were proposed to adopt the structure of an amphipathic α -helix known as amphipathic lipid packing sensor (ALPS) motif (Drin et al., 2007; Fan et al., 2011; Nguyen et al., 2017). As the ALPS motif was shown to be essential for *in vitro* liposome and *in vivo* ER recruitment, I was interested in what happens to complex I activity when the ALPS is deleted from ATG14L (ATG14L Δ ALPS 471-492, Figure 4-4A). Surprisingly, complex I with ATG14L Δ ALPS 471-488 was completely inactive on DO base GUVs (Figure 4-4B).

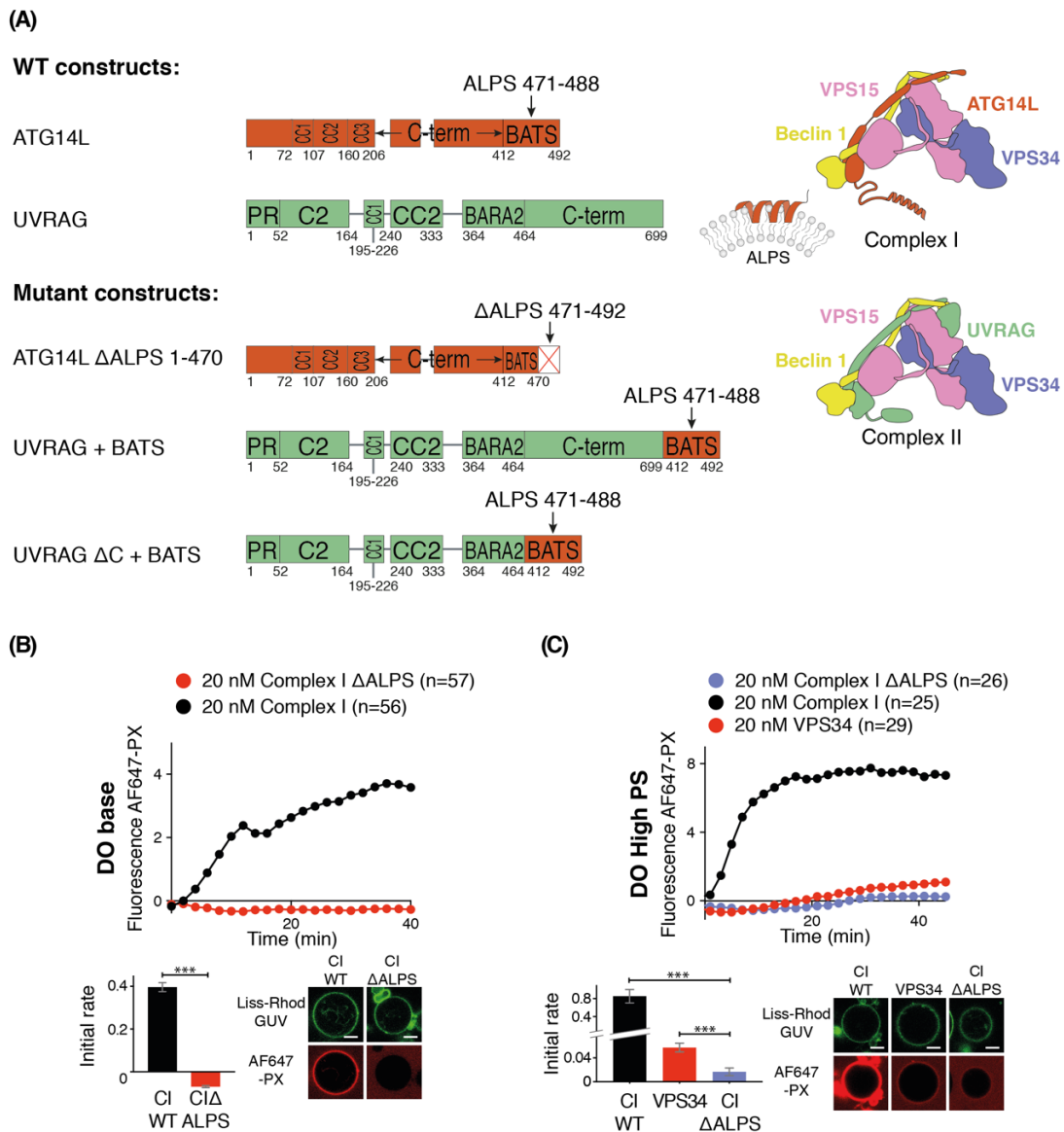


Figure 4–4: The ATG14L BATS domain is crucial for the activity of complex I on DO base membranes

(A) Protein constructs for the PI3K GUV assay. For ATG14L in complex I, the ALPS was deleted (ATG14L ΔALPS 471-492). For UVRAG in complex II, the BATS domain was either fused to the full length UVRAG (UVRAG+BATS) or a C-terminally truncated construct (UVRAGΔC+BATS). **(B)** Deleting the ALPS in complex I (ATG14L ΔALPS 471-492) rendered it inactive on DO base lipids. **(C)** VPS34 alone showed slightly higher activity than complex I ATG14L ΔALPS 471-492 on GUVs with higher PS. Scale bars: 5 μm. Significance level: *** p<0.001; ** p<0.01; * p<0.05; n.s. = not significant. The number of GUVs for analysis is indicated by (n).

In addition, even VPS34 alone exhibited slightly higher activity than complex I ATG14L ΔALPS 471-488 on membranes with a higher PS content (Figure 4–4C). It should be noted that neither VPS34 alone nor complex I ATG14L ΔALPS 471-488 showed detectable activity on DO base GUVs, but only VPS34 alone displayed

measurable activity on GUVs with a higher percentage of PS. The effect of PS will be outlined in more detail in chapter 4.1.4.

So far, no membrane binding motif has been found in UVRAG (Rostislavleva et al., 2015). Thus, I was interested in the effect of the BATS domain on UVRAG. Two constructs were made where the BATS domain (ATG14L 412-492) was either fused to full length or a truncated UVRAG in which the putative unstructured C-terminus was removed (Figure 4–4A). For both chimeras, a dramatic increase in complex II activity could be observed. Complex II UVRAG+BATS was activated ~7-fold and complex II UVRAG Δ C+BATS by ~11-fold over complex II UVRAG WT (Figure 4–5). Curiously, both complex II UVRAG+BATS and UVRAG Δ C+BATS were even more active than complex I WT. This suggests that ATG14L has inhibitory properties that are overcome by the strong affinity of the ALPS for membranes.

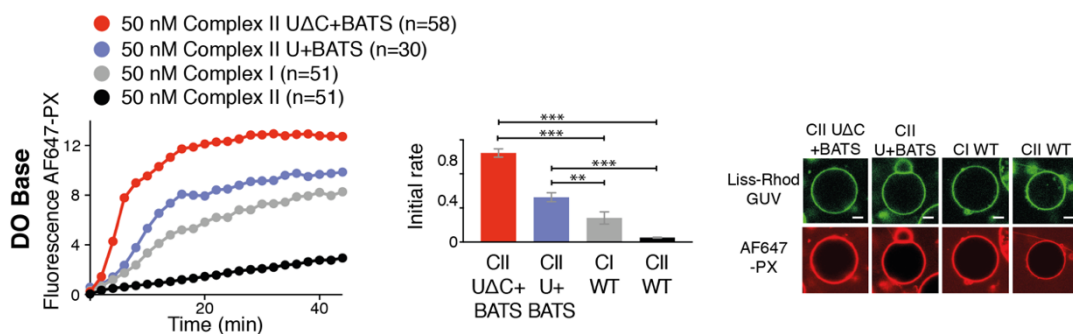


Figure 4–5: BATS domain activates complex II UVRAG fusion constructs

The BATS domain was either fused to full length UVRAG (UVRAG+BATS) or a C-terminally truncated construct (UVRAG Δ C+BATS). Fusing the BATS domain to UVRAG increased complex II's activity. Complex II UVRAG fusion constructs were even more active than complex I WT. Scale bars: 5 μ m. Significance level: *** $p < 0.001$; ** $p < 0.01$; * $p < 0.05$; n.s. = not significant. The number of GUVs for analysis is indicated by (n).

4.1.3 HDX-MS reveals crucial membrane binding motifs in Beclin 1

In order to characterise the membrane interaction of complexes I and II further, we have used hydrogen-deuterium exchange mass-spectrometry (HDX-MS) to map membrane binding regions. Glenn Masson and Yohei Ohashi carried out the experiment and data analysis shortly before I joined the lab. Yohei Ohashi used complex I and I used complex II in PI3K GUV assays to kinetically characterise site-specific mutants that were generated based on results of the HDX-MS analysis of membrane binding. For the HDX-MS experiments, complex I and complex II were either mixed with 100 nm liposomes made of DO base lipids or just buffer. The HDX changes in the peptides of complex I/II alone and complex I/II incubated with liposomes were compared. The peptides with significant changes are coloured according to their rate of exchange for complex I in Figure 4–6 and for complex II in Figure 4–7.

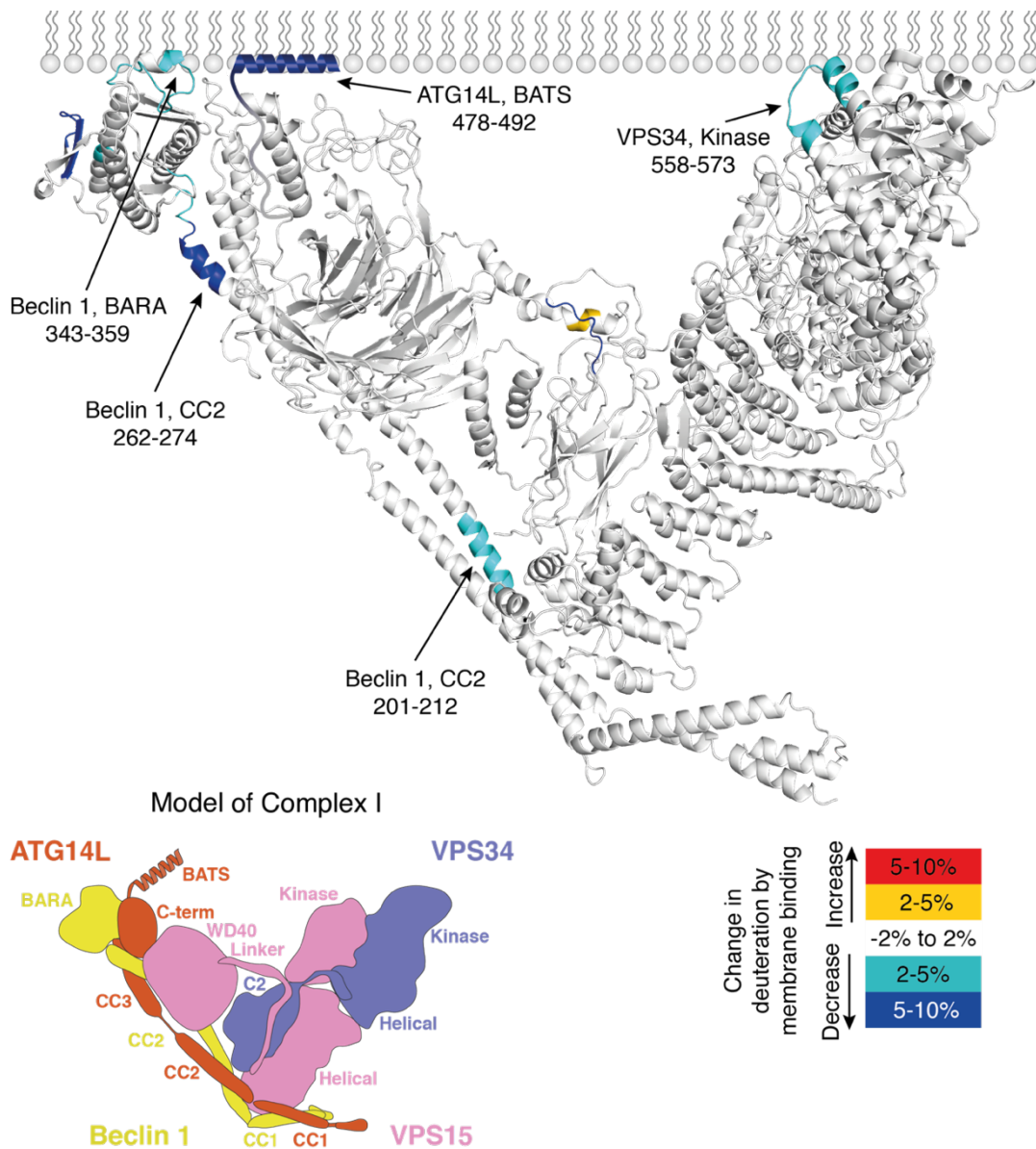


Figure 4-6: Analysis of membrane binding of human complex I using HDX-MS
 Changes in HDX levels in complex I upon membrane binding. Peptides that showed differences in HDX greater than 2% are highlighted on the structural model according to the legend.

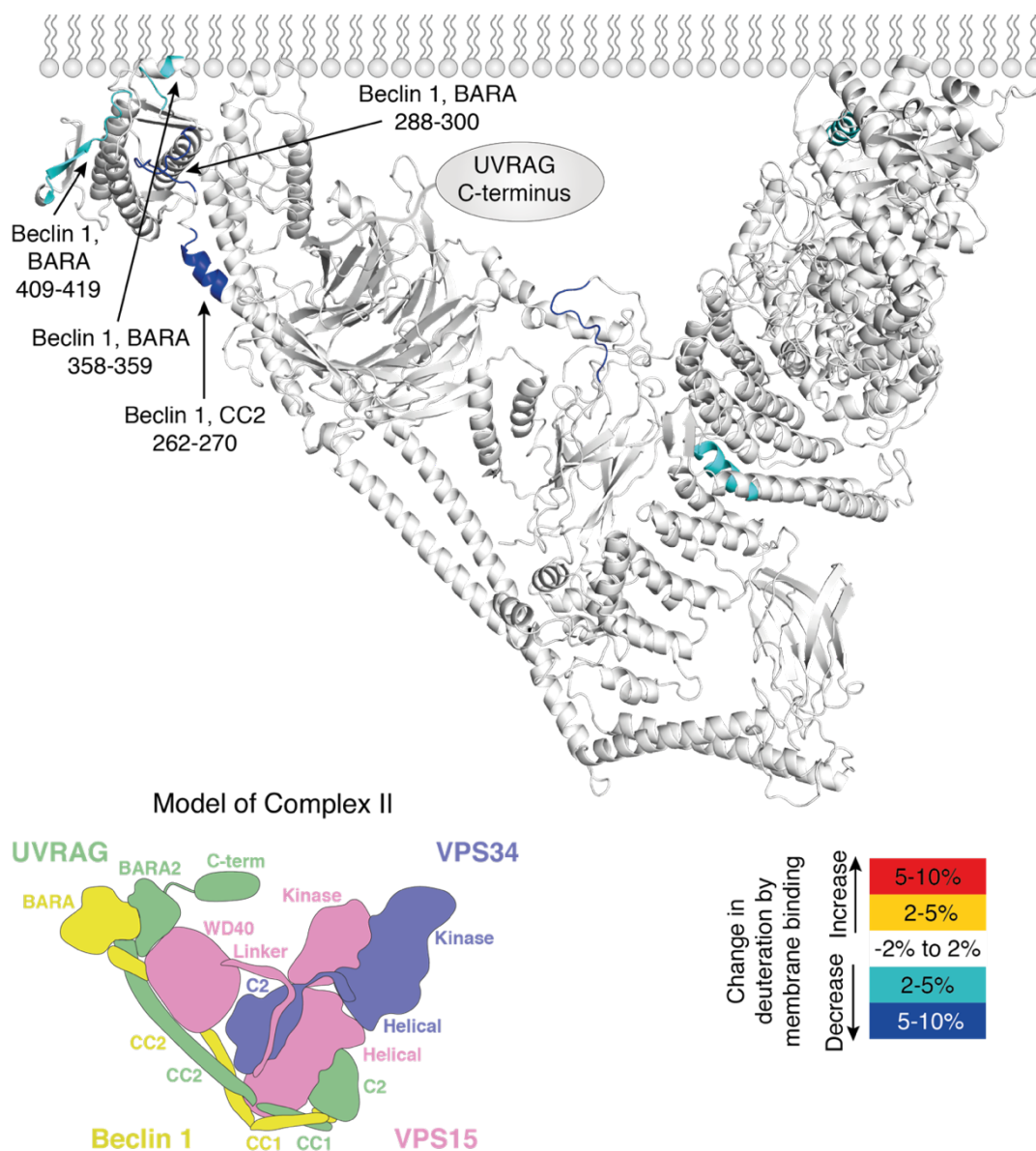


Figure 4-7: Analysis of membrane binding of human complex II using HDX-MS

Changes in HDX levels in complex II upon membrane binding. Peptides that showed differences in HDX greater than 2% are highlighted on the structural model according to the legend

Most changes were found in Beclin 1 for both complexes I and II (Figure 4-6, 4-7 and 4-8). However, complex I had a substantial reduction in HDX in peptides found within the ALPS motif of ATG14L (residues 478-492). Furthermore, two helices in VPS34 $\kappa\alpha 1$ - $\kappa\alpha 2$ (residues 558-578) showed protection. All of these motifs delineated a putative membrane interaction surface similar to the one in yeast complex II (Rostislavleva et al., 2015). Both complexes I and II showed protection

in Beclin 1 in the highly conserved aromatic finger motif (359-361 FFW, AF1) identified by Huang et al. (Huang et al., 2012) (Figure 4–8). They showed that this domain was essential for *in vitro* liposome binding and the initiation of autophagy *in vivo*. Corresponding residues were also found in the yeast Beclin 1 homologue (430-432 FRK) (Rostislavleva et al., 2015).

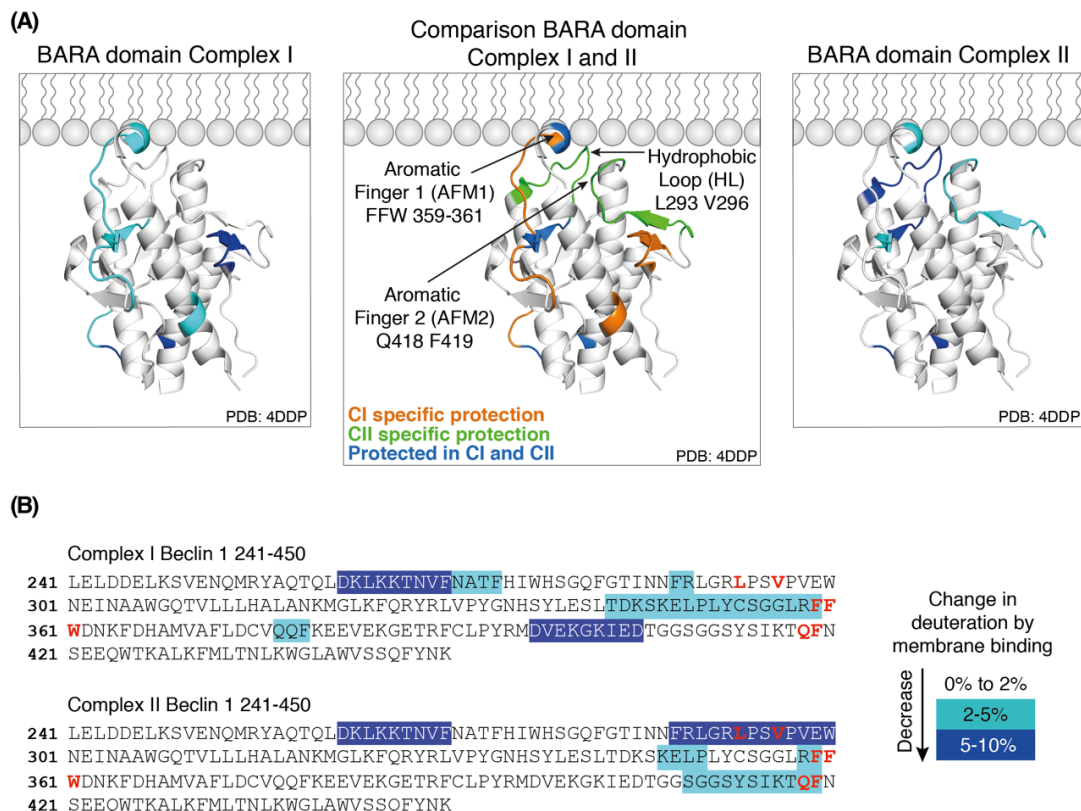


Figure 4–8: Complex dependent membrane binding of the BARA domain

(A) Summary of HDX changes for the Beclin 1 BARA domains of human complexes I (left) and II (right) on crystal structure (PDB: 4DDP, Huang et al., 2012). In the middle, peptides identified by HDX-MS are coloured by whether they were only protected in complex I (orange), complex II (green), or in both complexes I and II (blue). The three motifs, namely AF1 (Aromatic finger motif 1; 359-361 FFW), AF2 (Aromatic finger motif 2; Q418+F419), and HL (Hydrophobic loop; L293+V296) are pointed out. **(B)** Summary of HDX changes for the Beclin 1 BARA domains on amino acid sequence for complexes I and II. Residues for AF1, AF2 and HL are coloured in red.

Surprisingly, two additional regions were picked up in Beclin 1 in complex II at the putative membrane interaction surface (Figure 4–8A middle). The residues 288-300 and 409-419 also showed decreased deuteration. Accordingly, these two new

motifs were named: L293+V296 as the hydrophobic loop (HL) and Q418+F419 as the aromatic finger mutant 2 (AF2) (Figure 4–8). The activities of three mutants of both complexes I and II, AFM1 (F359D/ F360D/W360D), AFM2 (Q418D/F419D) and HLM (L293D/V296D) were analysed for both complexes I and II in the GUV PI3K assay (Figure 4–9). For complex I, only AFM1 showed a decrease in VPS34 activity (Figure 4–9A and B). Neither mutations in the HL nor AF2 had any further influence on activity. Significantly, complex II was affected by all three mutations (Figure 4–9C). Complex II with a mutated AF1 was completely inactive, while the activity of complex II AF2 mutant was reduced 2-fold. Furthermore, adding the mutation of the HL on top of AF2, reduces the activity of complex II again 2-fold over AF2. In conclusion, Beclin 1 has different membrane binding interfaces depending whether it forms a coiled coil with ATG14L in complex I or UVRAG in complex II. Whereas complex II is completely dependent on AF1 and to a lesser extent AF2 and HL, complex I is only minutely affected by mutating AF1 and unaffected by AF2 and HL. This also indicates that the membrane binding of complex I is more dependent on the ATG14L BATS domain.

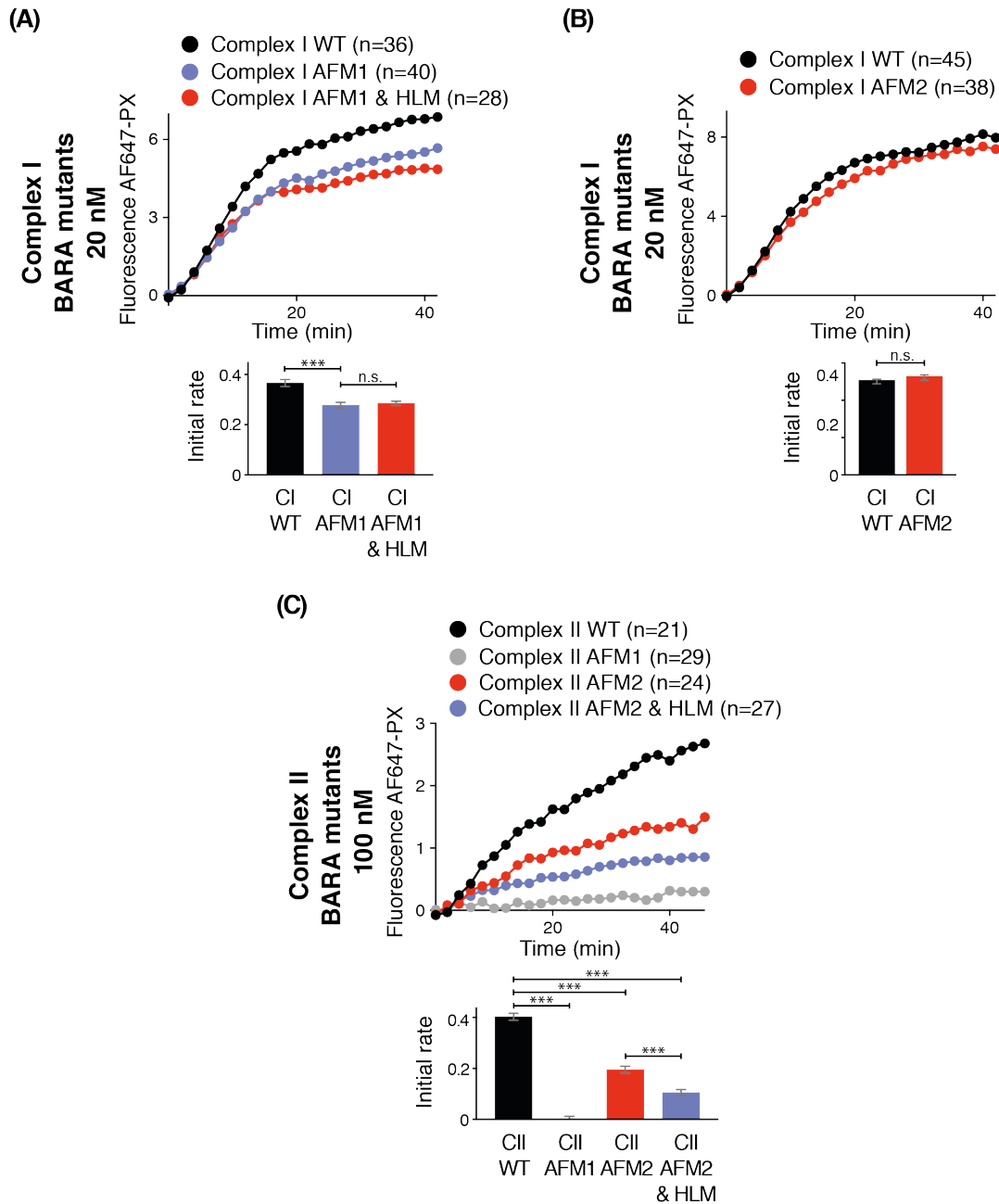


Figure 4-9: Complex II relies more on Beclin 1 BARA domain for membrane binding than complex I
(A) and (B) Influence of AF1, AF2 and HL motifs on complex I activity. Only AF1 reduced complex I activity slightly. **(C)** Influence of AF1, AF2 and HL motifs on complex II activity. Complex II was highly dependent on all three motifs with AF1 being the most important one. Significance level: *** p<0.001; ** p<0.01; * p<0.05; n.s. = not significant. The number of GUVs for analysis is indicated by (n).

4.1.4 Phosphatidylserine activates complex I, complex II, and VPS34

The activity of the VPS34 complexes is affected by their ability to bind to membranes. Consequently, the influence of lipid composition on VPS34 activity was explored. The focus was kept on three key characteristics of membranes: electrostatic charge, lipid packing, and curvature (Bigay and Antonny, 2012). PC, PE, PI, and PS are the most abundant lipids in mammalian cells (Vance, 2015). PC and PE have a neutral net charge whereas PS and PI are anionic phospholipids. As PI is the substrate in our membrane, the levels of PS were altered in order to investigate the relative contribution that membrane electrostatics play in VPS34 activity. In addition to DO base with 10% PS, a lipid composition called DO high PS with 25% PS was used (Figure 4-10A). As mentioned above, VPS34 alone is not active on DO base, however distinct activity can be seen on DO high PS GUVs (Figure 4-10B). Next, the effect of PS on complexes I and II was examined. DO high PS increased the activities of both complexes I and II by 2-fold over DO base (Figure 4-10C and D). Notably, although complexes I and II differ in activity on DO base GUVs when the same amount was used (Figure 4-10E), both had comparable activities when assayed on DO high PS lipids at the same concentration (Figure 4-10F). This suggests that complex II is more highly activated by membranes that include PS than complex I.

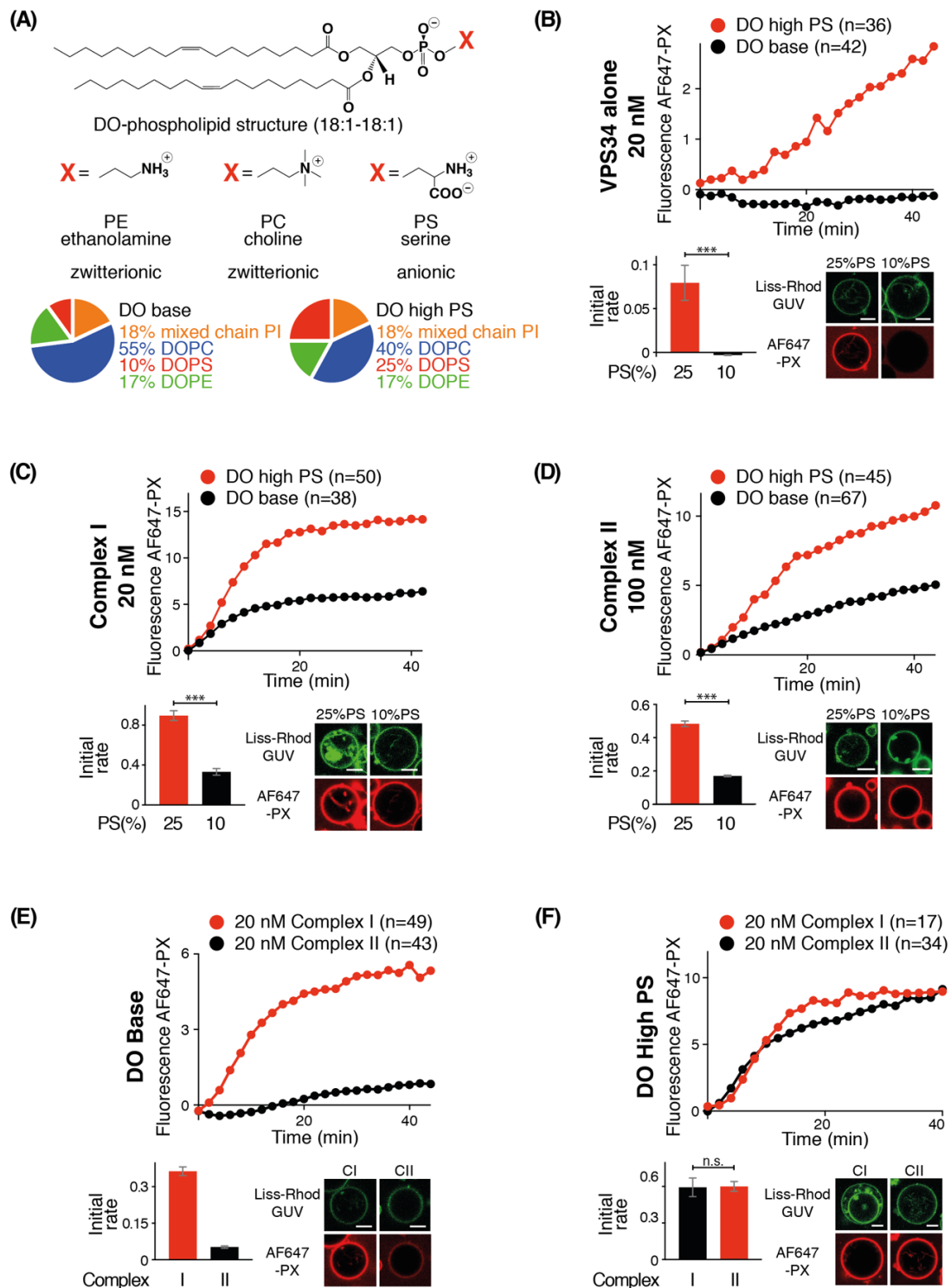


Figure 4-10: Increasing PS levels activate VPS34, complexes I and II

(A) Structure of a DO lipid with possible headgroups of ethanolamine (PE), choline (PC), and serine (PS). Lipid composition of DO base and DO high PS is indicated by pie charts. **(B)** VPS34 alone was activated by DO high PS compared to DO base. **(C) and (D)** Complexes I and II were activated by increasing PS content with DO high PS. **(E)** Complex I was more active than complex II on DO base. **(F)** Complexes I and complex II showed comparable activities on DO high PS, hence, complex II was more activated by PS than complex I. Scale bars: 5 μ m. Significance level: *** $p < 0.001$; ** $p < 0.01$; * $p < 0.05$; n.s. = not significant. The number of GUVs for analysis is indicated by (n).

4.1.5 Phosphoinositides activate complexes I and II

Phosphoinositides are rare but essential membrane lipids that make up only about 10% of total phospholipids, and less than 1% of total lipids in eukaryotic cells (Craene et al., 2017; Payraastre et al., 2001). They are generated by mono-, bis- and trisphosphorylation of the 3rd, 4th, and 5th position of their inositol headgroup, which makes them highly negatively charged (Figure 4–11B). They are concentrated in different pools in organelle membranes and thereby serve as unique docking sites for protein effectors. As it was shown that UVRAG binds to PI(3)P and PI(4)P (He et al., 2013) and ATG14L binds to PI(3)P and PI(4,5)P₂ (Fan et al., 2011; Tan et al., 2016), their influence on the activity of complexes I and II was examined. As PI(3)P is our substrate, only PI(4)P and PI(4,5)P₂ were analysed. Hence, either 5% DO-PI(4)P (18:1-18:1) or 5% DO-PI(4,5)P₂ (18:1-18:1) was added in place of 5% DOPC in our DO base mixture (Figure 4–11A and C). When complex I was assayed on these two lipids compositions, we saw an increase in activation of ~1.8 fold for PI(4)P and ~1.2 fold for PI(4,5)P₂ (Figure 4–11D and E). In contrast, complex II was similarly activated ~1.7 fold by PI(4)P but unaffected by PI(4,5)P₂ compared to DO base (Figure 4–11F and G).

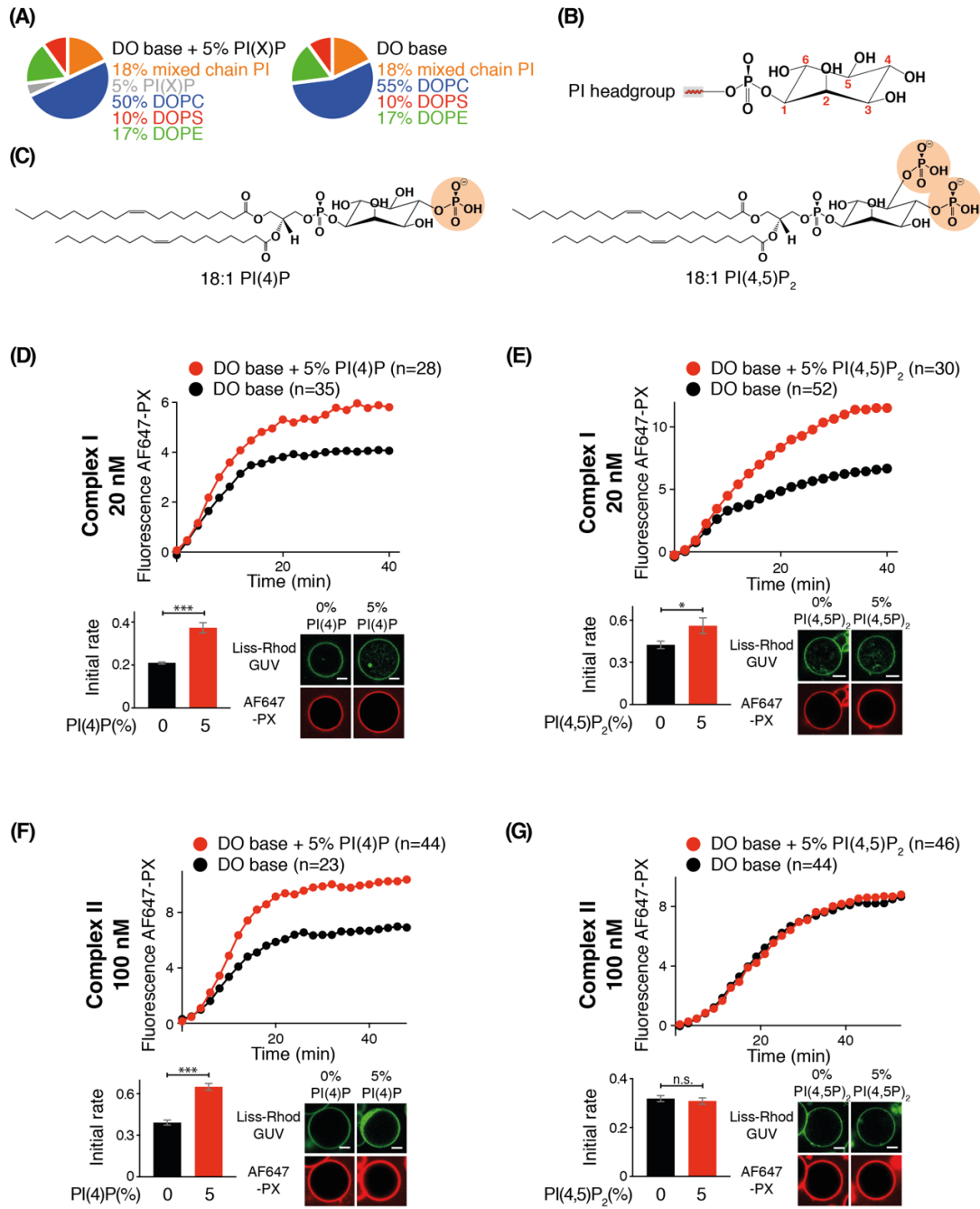


Figure 4-11: Phosphoinositides activate complexes I and II

(A) Pie chart of the lipid compositions for studying the effect of phosphoinositides. 5% of DOPC is either exchanged for PI(4)P or PI(4,5)P₂ in DO base. **(B)** Structure of inositol head group. **(C)** Structures of DO-PI(4)P and DO-PI(4,5)P₂. **(D)** and **(E)** Activity of complex I on DO base + 5% PI(4)P or PI(4,5)P₂. **(F)** and **(G)** Activity of complex II on DO base + 5% PI(4)P or PI(4,5)P₂. Scale bars: 5 μm. Significance level: *** p<0.001; ** p<0.01; * p<0.05; n.s. = not significant. The number of GUVs for analysis is indicated by (n).

4.1.6 Membrane curvature can counteract lipid packing

Finally, the influence of phospholipid unsaturation and degree of curvature on VPS34 activity was explored. GUVs with the same proportion of PC, PE, PS and PI were produced but with a varying level of lipid saturation by either having stearic (18:0) or oleic acid (18:1) as acyl chains (Figure 4–12A and B). Whereas, SO lipids are made with one stearic acid chain (18:0) and one oleic acid chain (18:1), DO lipids carry two oleic acid chains (18:1). Since stearic acyl chains are saturated, they cause denser lipid packing than the mono-unsaturated oleic chains. Overall, three different lipid compositions were investigated: 82% DO lipids, 55% SO with 27% DO lipids, and 82% SO lipids (Figure 4–12B). For all three mixtures the substrate was a mixed chain PI and the relative proportions of headgroup species (55% PC, 17% PE and 10% PS) were kept the same (Figure 4–12B).

When the activities of complexes I and II were analysed on all three lipid compositions, it became clear that both complexes were only active on 82% DO lipids (Figure 4–12C and D). Both complexes I and II were inactive on 55% SO+27% DO and 82% SO lipids (Figure 4–12C and D). However, most GUVs that were chosen for analysis have a diameter of $\sim 10\text{-}20\ \mu\text{m}$. A z-stack analysis of one area of a confocal field also showed smaller GUVs that lay in a lower z-plane (Figure 4–12E and F). Once we focused on these smaller GUVs, it was obvious that 82% DO lipids had strong activity, 55% SO+27% DO showed minor activity and 82% SO lipids were still inactive. In order to quantify the effect, the curvatures ($1/\text{radius}$) versus their fluorescence intensities were plotted (Figure 4–12G and H). Whereas, 55% SO+27% DO GUVs displayed a positive correlation between complexes I and II activity and

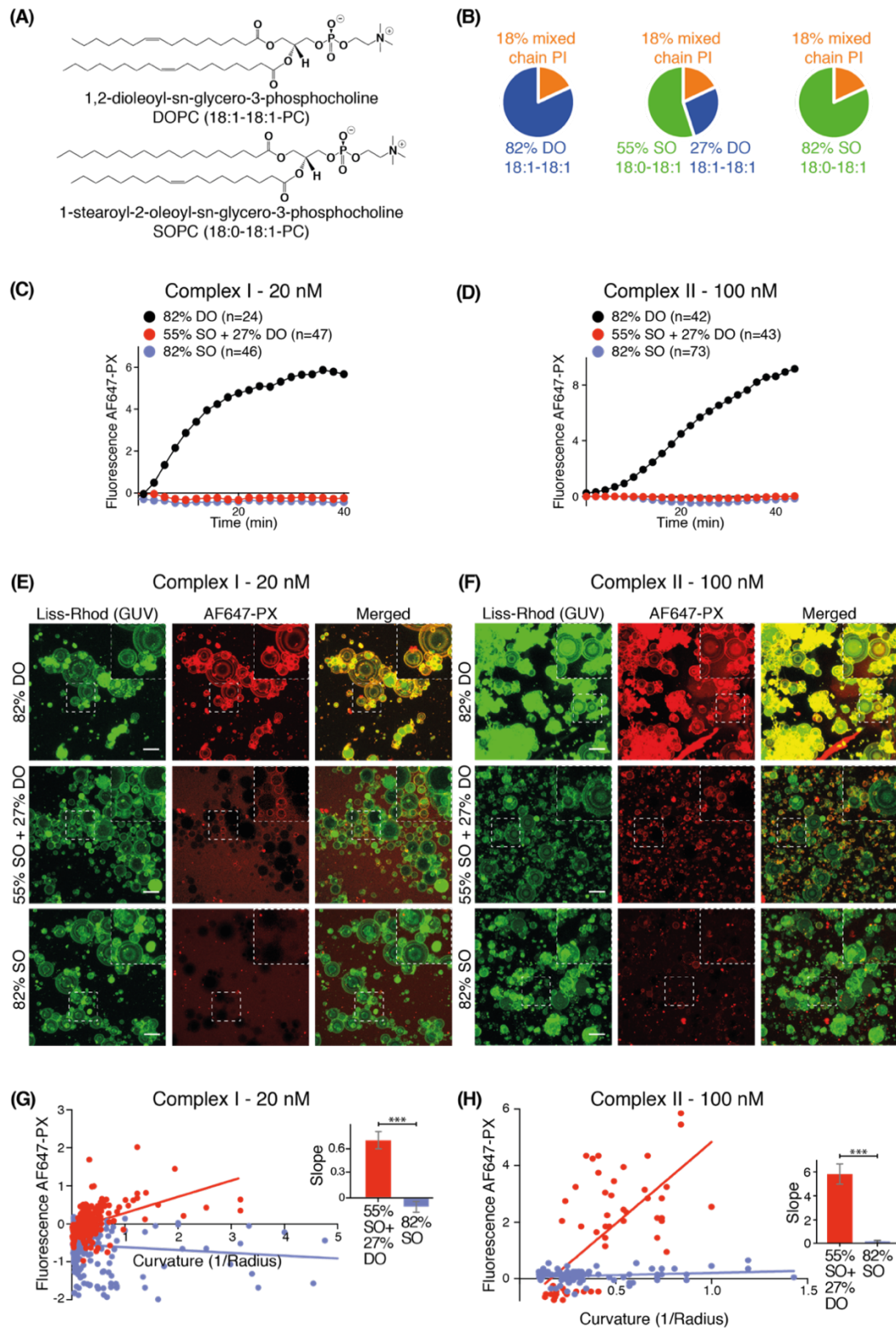


Figure 4-12: Packing defects increase the activity of complexes I and II
(A) Structure of DOPC and SOPC. **(B)** GUV mixtures indicated by pie charts with increasing percentage of SO lipids (82% DO, 55% SO+27% DO and 82% SO). **(C) and (D)** Complexes I and II activity on 82% DO, 55% SO+27% DO and 82% SO. Both complexes are only active on 82% DO. **(E) and (F)** Z-stacks of one area in confocal microscope shows smaller GUVs. **(G) and (H)** Correlation between fluorescence intensity and membrane curvature (1/curvature) for complexes I and II. With increasing curvature, more activity can be detected by AF647-PX. Scale bars: 15 μm . Significance level: **** $p < 0.001$; ** $p < 0.01$; * $p < 0.05$; n.s. = not significant. The number of GUVs for analysis is indicated by (n).

increasing membrane curvature, GUVs made of 82% SO did not exhibit the same correlation. With this in mind, we wanted to be sure that our substrate probe AF647-PX is not influenced by lipid packing. Thus, we tested how PI(3)P would be detected in membranes made of either 82% DO or SO lipids (Figure 4–13A). Satisfyingly, AF647-PX showed the same binding to both 82% DO or 82% SO GUVs (Figure 4–13B).

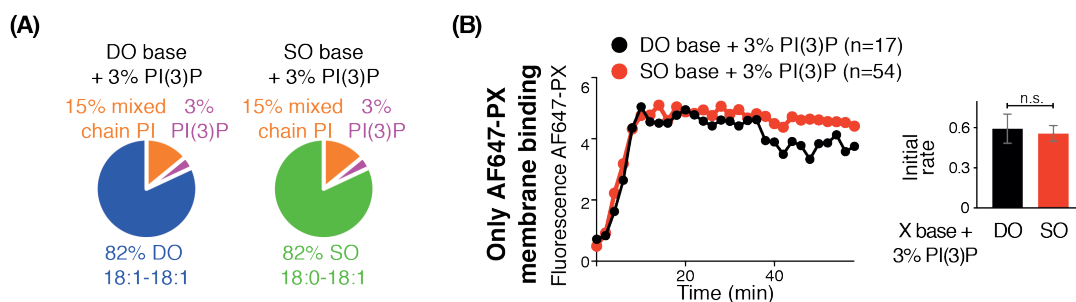


Figure 4–13: AF647-PX binds to PI(3)P regardless of lipid saturation

(A) Lipid mixture with either 82% DO or 82%SO lipids and constant amount 15% PI and 3% PI(3)P. **(B)** Binding of AF647 is unaffected by lipid saturation. Significance level: *** $p < 0.001$; ** $p < 0.01$; * $p < 0.05$; n.s. = not significant. The number of GUVs for analysis is indicated by (n).

4.1.7 The level of saturation in PI affects kinase activity

So far, the effect of lipid saturation in the surrounding lipids was examined. Next, the change in VPS34 activity to changing the acyl chain saturation of the lipid substrate PI was investigated. In addition to mixed chain PI (from bovine liver, 46% 18:0, 17% 20:4, 13% 20:3, 8% 18:1, 6% 18:2, 10% unknown), DOPI (18:1-18:1), SAPI (18:0-20:4), and DSPI (18:0-18:0) were also tested while the surrounding lipids were kept constant at 55% DOPC, 17% DOPE, 10% DOPS (Figure 4–14A).

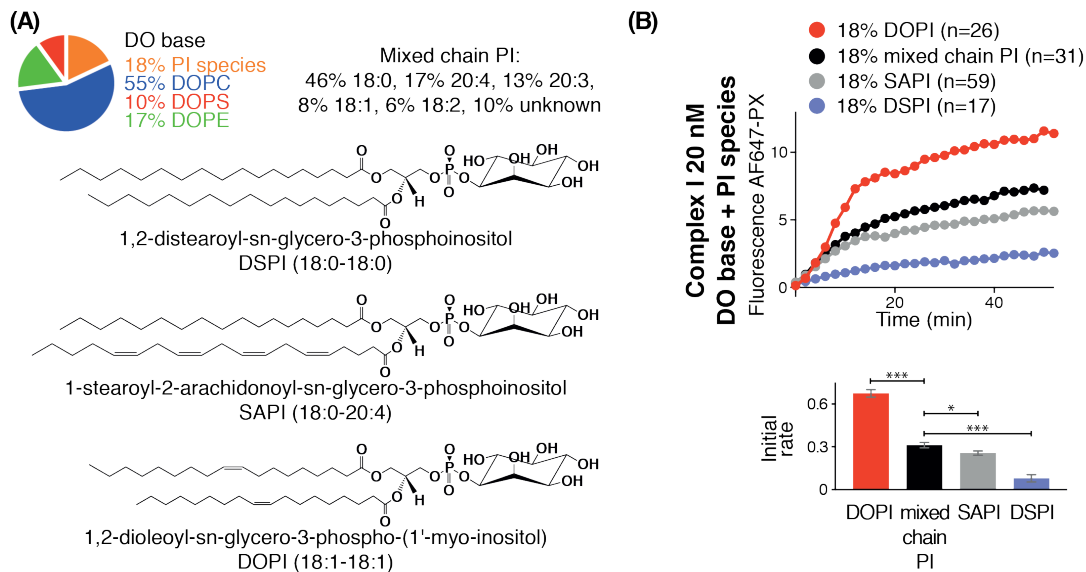


Figure 4–14: Saturation level of the substrate PI influences kinase activity

(A) Structures of DSPI, SAPI and DOPI. Pie chart indicates the percentage of phospholipids. DOPC, DOPS and DOPE was kept constant while the PI species was changed. **(B)** Activity of complex I on DO base with either 18% mixed chain PI, DSPI, SAPI or DOPI. DOPI activated complex I compared to mixed chain PI while SAPI and DSPI reduced activity. Significance level: *** $p < 0.001$; ** $p < 0.01$; * $p < 0.05$; n.s. = not significant. The number of GUVs for analysis is indicated by (n).

To our surprise, complex I was also heavily affected by the saturation level of PI. DOPI showed a ~2-fold increase in activity over mixed chain PI. In contrast, SAPI displayed a ~1.2-fold and DSPI a ~4-fold decrease in complex I activity (Figure 4–14B). In summary, complexes I and II are heavily affected by the acyl chain saturation of either the surrounding lipids or PI itself. Nonetheless, higher membrane curvature can countervail the increase in lipid packing by saturated lipids.

4.2 Discussion

With the help of the novel GUV PI3K assay and HDX, we were able to study the influence of protein domains and membrane composition on the kinase activity of the VPS34 complexes. The first surprising observation that was made is that human complex I was ~7-fold more active than complex II, compared to yeast where it was exactly the opposite (Rostislavleva et al., 2015) (Figure 4-2). This result was corroborated by Brier et al. who saw that human complex II was 50% less active than complex I by an endpoint assay on LUVs (Brier et al., 2019). This increase in activity is caused by complex I's greater ability of binding to membranes made evident by flotation assay (Figure 4-3). The activity of complex I was heavily dependent on the BATS domain and specifically the ALPS motif as deletion of it left complex I completely inactive (Figure 4-4B and C). Brier et al. also assayed complex I without the ALPS motif on LUVs made of 50% PI and 50% PS with unknown lipid saturation. In contrast to our results, they have found that complex I still retains 60% of its activity. However, this highlights the importance of choosing a more physiological lipid composition that reflects the intracellular conditions. Fan et al. have shown that the BATS domain is absolutely essential for targeting complex I to the ER for autophagy induction (Fan et al., 2011). With our results it can be concluded, that this is due to complex I being rendered catalytically inactive without the ALPS motif. The effect of the BATS domain could also be seen in UVRAG BATS fusion mutants as both complex II UVRAG+BATS and UVRAG Δ C+BATS were highly activated (Figure 4-5). Ma et al. has also shown that complex II UVRAG+BATS has increased membrane binding over complex II WT (Ma et al., 2017). Interestingly, both UVRAG+BATS and UVRAG Δ C+BATS exhibited even higher activity than complex I WT (Figure 4-5). If one also takes into account that complex I Δ ALPS

showed even less activity than VPS34 by itself, it suggests that ATG14L might have inhibitory properties (Figure 4–4B). This is similar to class I PI3K and its interaction with the GTPase H-Ras (Buckles et al., 2017). H-Ras has inhibiting properties on class I PI3K activity, however, this minor inhibition is overcome by the increase in membrane recruitment by H-Ras. In the same way, ATG14L might decrease the catalytic efficiency of VPS34, but the recruitment of the ALPS domain to membrane still increases kinase activity dramatically.

With the help of HDX-MS, we were also able to find two additional membrane binding motifs in Beclin 1 (Figure 4–6, Figure 4–7, Figure 4–8). Surprisingly, Beclin 1 seems to have different binding modes in complexes I and II. Whereas complex I uses only the already identified aromatic finger 1 (AF1, FFW 359-361; Huang et al., 2012), complex II possess two further motifs (Figure 4–9A). Beclin 1 also contacted the lipid bilayer with aromatic finger 2 (AF2, QF 418-419) and hydrophobic loop (HL, L293, V296) in complex II. When these residues were mutated to aspartates, complex I activity was only slightly affected by losing AF1, but not by AF2 or HL (Figure 4–9). In contrast, complex II relies heavily on AF1 as mutating it left it catalytically inactive. Moreover, mutating AF2 and HL also decreased kinase activity (Figure 4–9). These results would suggest that the BATS domain, rather than the Beclin 1 BARA domain, is the main membrane binding platform for complex I. Furthermore, ATG14L has an inhibitory effect on VPS34 by rearranging Beclin 1 as complex I Δ ALPS should have a functional AF1, whereas VPS34 does not. Still, VPS34 alone is still more active despite it having no additional membrane binding motif. Complex I is active at the ER to initiate omegasome formation whereas complex II is responsible for PI(3)P production on early endosomes (Axe et al., 2008; Itakura

et al., 2008). These two membranes have very different properties. While the ER contains a high percentage of loosely packed unsaturated lipids with little negative charge to support the folding of nascent transmembrane proteins, lipid composition in early endosomes resembles the one in the plasma membrane, which mainly consists of rigid saturated lipids, cholesterol and negatively charged phospholipids to protect the cell and serve as a barrier to reduce permeability (Vanni et al., 2014). As the influence of lipid composition on VPS34 activity has not been studied, we have focused on three membrane physicochemical parameters: electrostatic charge, lipid packing, and curvature. Firstly, the influence of electrostatic charge was investigated. Electrostatic interactions have been known to increase membrane binding of proteins like BAR domains and α synuclein and also activate protein kinases such as Protein Kinase C (PKC) and Akt (B. X. Huang et al., 2011; Newton and Koshland, 1989; Peter et al., 2004; Pranke et al., 2011). PS and PIPs make up the main acidic phospholipids in the cell. PS has a net charge of -1 but is present in relatively high numbers in some membranes. In contrast, PIPs often make up far less than 1% in the membrane but are highly ionic with a net charge of -2 for PI(3)P up to -4 for PI(3,4,5)P₃ (Lemmon, 2008). Proteins either recognize the stereospecific arrangement of the charged lipid residues or by the general physical charge of the membrane (Lemmon, 2008).

A high percentage of PS (~10-20%) can be found in the plasma membrane (Meer and Kroon, 2011). The plasma membrane has an asymmetric membrane composition maintained by flippases in which PE and PS are highly enriched in the inner leaflet and PC and SM are enriched in the outer leaflet (Casares et al., 2019; Vance, 2015). Recognising the disruption of this asymmetry and displaying PS one

the cell surface, is crucial for apoptosis through phagocytes and blood clotting. As the percentage of PS in GUVs was increased from 10% to 25%, VPS34 alone and complexes I and II showed an increase in kinase activity (Figure 4–10B-D). However, complex II seemed to be more activated by membranes that include PS than complex I (Figure 4–10F). This would make sense as complex II is responsible for the PI(3)P production on early endosomes, which consist of fused endocytic vesicles from the plasma membrane. Moreover, the ALPS motif found in complex I has the specific trait of being insensitive to membrane charge. It solely relies on hydrophobic amino acids on its apolar helix side to bind to membrane. The other side of the helix is scarce in basic residues and therefore insensitive to membrane charge (Drin et al., 2007; Drin and Antonny, 2009).

Next, the effect of the phosphoinositides PI(4)P and PI(4,5)P₂ were examined. Of all the PIPs, PI(4)P and PI(4,5)P₂ are the most abundant in the cells (Lemmon, 2008). A majority of PI(4)P is found in the Golgi and known to regulate the directionality of the secretory pathway. Recently, it has also been found to be important for receptor sorting on early endosomes (Henmi et al., 2016; Ketel et al., 2016) and at the autophagosome initiation site (Judith et al., 2019). PI(4,5)P₂ is a key lipid messenger at the plasma membrane where it is involved in regulating endocytosis, exocytosis and actin cytoskeleton dynamics (Tan et al., 2015). Additionally, small pools of PI(4,5)P₂ have been found at early autophagic vesicles (Moreau et al., 2012; Tan et al., 2016). The GUV PI3K assay confirmed that both complexes I and II can be activated by PI(4)P, but only complex I showed a preference for PI(4,5)P₂ (Figure 4–11). Tan et al. have already shown that ATG14L binds to PI(4,5)P₂ with the two arginines R423 and R442 in the BATS domain upstream of the ALPS motif (ALPS

471-488) (Tan et al., 2016; Fan et al., 2011). Consequently, the recruitment to the ER for omegasome formation could be strengthened by a cooperation of these two motifs. In contrast, complex II could be recruited to early endosomes by PI(4)P. Indeed, it has been already suggested that UVRAG binds to PI(4)P with its C2 domain that is situated at the opposite site of the membrane interaction surface (He et al., 2013).

The membrane landscape in the cell is very diverse and each organelle has a different lipid saturation and curvature spectrum. The plasma membrane needs saturated acyl chains to tightly pack and stabilise its lipid bilayer to withstand outside pressures and forces. In contrast, the ER and Golgi are part of the dynamic secretory and membrane network, which constantly form tubules and vesicle for signal transduction and cargo transport. That is why these membranes are rich in unsaturated acyl chains that produce more packing defects (Vanni et al., 2014). We have used various percentages of DO (18:1-18:1) and SO (18:0-18:1) lipids and measured the activity of complexes I and II (Figure 4-12). Surprisingly, already substituting one unsaturated acyl chain for a saturated one (55% SO+27% DO and 82% SO) left both complexes I and II dead on GUVs of about 5-15 μm (Figure 4-12C-F). Additionally, increasing the amount of saturation even only in substrate PI also decreases complex I activity (Figure 4-14B). It is well established that increasing the amount of double bonds causes 'kinks' in the acyl chains, which causes a looser lipid packing (Manni et al., 2018; Pinot et al., 2014). This in turn leads to the formation of shallow and deep gaps in the lipid bilayer, into which hydrophobic amino acids can insert (Vanni et al., 2019). A less appreciated relationship is the influence of curvature on lipid packing. Vanni et al. could show that the loss of

binding of the Arf ALPS to more saturated lipids could be rescued by increasing the membrane curvature (Vanni et al., 2014). The same effect could be seen in our GUV assay. GUVs of a smaller size in a lower z-plane showed some activity in 55% SO+27% DO. It could be correlated with increasing curvature the kinase activity increased (Figure 4–12G and H). Thus, curvature can counteract tight membrane packing.

Various types of curvature can be found in different organelles. Endocytosed vesicles have been measured to be ~30-150 nm in diameter depending on the endocytosis pathway (Klumperman and Raposo, 2014; Mayor and Pagano, 2007). Early endosomes have been measured to be slightly larger of about ~100-500 nm as they consist of fused vesicles (Klumperman and Raposo, 2014). However, early endosomes also form an elaborate network of tubular subdomains responsible for cargo sorting (Bonifacino and Rojas, 2006). These can have high curvature at the tip of the tubules. In autophagy, omegasomes and phagophores have also been shown to have high curvature at the forming tip. These tips have been measured to be smaller than 30 nm in diameter (Nguyen et al., 2017). In conclusion, both the endocytic and autophagic networks contain membranes with high curvature, which could attract both complexes I and II to bind.

Figure 4–15 summarises the factors that activate complexes I and II. Although some factors do suggest why complex I is recruited the ER for autophagosome initiation and why complex II is active on early endosomes, it is still not fully disentangled. Rab GTPases have been suggested as an additional piece of the puzzle. Their significance will be discussed in the next chapter.

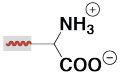
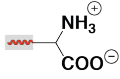
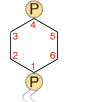
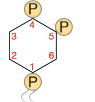
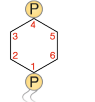
Factors that increase kinase activity	Complex I	Complex II
Beclin 1	/ Aromatic finger 1 FFW 359-361 /	Hydrophobic loop L293 V296 Aromatic finger 1 FFW 359-361 Aromatic finger 2 Q418 F419
ATG14L	ALPS amphipathic helix 471-488 	/
Curvature		
Lipid unsaturation		
Electrostatic effects	 Phosphatidylserine anionic	 Phosphatidylserine anionic
Phosphoinositides	 PI(4)P  PI(4,5)P ₂	 PI(4)P

Figure 4-15: Factors that increase activity of complexes I and II

Both complexes I and II share some membrane binding motifs such as the Beclin 1 aromatic finger 1 and the preference for curved and unsaturated membranes. However, both also have their unique pattern. While complex I heavily relies on ATG14L BATS domain, complex II depends on the two additional Beclin 1 motifs, aromatic finger 2 and hydrophobic loop.

5 Activation of VPS34 complexes by Rab GTPases

Christoforidis et al. have shown with *in vitro* translated proteins that VPS15, but not VPS34, binds to GST-Rab5a in a GTP dependent manner (Christoforidis et al., 1999). However, as it wasn't known then that VPS34 and VPS15 form complexes I and II with UVRAG or ATG14L, respectively, their involvement was not tested. Subsequent papers have reported an interaction between VPS34 or VPS15 with Rab5a (Behrends et al., 2010; Gillingham et al., 2014; Murray et al., 2002; Ravikumar et al., 2008; Stein et al., 2003). However, purified proteins of the VPS34 complexes I or II have not been used to actually study this interaction in detail. Furthermore, Christoforidis et al. have claimed to not be able to detect a stimulation of enzymatic activity for VPS34 but the corresponding data were not shown. I used an *in vitro* approach to investigate this interaction using immobilised Rab5a on GUVs and our PI3 kinase assay.

5.1 Results

5.1.1 Immobilisation of Rab GTPases on membranes

In the cell, Rab5a is prenylated and inserted into the membrane with the help of the Rab escort protein (REP). In order to mimic this Rab5a immobilisation *in vitro*, a lipid that has a maleimide moiety at its headgroup was chosen (18:1 PE-MCC/DOPE-MCC), which has been already used to study the activation of class I PI3K by Ras

GTPase (Buckles et al., 2017; Siempelkamp et al., 2017) (Figure 5–1A). Therefore, DO base was made with 10% DOPE-MCC instead of 10% DOPE (DO base + 10% PE-MCC = 18% mixed chain PI, 55% DOPC, 10% DOPS, 7% DOPE and 10% DOPE-MCC).

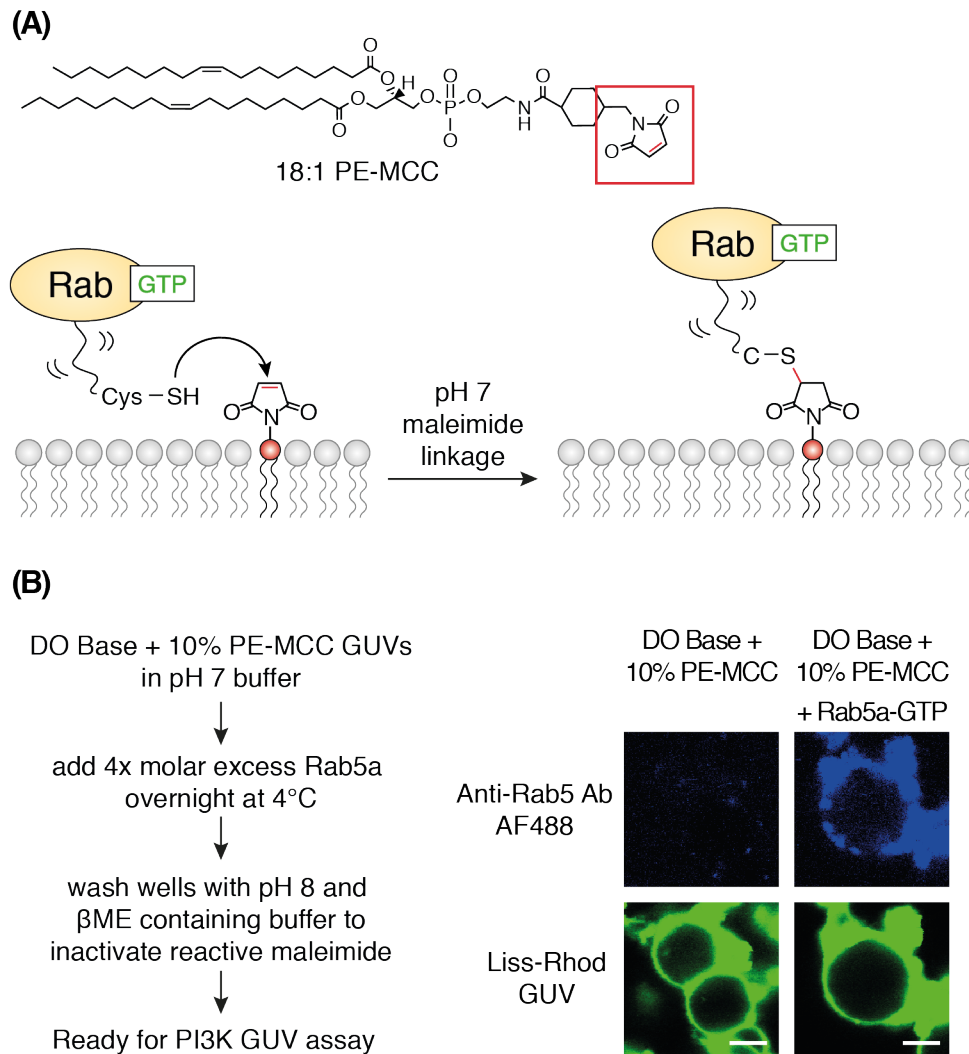


Figure 5–1: Immobilisation of Rab GTPases on membranes

(A) Strategy to *in vitro* capture Rab GTPases on vesicles. Vesicles contain maleimide lipid DOPE-MCC. When Rab is added, the C-terminal cysteine reacts with the maleimide at pH 7 to form a covalent linkage. **(B)** Labelling GUVs with Rab5a by maleimide chemistry. GUVs with 10% PE-MCC were incubated with Rab5a overnight and washed. Wells were then incubated with rabbit anti-Rab5a antibody and anti-rabbit antibody conjugated to Alexa Fluor 488 (AF488) for visualisation. Scale bars: 5 μm

The GUVs were then incubated at pH 7 with Rab5a overnight at 4°C. As GUVs were immobilised by the incorporated biotinylated lipid and avidin on the surfaces of the

wells in the GUV chamber, the wells could be carefully washed to decrease the concentration of unreacted Rab5a. The wells were washed with buffer at pH 8 containing β -mercaptoethanol to inactivate the remaining free maleimide groups. As can be seen in Figure 5–1B, the GUVs contained Rab5a on its surface after treatment.

5.1.2 Rab5a is a strong activator of complex II

For all experiments with Rab GTPases in this thesis, the QL mutants were used. The mutation of the catalytic glutamate to a leucine has been shown to strongly decrease the intrinsic GTPase activity of RabGTPases (Stenmark et al., 1994).

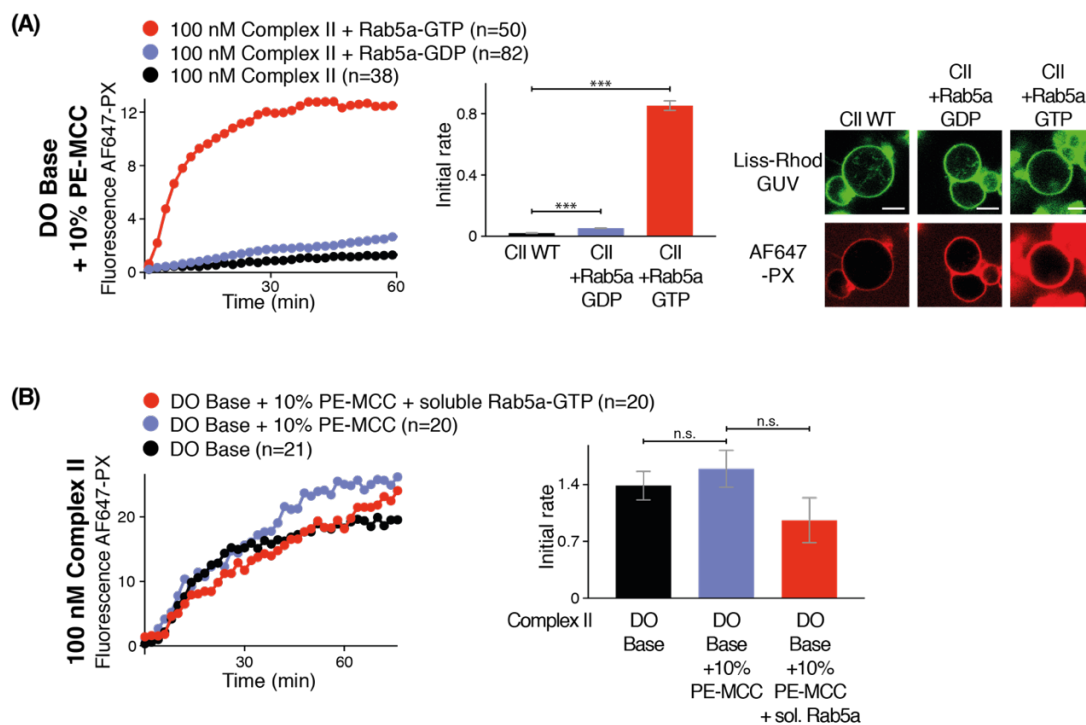


Figure 5–2: Membrane bound Rab5a activates complex II in a GTP dependent manner
(A) GUVs were either incubated with Rab5a-GTP, Rab5a-GDP or no Rab5a. The AF647 signal showed that complex II was strongly activated by Rab5a-GTP and mildly by Rab5a-GDP. **(B)** Complex II had the same activity on DO Base +10% PE-MCC and on DO Base. The addition of soluble Rab5a also did not activate complex II. Scale bars: 5 μ m. Significance level: *** $p < 0.001$; ** $p < 0.01$; * $p < 0.05$; n.s. = not significant. The number of GUVs for analysis is indicated by (n).

Results

In vivo, the QL mutant is often referred to as being constitutively active or “GTP-locked” as the concentration of GTP is 10-times higher than GDP in the cytosol (GDP 36 μM vs GTP 305 μM , Traut, 1994). Therefore, QL mutants are suspected to have GTP bound in cells. *In vitro* however, the QL mutant can be either loaded with GDP or GTP (Lee et al., 2009). DO Base + 10% PE-MCC GUVs were either incubated with Rab5a-GDP, Rab5a-GTP or no Rab5a. When the activity of complex II was measured, it became clear that membrane-coupled Rab5a-GTP increased kinase activity dramatically (Figure 5-2A). By comparing the initial rates, one could see that complex II was activated ~ 35 -fold by Rab5a-GTP and ~ 3 -fold by Rab5a-GDP. When complex II was assayed on DO Base, DO Base + 10% PE-MCC or DO Base + 10% PE-MCC + soluble Rab5a-GTP, *i.e.* Rab5a that did not contain the C-terminal cysteines for membrane anchoring, no difference in activity could be seen (Figure 5-2B). Consequently, only membrane bound Rab5a could activate complex II.

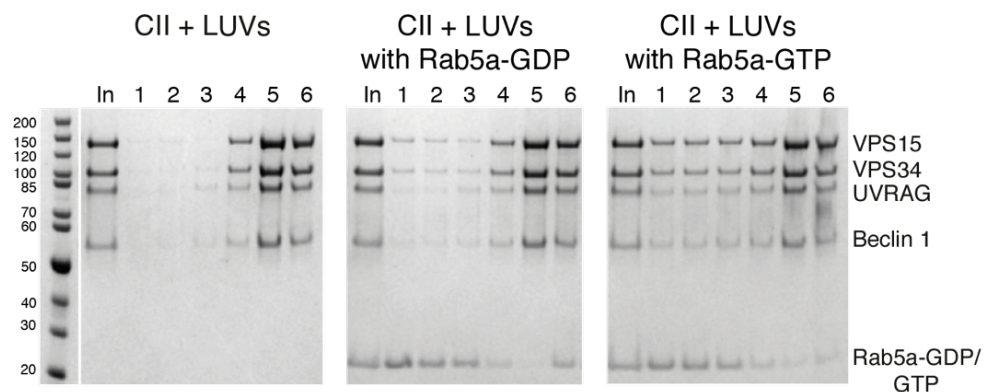


Figure 5-3: Rab5a recruits complex II to membranes

Flotation assay of complex II on LUVs with either no protein, Rab5a-GDP or Rab5a-GTP. Complex II showed increased recruitment to Rab5a coated membranes. Especially Rab5a-GTP showed the highest amount of complex II in the floating fractions 1-3.

In order to investigate the mechanism of activation, LUVs were either linked to Rab5a-GDP, Rab5a-GTP or no protein and were used for a flotation assay with complex II (Figure 5-3). By comparing the amount of protein in fractions 1-3, which

contain the floating LUVs, one can see that Rab5a-GDP increased complex II recruitment mildly, while Rab5a-GTP increases the amount of complex II on LUVs substantially more. Hence, Rab5a recruits complex II to membranes in a GTP-dependent manner.

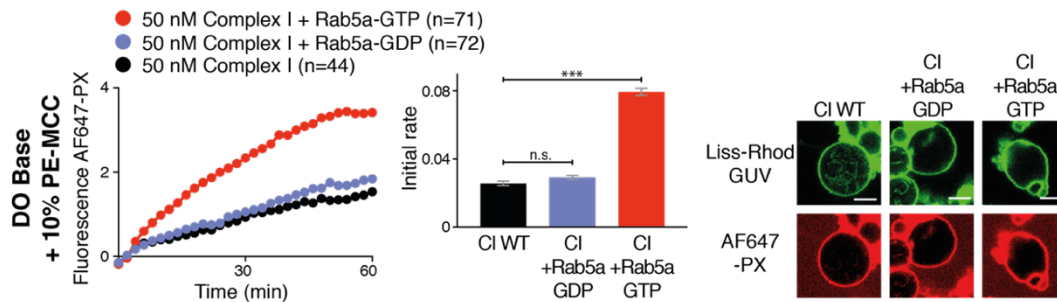


Figure 5-4: Complex I is less activated by Rab5a-GTP than complex II

GUVs were either incubated with Rab5a-GTP, Rab5a-GDP or no Ra5. Complex I showed some activation by Rab5a-GTP, but not to the same extent as complex II. Scale bars: 5 μ m. Significance level: *** $p < 0.001$; ** $p < 0.01$; * $p < 0.05$; n.s. = not significant. The number of GUVs for analysis is indicated by (n).

As either VPS34 or VPS15 have been suggested as the Rab5a interaction partner, we were also interested in the effect of Rab5a on complex I. To our surprise, complex I was only activated ~ 3 -fold by Rab5a-GTP and not activated by Rab5a-GDP (Figure 5-4). In summary, Rab5a is a very potent activator of complex II whereas it only mildly activates complex I.

5.1.3 Rab7a does not activate either complexes I or II

It has previously been suggested that Rab7a binds to VPS15 in pull down experiments (Stein et al., 2003). Therefore, the activities of complexes I and II were analysed with Rab7a-GDP and Rab7a-GTP. Using the PI3K GUV assay, no activation of either complexes I or II with Rab7a-GDP or Rab7a-GTP was observed (Figure 5-5A and B).

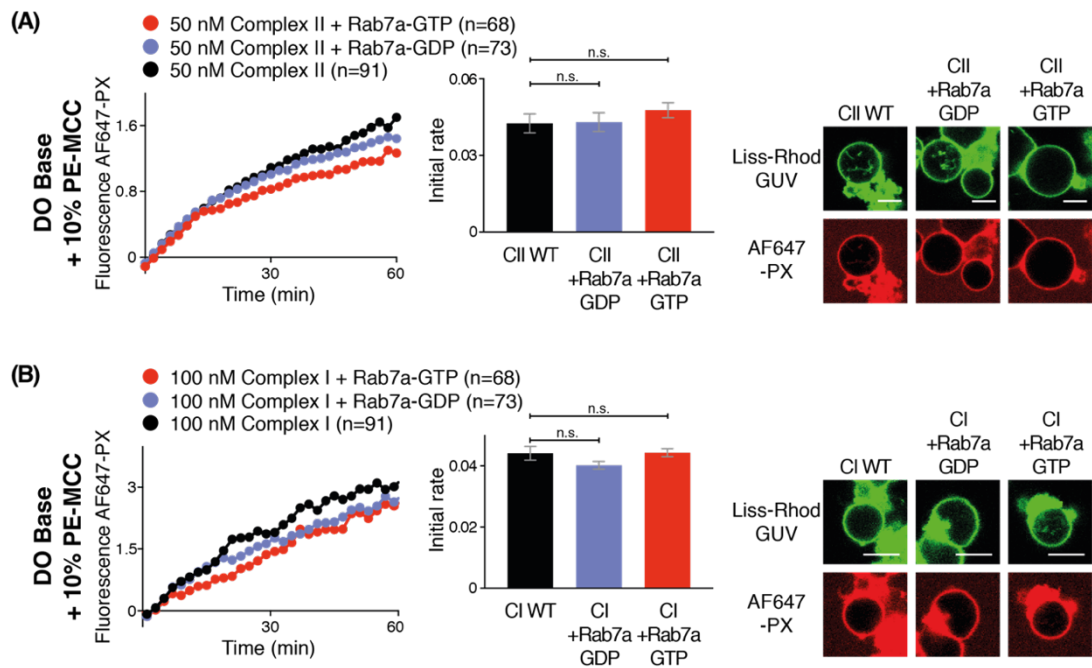


Figure 5-5: Rab7a does not activate complex I or II

A) and **(B)** GUVs were either incubated with Rab7a-GTP, Rab7a-GDP or no Rab7a. No activation of either complexes I or II could be detected. Scale bars: 5 μ m. Significance level: *** $p < 0.001$; ** $p < 0.01$; * $p < 0.05$; n.s. = not significant. The number of GUVs for analysis is indicated by (n).

UVRAG has been suggested to interact with Rab7a through the class-C-Vps complex independently of VPS34 (Liang et al., 2008). In order to confirm whether complex II still might interact with Rab7a, a flotation assay with complex II and Rab7a-GDP/GTP coated LUVs was done. However, no recruitment could be seen (Figure 5-6).

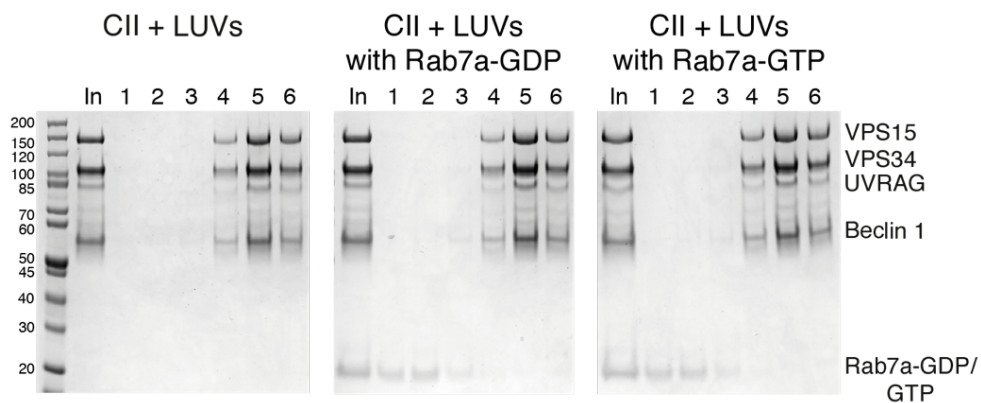


Figure 5-6: Rab7a does not recruit complex II to membranes

Flotation assay of complex II on LUVs with either no protein, Rab7a-GDP or Rab7a-GDP. No increase in complex II was visible in the floating fractions 1-3.

5.1.4 Rab7a is a strong activator of complex II Rubicon

Complex II is able to bind another protein subunit called Rubicon (Matsunaga et al., 2009; Zhong et al., 2009). Rubicon has been suggested to decrease VPS34 activity and bind Rab7a (Chang et al., 2019; Itakura et al., 2008; Sun et al., 2010; Zhong et al., 2009). I investigated these observations using the PI3K GUV assay. Using this method, I observed that, Rubicon did not decrease kinase activity of complex II (Figure 5-7A). However, complex II Rubicon was activated by Rab7a-GDP ~5-fold and by Rab7a-GTP ~50-fold (Figure 5-7B). In order to see whether this activation is caused by recruitment, a flotation assay with Rab7a-GTP or Rab7a-GDP and complex II Rubicon was carried out. Complex II Rubicon was recruited to Rab7a coated LUVs in a GTP dependent manner as seen by fraction 1-3 (Figure 5-8).

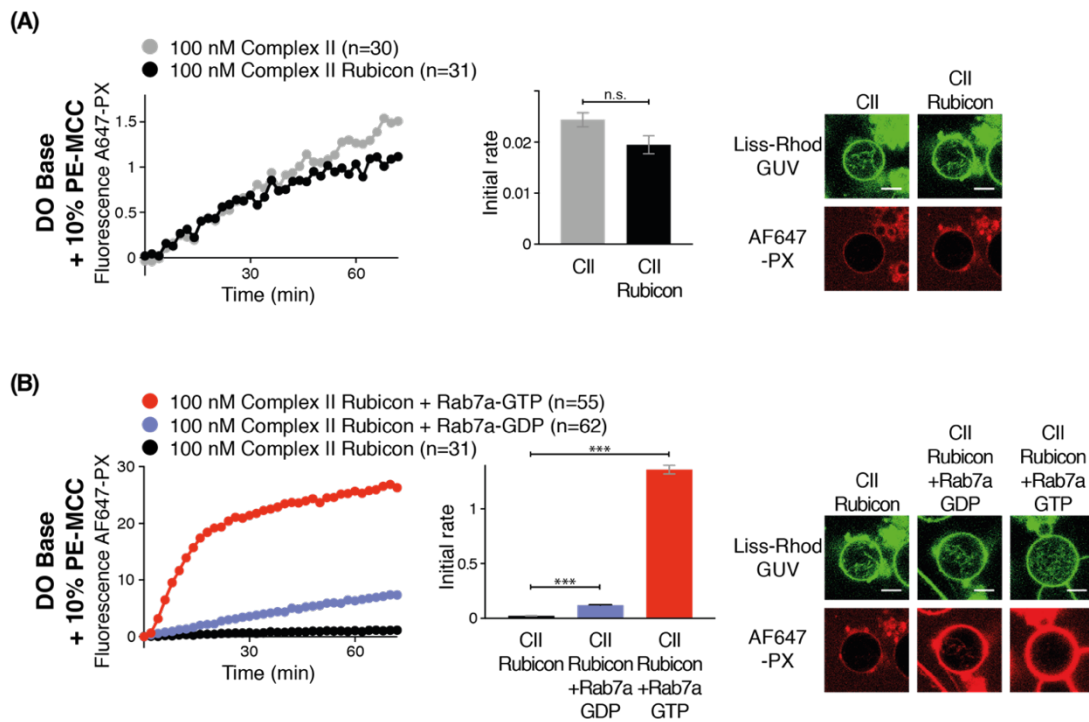


Figure 5-7: Membrane bound Rab7a is an activator for complex II Rubicon

A) Comparison of activities of complex II and complex II with Rubicon. No significant difference in kinase activity could be detected. **(B)** GUVs were either incubated with Rab7a-GTP, Rab7a-GDP or no protein at all. Complex II with Rubicon was significantly activated by Rab7a in a GTP dependent manner. Scale bars: 5 μ m. Significance level: *** $p < 0.001$; ** $p < 0.01$; * $p < 0.05$; n.s. = not significant. The number of GUVs for analysis is indicated by (n).

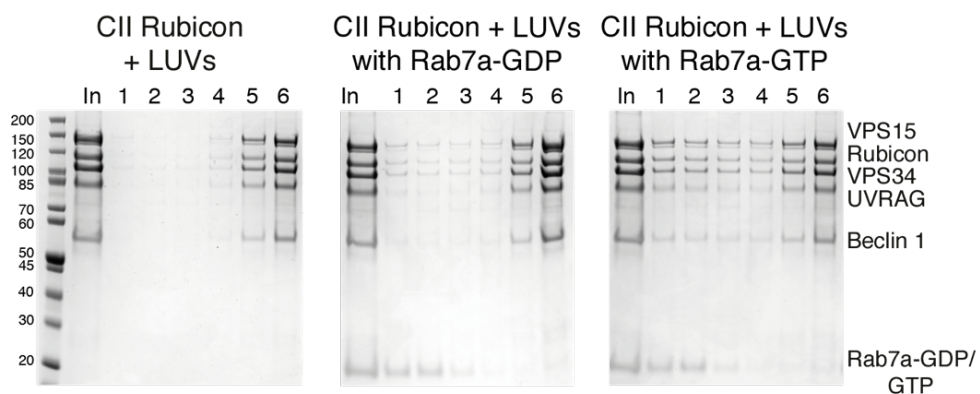


Figure 5-8: Rab7a recruits complex II Rubicon to the membrane

Flotation assay of complex II Rubicon on LUVs with either no protein, Rab7a-GDP or Rab7a-GDP. Complex II Rubicon was recruited to Rab7a coated membranes in a GTP dependent manner.

5.1.5 Rab1a is a complex I specific activator

During the course of our investigations, it was noted by our collaborator Jessica Bertram and Sean Munro that Rab1a may also interact with complex I. This evidence was acquired from a method called MitoID (Gillingham et al., 2019). For MitoID, Rab GTPases are fused to a promiscuous biotin ligase BirA that biotinylates available lysine residues within a ~10 nm radius. In order to decrease background signal and focus on specific GTPase effectors, a mitochondria relocation signal was added at the Rab C-terminus (Hoogenraad et al., 2003). The relocation sequence is a fragment of the mitochondrial outer membrane protein monoamine oxidase (MAO). The final transfected construct consists of Rab-BirA-HA-tag-MAO. Following transient transfection, the biotinylated proteins can be pulled down with streptavidin beads and either immunoblotted for known effectors or analysed by mass spectrometry for unknown interactors. Figure 5-9 shows immunoblots of streptavidin precipitates of Rab1a (WT/ QL/ SN) and Rab5a (QL) Mito ID constructs. Rab1a interacted only with complex I subunits VPS34, VPS15, Beclin 1, and ATG14L but not with the complex II specific UVRAG. However, Rab5a showed interaction with all subunits.

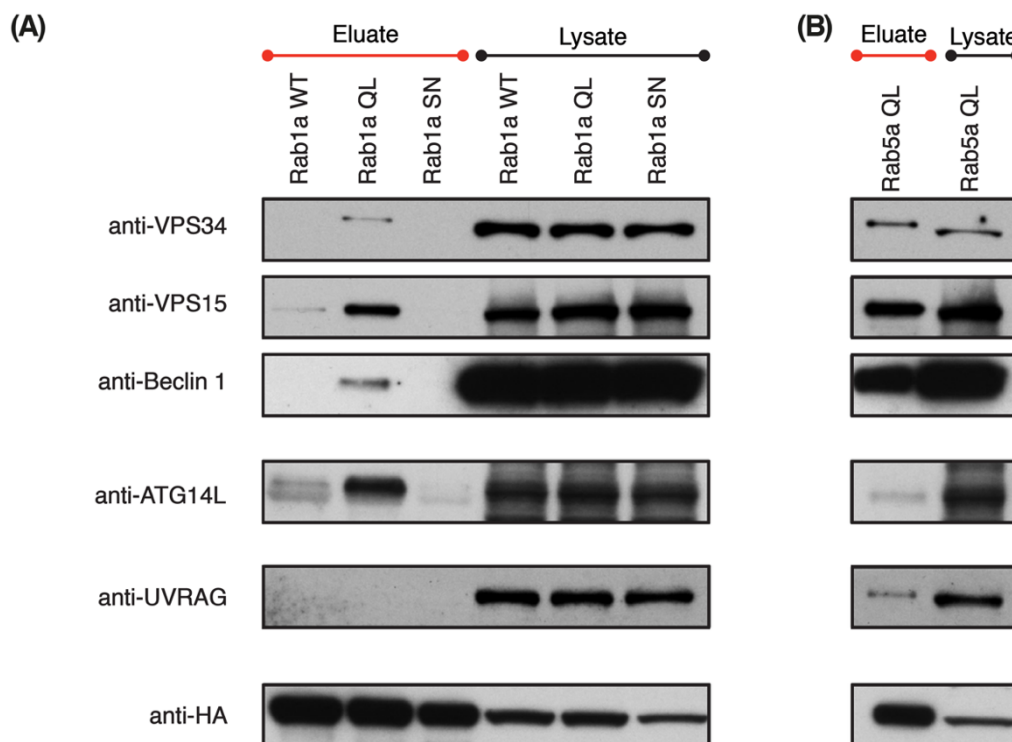


Figure 5-9: Mitochondrial results show Rab1a interacts only with complex I subunits

Immunoblot of streptavidin precipitates from cells in which Mitochondrial Interaction (MitoID) had been carried out for Rab1a WT/ QL/ SN (A) or Rab5 QL (B). **(A)** Rab1a interacts specifically with components of complex I (VPS34, VPS15, Beclin 1, ATG14L) but not with the complex II specific UVRAG. **(B)** Rab5 shows interaction with both complexes I and II subunits. Results by Jessica Bertram.

Thus, the nature of this interaction was analysed in our PI3K GUIN assay. GUINs were either incubated with Rab1a-GDP, Rab1a-GTP or no Rab1a. Figure 5-10A shows that complex I was activated 2-fold by Rab1a-GDP and 12-fold by Rab1a-GTP. However, when complex I was assayed on DO Base +10% PE-MCC and DO Base, it became clear that complex I showed a lower activity when 10% PE-MCC was incorporated (Figure 5-10B). It is not clear why this was the case as complex II does not exhibit the same behaviour. ATG14L has two CXXC motifs of unknown function at its N-terminus (CXXC 44-47, CXXC 56-58), which are normally found in redox proteins (Fomenko and Gladyshev, 2003). Although the reducing agent β -mercaptoethanol was added to quench unreacted maleimide groups, not all unreacted molecules might get inactivated. Since the CXXC motifs are located at the

CC1 of ATG14L away from the membrane binding site, any residual active maleimide might react to these cysteines and thereby render complex I inactive. The addition of soluble Rab1a to DO Base +10% PE-MCC did not show an increase in complex I activity (Figure 5–10B).

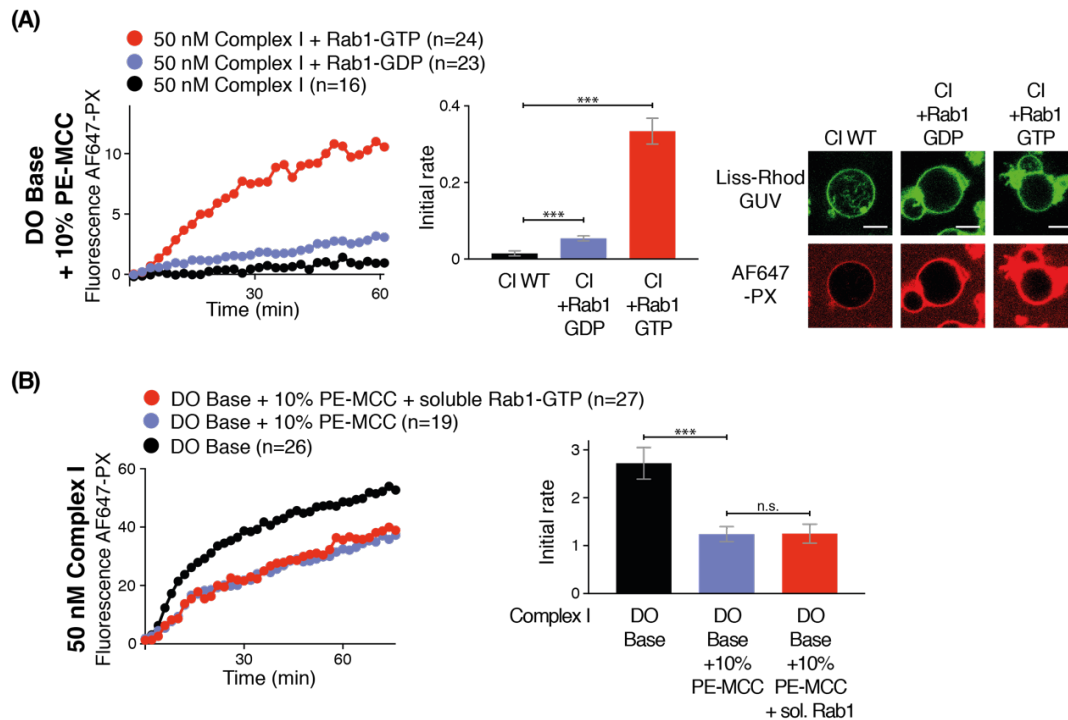


Figure 5–10: Membrane bound Rab1a activates complex I

(A) GUUVs were either incubated with Rab1a-GTP, Rab5a-GDP or no Rab1a. Complex I was strongly activated by Rab1a-GTP and mildly by Rab1a-GDP. **(B)** Complex I showed a decreased activity on DO Base +10% PE-MCC compared to DO Base. However, the addition of soluble Rab1a did not cause any activation of complex I on DO Base +10% PE-MCC. Scale bars: 5 μ m. Significance level: *** $p < 0.001$; ** $p < 0.01$; * $p < 0.05$; n.s. = not significant. The number of GUUVs for analysis is indicated by (n).

To determine whether Rab1a recruits complex I to membranes, LUVs were either linked to Rab1a-GDP, Rab1a-GTP or no Rab1a and were used in a flotation assay with complex I (Figure 5–11). From fractions 1-3, which contain floating LUVs, one can see that Rab1a was recruited to membranes in a GTP-dependent manner.

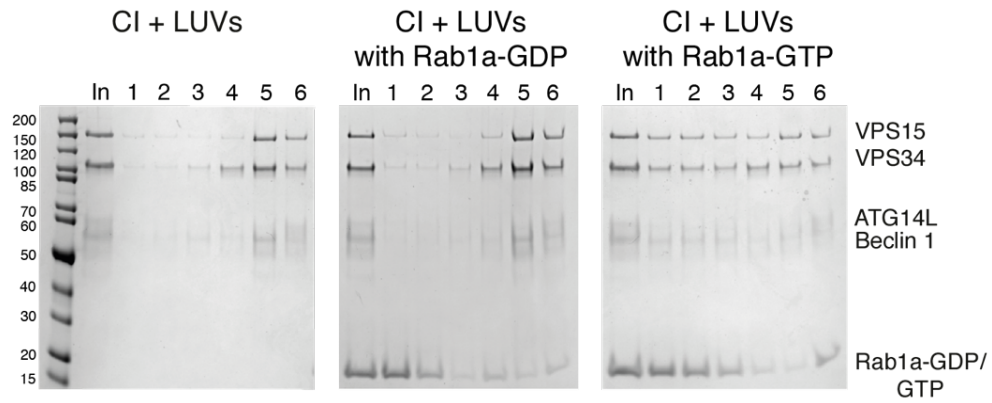


Figure 5-11: Rab1a recruits complex I to membranes

Flotation assay of complex II on LUVs with either no Rab1a, Rab1a-GDP or Rab1a-GDP. Complex I was recruited to Rab1a coated membranes in a GTP dependent manner.

Furthermore, it was investigated whether the PI3K GU assay results would reflect the MitoID results. When the same assay was done with Rab1a-GDP/-GTP and complex II, no activation could be seen. Accordingly, Rab1a is a complex I specific activator.

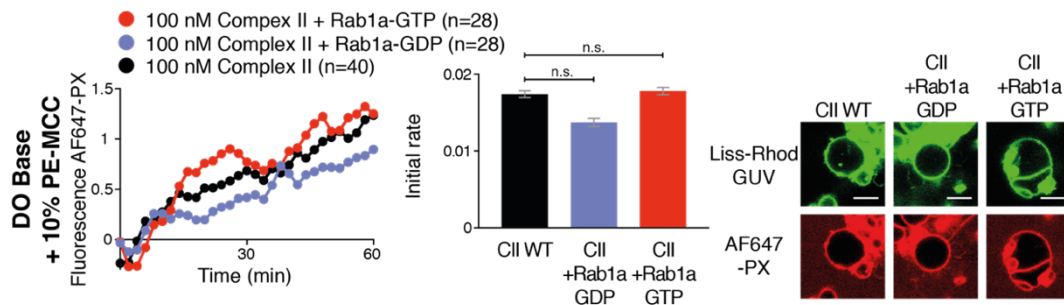


Figure 5-12: Rab1a does not activate complex II

(A) and (B) GUVs were either incubated with Rab1a-GTP, Rab1a-GDP or no Rab1a. No activation of complex II could be detected. Scale bars: 5 μ m. Significance level: *** $p < 0.001$; ** $p < 0.01$; * $p < 0.05$; n.s. = not significant. The number of GUVs for analysis is indicated by (n).

5.2 Discussion

With the help of purified proteins and the GUV PI3K and floatation assay, Rab5a, Rab7a and Rab1a were shown to be activators and membrane recruiter of specific VPS34 complexes. As long suspected, assay results were able to verify that complex II is recruited and activated by the GTPase Rab5a, which is often found on early endosomes (Figure 5-2A and Figure 5-3). It thereby fulfils the Rab effector requirement in that it prefers to interact with the active GTP form compared to the inactive GDP form. Surprisingly, autophagic complex I is also activated by Rab5a but only by ~3-fold compared to ~35-fold for complex II (Figure 5-4). This is exciting, as this is the first time that WT complex II possesses a higher kinase activity than complex I despite its higher basal activity. This is an important puzzle piece why the two VPS34 complexes are active in two different cellular pathways. The produced PI(3)P by complex II on Rab5 positive membranes then attracts further endocytosis proteins with specific PI(3)P binding domains such as FYVE or PX to coordinate events such as vesicle fusion, intraluminal vesicle formation and, tubulation. Proteins like the early endosome autoantigen 1 (EEA1), ESCRT components or endosomal sorting nexins (SNXs) are prominent examples in the endocytic system to directly bind to PI(3)P (Kutateladze, 2010).

Despite claims from previous studies that VPS15 binds to the late endosomal GTPase Rab7a, no activation or interaction was visible *in vitro* with complex I or II (Stein et al., 2003) (Figure 5-5 and Figure 5-6). However, the produced PI(3)P on early endosomes by complex II could contribute to the Rab5-Rab7 conversion as the Rab7-GEF Mon1/Ccz1 binds to it and in turn its GEF activity is stimulated (Cabrera et al., 2014). Although complex I or II alone do not interact with Rab7a, the GUV PI3K

and flotation assay showed that complex II together with Rubicon was a strong Rab7a effector (Figure 5-7 and Figure 5-8). Despite the fact that Rubicon has already been shown to interact with Rab7 with its C-terminus, it was not clear whether Rab7 would increase PI3K activity (Sun et al., 2010; Tabata et al., 2010). Assay results could show that Rab7a-GTP activates complex II Rubicon by ~50-fold and also recruits it to membranes (Figure 5-7 and Figure 5-8). Rubicon has long been suspected to be involved in autophagosome maturation but also recently in a specific type of phagocytosis called LC3-associated phagocytosis (LAP) (Wong et al., 2017). Here, autophagic proteins are involved in the maturation and degradation of the phagosomal content (Martinez et al., 2015). Numerous studies have identified Rubicon as a negative regulator for autophagy, specifically autophagosome maturation (Kim et al., 2015; Matsunaga et al., 2009; Nakamura et al., 2019; Zhong et al., 2009). Three groups have showed that Rubicon leads to a decrease in VPS34 activity (Chang et al., 2019; Kim et al., 2015; Zhong et al., 2009). Kim et al. and Zhong et al. have used immunoprecipitated proteins and TLC analysis to analyse PI(3)P production. However, Chang et al. have used purified proteins and GUV and LUV assays to probe VPS34 activity. It was found that Rubicon decreases the activity on LUVs 2-fold and completely inhibits PI(3)P production and membrane binding on GUVs (Chang et al., 2019). This stands in contrast to our results, as we could not see a significant decrease in VPS34 activity on GUVs (Figure 5-7A). In comparison, Chang et al. have used GUVs made of 50% mixed chain PI and 50% PS with a relatively rigid acyl chain composition of 18:1, 16:0, 18:0, and 20:4 acyl chains while we have found it to be essential to use a more physiological mixture of DO lipids on GUVs in order to see complex I or II activity (Figure 4-12). Chang et al. have also claimed to have found a new membrane binding motif in complex II in the amino

acids Phe270 and Phe274 in Beclin 1. In the crystal structure, these residues are at the end of CC2 of Beclin 1 and near the β -sheets $\beta 1/\beta 2$ (Huang et al., 2012). These beta sheets are supposed to unfold in WT complex II and insert into the lipid bilayer upon membrane contact. The inhibition of complex II by Rubicon is supposedly caused by re-stabilising the β -sheets and inhibiting Phe270 and Phe274 to contact the membrane thereby decreasing membrane recruitment. In our HDX, we can see protection for Phe270 in complexes I and II and for Phe274 in complex I (Figure 4–8). However, we did not see any changes in the $\beta 1/\beta 2$ (276–289) upon LUV incubation in complex I or II that would suggest unfolding. It is hard to reconcile how the two *in vitro* studies can result in these two different results.

An important finding is that the GTPase Rab1a works as a specific activator for complex I. Rab1a-GTP activated complex I by ~ 12 -fold and recruited it to membranes (Figure 5–10 and Figure 5–11). In contrast, complex II shows no activation by Rab1a. In general, studies of Rab1 have proven to be difficult as a double knockout of Rab1a and Rab1b is lethal (Blomen et al., 2015; Homma et al., 2019). Nevertheless, Rab1 is known to regulate protein trafficking in the secretory pathway by mediating anterograde transport from the ER to the Golgi apparatus (Plutner et al., 1991). However, the role of Rab1 in autophagy has also been recently appreciated (Huang et al., 2011; Kakuta et al., 2017; Mochizuki et al., 2012; Wang et al., 2013; Webster et al., 2016; Winslow et al., 2010; Zoppino et al., 2010). It was found to be involved in the initiation of autophagy as partial deletions lead to a mislocalisation of ATG9 vesicles and a reduction of phagophores (Kakuta et al., 2017; Winslow et al., 2010). Additionally, two studies have showed that Rab1a is responsible for recruiting ULK1 for autophagy initiation (Wang et al., 2013; Webster

et al., 2016). It is generally agreed that ULK1 recruitment to specific initiation sites is one of the earliest steps in the autophagy cascade (Hara et al., 2008; Karanasios et al., 2016; Koyama-Honda et al., 2013; Walker and Ktistakis, 2019). Wang et al. focussed on the yeast homologue of ULK1 called Atg1 and showed that it is recruited by the yeast Rab1 homologue Ypt1 to the pre-autophagosomal structure to initiate autophagosome formation (Wang et al., 2013). Although, there are significant differences in the autophagy initiation between yeast and humans, they were still able to show that immunoprecipitated ULK1 pulled down Rab1a but not another ER GTPase Sar1 or the endosomal GTPases Rab5 or Rab9. Webster et al. focused on a new protein called C9orf72, which is involved in amyotrophic lateral sclerosis (ALS) and frontotemporal dementia (FTD) (Webster et al., 2016). They showed that C9orf72 is a Rab1a effector and that Rab1a and C9orf72 are needed for ULK1 to form the characteristic puncta in the cell for omegasome formation. One could speculate that Rab1a not only recruits ULK1 but also complex I for autophagy initiation. Rab1 would therefore bring ULK1 and complex I in proximity so that ULK1 can phosphorylate VPS34, ATG14L and Beclin 1 for further activation (Egan et al., 2015; Park et al., 2018, 2016; Russell et al., 2013; Wold et al., 2016). Interestingly, Rab1a has been shown to recruit other kinases in order to modulate their activity in time and space. Rab1a was shown to recruit the protein kinase CK1 δ (casein kinase 1 δ), which is involved in the phosphorylation of COP-II and thereby regulating the formation of ER-derived vesicles to the Golgi (Wang et al., 2015). Wang et al. showed that Rab1a was responsible for recruiting CK1 δ to membranes in a GTP dependent manner.

6 Studying VPS34 complex II on Rab5a coated membranes by MS and cryo-ET

6.1 Results

6.1.1 Mapping Rab5a binding to complex II by HDX-MS

As Rab5a seemed to activate both complexes I and II, I was curious about its binding site. I decided to take two approaches in mass spectrometry: HDX-MS and unnatural amino acid crosslinking. HDX-MS has been routinely used in the lab to identify protein-protein or protein-membrane interaction surfaces (Burke et al., 2012; Masson et al., 2015; Ohashi et al., 2016; Rostislavleva et al., 2015). In order to find the binding site of Rab5a on complex II, Rab5 has to be in excess of complex II in order to fully occupy its binding site. Otherwise, a mixed population of deuterated peptides would dilute and mask the actual signal. Since we have seen good membrane recruitment of complex II in our flotation assays, our initial goal was to use LUVs with maleimide bound Rab5a-GTP as the Rab5 source. However, several problems arose. Firstly, the digested peptides are injected into a reverse phase chromatography column. If a too high concentration of lipids is injected, the column might get clogged and cause adverse effect on the chromatographic separation of the peptides. Secondly, the labelling of Rab5 on LUVs also caused some difficulties. Membrane-anchored human Rab GTPases can act as a tethering factor and directly mediate membrane tethering events. Rab5a especially was shown to induce the formation of clusters of aggregated liposomes (Tamura and Mima, 2014). I found this behaviour to be concentration dependent, the more Rab5a that was covalently

Results

linked to the membrane via the maleimide reaction, the more aggregation appeared. Aggregates were undesirable due to the nature of the fluidics system employed upstream of the mass spectrometer. Additionally, in order to have fully occupied complex II, a high excess of Rab5a was needed, however, that in turn caused further aggregation. In conclusion, a balance between enough Rab5 but a low amount of lipids and aggregated LUVs was required. Two data sets were collected where LUV-coupled Rab5a-GTP was added to complex II in a molar ratio of 2:1. Unfortunately, no valuable information could be derived from them.

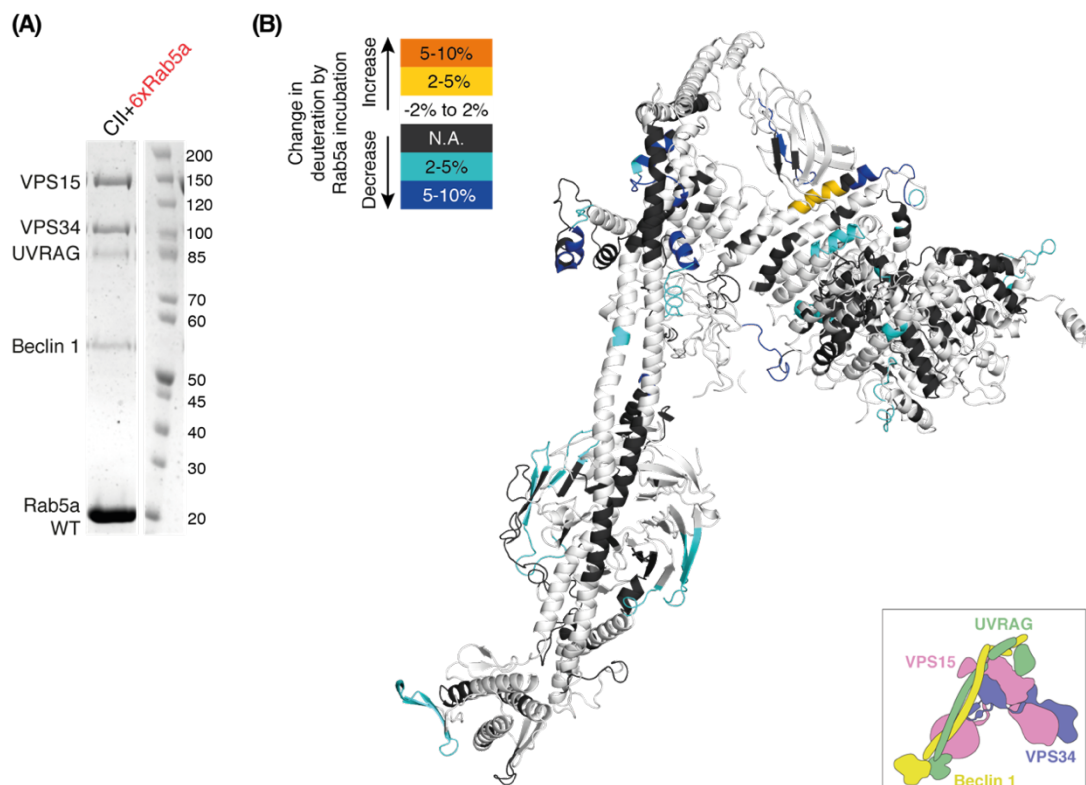


Figure 6-1: Mapping the binding of Rab5a to complex II by HDX-MS

(A) 5 μ M Complex II was mixed with 30 μ M Rab5a-GTP for HDX measurements. **(B)** A model of complex II coloured according to changes in deuterium incorporation upon Rab5a-GTP incubation. Regions showing an increase in HDX are depicted in yellow and orange and regions with a decreased rate of HDX are coloured in cyan and blue. Black regions indicate that no peptide was available for analysis.

Thus, I turned to using soluble Rab5 to be able to increase the concentration. In the end, soluble Rab5a-GTP was mixed with complex II in a molar ratio of 6:1 (30 μ M: 5 μ M) (Figure 6-1A). Sarah Maslen guided me through the sample injection and Yohei Ohashi assisted in the peptide identification analysis. Using this strategy, we were successful in identifying localised changes in deuteration primarily in VPS34 and VPS15 upon Rab5a incubation (Figure 6-1B).

6.1.2 Mapping Rab5a binding to complex II by UAA crosslinking

As a second approach, I tried to map the Rab5 interaction site using unnatural amino acid crosslinking by genetic code expansion. A collaboration with Kathrin Lang was started, who had successfully used this strategy for crosslinking Rab1b-GDP to its GEF DrrA (Cigler et al., 2017). The unnatural amino acid and plasmids were provided by Kathrin Lang. Rab5 was expressed with an orthogonal pyrrolysyl-tRNA synthetase/tRNA pair and the unnatural amino acid (UAA) BrCO6K (Figure 6-2A). BrCO6K is a lysine derivative bearing a structurally flexible bromoalkyl chain that is able to crosslink to several amino acids such as cysteines, histidines, lysines but also glutamates (Nguyen et al., 2018). Because of the flexible bromoalkyl chains, the UAAs can span distances of up to 15 Å. Several positions were screened in the switch 1 and 2 regions of Rab5a. A mutant in which the codon for S84 in switch 2 was replaced by the stop codon TAG showed the best ability to crosslink (Figure 6-2B).

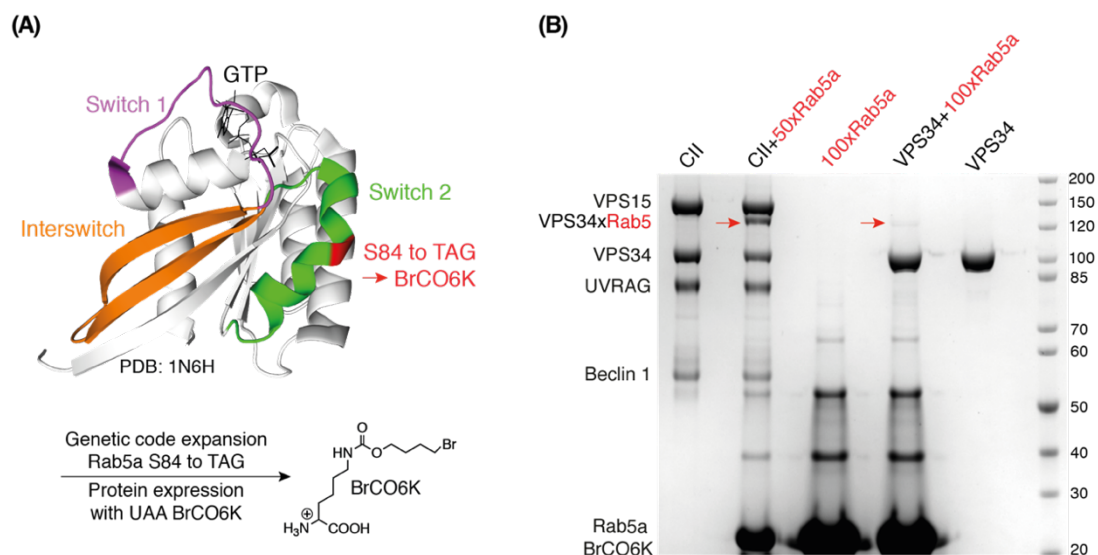


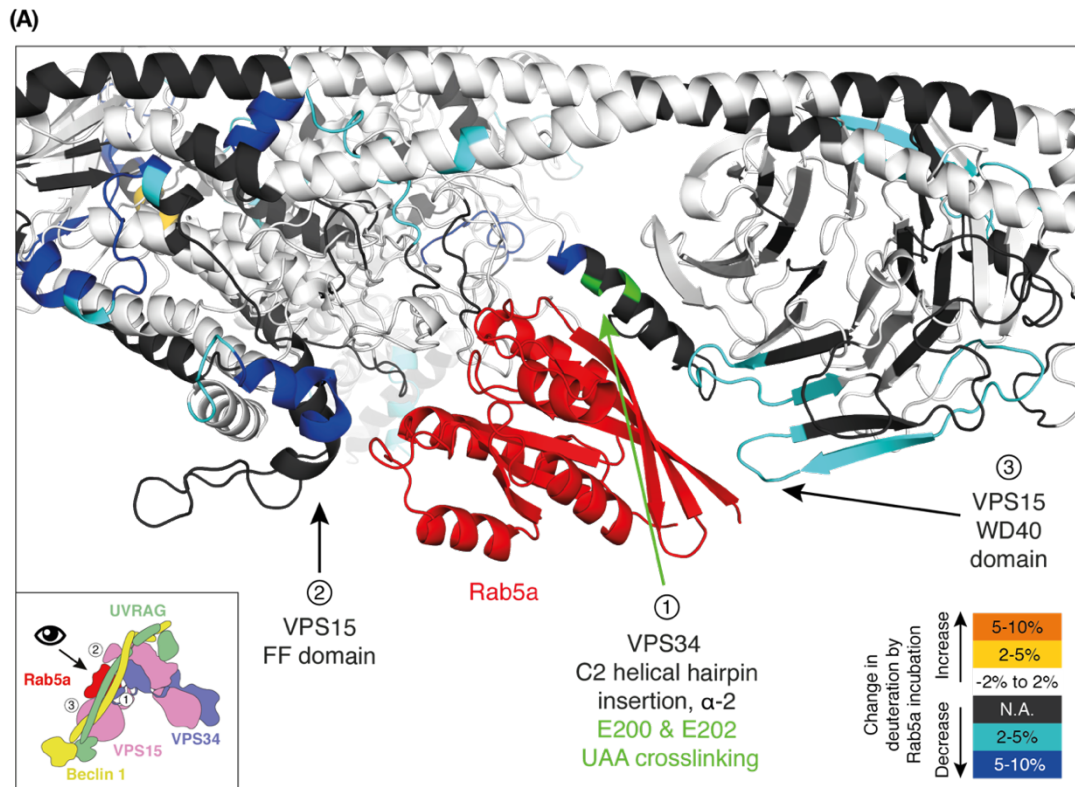
Figure 6-2: UAA crosslinking of Rab5a to VPS34 in complex II

(A) Rab5a was expressed with the unnatural amino acid (UAA) BrCO6K in switch 2 at S84. **(B)** Coomassie stained SDS-PAGE gel of the crosslinking reaction between either complex II or VPS34 with Rab5a-GTP S84→BrCO6K. Crosslinking products are indicated by red arrow.

Complex II and VPS34 were mixed with a large excess of Rab5a-GTP S84→BrCO6K and left overnight at 4°C in pH 8 buffer. VPS15 alone could not be tested as it cannot be purified by itself. The samples were then loaded on a SDS-PAGE gel. Figure 6-2B shows a Coomassie stained gel in which the crosslinked products are indicated by red arrows. Both complex II and VPS34 showed an extra band slightly above the 120 kDa molecular weight marker, which would account for the mass of VPS34 crosslinked to Rab5a (VPS34 + Rab5a, 102 kDa + 24kDa = 126 kDa). Notably, the efficiency of Rab5a crosslinking to complex II was much higher than to VPS34, suggesting that other subunits like VPS15, Beclin 1 or UVRAG might be part of the interaction. The gel bands were cut and our collaborators Juri Rappsilber and Zhuo Chen carried out the mass spectrometry analysis for identifying the crosslinks.

6.1.3 Rab5a uses a tripartite binding site made of VPS34 and VPS15

In Figure 6–3A, complex II is coloured by HDX changes and UAA crosslinking. I found that both sets of mass spectrometry results were complementary. Figure 6–3B shows multiple sequence alignment of different orthologues of VPS34 and VPS15. The lowest amino acid sequence is coloured in cyan and blue for decreased HDX and green for UAA crosslinks. Black regions indicate where no peptide was observed in the HDX-MS analysis. UAA crosslinking analysis confirmed two crosslinks. In Rab5a-GTP S84→BrCO6K + VPS34, Rab5a was crosslinked to VPS34 E202. In Rab5a-GTP S84→BrCO6K + complex II, Rab5a was crosslinked to VPS34 E200 & E202. With this, Rab5a was modelled with S84 in switch 2 facing VPS34 E200 & E202, which lie in the helix α 2 of the C2 helical hairpin insertion (C2HH). The analysis of the HDX changes was now focused on this area. The FF domain (aa 771-787) and WD40 domain (aa 1213-1224 and 1278-1299) of VPS15 showed a decrease deuterium uptake adjacent to the C2HH. Unfortunately, no peptides for the C2HH were observed in HDX. Only a small portion at the end of the helix α 2 (aa 204-206) showed a decrease in HDX. For the bulk of the helix (aa 176-203), no peptide was available for analysis as indicated by its black colour in Figure 6–3B. However, by having two different approaches, were able to shed light on how Rab5a binds VPS34 and VPS15 in complex II. Rab5a uses a tripartite binding site in which it contacts the VPS34 helix α 2 of the C2HH ((1) in Figure 6–3), the VPS15 FF domain ((2) in Figure 6–3), and WD40 domain ((3) in Figure 6–3).



(B)

① VPS34 C2 helical hairpin insertion

Vps34 Human	152	DGSEPTKTPGRTSSTLSE	DQMSRLAKLTKAHR	QCHMVKVDWLDRLTFRE	IFEMINSEKRSSN	213
Vps34 Drosophila	153	DGNFPSRTPGK.GKES	SKSQRLGKLAKKHR	NCVQKVDWLDRLTFRE	IEVINPREKRMSD	213
VPS34 Yeast	153	H.....CEVV	TDNKDQENLNKYF	QGEFTRLPLWLD	ITLTKLRQRENRTW	200
Vps34 Human	152	DGSEPTKTPGRTSSTLSE	DQMSRLAKLTKAHR	QCHMVKVDWLDRLTFRE	IFEMINSEKRSSN	213

② VPS15 FF domain

Vps15 Human	740	SLFRHLHM	RQKRNGSLPDCPP.....	PEDPAIAQLL	KLKLLSQGMTE	EEEDKLLAIKDF	MMKSNKAKAN	803
Vps15 Mouse	740	SLFRHLHM	RQKRNGSLDCPP.....	PEDPTIAQLL	KLKLLSQGMTE	EEEDKLLAIKDF	MMKSNRAKAN	803
VPS15 Yeast	811	SKNYGFNR	DTKSSSLKGIKTSSTVY	SHDNKEIPLTAEDRN	WIDAFHIIIGL	TEKDIWIVAI	RGYVIRTARVMA	886
Vps15 Human	740	SLFRHLHM	RQKRNGSLPDCPP.....	PEDPAIAQLL	KLKLLSQGMTE	EEEDKLLAIKDF	MMKSNKAKAN	803

③ VPS15 WD40 domain

Vps15 Human	1208	NE..VSMWDMET	QDRRFTLWASS.APPL	SELQ	1236	1274	ERSYV	VAGSTSSPSVSYR	KIIEGTEV	1300
Vps15 Mouse	1208	NE..VSMWDMET	QDRRLTLWASS.APPL	SELQ	1236	1274	ERSYV	VAGSTGSPSVSYR	KIIEGTEV	1300
VPS15 Yeast	1298	SKTFL	LTINNFVKGHCQYAF	INSDEQPSMEHFL	1329	1369	IVMFL	NLNLSSKAVIS	PSRFSDFV	1395
Vps15 Human	1208	NE..VSMWDMET	QDRRFTLWASS.APPL	SELQ	1236	1274	ERSYV	VAGSTSSPSVSYR	KIIEGTEV	1300

Figure 6-3: Summary of HDX and UAA crosslinking of Rab5a and complex II

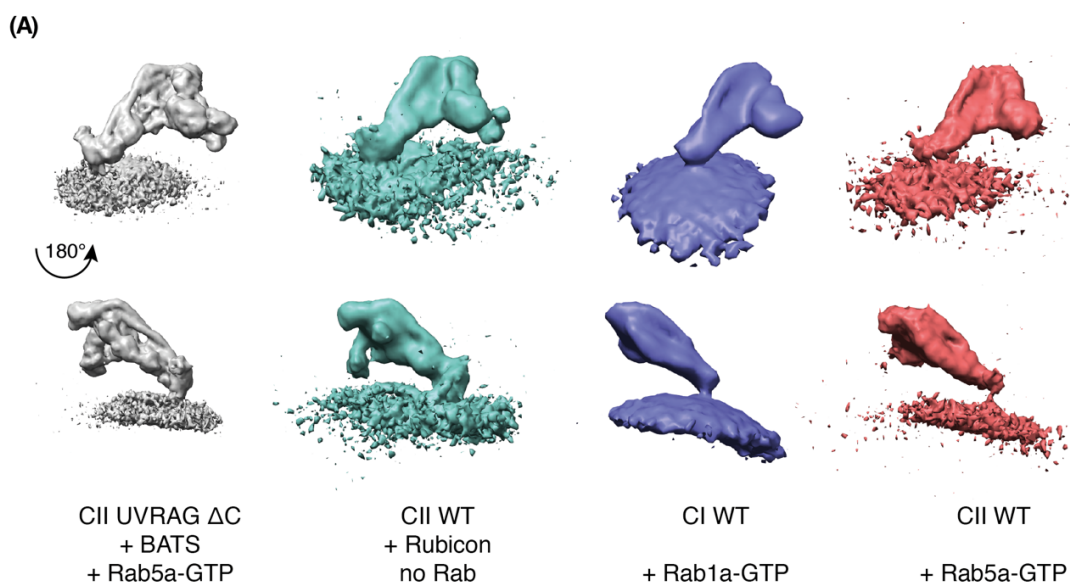
(A) A model of complex II coloured in cyan, blue and yellow for HDX changes. Contact residues discovered by amino acid crosslinking are coloured in green. Rab5a was modelled based on HDX and UAA crosslinking results. Rab5a binds with its switch 2 to VPS34 helix α 2 of the C2 helical hairpin insertion (C2HH) (1). It also contacts VPS15 FF (2) and WD40 domain (3). (B) The human VPS15 and VPS34 amino acid sequences (bottom line) are coloured by HDX and UAA crosslinking. Above, a multiple sequence alignment of different orthologues coloured by conservation is depicted.

6.1.4 Cryo-ET to study membrane bound VPS34 complex

So far, several structures of different complexes I or II constructs have been solved: a 4.4 Å crystal structure of yeast complex II (Rostislavleva et al., 2015), a 6.8 Å cryo-EM structure of human complex II + a Rubicon fragment (VPS34 kinase domain was not resolved, (Chang et al., 2019)), and a 6.6Å cryo-EM structure of human complex I + an NRBF2 fragment (Young et al., 2019). However, one essential element has been missing in all these structures: the membrane. That is why I decided to pursue structural studies of the VPS34 complex on membranes by cryo-electron tomography. Therefore, we started a collaboration with the group of John Briggs. Dustin Morado in the Briggs group has helped in acquiring the tomograms and making the subtomogram averaging pipeline of the Briggs lab accessible to me.

6.1.5 Sample preparation strategy for subtomogram averaging

Several data sets were collected during my PhD and the most successful reconstructions are shown in Figure 6-4A. In Figure 6-4B, the details of each data set are specified. These datasets yielded different resolutions with the data set for complex II UVRAGΔC+BATS on Rab5a-GTP decorated SUVs being the most successful with a resolution of 9.8 Å. It is hard to exactly determine why this data set was outstanding, but it probably can be attributed to the number of particles, protein stability, and the construct's affinity for membranes.



(B)

	CII UVRAG Δ C + BATS + Rab5a-GTP	CII Rubicon no Rab	CI WT + Rab1a-GTP	CII WT + Rab5a-GTP
Lipid composition				
Liver PI	16%	17%	16%	16%
DOPS		78%		10%
DOPE	12%		12%	12%
DOPC	66%		66%	57%
DOPE-MCC	6%	5%	6%	5%
Detector	Gatan K3	Gatan K3	Gatan K3	Gatan K2
Electron exposure ($e/\text{\AA}^2$)	~ 120	~ 110	~ 120	~ 130
Defocus range (μm)	-2.5 to 5	-2 to -4.5	-2.5 to 5	-3 to -6
Tilt range (min/max, step)	from -60° to $+60^\circ$, 3° increment			
Tilt scheme	dose-symmetrical (Hagen scheme)			
Tomogram used/acquired (no.)	105/115	29/46	44/52	16/17
Pixel size (\AA)	2.133	1.379	2.133	1.545
Subtomograms after picking	191,169	5,304	14,313	2,407
Final subtomograms	31,307	1,075	935	503
Final resolution (\AA)	9.8	~ 30	> 50	> 50

Figure 6–4: Comparison of acquired cryo-electron tomography data sets and their subtomogram averaging results

(A) Final reconstructions of data sets are shown from two angles. (B) Table about sample preparation, tomogram collection and processing parameters of each data set are depicted.

The data set of the complex II BATS fusion had by far the greatest number of subtomograms with 191,169 after particle picking. The final reconstruction consisted of 31,307 subtomograms whereas the other had only ~ 500 -1,000 subtomograms. Furthermore, complex II seemed to be far more stable than complex I. It is not clear exactly why complex I was more fragile than complex II under similar

conditions. Potentially, other binding partners or buffers might still require optimisation so that complex I would be a better target for structural studies. One of the most important factors to optimise cryo-EM grid quality was the ability of the VPS34 complex construct to bind to membranes. Complex II UVRAG Δ C+BATS was the most active construct that we tested so far (Figure 4–5). Moreover, it could be further activated by membrane bound Rab5a-GTP (Figure 6–5). The efficiency of decorating SUVs with Rab5a via the maleimide lipid was also crucial. During optimisation experiments, it became clear that the aggregation of SUVs was increased with increasing amounts of PS in the lipid mixture. Consequently, PS was omitted from the SUVs (Figure 6–4B). It should also be noted, that no ATP was present in the buffer. Since this data set yielded the highest resolution and this construct behaved similarly on membranes compared to the others, only its results will be discussed.

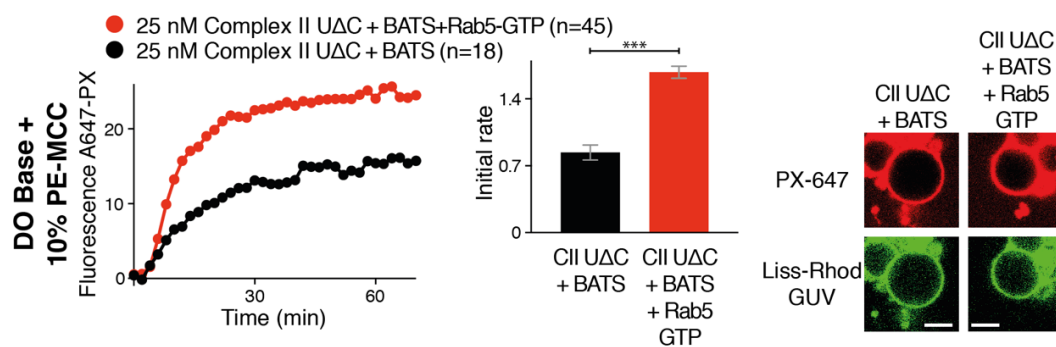


Figure 6–5: Membrane bound Rab5a can activate complex II UVRAG Δ C+BATS

GUVs were either incubated with Rab5a-GTP or no Rab5a. Complex II UVRAG Δ C+BATS was strongly activated by Rab5a-GTP. Scale bars: 5 μ m. Significance level: *** $p < 0.001$; ** $p < 0.01$; * $p < 0.05$; n.s. = not significant. The number of GUVs for analysis is indicated by (n).

6.1.6 Particle extraction and identification in subtomogram averaging

115 tilt series were collected on a FEI Titan Krios from which 105 tomogram reconstructions were selected for subtomogram averaging. The others either showed unsatisfactory deviations during gold fiducial alignment or contained contamination such as dirt or ice. Figure 6-6 shows a representative slice of a reconstructed tomogram of Rab5a coated SUVs decorated with complex II UVRAG Δ C+BATS. The diameter of picked vesicles had a mean diameter of 81.3 nm \pm 19.5 nm. From the side view, the ice thickness can be measured as \sim 50 nm. Due to the very thin ice, particles on the top and bottom of the vesicle are not captured in ice as indicated by the white arrow. Furthermore, as the top and bottom part of the membrane is horizontally oriented it is also lost due to the missing wedge. Consequently, mostly side views of the particles were used for subtomogram averaging.

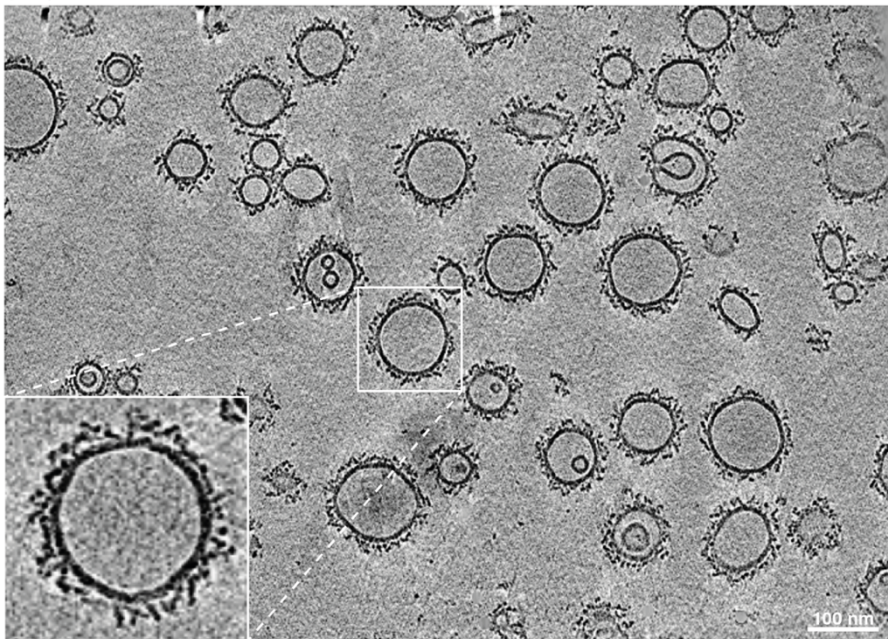
For single particle cryo-EM, the localisation of particles in 2D images has evolved to a relatively straightforward task. Whereas in cryo-ET, due to the low S/N ratio, distortions as a result of the missing wedge effect and the ambiguous character of particles in tomograms, locating copies of the protein of interest remains a complex process. However, as some proteins of interest can be part of regular structures such as filaments or membrane coats, their repetitive geometry can be harnessed. Their surface can be sampled with a dense distribution of subtomograms in random positions, which should ensure that some of the boxes will contain particles. This method was employed for selecting complex II UVRAG Δ C+BATS particles on the vesicle membranes (Figure 6-7A). First, the vesicle centre and radius were set for each vesicle in order to identify the membrane surface. The surface was then

Results

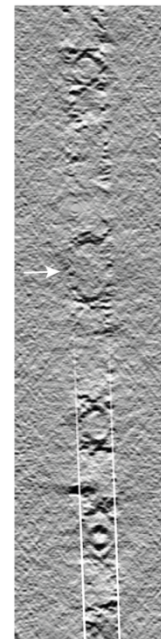
sampled with overlapping subtomogram boxes. That way, several boxes in the vicinity should contain the same particle. Next, an angular alignment was carried out with a chosen starting reference. In this alignment, a large search in all three Euler angles and in x/y/z was performed.

(A)

i) Top view



iii) Side view



ii) Zoom in of top view

(B)

Complex II with UVRAG Δ C+BATS + Rab5a-GTP bound to maleimide DOPE

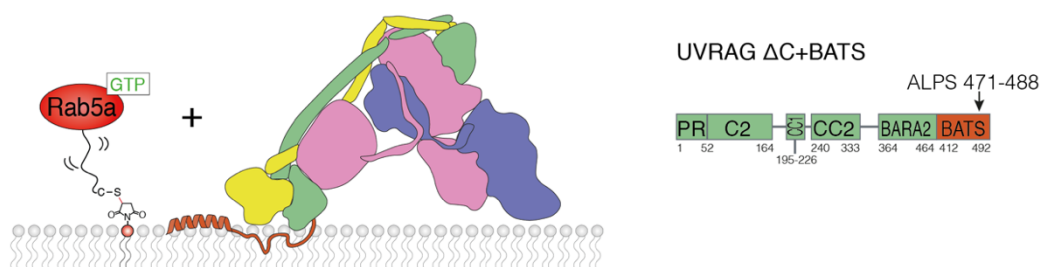


Figure 6-6: Rab5a coated vesicles decorated with complex II UVRAG Δ C+BATS

(A) Representative slice of a tomogram of Rab5a coated membranes decorated with complex II UVRAG Δ C+BATS. The top view shows vesicles highly decorated by VPS34 complexes. The side view shows the ice thickness for the tomogram. As the ice is so thin, the top and bottom of larger vesicles were outside of the ice layer (indicated by white arrow). **(B) Left:** A model of sample used for cryo-electron tomography and subtomogram averaging. Right: A schematic representation of the UVRAG Δ C+BATS.

After several iterations, overlapping subtomograms would have ideally identified the same particle in the vicinity and converge to the same position within a few pixels. Finally, duplicates were cleaned by a minimal distance threshold so that each particle was only contained within one subtomogram. In order to decrease processing time, the number of voxels in tomograms can be reduced by binning. When a voxel array is binned by factor 2, four adjacent voxels are combined to one. Voxel binning increases the speed of the processing but limits the achievable resolution according to the Nyquist limit (Cheng et al., 2015). The Nyquist theorem defines that the theoretically attainable resolution is restricted to twice the pixel size, *e.g.* in bin2 tomograms, with an original voxel size of 2.133 Å, the voxel size is 4.266 Å and the attainable resolution is 8.532 Å. Consequently, the particle picking was carried out in bin8 tomograms and processing was then continued further in bin4, bin2, and bin1 tomograms to increase the attainable resolution.

In my experience, particle picking and choosing a starting reference was the most difficult and time-consuming but crucial part in the whole subtomogram pipeline. Every step afterwards, relied on the selection of actual protein densities instead of random noise. Especially, choosing the right starting references was crucial. Being vigilant of reference bias was important in choosing the starting reference and several different strategies were tried as depicted in Figure 6–7B. A good reference can be a shape that loosely resembles the final structure but has no distinct features that could infer reference bias. As the alignment of the picked particles improves, more distinct higher resolution features should appear thereby validating the protein structure.

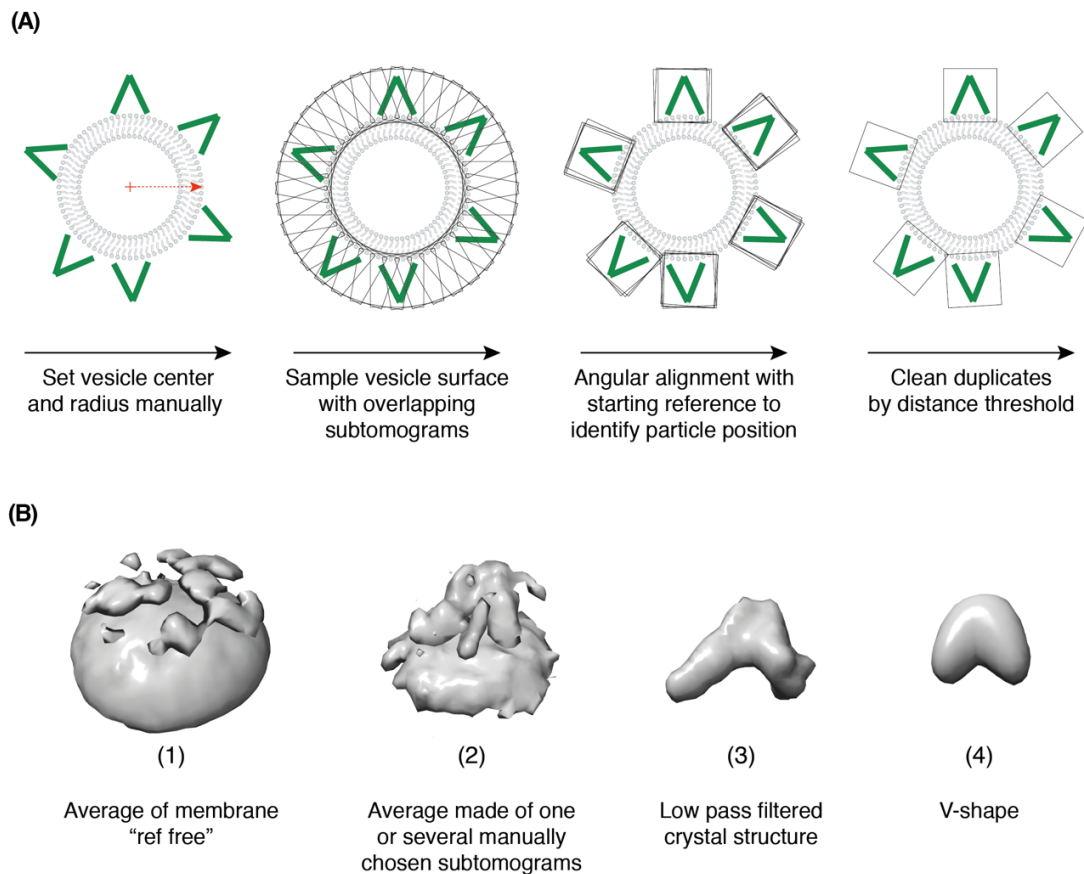


Figure 6-7: Particle picking along vesicle membranes

(A) First, the vesicle centre and radius are set for each vesicle in order to oversample the sphere surface with overlapping subtomogram boxes. Next, an angular alignment run is carried out with a chosen starting reference seen in **(B)**. After several iterations, overlapping subtomograms boxes will converge to the same position. Finally, duplicates are cleaned by a minimal distance threshold so that each subtomogram contains one particle. **(B)** Examples of starting references for particle picking.

In an ideal situation, of course a reference free approach would be best. Reference free in this case means that the oversampled subtomograms, containing mostly membranes with no defined protein feature, were averaged (Figure 6-7B (1)). Several studies of membrane coat proteins such as COP-I, retromer or clathrin were picked by reference free subtomogram averaging (Dodonova et al., 2015; Kovtun et al., 2020, 2018). However, these are highly rigid protein structures with a high membrane affinity organised in a regular and symmetric lattice. As expected, reference free particle picking did not converge to a valid structure. Another approach can be to create a reference out of the original data itself. In Nicastro et al.,

Results

a single representative subtomogram was used as a reference and was aligned over multiple search iterations (Nicastro et al., 2006). At the same time, they had the advantage of narrowing their search parameter as their protein target dynein was ordered in 96 nm spaced repeats on microtubules. A similar method for reference generation was tested (Figure 6–7B (2)). Although this previously had worked well for the highly ordered dynein repeats, it gave mediocre results for the less ordered and more flexible complex II.

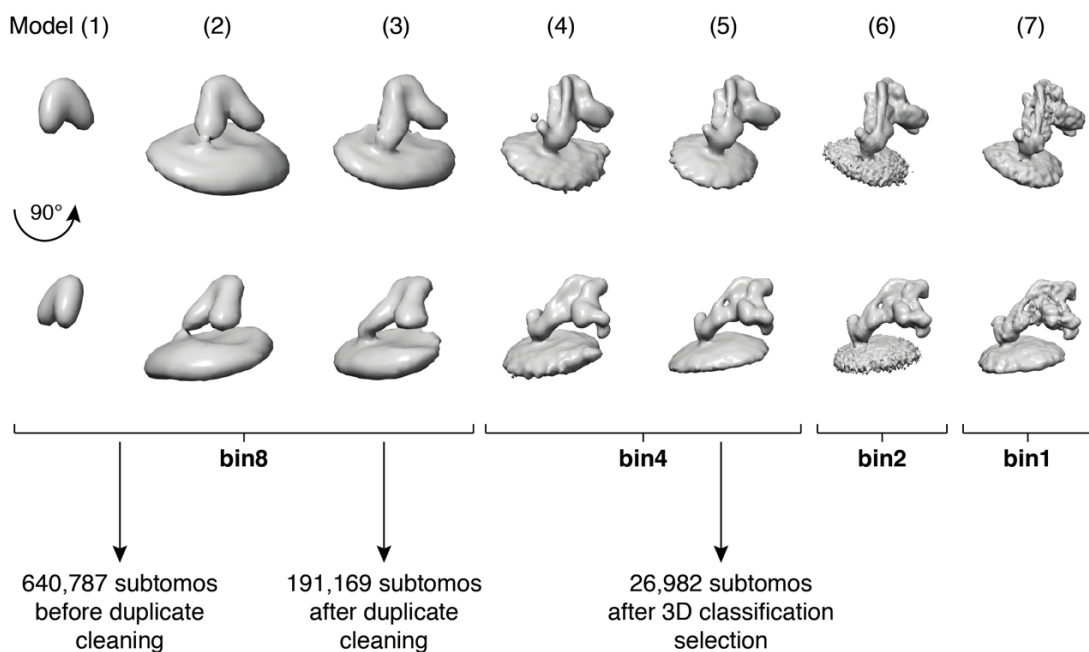


Figure 6–8: Structure determination progress of complex II by subtomogram averaging Model (1) - (7) show the alignment progress of particles from bin8, bin4, bin2, and bin1 tomograms.

When it was used as a starting reference, the reference bias was too strong and no converged subtomograms could be seen. As predicted, using a low pass filtered crystal structure did also not serve as a satisfactory starting reference due to imposing too much reference bias (Figure 6–7B (3)). Only a general V-shape, worked well for picking convincing protein particles (Figure 6–7B (4)). Figure 6–8 shows the evolution from the reference (model 1) to converged particle (model 3).

Here, the reference acquired different features over iterations such as the membrane and one arm of the V being docked on the membrane. After duplicate cleaning, 191,196 subtomograms remained and alignment continued further in bin4. After several rounds of alignment using a cylindrical alignment mask that hovered above the membrane, a maximum resolution of ~ 20 Å could be obtained (Figure 6–8, model (4)).

6.1.7 Analysing structural heterogeneity by 3D classification

Because of the low resolution, a principal component analysis (PCA) classification on wedge-masked difference maps was used to classify the subtomograms (Heumann et al., 2011). The PCA was performed on the protein density without including the membrane. The first 5 eigenvectors were used to sort the data into 20 classes. The 3D classification yielded a variety of classes that were manually sorted in Figure 6–9. It was obvious that classes 1-6 had the most distinct features and were combined for further alignment. In contrast, classes 7-11 lacked detailed features and classes 12-20 showed no membrane density. It also became clear that classes 1-6 showed missing wedge effects. In Figure 6–10, class 1 and 4 appear to be stretched in vertical and horizontal directions, respectively. These are classic signs of missing information in Fourier space as it causes blurring and elongation along the axis of the missing wedge (Walz et al., 1997). Classification is routinely used in single particle cryo-EM for attaining high resolution structures. However, these techniques are not directly applicable for aligning tomographic data because of the missing wedge (Bartesaghi et al., 2008; Förster et al., 2008; Heumann et al.,

2011; Winkler et al., 2008). Often, this leads to data being classified primarily by the missing information.

3D particle classification

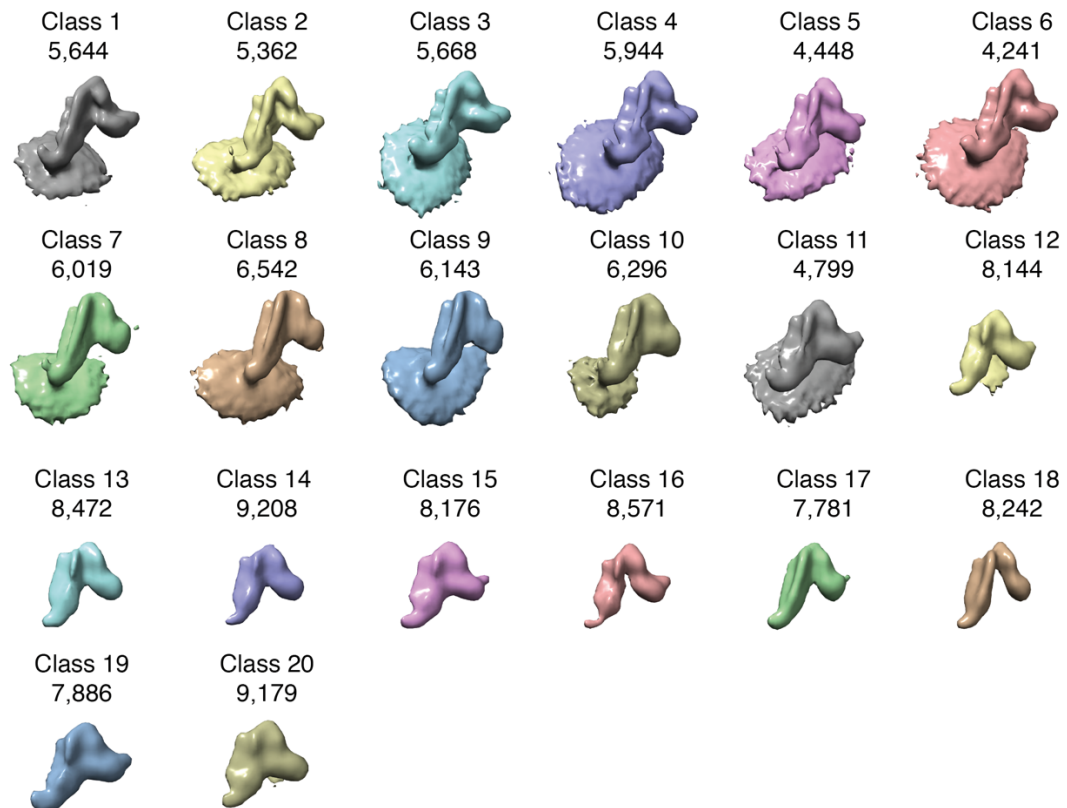


Figure 6-9: Analysis of heterogeneity by 3D classification

20 classes obtained from 3D classification are displayed. For each class, the number of particles is labelled above. Classes 1-6, with the most distinct features, were chosen for further refinement.

This can be partly seen in the orientation of the wedge for classes 1 and 4 (Figure 6-10). However, although the classification was partly influenced by the missing wedge, certainly other differences also influenced the classification as well, such as the presence of a membrane. In spite of this, when classes 1-6 were averaged, the Fourier space was again evenly sampled (Figure 6-10).

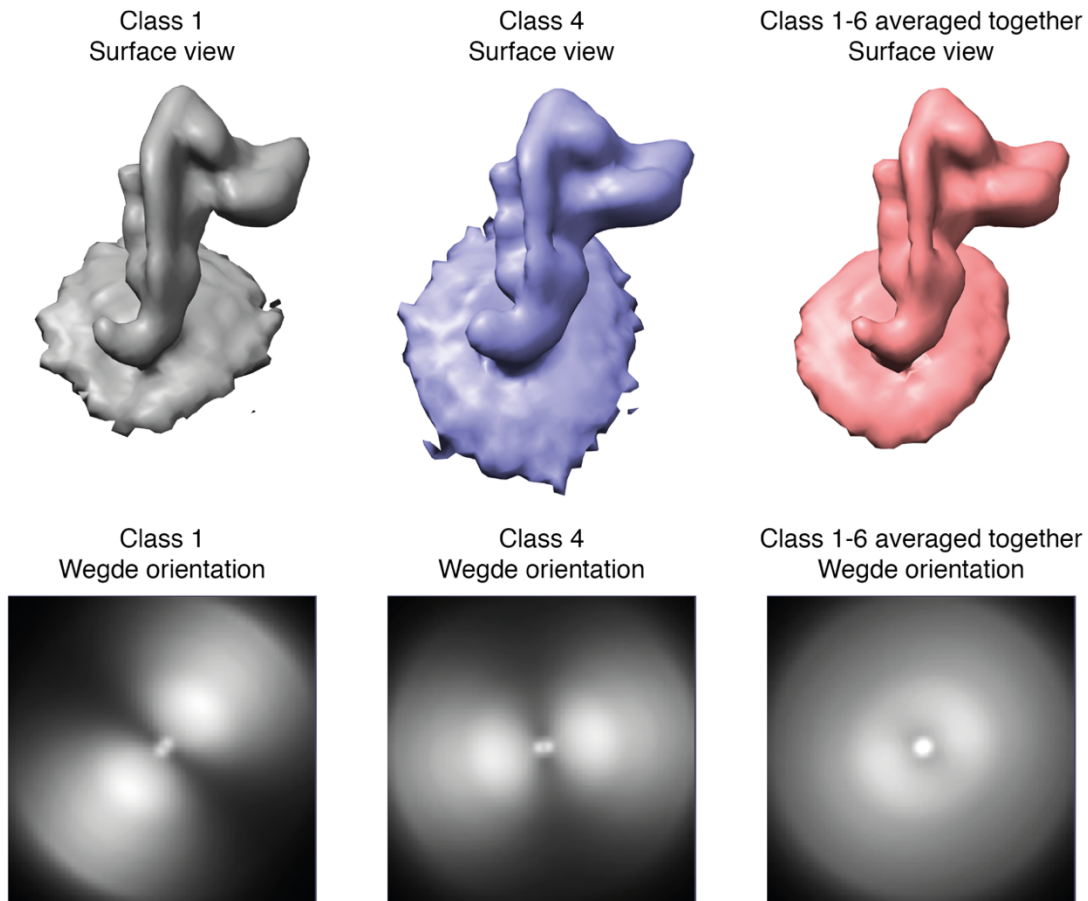


Figure 6-10: Wedge bias in 3D classification

Class 1 and 4 show wedge bias by their elongated shape. Below, the orientation of the wedge of both classes is displayed. However, by averaging classes 1-6, the Fourier space can be evenly sampled again.

When classes 1-6 were combined, the number of subtomograms was reduced from 191,169 to 26,982 (Figure 6-8). However, these subtomograms from bin1 tomograms could now be aligned to a final resolution of 9.8 Å (Figure 6-11A). Additionally, the LAFTER algorithm was used for local de-noising (Ramlal et al., 2018) (Figure 6-11B).

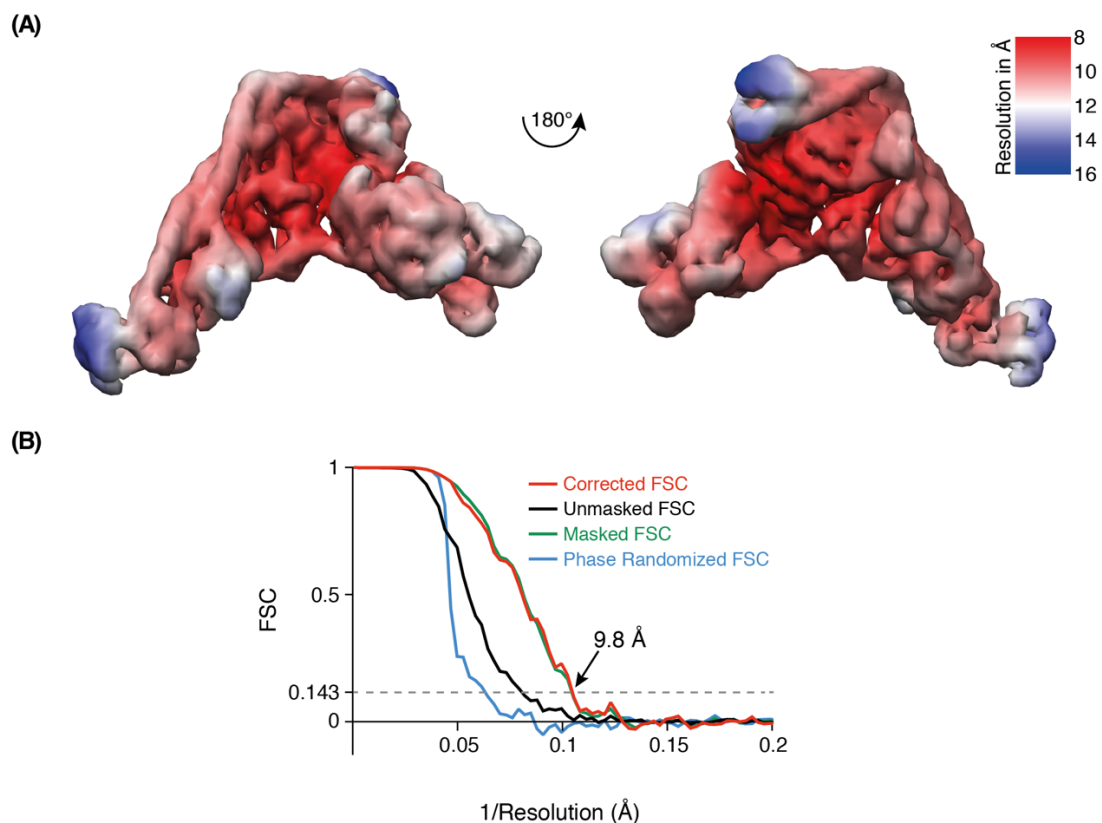


Figure 6-11: 9.8 Å reconstruction of complex II UVRAG Δ C+BATS on Rab5a decorated membranes

(A) Map after local-denoising with the LAFTER algorithm (Ramlal et al., 2018) and coloured by local resolution calculated in Relion 3.0 (Zivanov et al., 2018). **(B)** FSC curves for corrected, unmasked, masked and phase randomized reconstructions. The 9.8 Å overall resolution at the 0.143 criterion is marked by an arrow.

6.1.8 Subtomogram averaging of complex II UVRAG Δ C+BATS on Rab5a decorated membranes at 9.8 Å

Complex II UVRAG Δ C+BATS on Rab5a decorated membranes adopts the characteristic V-shape as in the structures solved before (Chang et al., 2019; Rostislavleva et al., 2015; Young et al., 2019). As no map coordinates have been deposited for the cryo-EM structures by Chang et al. or Young et al., we have used a SWISS-MODEL homology-modelling server and the crystal structure of yeast complex II (PDB: 5DFZ) to generate an initial model (Biasini et al., 2014).

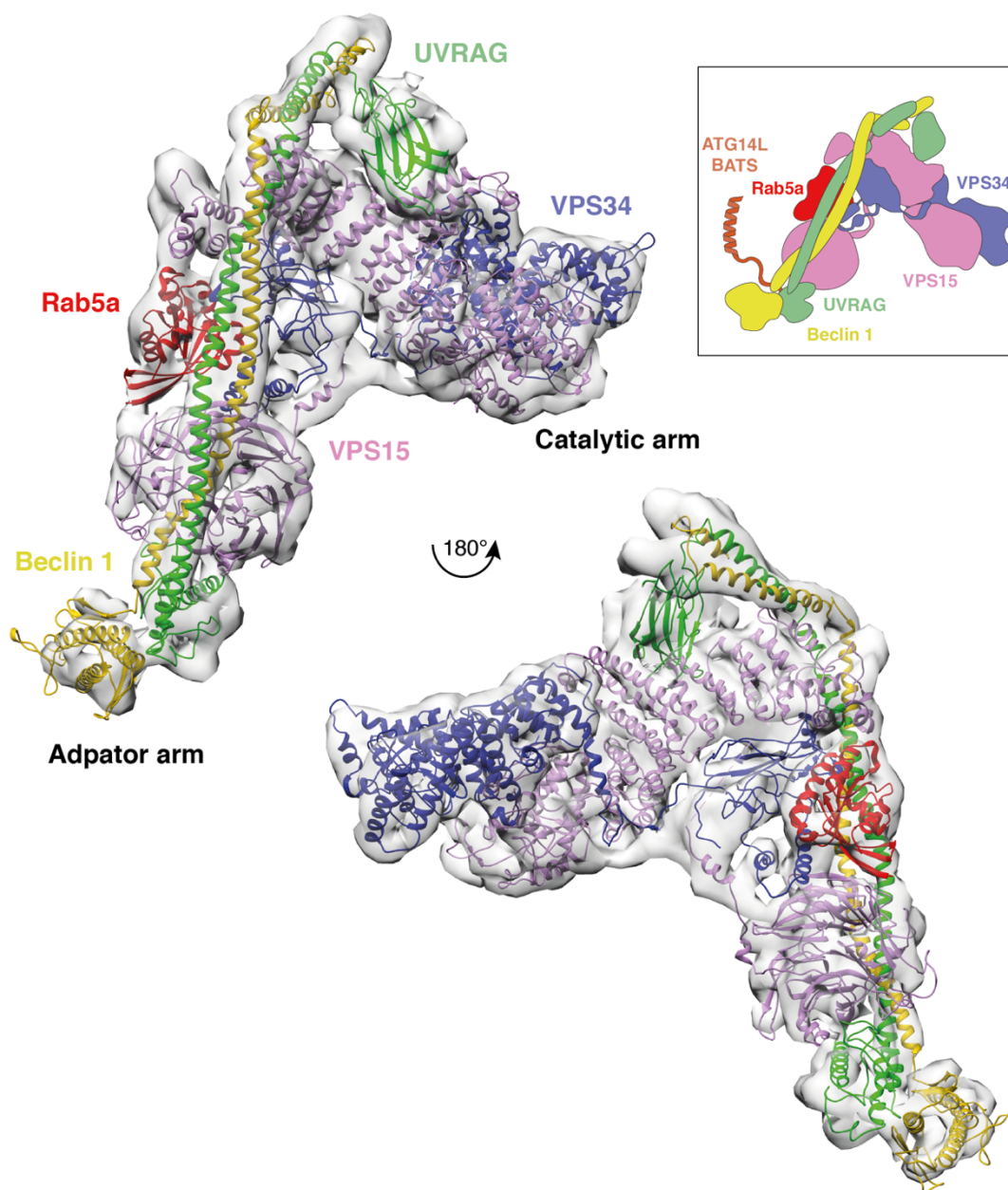


Figure 6-12: Model of Rab5a bound to human complex II UVRAG Δ C+BATS

A human model of complex II was made with SWISS-MODEL and the yeast complex II crystal structure (5DFZ). The model and a crystal structure of Rab5a (PDB: 1N6H) initially was fitted into the cryo-ET density with chimera, then manually modified locally using Coot to fit to the density. No density for the ATG14L BATS could be seen at the tip of the adaptor arm.

The human homology model and a crystal structure for Rab5a-GTP (PDB: 1N6H) were then fitted with Chimera into the cryo-ET density map (Goddard et al., 2007) (Figure 6-12). Following this, the kinase domains of VPS34 and VPS15 were adjusted with Coot as rigid bodies to fit the EM density (Emsley and Cowtan, 2004). The coiled-coil regions of Beclin 1 and UVRAG were also manually adjusted in Coot.

The region that we refer to as the FF domain in VPS15 was clearer in the cryo-EM map than it had been in the original X-ray crystal structure of yeast complex II, so it too was manually fitted to the density using Coot. The C2 domain, CBR1 and the C2 helical hairpin insertion also required manual adjustment to match the EM density. The AF1 loop was modelled into the density at the contact site of the adaptor arm with the membrane. As there was no density at the tip of the adaptor arm, the fused ATG14L BATS could not be modelled.

In general, the yeast crystal structure and the human cryo-ET model bear a high similarity to each other. However, three key differences will be discussed in detail. Firstly, a clear density for Rab5a can be seen at the adaptor arm. Secondly, the VPS34 kinase domain adopts a different conformation compared to the crystal structure of yeast complex II. Lastly, a clear membrane density can be seen and therefore I will analyse how human complex II UVRAG Δ C+BATS binds to lipid bilayers.

6.1.9 Cryo-ET confirms Rab5a tripartite binding site

In the cryo-ET density, an extra density at the adaptor arm that could not be allocated to any of the complex II components can be seen. The density is exactly located where Rab5a was positioned by HDX-MS and UAA crosslinking analysis (Figure 6–13A and Figure 6–3).

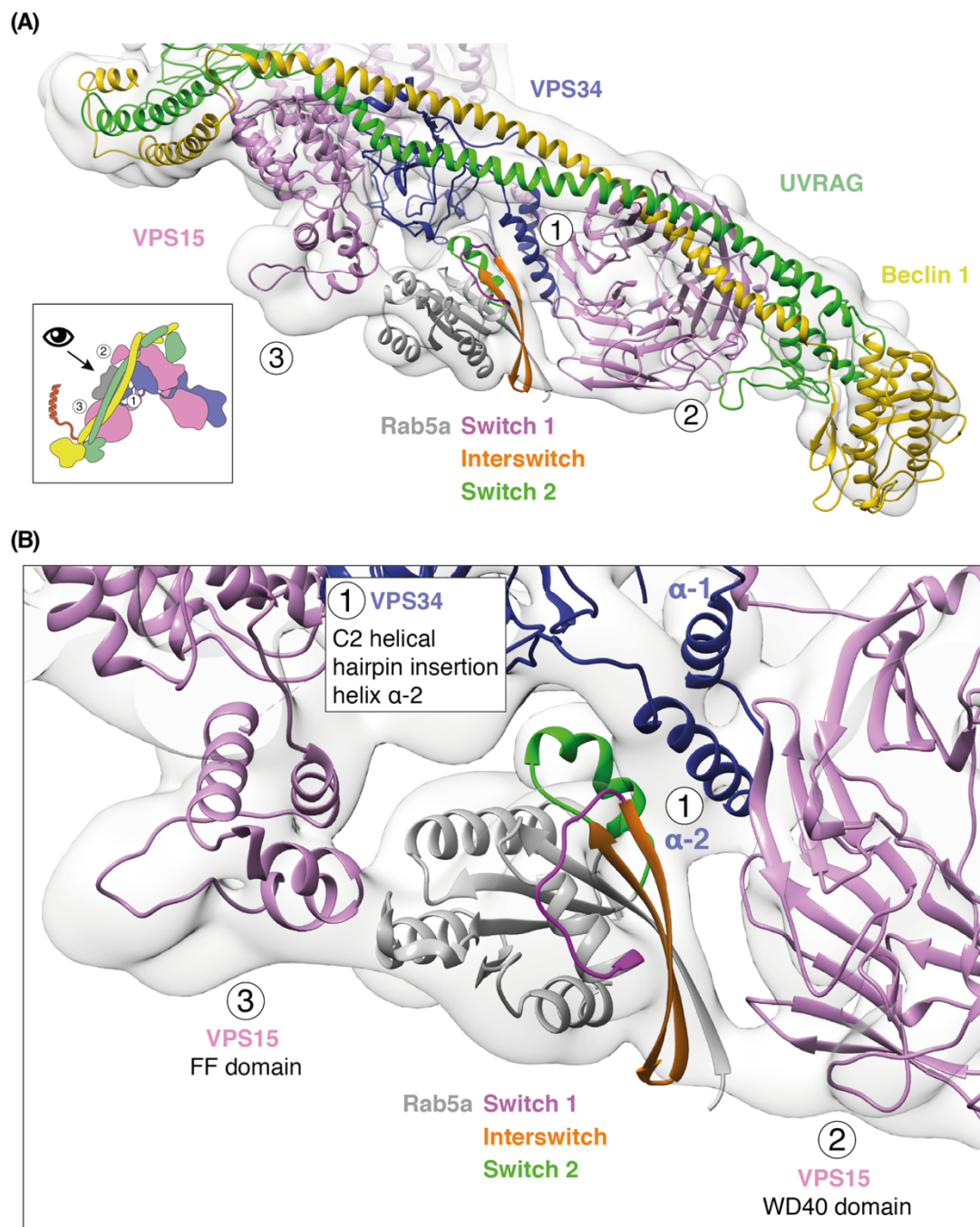


Figure 6-13: Rab5a binds to three regions in VPS34 and VPS15 in complex II

Rab5a was modelled into the cryo-ET density with its switch 2 facing the VPS34 C2 helical hairpin insertion (C2HH). Connections can be seen from the Rab5a density towards the complex II density. Consequently, cryo-ET shows that Rab5a occupies the tripartite binding site identified in HDX-MS and UAA crosslinking, involving helix α 2 of the VPS34 C2HH (1), the VPS15 WD40 domain (2), and the VPS15 FF domain (3).

With the help of the LAFTER sharpened map, Rab5a could be confidently positioned in it with its switch 2 domain facing the VPS34 C2 helical hairpin insertion (C2HH).

Furthermore, the Rab5a density shows connections to surrounding regions of the

complex II density depending on the threshold (Figure 6–13B). Three connections can be seen to the helix α -2 of the VPS34 C2HH, the VPS15 WD40 domain, and the VPS15 FF domain. The cryo-ET density thereby recapitulates that Rab5a binds to complex II via a tripartite binding site made of VPS34 and VPS15.

6.1.10 Capturing VPS34 in its activated state

VPS34 complexes have proven to be very dynamic in movement. The VPS34/VPS15 catalytic arm is especially dynamic. Both the helical and kinase domains (HELCAT) of VPS34 and VPS15 are connected to the rest of the complex by a flexible linker. Stjepanovic et al. showed that the VPS34 HELCAT dislodges from the complex and assumes various conformations (Stjepanovic et al., 2017). The difficult task of getting crystals for yeast complex II was facilitated by the use of a nanobody that binds to the VPS34 kinase and helical domains and thereby stabilises them (Rostislavleva et al., 2015). Although VPS15 is thought to be a pseudokinase, it seems to serve as an important scaffolding protein for VPS34 and can influence the activity of VPS34. In the yeast crystal structure, the N-terminal kinase domain of VPS15 binds to the VPS34 kinase activation loop thereby rendering the VPS34 inactive (Figure 6–14A). The cryo-ET structure has captured a different conformation of the VPS34 kinase domain, where the domain is rotated and flipped out, releasing the activation loop from the inhibitory grasp of the VPS15 kinase domain (Figure 6–14B). The distance between the VPS15 N-terminus and the VPS34 activation loop increases to 24 Å compared to 5 Å in the yeast crystal structure. This suggests an allosteric activation of VPS34 by binding to Rab5a coated membranes.

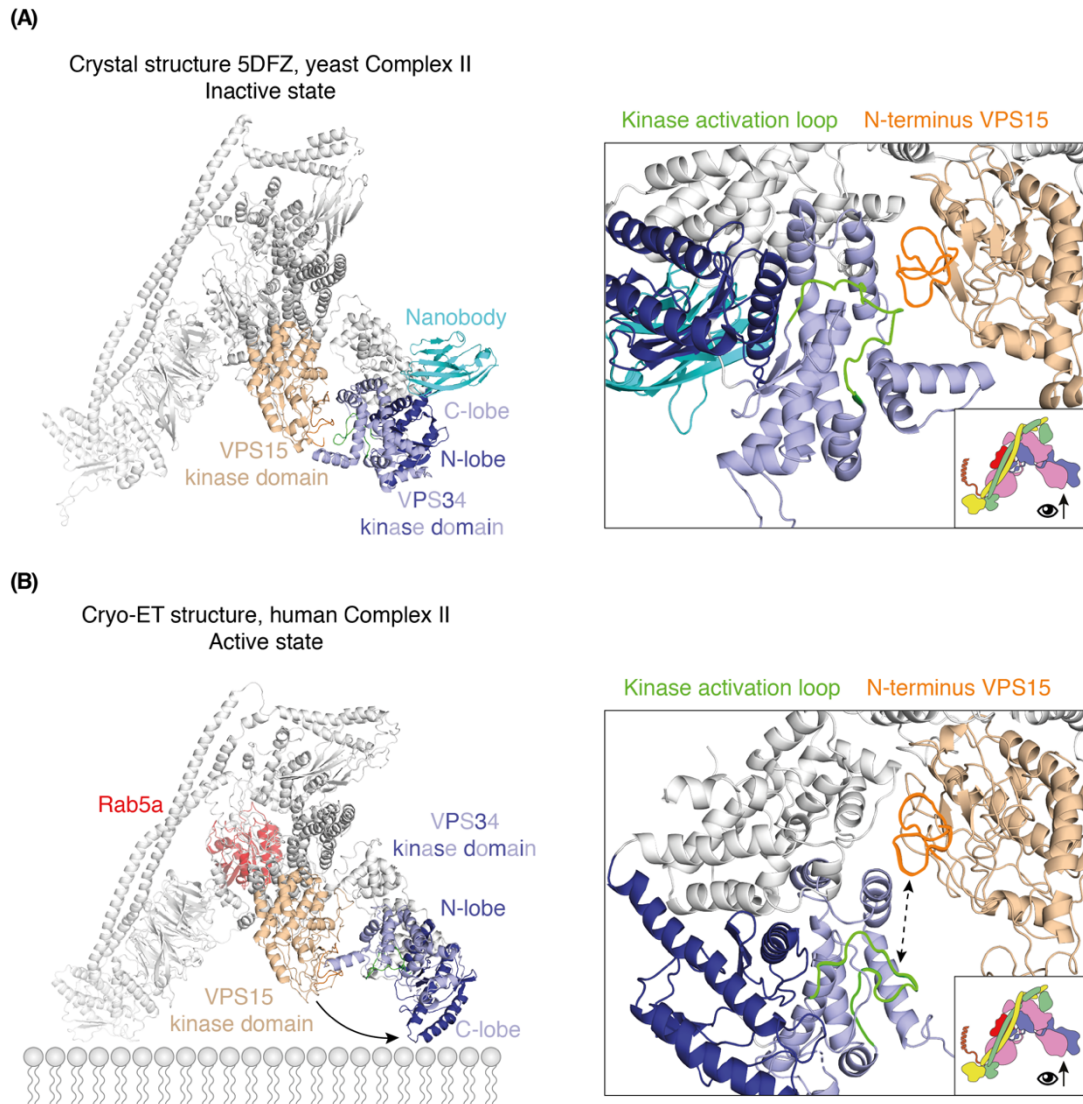


Figure 6–14: Cryo-ET catches VPS34 kinase domain in its active state

(A) Yeast complex II was crystallized with the help of a nanobody stabilising the VPS34 kinase and helical domains. The crystal structure captures an inactive state as the VPS15 N-terminus contacts and thereby inhibits the VPS34 kinase activation loop. **(B)** The cryo-ET structure shows an active conformation as the VPS34 kinase domain flips out and thereby liberates the activation loop.

6.1.11 Beclin-1 BARA is the main membrane binding site

VPS34 complexes belong to the family of peripheral membrane proteins that are water-soluble and reversibly bind to lipid bilayers with relatively low affinity. They do not contain any protein domains that span the membrane but use hydrophobic

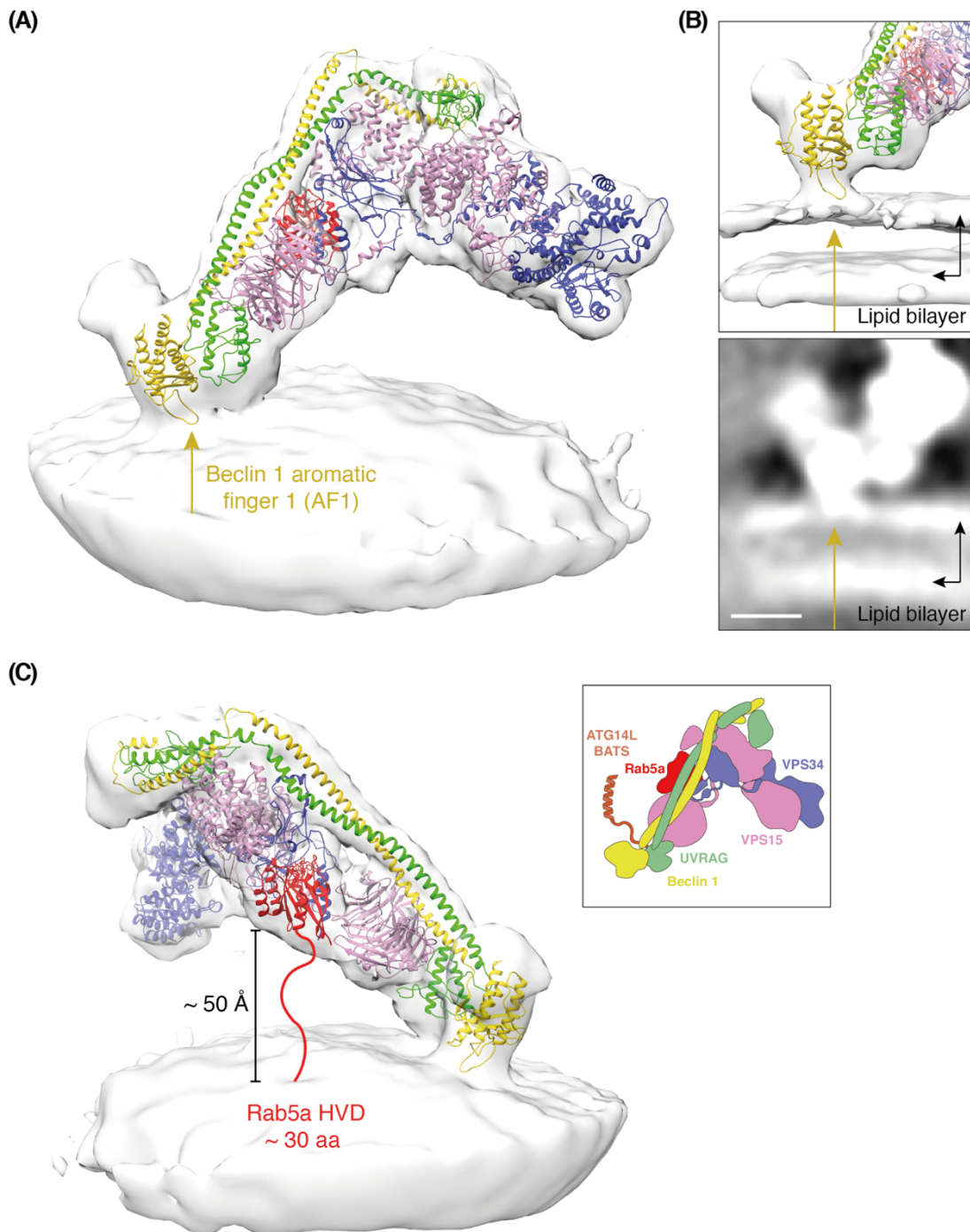


Figure 6-15: Cryo-ET structure of membrane-associated human complex II UVRAG Δ C+BATS

(A) Complex II UVRAG Δ C+BATS was observed to stably bind to membranes solely with its adaptor arm. The catalytic arm hovers over the membrane with little direct membrane contact. No density or membrane contact can be seen for the ATG14L BATS domain. (B) The adaptor arm shows density that extends towards the membrane and contacts the first leaflet of the lipid bilayer. The Beclin 1 aromatic finger loop was modelled in this density as it was shown to be a crucial membrane binding element. Scale bar 4 nm (C) No density for the C-terminal HVD can be seen. The distance between the Rab5a density and membrane is ~ 50 Å. amino acids or the ALPS motifs to anchor to the membrane. To our knowledge, this

is the first structure of a peripheral membrane protein on a lipid bilayer that does

not belong to the family of coat proteins. The cryo-ET structure of complex II UVRAG Δ C+BATS shows clear membrane density. Surprisingly, only the adaptor arm is solidly attached to the membrane while the catalytic arm does not seem to be permanently attached (Figure 6–15A). At a lower threshold, a density contacting the first lipid bilayer can be seen (Figure 6–15B). As the Beclin 1 aromatic finger 1 (AF1) is an important membrane binding motif for complex II, the loop was modelled into the density. No density could be seen for the ATG14L BATS domain despite some extra density at the adaptor arm. However, as the BATS domain is attached to a flexible linker, it might not remain in one conformation. The Rab5a density is approximately 50 Å above the membrane. As the C-terminal HVD of Rab5a contains ~30 amino acids, it can theoretically span even longer distances (~110 Å).

6.1.12 Analysing flexibility of membrane binding by 3D classification

If one compares the membrane density of this data set to the other cryo-ET maps of the retromer or COP-1 coat, it appears to be more disordered (Dodonova et al., 2015; Kovtun et al., 2020, 2018). Thus, we used again PCA classification to focus on the membrane. To our surprise, complex II UVRAG Δ C+BATS is highly flexible on the membrane. The classification generated 12 classes, however, the 3 most extreme classes are depicted in Figure 6–16A. For all classes, the membrane binding of the adaptor arm is the main anchor point, while the rest of complex II rotates and tilts around it. Interestingly, in all classes the density of the kinase domain can be seen and therefore seems to be stable.

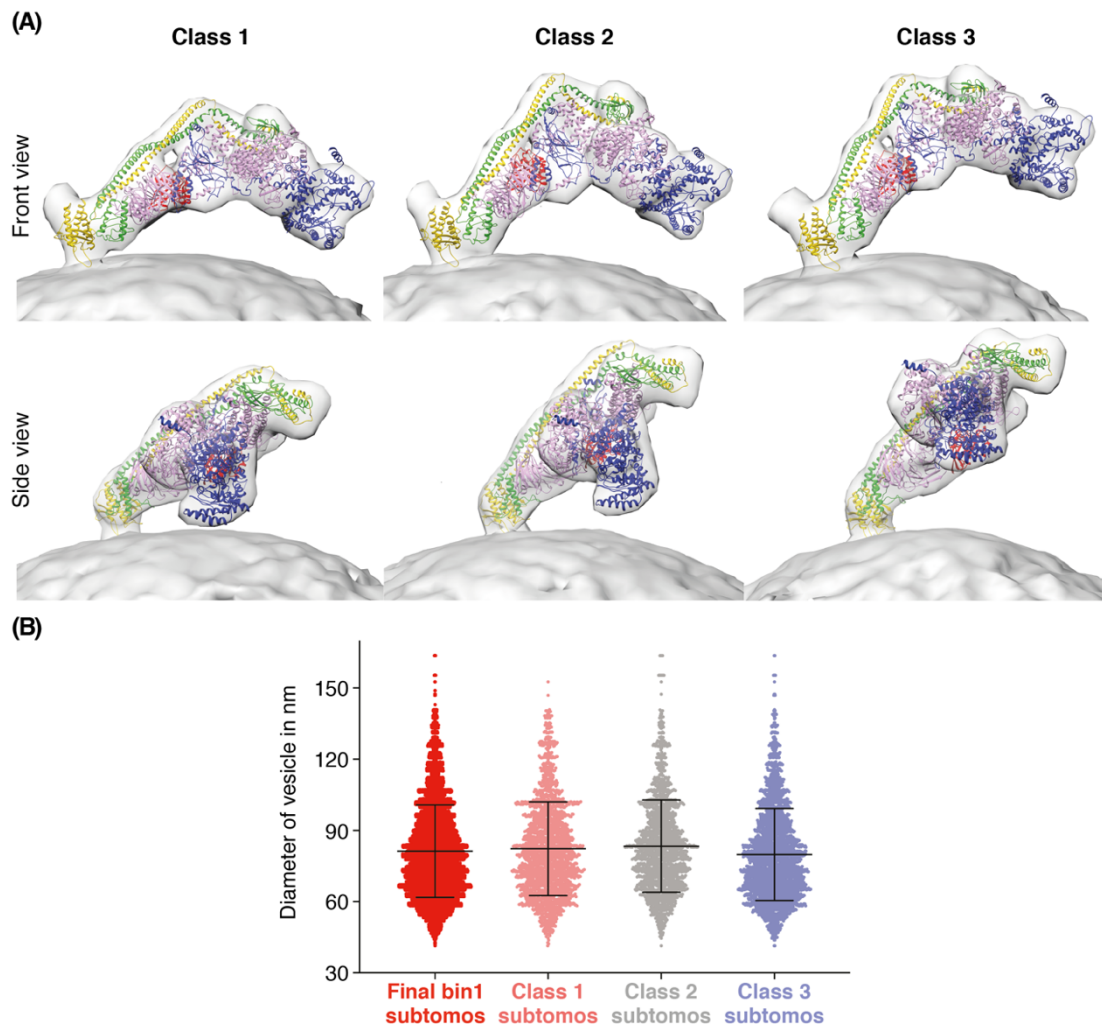


Figure 6-16: Complex II UVRAG Δ C+BATS is highly flexible on membranes

(A) Three different classes from 3D classification of Rab5a-GTP/complex II UVRAG Δ C+BATS show different orientations relative to the membrane. While the adaptor arm stays bound to the membrane and serves as an anchor point, complex II can tilt both up/down as well as sideways. **(B)** Classes 1-3 of the 3D classification have similar mean vesicle diameters, suggesting that different orientations of the complex II with respect to the membrane are not caused by different membrane curvatures.

Complex II undergoes two major movements. Firstly, complex II tilts up and down from the membrane with a wide angular range. Here, the catalytic arm is at various distances to the membrane but does not contact it. Secondly, complex II seems to lean back. It is interesting that this behaviour was independent of vesicle curvature

as the diameter of the three classes varied very little (Figure 6-16B). Consequently, flexibility on the membrane is not linked to membrane curvature.

6.2 Discussion

With the help of cryo-ET and subtomogram averaging, the structure of complex II UVRAG Δ C+BATS on Rab5a decorated membranes has been solved to 9.8 Å (Figure 6–11 and Figure 6–12). Additionally, UAA crosslinking and HDX-MS further substantiated the binding site of Rab5a on complex II (Figure 6–3). Rab5a uses a tripartite binding site made of VPS34 and VPS15. It binds with its switch 2 domain to the helix α -2 of the C2 helical hairpin insertion (C2HH) (Figure 6–17A). Furthermore, VPS15 is contacting two regions in Rab5a that are located adjacent to the switch region. The VPS15 FF domain contacts the Rab5a α -3/-4 helices and VPS15 WD40 domain binds to the Rab5a β -1 beta sheet (Figure 6–17A). In order to understand why the interaction is GTP dependent, the Rab5a-GTP structure (PDB: 1N6H) was replaced with the Rab5a-GDP (PDB: 1TU4) (Figure 6–17B). Rab5a undergoes a dramatic conformational change after GTP hydrolysis (Zhu et al., 2004). The switch 1 loop dislocates \sim 20 Å upon GTP hydrolysis and would clash with the α -2 of the C2HH (Figure 6–17B, red circle). This would create a steric hinderance for complex II to bind to Rab5a-GDP.

The binding site of Rab5 to its effectors such as EEA1 (Figure 6–17C), Rabaptin-5 (Figure 6–17D) and Rabenosyn-5 has been studied in detail by protein crystallography (Eathiraj et al., 2005; Lucas et al., 2014; Mishra et al., 2010; Zhu et al., 2004). In general, Rab effectors can adopt different tertiary structures but often the main binding site can be made of two helices (Mott and Owen, 2015). Complex II adopts a rather unusual interaction, with only one helix of the C2HH involved in the interaction with the Rab5a switch regions and with additional contacts involving non-switch regions (Figure 6–17A). EEA1 also contacts Rab5, using a

single helix, however, this helix is connected to a Zn²⁺ ion coordinated β -hairpin that also interacts with the switch regions (Figure 6–17C).

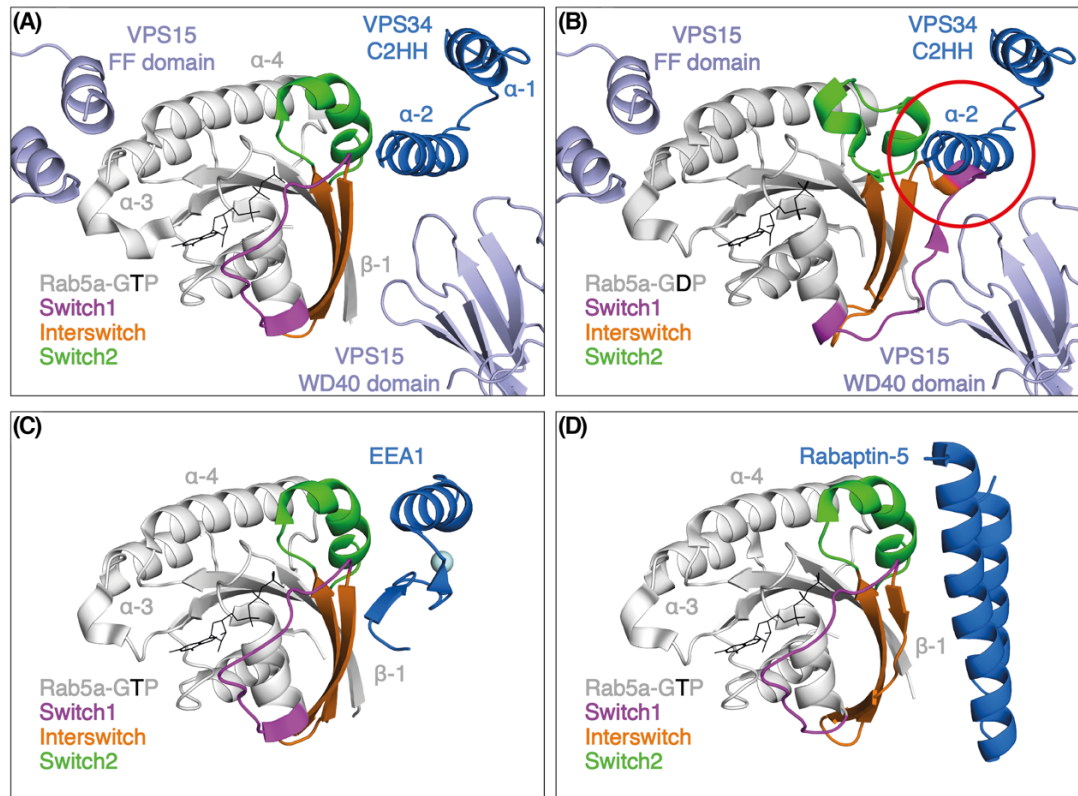


Figure 6–17: Rab5a effector binding surface

(A) Cryo-ET structure of VPS34 and VPS15 bound to Rab5a-GTP. VPS34 C2 helical hairpin insertion (C2HH) binds to the Rab5a switch 2 region. The VPS15 FF domain binds to Rab5a α -3/-4 helices and the VPS15 WD40 domain binds to the β -1 sheet. **(B)** Superimposing the structure of Rab5a-GDP (PDB: 1TU4) on the Rab5a-GTP structure (PDB: 1N6H), shows that the switch 1 loop in the GDP-bound conformation would clash with VPS34 C2HH. **(C)** EEA1 binds to Rab5a with a single helix that is coordinated to a β -hairpin by a Zn²⁺ ion (PDB: 3MJH). **(D)** Rabaptin5 forms a dimeric parallel coiled coil made of two long helices that bind to the Rab5a switches (PDB: 1TU3).

In contrast, Rabaptin-5 uses two helices from a helical pair for Rab5a interaction (Figure 6–17D). The binding of these effectors to Rab5a is restricted to the switch1-interswitch-switch2 surface and the conserved hydrophobic triad motif of Rab GTPases (Phe57, Trp74, and Tyr89) is crucial for these interactions (Lucas et al., 2014). The resolution of the assembly of Rab5a with complex II by cryo-ET is 9.8 Å, which is too low to draw detailed conclusions about the nature of the interactions.

Higher resolution and mutational analysis will be needed to test whether complex II uses similar hydrophobic interactions as other Rab5a effectors.

Studying the interaction of proteins with membranes has been very challenging for structural techniques. Recently, the use of lipid cubic phase X-ray crystallography and nanodisc-mediated cryo-EM have produced essential insights for integral membrane proteins (Caffrey and Cherezov, 2009; Efremov et al., 2017). However, as peripheral membrane proteins only transiently associate with membranes, their interactions are more challenging to capture. In theory, nanodiscs and single particle cryo-EM could be used to study peripheral membrane proteins similarly to how they have been used to study integral membrane proteins. However, to my knowledge, no such study using these techniques for peripheral proteins has been published yet. Nanodiscs can pose several challenges due to heterogeneity in size and percentage of protein occupancy (Matthies et al., 2016). Furthermore, the density of the nanodiscs is often subtracted from the protein density during processing in order to increase resolution. At the same time, the use of liposomes for single particle cryo-EM causes challenges for the processing. Single particle cryo-EM relies on capturing a full range of projections of a single type of particle. However, in one projection image of protein coated liposomes, several particles would be captured bound to the top, bottom and side of the liposome. These layers of protein would be difficult to separate by processing softwares. Although studies have used liposomes to investigate the structures of pore-forming complexes, they typically have used low protein concentrations so that only a single protein is captured in one projection (Pang et al., 2019; Tilley et al., 2005). As a result, these structures are only at ~ 30 Å or less due to the small number of particles and

orientation bias. Instead, cryo-ET and subtomogram averaging have proven to be a powerful tool to study peripheral membrane proteins. The most prominent examples are protein coat structures such as COP, clathrin and retromer (Dodonova et al., 2015; Kovtun et al., 2020, 2018). Due to their rigidity, higher order and high membrane affinity, their resolution has reached $\sim 9\text{-}13$ Å compared to a typical average resolution of ~ 30 Å in subtomogram averaging (Leigh et al., 2019). The VPS34 complexes belong to the family of peripheral membrane proteins that bind to cellular membranes transiently but can be purified as soluble complexes. The VPS34 complexes have proven to be flexible and partially unstructured with a low membrane affinity compared to coat proteins (Stjepanovic et al., 2017). Whereas the COP-I coat was shown to be stable on membranes with a half-life of ~ 28 hours, we expect complex II to adhere to the membrane for milliseconds to seconds (Buckles et al., 2017; Lowe and Kreis, 1996). Nevertheless, we were able to solve the structure of complex II UVRAG Δ C+BATS on Rab5a decorated membranes to 9.8 Å. When examining the structure, it became clear that only the adaptor arm is solidly anchored on the membrane and that the catalytic arm hovers over it. Indeed, other constructs such as wildtype complexes I and II and complex II with Rubicon exhibited the same behaviour (Figure 6–4). The subtomogram averaging progress mirrors the results of the *in vitro* GUV assay as the most active construct seemed to be the most stable structural target. This is because all factors combined, *i.e.*, membrane bound Rab5a-GTP, Beclin 1's membrane binding motifs and the ATG14L ALPS, increased membrane binding and stability.

Complex II shows an incredible flexibility in membrane binding. The 3D classification shows that complex II undergoes dramatic conformational changes while being bound to the membrane. While the adaptor arm stays bound to the

membrane, complex II tilts up and down with a wide angular range (Figure 6–16). Furthermore, complex II also appears to tilt back and forth slightly although not as much as moving up and down. On the other hand, the catalytic arm does not seem to be always in contact with the membrane. It is unclear whether the absence of ATP in the buffer might contribute to this. This movement is independent of vesicle curvature in our setting. However, it should be noted that the vesicle diameter only ranges from 27 to 82 nm, while in cells larger radii or even flat membranes are part of the organelle landscape. The flexibility might be a catalytic mechanism for complex II. As Rab5a binds to the adaptor arm, the catalytic arm is left to move freely. The hypervariable region of Rab5a could theoretically span ~ 110 Å due to its unstructured character, thereby leaving complex II enough slack to move. The production of PI(3)P might be accompanied by complex II tilting up and down and encountering its substrate PI by coincidence. Enzymes that carry out catalysis on lipid substrates can be described as interfacial enzymes. Two extreme forms have been characterised, which have been referred to as “hopping” and “scouting” (Jain et al., 1986; Masson et al., 2015). Enzymes with a hopping mechanism interact with the membrane only transiently and immediately release. Scouting enzymes attach to the membrane and do not dissociate until all of the substrate lipids are exhausted. Scouting behaviour is associated with a faster catalysis rate that is restricted to one compartment, while hopping behaviour enables enzymes to switch between several compartments, but with a diminished rate of catalysis. Typically, PI3Ks are intermediate between these two extremes. The interaction of complex II with membranes suggests that the adaptor arm displays a scouting behaviour, while the catalytic arm has a hopping behaviour.

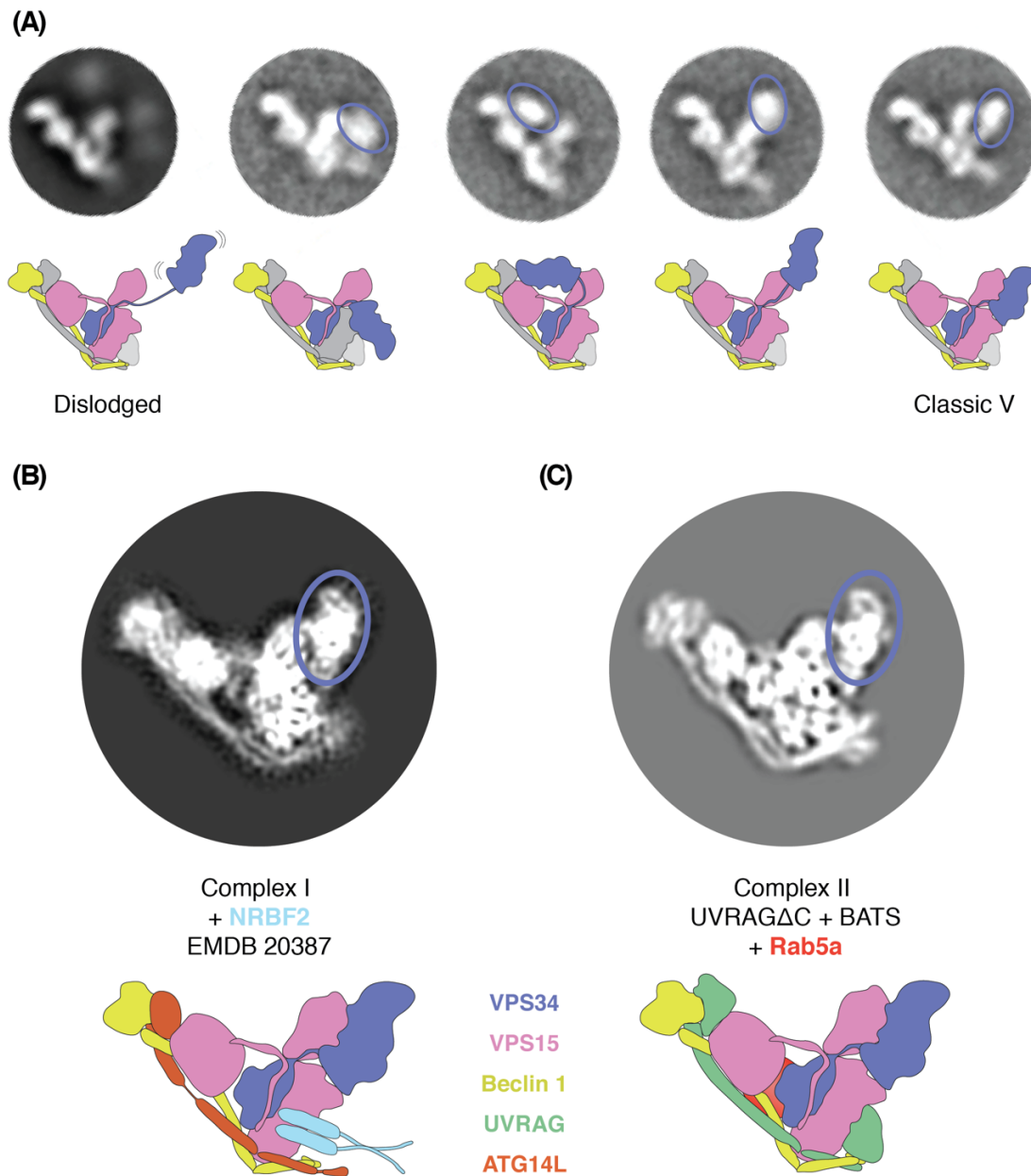


Figure 6-18: VPS34 HELCAT dynamics

(A) Negative stain electron microscopy class averages of VPS34 HELCAT (purple ellipse) in a variety of conformations. In two extreme cases, the HELCAT can be completely dislodged or be in the classic V-shape. Figure adapted from Stjepanovic et al., 2017. **(B)** 6.6 Å cryo-EM structure of human complex I + NRBF2 (EMDB: 20390) (Young et al., 2019). **(C)** 9.8 Å cryo-ET structure of human complex II UVRAG Δ C+BATS + Rab5a. Both (B) and (C) adopt the classic V-shape with VPS34 being in an activated state.

Stjepanovic et al. have described the ability of the VPS34 HELCAT to unlock and adopt several conformations (Figure 6-18A) (Stjepanovic et al., 2017). At one extreme, the HELCAT domain completely dislodges from the complex. At the other extreme, the HELCAT is stabilised by the kinase domain of VPS15 to adopt the

classic V-shape. The importance of the flexibility of the kinase domain was suggested by the inactive construct where the C-terminus of the VPS34 kinase domain tethered to the N-terminal kinase domain of VPS15 (Stjepanovic et al., 2017). As this construct was catalytically dead, it was thought to be necessary for VPS34 to dislodge to be catalytically active. Interestingly, although complex II showed a high degree of flexibility in the cryo-ET, the VPS34 HELACT can be seen in the classic V-shape in all conformations and was not dislodged (Figure 6–16A and B) (Stjepanovic et al., 2017). In fact, the kinase domain in all cryo-ET maps was always captured in its activated state where the VPS34 kinase is not inhibited by the VPS15 kinase domain like in the yeast complex II crystal structure (Figure 6–14A). This indicates that the presence of the membrane or Rab5a stabilised the activated conformation of the VPS34 kinase domain allosterically. Young et al. have also shown recently that complex I can be locked in its activated state in solution with the complex I specific subunit NRBF2 by solving a 6.6 Å cryo-EM structure (Young et al., 2019). The VPS34 HELCAT domain adopts the same activated conformation in both the cryo-ET and cryo-EM structure (Figure 6–18B and C). This might suggest that the kinase does not have to dislodge to be catalytically active and VPS34 complex subunits and the presence of the membrane can activate and stabilise VPS34.

In the cryo-ET map, no density for the BATS domain can be seen (Figure 6–15). However, the BATS domain consists of a 60 residue flexible linker before the 18 residue ALPS motif. Consequently, the ALPS might not be attached in a fixed position relative to the rest of the complex, leading it to disappear in the subtomogram averaging. Still, the Beclin 1 BARA domain can be seen bound to the membrane. As

predicted for hydrophobic interactions in peripheral membrane proteins, the BARA domain only contacts the outer leaflet of the lipid bilayer (Figure 6–15B). As DO (18:1-18:1) lipids with packing defects were used to form vesicles for cryo-ET, the lipid bilayer is likely to be accessible for hydrophobic amino acids to insert into. As the orientation of the Beclin 1 BARA domain towards the membrane can now be modelled, the predicted membrane binding of Beclin 1 can be traced. In Figure 6–19A, the peptides of Beclin 1 protected upon membrane binding in HDX are coloured in dark blue (Figure 4–7). The aromatic fingers 1 and 2 and the hydrophobic loop can be seen positioned near the membrane interface and are shown in red. Chang et al. have proposed that $\beta 1/\beta 2$ become unstructured so that Phe270 and Phe274 can form another membrane interaction site (Chang et al., 2019). The Phe270 and Phe274 identified by Chang et al. sit at the end of the Beclin 1 coiled coil 2 (Chang et al., 2019). Yet, for these residues to contact the membrane, it would require rearrangements of the coiled coil dimer in the region proximal to the membrane. We cannot see any rearrangements in our cryo-ET map that would suggest such a conformation. Instead, the protection observed in the HDX analysis might be caused by the adaptor arm tilting up and down as seen in the 3D classification (Figure 6–19B and C).

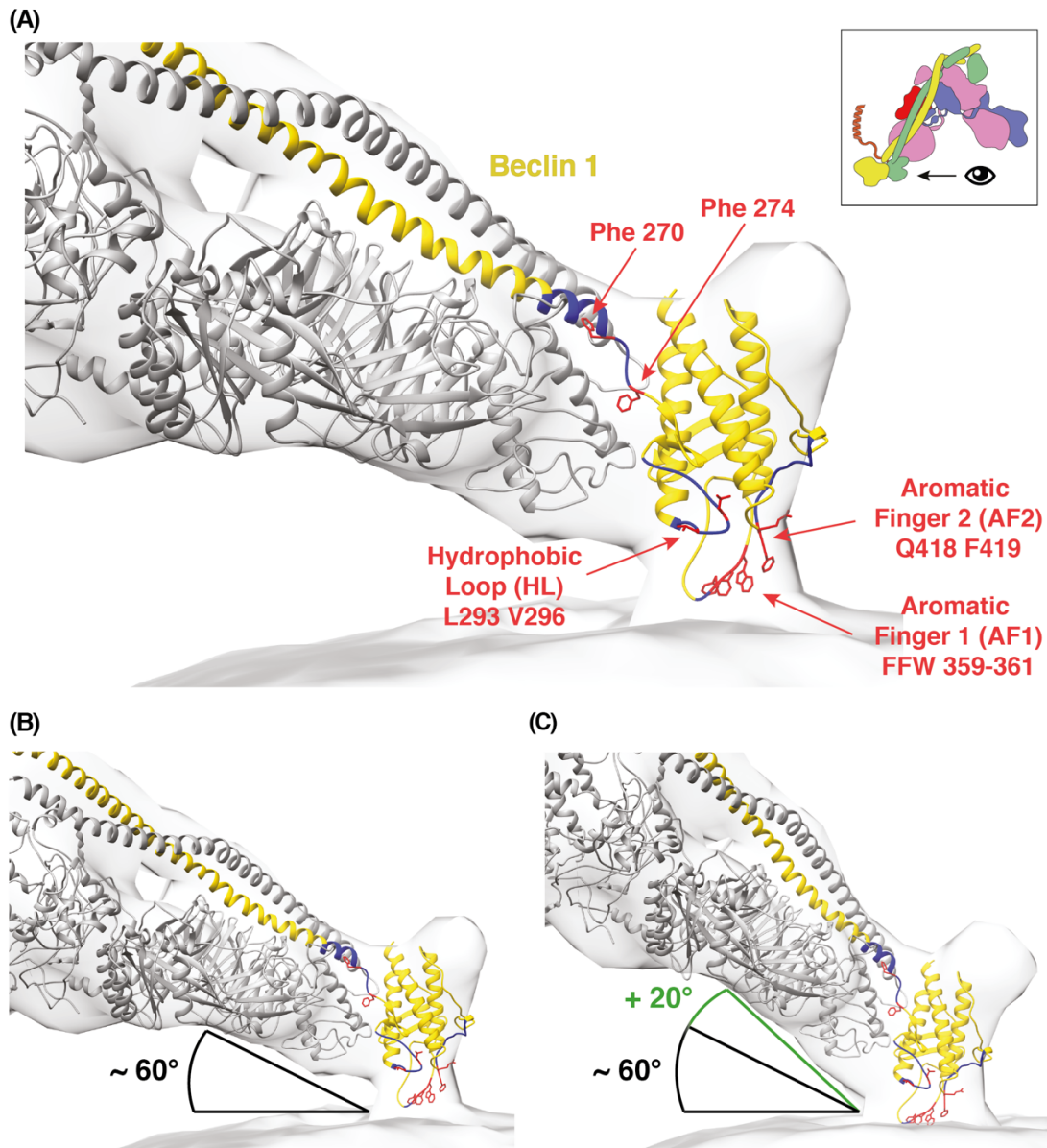


Figure 6-19: Beclin 1 BARA domain membrane contacts

A) Regions showing HDX-MS protection are coloured in blue on the modelled Beclin 1 BARA domain. The Beclin 1 BARA membrane binding motifs are coloured in red. Aromatic finger 1 (AF1) and 2 (AF2) and the hydrophobic loop are facing the membrane. In contrast Phe 270 and 274 are located further away at the tip of the coiled coil dimer. **(B)** and **(C)** show the conformation of the adaptor arm being tilted at different angles with respect to the membrane.

The question remains why Rab5a recognises complex II and to a lesser extent also complex I, but Rab1a interacts exclusively with complex I. If one compares the final cryo-ET reconstructions, it is interesting to compare the occupancies of the mapped Rab5a binding site (Figure 6-4). While complex II UVRAG Δ C+BATS + Rab5a-GTP,

complex II WT + Rab5a-GTP and complex I WT + Rab1a-GTP all show density in this site, complex II + Rubicon without Rab does not. Although complex I WT + Rab1a-GTP is only of low resolution, one could conclude that Rab1a occupies the same binding site as Rab5a. An HDX data set with complex I and Rab1a-GTP has been recently been acquired by Yohei Ohashi to test this proposal. The specificities of Rab1 and Rab5 for the VPS34 complexes can be viewed from two perspectives: how do Rab5 and Rab1 and how do complexes I and II differ from each other. First, the differences between Rab5 and Rab1 will be discussed.

Rab5 and Rab1 belong to the five Rab GTPases (also Rab6, Rab7 and Rab11) that are found in all eukaryotic genomes (Klöpffer et al., 2012). Additionally, Homma et al. found in a knockout study for the entire Rab family that only the isoforms of Rab1 (a and b) and Rab5 (a,b and c) were critical for cell survival (Homma et al., 2019). Rab1 and Rab5 belong to different groups in the Rab family tree. While Rab5 is more closely related to Rab21 and Rab22, Rab1 is related to Rab33 and Rab35 (Klöpffer et al., 2012). In general, it is remarkable how the Rab family members have maintained surface motifs to recognize the common binding partners REP, GDI and RabGGTase II but have acquired sufficient differences during evolution to recognize specific effectors, GEF and GAPs. Most effectors bind to the switch 1-interswitch-switch 2 interface. Other regions such as the Rab-family motifs (RabF1-RabF5) and the conserved residues of the hydrophobic triad have also been shown to be important for Rab specific interactions. The RabF sequences cluster around the switch regions and have been used to specify Rab binding (Pereira-Leal and Seabra, 2000). The hydrophobic triad is also situated at the switch interface and is composed of three conserved aromatic residues (Pylypenko et al., 2017). Figure 6–

20A shows a multiple sequence alignment of Rab5 and Rab1 isoforms. Rab1 and Rab5 do share identical residues (white letters, red background) and residues with similar physicochemical properties (red letters). However, the RabF3 regions and the following 3 amino acids in switch 2 contain some differences. Additionally, the switch 2 helix is structurally different between Rab5a and Rab1a/b (Figure 6-20B). While the Rab5a switch 2 helix stretches for much longer, the Rab1a and b switch 2 helix is interrupted. It should be noted that Rab1b (PDB: 3NKV) contains an unusual post-translational modification in its switch 2 helix at its hydrophobic triad residue Y77. Rab1b is AMPylated by the bacterial Drpa of *Legionella pneumophila* and thereby cannot be retrieved from its membranes by GDIs (Muller et al., 2010). By hijacking these Rab1b coated vesicles, the bacterium evades detection and degradation. The AMPylation is probably the reason why the switch 2 helix is disrupted and why Rab1a and b switch 2 regions differ so much between each other. The Rab5a Met88 in switch 2 has been shown to be involved in direct binding to Rabaptin-5 (Zhu et al., 2004). In contrast, Rab1 contains Ser76 in the same position. Furthermore, the conserved residues of the hydrophobic triad coloured in yellow contain slight changes in the arrangement between Rab5a and Rab1a/b. Small changes in their arrangement have been shown to be crucial for Rab discrimination and the presence of non-conserved residues can influence their orientation (Merithew et al., 2001). Mishra et al. have tried to convert Rab4 to recognise EEA1 by site-directed mutagenesis (Mishra et al., 2010). EEA1 does not normally bind to Rab4. Rab4 mutant variants, where the switch regions were substituted with the Rab5 switch residues responsible for EEA1 binding still could not bind to EEA1 with high affinity. Mutations of additional residues were necessary to confer comparable affinity. This work demonstrates that even if switch residues have the same

sequences, their conformations are also influenced by non-conserved surrounding residues.

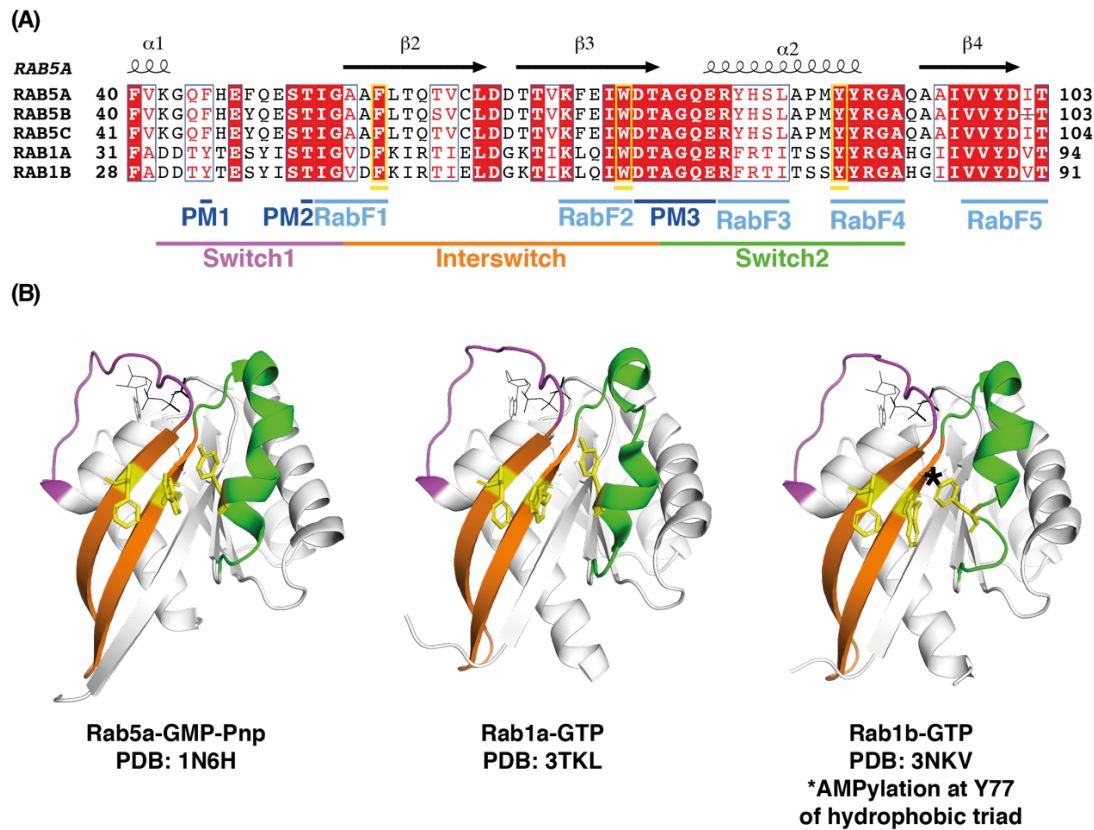


Figure 6–20: Comparison of Rab5 and Rab1 amino acid sequence and tertiary structure
(A) Multiple sequence alignment of Rab1 and Rab5 isoform sequences. The secondary structure elements are shown above the sequences and based on the three-dimensional structure of Rab5a PDB: 1N6H. Strictly identical residues are highlighted in white letters with a red background. Residues with similar physico-chemical properties are shown in red letters. Residues that do not share similar properties and are not conserved are written in black. Alignment positions are framed in blue if the corresponding residues are identical or similar. The conserved residues of the hydrophobic triad are framed in yellow. The switch, RabF (F1-5) and phosphate/magnesium-binding motifs (PM1-PM3) regions are marked below. **(B)** Comparison of the “active” GTP structures of Rab5a (PDB: 1N6H), Rab1a (PDB: 3TKL) and Rab1b, (PDB: 3NKV). Switch 1, interswitch, switch 2 and hydrophobic triad is coloured as above.

Complexes I and II differ in the subunit ATG14L and UVRAG but have VPS34, VPS15 and Beclin 1 in common. The GUV results indicate that ATG14L and UVRAG differently regulate Beclin 1 binding to the membrane (Figure 4–8). Consequently, the unique subunits can cause specific structural differences, even in the

conformations of the shared subunits of the complex. To date, there is no high resolution structure of either human complexes I or II. The only human structures solved so far are a 6.8 Å cryo-EM structure of human complex II + a Rubicon fragment (VPS34 kinase domain not resolved, Chang et al., 2019), and a 6.6 Å cryo-EM structure of human complex I + a NRBF2 fragment (Young et al., 2019). These two and our cryo-ET structure of human complex II UVRAG Δ C+BATS + Rab5a can be seen side by side in Figure 6–21A. The adaptor arms of all three complexes have a similar architecture to each other. The biggest difference is the C2 domain in UVRAG/complex II, which is absent in ATG14L/complex I. However, NRBF2 binds to a similar region on complex I. Remarkably, although the helices α -1 and α -2 of the C2HH are connected by unstructured loops to the C2 domain, they adopt an identical conformation in all three structures (Figure 6–21A). The two helices cross each other with helix α -2 being in contact with the VPS15 WD40 domain (Figure 6–21). If one compares the position of these helices carefully, it becomes evident that there is a slight shift in the complex I + NRBF2 fragment map compared with complex II UVRAG Δ C+BATS + Rab5a and with complex II + Rubicon fragment. The orientation of the Beclin 1/UVRAG or Beclin 1/ATG14L coiled coil and WD40 differ from each other. While the Beclin 1/UVRAG coiled coil seems rather straight, the Beclin 1/ATG14L coiled coil is angled towards away from the body of the complex thereby moving the WD40 domain away from the C2HH (figure 5-20B). Since the C2HH and the WD40 domain are two elements of the binding site for Rab5a, this could explain the preferential activation of complex II over complex I. With the WD40 domain angled away in complex I, this may interfere with Rab5a binding.

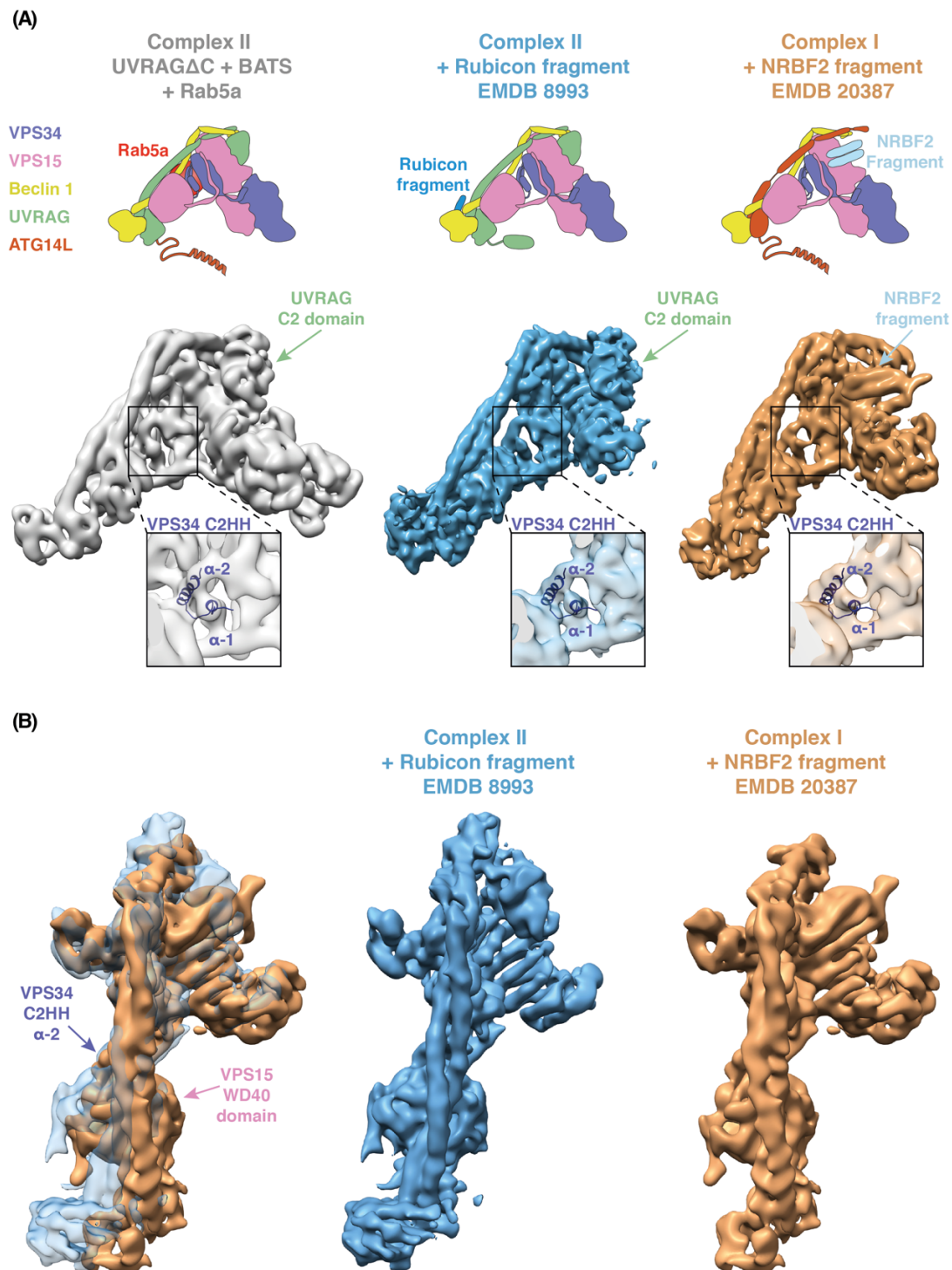


Figure 6-21: Comparison of complexes I and II architecture

(A) The only structures solved so far of the human VPS34 complexes are: 9.8 Å cryo-ET structure of human complex II UVRAGΔC+BATS + Rab5a, a 6.8 Å cryo-EM structure of human complex II + Rubicon fragment (EMDB 899), and a 6.6Å cryo-EM structure of human complex I + NRBF2 fragment (EMDB 20387). The C2HH adopts a slightly different conformation in complex I than in complex II. (B) Structural comparison between complex II + Rubicon fragment (middle) and complex I + NRBF2 fragment (right). On the left, is shown an optimal superposition of the two structures, using Chimera. The Beclin 1/UVRAG and Beclin 1/ATG14L coiled coils are oriented differently in complexes II and I. In complex I, the coiled coil is angled to the left and thereby shifts the position of the VPS15 WD40 domain.

Furthermore, the C2HH has a different orientation, so that it might be able to make different interactions with Rab1a, thereby making it an exclusive complex I binder. Future experiments will require detailed mutational analysis in complexes I and II as well as Rab1a and Rab5a in order to verify these interactions. In conclusion, it is remarkable that VPS34 and VPS15, which are common to both complexes I and II, coordinate the differential Rab binding. This shared interface seems to be altered uniquely for each complex depending whether Beclin 1 forms a coiled coil with UVRAG in complex II or ATG14L in complex I.

7 Conclusion

The production of PI(3)P is essential for two major processes in the cell: Autophagy and endocytic trafficking. While the role of complex I in the initiation of autophagy has gained much attention, the influence of complex II in the endocytic pathway is poorly understood. Furthermore, the question of how these two complexes are specifically recruited to each compartment is still unclear. During the course of my PhD, I have used a GUV PI3K assay, mass spectrometry and cryo-electron tomography to shed light on the differential regulation of VPS34 complexes I and II. Figure 7-1 summarises the key findings and depicts them in a cellular context.

Firstly, complex I has persistently demonstrated an increased kinase activity on various membrane types compared to complex II. This enhanced rate of PI(3)P production can be ascribed to the membrane-binding ALPS helix in ATG14L as without it, complex I is not catalytically active. In contrast, UVRAG in complex II does not possess a membrane-binding domain. Instead, complex II heavily relies on aromatic residues in three loops of the Beclin 1 BARA domain. The most important one is the aromatic finger 1 but also aromatic finger 2 and the hydrophobic loop contribute to complex II activity. Conversely, complex I activity is only slightly dependent on the aromatic finger 1 and unperturbed by losing the aromatic finger 2 and the hydrophobic loop. A shared property of both complexes I and II is their preference for membranes with high packing defects, *i.e.*, higher curvature and unsaturated lipids. These defects are gaps in the membrane surface into which hydrophobic amino acid chains of the Beclin 1 BARA domain and ALPS motif can insert. The GUV PI3K assay also demonstrated that although complexes I and II and VPS34 all show an increase in PI(3)P production due to PS, complex II is

Conclusion

preferentially activated. PS is found in the cytosolic leaflet of the plasma membrane, which gives rise to endocytic vesicles and early endosomes. On the other hand, complexes I and II can also both be activated by PI(4)P, which is found on early endosomes, but only complex I displayed a preference for PI(4,5)P₂, which is found at early autophagic structures.

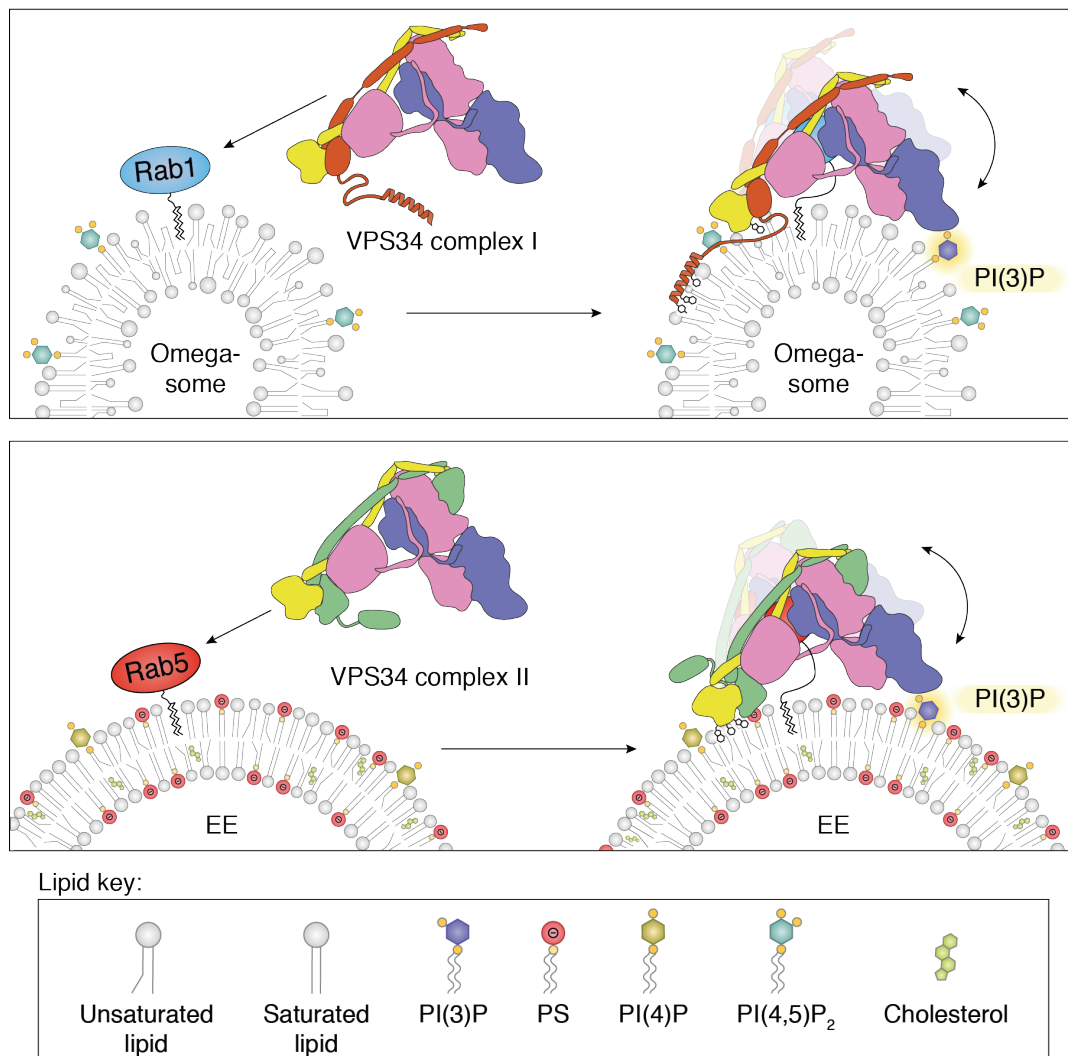


Figure 7-1: Differential membrane recruitment of VPS34 complexes I and II to omegasomes and early endosomes

In conclusion, the activity of complexes I and II are highly dependent on the membrane composition and its physicochemical properties. However, even under

these conditions, complex I still displays a higher activity than complex II. It had been proposed that the ATG14L ALPS motif is in charge of recruiting complex I specifically to the ER membrane, and it is true that the ALPS motif is a strong membrane binder and likely senses lipid packing defects. However, this still does not explain why complex I is specifically targeted to the ER membrane. Additionally, no intrinsic membrane recruitment signal specific for complex II had been described yet.

My discovery during my PhD studies that organelle specific Rab GTPases strongly activate and recruit different VPS34 complexes helps fill this knowledge gap. Once complex II is recruited to Rab5 positive membranes, it is activated by 35-fold and thus displays a higher activity than complex I for the first time. In contrast, complex I is only mildly activated by Rab5. Instead, Rab1 turned out to be a strong complex I-specific activator. Although complex I displayed only a 12-fold activation by Rab1, it might actually be higher without the inactivating effects of the maleimide lipids. Additionally, Rab7 was shown to activate by 50-fold complex II only if Rubicon was present. As the recruitment of Rab GTPases to specific compartments is tightly regulated, this class of proteins is ideal for directing VPS34 complexes in a spatiotemporal manner.

Rab5 is one of the most well studied Rab GTPases and is crucial for the fusion of early endosomes and the maturation of early to late endosomes. Although it was suggested already in 1999 that Rab5 interacts with VPS15, no further studies have investigated whether this interaction is specific for complex I or for complex II. Finally, I can confirm that complex II is specifically recruited by Rab5 to early endosomes to produce PI(3)P, which in turn attracts further endocytic proteins like EEA1 to coordinate the homotypic fusion of early endosomes.

Rab1 is known to regulate protein trafficking in the secretory pathway by mediating anterograde transport but its role in autophagy has only been recently appreciated. It was shown to be involved in the early stages of autophagy and responsible for recruiting the ULK1 complex for autophagy initiation. As the production of PI(3)P is an essential step for the formation of autophagy, I suggest Rab1 not only recruits ULK1 but also complex I. The recruitment of both ULK1 and complex I to the same membrane would bring them in proximity and give ULK1 the opportunity to phosphorylate VPS34, ATG14L and Beclin 1 for further activation. The generated PI(3)P then recruits further autophagic protein like WIPIs and DFCP1 for phagophore maturation.

With the help of HDX-MS, UAA crosslinking and cryo-ET, I could map Rab5 binding to a tripartite binding motif made of VPS15 and VPS34 on the adaptor arm of complex II. Furthermore, preliminary cryo-ET data suggests that Rab1 binds to the same area in complex I. Moreover, subtomogram averaging shows that only the adaptor arm is permanently bound to the membrane, while the catalytic arm hovers over it. However, while the adaptor arm stays bound to the membrane, the catalytic arm undergoes dramatic conformational changes by tilting up and down with a wide angular range. This flexibility could be a general catalytic mechanism for VPS34 complexes as most additional subunits have been mapped to bind somewhere on the adaptor arm. Thus, the binding of either Rab5 or Rab1 to VPS34 and VPS15 is unique for each complex as it depends whether Beclin 1 forms a coiled coil with UVRAG in complex II or with ATG14L in complex I. This mechanism could also be observed in the differential membrane contact of the Beclin 1 BARA domain in complexes I and II. By recruiting the adaptor arm to the membrane, the catalytic arm is given free rein to tilt and constantly find new substrate in the membrane.

Conclusion

Accordingly, the VPS34 kinase domain was found to be in an activated state on the membrane compared to the yeast crystal structure. Although the VPS15 kinase domain active site releases its inhibitory contact with the VPS34 kinase domain, the VPS34 HELCAT unit was found not to be dislodged in any of the membrane bound 3D classes. Thus, the HELCAT might not have to dislodge to encounter the membrane as had been previously suggested, but instead the whole complex could use the tilting motion to encounter new substrate for VPS34.

Overall my study has shed light on the activation mechanisms of VPS34 complexes *in vitro* for the first time. Since defects in autophagy and endocytic pathways are known to be connected with various types of human diseases, my findings may provide useful insights into developing effective drugs.

8 References

- Alam A, Kowal J, Broude E, Roninson I, Locher KP. 2019. Structural insight into substrate and inhibitor discrimination by human P-glycoprotein. *Sci New York N Y* **363**:753–756. doi:10.1126/science.aav7102
- Angelova MI, Dimitrov DS. 1986. Liposome electroformation. *Faraday Discuss Chem Soc* **81**:303. doi:10.1039/dc9868100303
- Antonny B. 2011. Mechanisms of membrane curvature sensing. *Annu Rev Biochem* **80**:101–23. doi:10.1146/annurev-biochem-052809-155121
- Aoyagi K, Sugaya T, Umeda M, Yamamoto S, Terakawa S, Takahashi M. 2005. The Activation of Exocytotic Sites by the Formation of Phosphatidylinositol 4,5-Bisphosphate Microdomains at Syntaxin Clusters. *J Biol Chem* **280**:17346–17352. doi:10.1074/jbc.m413307200
- Axe EL, Walker SA, Manifava M, Chandra P, Roderick HL, Habermann A, Griffiths G, Ktistakis NT. 2008. Autophagosome formation from membrane compartments enriched in phosphatidylinositol 3-phosphate and dynamically connected to the endoplasmic reticulum. *J Cell Biology* **182**:685–701. doi:10.1083/jcb.200803137
- Backer JM. 2016. The intricate regulation and complex functions of the Class III phosphoinositide 3-kinase Vps34. *Biochem J* **473**:2251–2271. doi:10.1042/bcj20160170
- Backer JM. 2008. The regulation and function of Class III PI3Ks: novel roles for Vps34. *Biochem J* **410**:1–17. doi:10.1042/bj20071427
- Balderhaar HJ kleine, Lachmann J, Yavavli E, Bröcker C, Lürick A, Ungermann C. 2013. The CORVET complex promotes tethering and fusion of Rab5/Vps21-positive membranes. *Proc National Acad Sci* **110**:3823–3828. doi:10.1073/pnas.1221785110
- Balderhaar HJ kleine, Ungermann C. 2013. CORVET and HOPS tethering complexes – coordinators of endosome and lysosome fusion. *J Cell Sci* **126**:1307–1316. doi:10.1242/jcs.107805
- Ballabio A, Bonifacino JS. 2019. Lysosomes as dynamic regulators of cell and organismal homeostasis. *Nat Rev Mol Cell Bio* **21**:101–118. doi:10.1038/s41580-019-0185-4

References

- Bartesaghi A, Sprechmann P, Liu J, Randall G, Sapiro G, Subramaniam S. 2008. Classification and 3D averaging with missing wedge correction in biological electron tomography. *J Struct Biol* **162**:436–50. doi:10.1016/j.jsb.2008.02.008
- Barr F, Lambright DG. 2010. Rab GEFs and GAPs. *Curr Opin Cell Biol* **22**:461–70. doi:10.1016/j.ceb.2010.04.007
- Behrends C, Sowa ME, Gygi SP, Harper JW. 2010. Network organization of the human autophagy system. *Nature* **466**:68–76. doi:10.1038/nature09204
- Bergbrede T, Pylypenko O, Rak A, Alexandrov K. 2005. Structure of the extremely slow GTPase Rab6A in the GTP bound form at 1.8Å resolution. *J Struct Biol* **152**:235–238. doi:10.1016/j.jsb.2005.10.001
- Biasini M, Bienert S, Waterhouse A, Arnold K, Studer G, Schmidt T, Kiefer F, Cassarino TG, Bertoni M, Bordoli L, Schwede T. 2014. SWISS-MODEL: modelling protein tertiary and quaternary structure using evolutionary information. *Nucleic Acids Res* **42**:W252-8. doi:10.1093/nar/gku340
- Bigay J, Casella J-F, Drin G, Mesmin B, Antonny B. 2005. ArfGAP1 responds to membrane curvature through the folding of a lipid packing sensor motif. *Embo J* **24**:2244–2253. doi:10.1038/sj.emboj.7600714
- Bigay J, Antonny B. 2012. Curvature, Lipid Packing, and Electrostatics of Membrane Organelles: Defining Cellular Territories in Determining Specificity. *Dev Cell* **23**:886–895. doi:10.1016/j.devcel.2012.10.009
- Bilanges B, Posor Y, Vanhaesebroeck B. 2019. PI3K isoforms in cell signalling and vesicle trafficking. *Nat Rev Mol Cell Biology* **20**:515–534. doi:10.1038/s41580-019-0129-z
- Bjørkøy G, Lamark T, Brech A, Outzen H, Perander M, Øvervatn A, Stenmark H, Johansen T. 2005. p62/SQSTM1 forms protein aggregates degraded by autophagy and has a protective effect on huntingtin-induced cell death. *J Cell Biology* **171**:603–614. doi:10.1083/jcb.200507002
- Blomen VA, Májek P, Jae LT, Bigenzahn JW, Nieuwenhuis J, Staring J, Sacco R, Diemen FR van, Olk N, Stukalov A, Marceau C, Janssen H, Carette JE, Bennett KL, Colinge J, Superti-Furga G, Brummelkamp TR. 2015. Gene essentiality and synthetic lethality in haploid human cells. *Sci New York N Y* **350**:1092–6. doi:10.1126/science.aac7557
- Bogdanov M, Mileykovskaya E, Dowhan W. 2008. Lipids in the assembly of membrane proteins and organization of protein supercomplexes: implications for lipid-linked disorders. *Sub-cell Biochem* **49**:197–239. doi:10.1007/978-1-4020-8831-5_8
- Bonifacino JS, Rojas R. 2006. Retrograde transport from endosomes to the trans-Golgi network. *Nat Rev Mol Cell Bio* **7**:568–579. doi:10.1038/nrm1985

References

- Brier LW, Ge L, Stjepanovic G, Thelen AM, Hurley JH, Schekman R. 2019. Regulation of LC3 lipidation by the autophagy-specific class III phosphatidylinositol-3 kinase complex. *Mol Biol Cell* **30**:1098–1107. doi:10.1091/mbc.e18-11-0743
- Bucci C, Parton RG, Mather IH, Stunnenberg H, Simons K, Hoflack B, Zerial M. 1992. The small GTPase rab5 functions as a regulatory factor in the early endocytic pathway. *Cell* **70**:715–728. doi:10.1016/0092-8674(92)90306-w
- Buckles TC, Ziemba BP, Masson GR, Williams RL, Falke JJ. 2017. Single-Molecule Study Reveals How Receptor and Ras Synergistically Activate PI3K α and PIP3 Signaling. *Biophys J* **113**:2396–2405. doi:10.1016/j.bpj.2017.09.018
- Burke JE. 2018. Structural Basis for Regulation of Phosphoinositide Kinases and Their Involvement in Human Disease. *Mol Cell* **71**:653–673. doi:10.1016/j.molcel.2018.08.005
- Burke JE, Perisic O, Masson GR, Vadas O, Williams RL. 2012. Oncogenic mutations mimic and enhance dynamic events in the natural activation of phosphoinositide 3-kinase p110 (PIK3CA). *Proc National Acad Sci* **109**:15259–15264. doi:10.1073/pnas.1205508109
- Burke JE, Williams RL. 2015. Synergy in activating class I PI3Ks. *Trends Biochem Sci* **40**:88–100. doi:10.1016/j.tibs.2014.12.003
- Cabrera M, Ungermann C. 2010. Guiding endosomal maturation. *Cell* **141**:404–6. doi:10.1016/j.cell.2010.04.013
- Cabrera M, Nordmann M, Perz A, Schmedt D, Gerondopoulos A, Barr F, Piehler J, Engelbrecht-Vandré S, Ungermann C. 2014. The Mon1-Ccz1 GEF activates the Rab7 GTPase Ypt7 via a longin-fold-Rab interface and association with PI3P-positive membranes. *J Cell Sci* **127**:1043–51. doi:10.1242/jcs.140921
- Caffrey M, Cherezov V. 2009. Crystallizing membrane proteins using lipidic mesophases. *Nat Protoc* **4**:706–31. doi:10.1038/nprot.2009.31
- Casares D, Escribá PV, Rosselló CA. 2019. Membrane Lipid Composition: Effect on Membrane and Organelle Structure, Function and Compartmentalization and Therapeutic Avenues. *Int J Mol Sci* **20**:2167. doi:10.3390/ijms20092167
- Chan EYW, Longatti A, McKnight NC, Tooze SA. 2008. Kinase-inactivated ULK proteins inhibit autophagy via their conserved C-terminal domains using an Atg13-independent mechanism. *Mol Cell Biol* **29**:157–71. doi:10.1128/mcb.01082-08
- Chang C, Young LN, Morris KL, Bülow S von, Schöneberg J, Yamamoto-Imoto H, Oe Y, Yamamoto K, Nakamura S, Stjepanovic G, Hummer G, Yoshimori T, Hurley JH. 2019. Bidirectional Control of Autophagy by BECN1 BARA Domain Dynamics. *Mol Cell* **73**:339-353.e6. doi:10.1016/j.molcel.2018.10.035

References

- Chavrier P, Gorvel J-P, Stelzer E, Simons K, Gruenberg J, Zerial M. 1991. Hypervariable C-terminal domain of rab proteins acts as a targeting signal. *Nature* **353**:769–772. doi:10.1038/353769a0
- Chen C, Huang Q, Jiang S, Pan X, Hua Z. 2006. Immobilized protein ZZ, an affinity tool for immunoglobulin isolation and immunological experimentation. *Biotechnol Appl Bioc* **45**:87–92. doi:10.1042/ba20060055
- Cheng Y, Grigorieff N, Penczek PA, Walz T. 2015. A primer to single-particle cryo-electron microscopy. *Cell* **161**:438–49. doi:10.1016/j.cell.2015.03.050
- Christoforidis S, Miaczynska M, Ashman K, Wilm M, Zhao L, Yip S-C, Waterfield MD, Backer JM, Zerial M. 1999. Phosphatidylinositol-3-OH kinases are Rab5 effectors. *Nat Cell Biol* **1**:249–252. doi:10.1038/12075
- Chowdhury S, Otomo C, Leitner A, Ohashi K, Aebersold R, Lander GC, Otomo T. 2018. Insights into autophagosome biogenesis from structural and biochemical analyses of the ATG2A-WIP1 complex. *Proc National Acad Sci* **115**:E9792–E9801. doi:10.1073/pnas.1811874115
- Cigler M, Müller TG, Horn-Ghetko D, Wrisberg M von, Fottner M, Goody RS, Itzen A, Müller MP, Lang K. 2017. Proximity-Triggered Covalent Stabilization of Low-Affinity Protein Complexes In Vitro and In Vivo. *Angewandte Chemie Int Ed* **56**:15737–15741. doi:10.1002/anie.201706927
- Colicelli J. 2004. Human RAS Superfamily Proteins and Related GTPases. *Sci Signal* **2004**:re13–re13. doi:10.1126/stke.2502004re13
- Craene J-OD, Bertazzi D, Bär S, Friant S. 2017. Phosphoinositides, Major Actors in Membrane Trafficking and Lipid Signaling Pathways. *Int J Mol Sci* **18**:634. doi:10.3390/ijms18030634
- Cullen PJ, Steinberg F. 2018. To degrade or not to degrade: mechanisms and significance of endocytic recycling. *Nat Rev Mol Cell Bio* **19**:679–696. doi:10.1038/s41580-018-0053-7
- Dierksen K, Typke D, Hegerl R, Koster AJ, Baumeister W. 1992. Towards automatic electron tomography. *Ultramicroscopy* **40**:71–87. doi:10.1016/0304-3991(92)90235-c
- Dikic I, Elazar Z. 2018. Mechanism and medical implications of mammalian autophagy. *Nat Rev Mol Cell Bio* **19**:349–364. doi:10.1038/s41580-018-0003-4
- Dodonova SO, Diestelkoetter-Bachert P, Appen A von, Hagen WJH, Beck R, Beck M, Wieland F, Briggs JAG. 2015. VESICULAR TRANSPORT. A structure of the COPI coat and the role of coat proteins in membrane vesicle assembly. *Sci New York N Y* **349**:195–8. doi:10.1126/science.aab1121

- Dooley HC, Razi M, Polson HEJ, Girardin SE, Wilson MI, Tooze SA. 2014. WIP12 links LC3 conjugation with PI3P, autophagosome formation, and pathogen clearance by recruiting Atg12-5-16L1. *Mol Cell* **55**:238–52. doi:10.1016/j.molcel.2014.05.021
- Drin G, Antonny B. 2009. Amphipathic helices and membrane curvature. *Febs Lett* **584**:1840–7. doi:10.1016/j.febslet.2009.10.022
- Drin G, Casella J-F, Gautier R, Boehmer T, Schwartz TU, Antonny B. 2007. A general amphipathic α -helical motif for sensing membrane curvature. *Nat Struct Mol Biol* **14**:138–146. doi:10.1038/nsmb1194
- Dubochet J, Adrian M, Chang J-J, Homo J-C, Lepault J, McDowell AW, Schultz P. 1988. Cryo-electron microscopy of vitrified specimens. *Q Rev Biophys* **21**:129–228. doi:10.1017/s0033583500004297
- Eathiraj S, Pan X, Ritacco C, Lambright DG. 2005. Structural basis of family-wide Rab GTPase recognition by rabenosyn-5. *Nature* **436**:415–419. doi:10.1038/nature03798
- Efremov RG, Gatsogiannis C, Raunser S. 2017. Methods in Enzymology. *Methods Enzymol* **594**:1–30. doi:10.1016/bs.mie.2017.05.007
- Egan DF, Chun MGH, Vamos M, Zou H, Rong J, Miller CJ, Lou HJ, Raveendra-Panickar D, Yang C-C, Sheffler DJ, Teriete P, Asara JM, Turk BE, Cosford NDP, Shaw RJ. 2015. Small Molecule Inhibition of the Autophagy Kinase ULK1 and Identification of ULK1 Substrates. *Mol Cell* **59**:285–97. doi:10.1016/j.molcel.2015.05.031
- Ellson CD, Gobert-Gosse S, Anderson KE, Davidson K, Erdjument-Bromage H, Tempst P, Thuring JW, Cooper MA, Lim Z-Y, Holmes AB, Gaffney PRJ, Coadwell J, Chilvers ER, Hawkins PT, Stephens LR. 2001. PtdIns(3)P regulates the neutrophil oxidase complex by binding to the PX domain of p40phox. *Nat Cell Biol* **3**:679–682. doi:10.1038/35083076
- Emsley P, Cowtan K. 2004. Coot : model-building tools for molecular graphics. *Acta Crystallogr Sect D Biological Crystallogr* **60**:2126–2132. doi:10.1107/s0907444904019158
- Engelman JA, Luo J, Cantley LC. 2006. The evolution of phosphatidylinositol 3-kinases as regulators of growth and metabolism. *Nat Rev Genet* **7**:606–619. doi:10.1038/nrg1879
- Engen JR, Wales TE. 2015. Analytical Aspects of Hydrogen Exchange Mass Spectrometry. *Annu Rev Anal Chem Palo Alto Calif* **8**:127–48. doi:10.1146/annurev-anchem-062011-143113
- Englander SW, Downer NW, Teitelbaum H. 1972. Hydrogen Exchange. *Annu Rev Biochem* **41**:903–924. doi:10.1146/annurev.bi.41.070172.004351

References

- Englander SW, Sosnick TR, Englander JJ, Mayne L. 1996. Mechanisms and uses of hydrogen exchange. *Curr Opin Struc Biol* **6**:18–23. doi:10.1016/s0959-440x(96)80090-x
- Erickson HP, Klug A. 1971. Measurement and compensation of defocusing and aberrations by Fourier processing of electron micrographs. *Philosophical Transactions Royal Soc Lond B Biological Sci* **261**:105–118. doi:10.1098/rstb.1971.0040
- Fan W, Nassiri A, Zhong Q. 2011. Autophagosome targeting and membrane curvature sensing by Barkor/Atg14(L). *Proc National Acad Sci* **108**:7769–7774. doi:10.1073/pnas.1016472108
- Farre J-C, Mathewson RD, Manjithaya R, Subramani S. 2010. Roles of *Pichia pastoris* Uvrag in vacuolar protein sorting and the phosphatidylinositol 3-kinase complex in phagophore elongation in autophagy pathways. *Autophagy* **6**:86–99. doi:10.4161/auto.6.1.10535
- Fioramonte M, Gozzo FC, Oliveira CLP de, Portugal RV, Heel M van. 2017. Introduction to Biomolecular Structure and Biophysics 245–274. doi:10.1007/978-981-10-4968-2_9
- Fomenko DE, Gladyshev VN. 2003. Identity and Functions of CxxC-Derived Motifs †. *Biochemistry-us* **42**:11214–11225. doi:10.1021/bi034459s
- Förster F, Medalia O, Zauberman N, Baumeister W, Fass D. 2005. Retrovirus envelope protein complex structure in situ studied by cryo-electron tomography. *Proc National Acad Sci* **102**:4729–4734. doi:10.1073/pnas.0409178102
- Förster F, Pruggnaller S, Seybert A, Frangakis AS. 2008. Classification of cryo-electron sub-tomograms using constrained correlation. *J Struct Biol* **161**:276–286. doi:10.1016/j.jsb.2007.07.006
- Galaz-Montoya JG, Ludtke SJ. 2017. The advent of structural biology in situ by single particle cryo-electron tomography. *Biophysics Reports* **3**:17–35. doi:10.1007/s41048-017-0040-0
- Gillingham AK, Sinka R, Torres IL, Lilley KS, Munro S. 2014. Toward a comprehensive map of the effectors of rab GTPases. *Dev Cell* **31**:358–73. doi:10.1016/j.devcel.2014.10.007
- Gillingham AK, Bertram J, Begum F, Munro S. 2019. In vivo identification of GTPase interactors by mitochondrial relocalization and proximity biotinylation. *Elife* **8**:e45916. doi:10.7554/elife.45916
- Gillooly DJ, Raiborg C, Stenmark H. 2003. Phosphatidylinositol 3-phosphate is found in microdomains of early endosomes. *Histochem Cell Biol* **120**:445–453. doi:10.1007/s00418-003-0591-7

- Glaeser RM. 2008. Retrospective: radiation damage and its associated “information limitations”. *J Struct Biol* **163**:271–6. doi:10.1016/j.jsb.2008.06.001
- Goddard TD, Huang CC, Ferrin TE. 2007. Visualizing density maps with UCSF Chimera. *J Struct Biol* **157**:281–287. doi:10.1016/j.jsb.2006.06.010
- Goody RS, Müller MP, Wu Y-W. 2017. Mechanisms of action of Rab proteins, key regulators of intracellular vesicular transport. *Biol Chem* **398**:565–575. doi:10.1515/hsz-2016-0274
- Grant T, Grigorieff N. 2015. Measuring the optimal exposure for single particle cryo-EM using a 2.6 Å reconstruction of rotavirus VP6. *Elife* **4**:e06980. doi:10.7554/elife.06980
- Hagen WJH, Wan W, Briggs JAG. 2016. Implementation of a cryo-electron tomography tilt-scheme optimized for high resolution subtomogram averaging. *J Struct Biol* **197**:191–198. doi:10.1016/j.jsb.2016.06.007
- Hailey DW, Rambold AS, Satpute-Krishnan P, Mitra K, Sougrat R, Kim PK, Lippincott-Schwartz J. 2010. Mitochondria supply membranes for autophagosome biogenesis during starvation. *Cell* **141**:656–67. doi:10.1016/j.cell.2010.04.009
- Hamasaki M, Furuta N, Matsuda A, Nezu A, Yamamoto A, Fujita N, Oomori H, Noda T, Haraguchi T, Hiraoka Y, Amano A, Yoshimori T. 2013. Autophagosomes form at ER-mitochondria contact sites. *Nature* **495**:389–393. doi:10.1038/nature11910
- Hamuro Y, Coales SJ, Southern MR, Nemeth-Cawley JF, Stranz DD, Griffin PR. 2003. Rapid analysis of protein structure and dynamics by hydrogen/deuterium exchange mass spectrometry. *J Biomol Techniques Jbt* **14**:171–82.
- Hara T, Takamura A, Kishi C, Iemura S-I, Natsume T, Guan J-L, Mizushima N. 2008. FIP200, a ULK-interacting protein, is required for autophagosome formation in mammalian cells. *J Cell Biology* **181**:497–510. doi:10.1083/jcb.200712064
- Hart RG. 1968. Electron Microscopy of Unstained Biological Material: The Polytropic Montage. *Science* **159**:1464–1467. doi:10.1126/science.159.3822.1464
- He S, Ni D, Ma B, Lee J-H, Zhang T, Ghosalli I, Pirooz SD, Zhao Z, Bharatham N, Li B, Oh S, Lee W-H, Takahashi Y, Wang H-G, Minassian A, Feng P, Deretic V, Pepperkok R, Tagaya M, Yoon HS, Liang C. 2013. PtdIns(3)P-bound UVRAG coordinates Golgi-ER retrograde and ATG9 transport by differential interactions with the ER tether and the beclin 1 complex. *Nat Cell Biol* **15**:1206–19. doi:10.1038/ncb2848

- Henderson R. 1995. The potential and limitations of neutrons, electrons and X-rays for atomic resolution microscopy of unstained biological molecules. *Q Rev Biophys* **28**:171–193. doi:10.1017/s003358350000305x
- Henmi Y, Morikawa Y, Oe N, Ikeda N, Fujita A, Takei K, Minogue S, Tanabe K. 2016. PtdIns4KII α generates endosomal PtdIns(4)P and is required for receptor sorting at early endosomes. *Mol Biol Cell* **27**:990–1001. doi:10.1091/mbc.e15-08-0564
- Herman PK, Emr SD. 1990. Characterization of VPS34, a gene required for vacuolar protein sorting and vacuole segregation in *Saccharomyces cerevisiae*. *Mol Cell Biol* **10**:6742–6754. doi:10.1128/mcb.10.12.6742
- Heumann JM, Hoenger A, Mastronarde DN. 2011. Clustering and variance maps for cryo-electron tomography using wedge-masked differences. *J Struct Biol* **175**:288–99. doi:10.1016/j.jsb.2011.05.011
- Homma Y, Kinoshita R, Kuchitsu Y, Wawro PS, Marubashi S, Oguchi ME, Ishida M, Fujita N, Fukuda M. 2019. Comprehensive knockout analysis of the Rab family GTPases in epithelial cells. *J Cell Biology* **218**:2035–2050. doi:10.1083/jcb.201810134
- Hoogenraad CC, Wulf P, Schiefermeier N, Stepanova T, Galjart N, Small JV, Grosveld F, Zeeuw CI de, Akhmanova A. 2003. Bicaudal D induces selective dynein-mediated microtubule minus end-directed transport. *Embo J* **22**:6004–6015. doi:10.1093/emboj/cdg592
- Hoppe W. 1974. Towards three-dimensional ?electron microscopy? at atomic resolution. *Die Naturwissenschaften* **61**:239–249. doi:10.1007/bf00595655
- Hoppe W, Langer R, Knesch G, Poppe C. 1968. Protein-Kristallstrukturanalyse mit Elektronenstrahlen. *Die Naturwissenschaften* **55**:333–336. doi:10.1007/bf00600449
- Horiuchi H, Lippé R, McBride HM, Rubino M, Woodman P, Stenmark H, Rybin V, Wilm M, Ashman K, Mann M, Zerial M. 1997. A Novel Rab5 GDP/GTP Exchange Factor Complexed to Rabaptin-5 Links Nucleotide Exchange to Effector Recruitment and Function. *Cell* **90**:1149–1159. doi:10.1016/s0092-8674(00)80380-3
- Huang BX, Akbar M, Kevala K, Kim H-Y. 2011. Phosphatidylserine is a critical modulator for Akt activation. *J Cell Biology* **192**:979–92. doi:10.1083/jcb.201005100
- Huang J, Birmingham CL, Shahnazari S, Shiu J, Zheng YT, Smith AC, Campellone KG, Heo WD, Gruenheid S, Meyer T, Welch MD, Ktistakis NT, Kim PK, Klionsky DJ, Brumell JH. 2011. Antibacterial autophagy occurs at PI(3)P-enriched domains of the endoplasmic reticulum and requires Rab1 GTPase. *Autophagy* **7**:17–26. doi:10.4161/auto.7.1.13840

- Huang W, Choi W, Hu W, Mi N, Guo Q, Ma M, Liu M, Tian Y, Lu P, Wang F-L, Deng H, Liu L, Gao N, Yu L, Shi Y. 2012. Crystal structure and biochemical analyses reveal Beclin 1 as a novel membrane binding protein. *Cell Res* **22**:473–489. doi:10.1038/cr.2012.24
- Huotari J, Helenius A. 2011. Endosome maturation. *Embo J* **30**:3481–500. doi:10.1038/emboj.2011.286
- Ichimura Y, Kirisako T, Takao T, Satomi Y, Shimonishi Y, Ishihara N, Mizushima N, Tanida I, Kominami E, Ohsumi M, Noda T, Ohsumi Y. 2000. A ubiquitin-like system mediates protein lipidation. *Nature* **408**:488–492. doi:10.1038/35044114
- Itakura E, Kishi C, Inoue K, Mizushima N. 2008. Beclin 1 forms two distinct phosphatidylinositol 3-kinase complexes with mammalian Atg14 and UVRAG. *Mol Biol Cell* **19**:5360–72. doi:10.1091/mbc.e08-01-0080
- Itakura E, Kishi-Itakura C, Mizushima N. 2012. The Hairpin-type Tail-Anchored SNARE Syntaxin 17 Targets to Autophagosomes for Fusion with Endosomes/Lysosomes. *Cell* **151**:1256–1269. doi:10.1016/j.cell.2012.11.001
- Itakura E, Mizushima N. 2010. Characterization of autophagosome formation site by a hierarchical analysis of mammalian Atg proteins. *Autophagy* **6**:764–776. doi:10.4161/auto.6.6.12709
- Itakura E, Mizushima N. 2009. Atg14 and UVRAG: Mutually exclusive subunits of mammalian Beclin 1-PI3K complexes. *Autophagy* **5**:534–536. doi:10.4161/auto.5.4.8062
- Jain MK, Rogers J, Jahagirdar DV, Marecek JF, Ramirez F. 1986. Kinetics of interfacial catalysis by phospholipase A2 in intravesicle scooting mode, and heterofusion of anionic and zwitterionic vesicles. *Biochimica Et Biophysica Acta Bba - Biomembr* **860**:435–447. doi:10.1016/0005-2736(86)90541-9
- Jiang P, Nishimura T, Sakamaki Y, Itakura E, Hatta T, Natsume T, Mizushima N. 2014. The HOPS complex mediates autophagosome-lysosome fusion through interaction with syntaxin 17. *Mol Biol Cell* **25**:1327–37. doi:10.1091/mbc.e13-08-0447
- Johansson M, Rocha N, Zwart W, Jordens I, Janssen L, Kuijl C, Olkkonen VM, Neeffjes J. 2007. Activation of endosomal dynein motors by stepwise assembly of Rab7-RILP-p150Glued, ORP1L, and the receptor betalll spectrin. *J Cell Biology* **176**:459–71. doi:10.1083/jcb.200606077
- Johnson DE, Ostrowski P, Jaumouillé V, Grinstein S. 2016. The position of lysosomes within the cell determines their luminal pH. *J Cell Biology* **212**:677–92. doi:10.1083/jcb.201507112

- Judith D, Jefferies HBJ, Boeing S, Frith D, Snijders AP, Tooze SA. 2019. ATG9A shapes the forming autophagosome through Arfaptin 2 and phosphatidylinositol 4-kinase III β ATG9A and ARFIP2 drive autophagy via PI4KIII β . *J Cell Biology* **218**:1634–1652. doi:10.1083/jcb.201901115
- Kabeya Y, Mizushima N, Ueno T, Yamamoto A, Kirisako T, Noda T, Kominami E, Ohsumi Y, Yoshimori T. 2000. LC3, a mammalian homologue of yeast Apg8p, is localized in autophagosome membranes after processing. *Embo J* **19**:5720–5728. doi:10.1093/emboj/19.21.5720
- Kakuta S, Yamaguchi J, Suzuki C, Sasaki M, Kazuno S, Uchiyama Y. 2017. Small GTPase Rab1B is associated with ATG9A vesicles and regulates autophagosome formation. *Faseb J Official Publ Fed Am Soc Exp Biology* **31**:3757–3773. doi:10.1096/fj.201601052r
- Karanasios E, Stapleton E, Manifava M, Kaizuka T, Mizushima N, Walker SA, Ktistakis NT. 2013. Dynamic association of the ULK1 complex with omegasomes during autophagy induction. *J Cell Sci* **126**:5224–5238. doi:10.1242/jcs.132415
- Karanasios E, Walker SA, Okkenhaug H, Manifava M, Hummel E, Zimmermann H, Ahmed Q, Domart M-C, Collinson L, Ktistakis NT. 2016. Autophagy initiation by ULK complex assembly on ER tubulovesicular regions marked by ATG9 vesicles. *Nat Commun* **7**:12420. doi:10.1038/ncomms12420
- Ketel K, Krauss M, Nicot A-S, Puchkov D, Wieffer M, Müller R, Subramanian D, Schultz C, Laporte J, Haucke V. 2016. A phosphoinositide conversion mechanism for exit from endosomes. *Nature* **529**:408–12. doi:10.1038/nature16516
- Kihara A, Noda T, Ishihara N, Ohsumi Y. 2001. Two Distinct Vps34 Phosphatidylinositol 3-Kinase Complexes Function in Autophagy and Carboxypeptidase Y Sorting in *Saccharomyces cerevisiae*. *J Cell Biol* **152**:519–530. doi:10.1083/jcb.152.3.519
- Kim J, Kundu M, Viollet B, Guan K-L. 2011. AMPK and mTOR regulate autophagy through direct phosphorylation of ULK1. *Nat Cell Biol* **13**:132–41. doi:10.1038/ncb2152
- Kim J, Kim YC, Fang C, Russell RC, Kim JH, Fan W, Liu R, Zhong Q, Guan K-L. 2013. Differential Regulation of Distinct Vps34 Complexes by AMPK in Nutrient Stress and Autophagy. *Cell* **152**:290–303. doi:10.1016/j.cell.2012.12.016
- Kim Y-M, Jung CH, Seo M, Kim EK, Park J-M, Bae SS, Kim D-H. 2015. mTORC1 Phosphorylates UVRAG to Negatively Regulate Autophagosome and Endosome Maturation. *Mol Cell* **57**:207–218. doi:10.1016/j.molcel.2014.11.013
- Kinchen JM, Doukoumetzidis K, Almendinger J, Stergiou L, Tosello-Tramont A, Sifri CD, Hengartner MO, Ravichandran KS. 2008. A pathway for phagosome maturation during engulfment of apoptotic cells. *Nat Cell Biol* **10**:556–66. doi:10.1038/ncb1718

References

- Klionsky DJ, Schulman BA. 2014. Dynamic regulation of macroautophagy by distinctive ubiquitin-like proteins. *Nat Struct Mol Biol* **21**:336–45. doi:10.1038/nsmb.2787
- Klöpffer TH, Kienle N, Fasshauer D, Munro S. 2012. Untangling the evolution of Rab G proteins: implications of a comprehensive genomic analysis. *Bmc Biol* **10**:71. doi:10.1186/1741-7007-10-71
- Klumperman J, Raposo G. 2014. The Complex Ultrastructure of the Endolysosomal System. *Csh Perspect Biol* **6**:a016857–a016857. doi:10.1101/cshperspect.a016857
- Knævelsrud H, Ahlquist T, Merok MA, Nesbakken A, Stenmark H, Lothe RA, Simonsen A. 2010. UVRAG mutations associated with microsatellite unstable colon cancer do not affect autophagy. *Autophagy* **6**:863–70. doi:10.4161/auto.6.7.13033
- Koster AJ, Chen H, Sedat JW, Agard DA. 1992. Automated microscopy for electron tomography. *Ultramicroscopy* **46**:207–227. doi:10.1016/0304-3991(92)90016-d
- Koster AJ, Grimm R, Typke D, Hegerl R, Stoschek A, Walz J, Baumeister W. 1997. Perspectives of Molecular and Cellular Electron Tomography. *J Struct Biol* **120**:276–308. doi:10.1006/jsbi.1997.3933
- Kovtun O, Dickson VK, Kelly BT, Owen DJ, Briggs JAG. 2020. Architecture of the AP2:clathrin coat on the membranes of clathrin-coated vesicles. *Biorxiv* 2020.01.28.922591. doi:10.1101/2020.01.28.922591
- Kovtun O, Leneva N, Bykov YS, Ariotti N, Teasdale RD, Schaffer M, Engel BD, Owen DavidJ, Briggs JAG, Collins BM. 2018. Structure of the membrane-assembled retromer coat determined by cryo-electron tomography. *Nature* **561**:561–564. doi:10.1038/s41586-018-0526-z
- Koyama-Honda I, Itakura E, Fujiwara TK, Mizushima N. 2013. Temporal analysis of recruitment of mammalian ATG proteins to the autophagosome formation site. *Autophagy* **9**:1491–9. doi:10.4161/auto.25529
- Kremer JR, Mastronarde DN, McIntosh JR. 1996. Computer Visualization of Three-Dimensional Image Data Using IMOD. *J Struct Biol* **116**:71–76. doi:10.1006/jsbi.1996.0013
- Ktistakis NT, Tooze SA. 2016. Digesting the Expanding Mechanisms of Autophagy. *Trends Cell Biol* **26**:624–35. doi:10.1016/j.tcb.2016.03.006
- Kudryashev M. 2017. Biological and Medical Physics, Biomedical Engineering 261–282. doi:10.1007/978-3-319-68997-5_10

- Kudryashev M, Castaño-Díez D, Stahlberg H. 2012. Limiting factors in single particle cryo electron tomography. *Comput Struct Biotechnology J* **1**:e201207002. doi:10.5936/csbj.201207002
- Kühlbrandt W. 2014. The Resolution Revolution. *Science* **343**:1443–1444. doi:10.1126/science.1251652
- Kutateladze TG. 2010. Translation of the phosphoinositide code by PI effectors. *Nat Chem Biol* **6**:507–13. doi:10.1038/nchembio.390
- Lee MG, Mishra A, Lambright DG. 2009. Structural Mechanisms for Regulation of Membrane Traffic by Rab GTPases. *Traffic* **10**:1377–1389. doi:10.1111/j.1600-0854.2009.00942.x
- Leigh KE, Navarro PP, Scaramuzza S, Chen W, Zhang Y, Castaño-Díez D, Kudryashev M. 2019. Methods in Cell Biology. *Methods Cell Biol* **152**:217–259. doi:10.1016/bs.mcb.2019.04.003
- Lemmon MA. 2008. Membrane recognition by phospholipid-binding domains. *Nat Rev Mol Cell Bio* **9**:99–111. doi:10.1038/nrm2328
- Li X, He L, Che KH, Funderburk SF, Pan L, Pan N, Zhang M, Yue Z, Zhao Y. 2012. Imperfect interface of Beclin1 coiled-coil domain regulates homodimer and heterodimer formation with ATG14L and UVRAG. *Nat Commun* **3**:662. doi:10.1038/ncomms1648
- Li F, Yi L, Zhao L, Itzen A, Goody RS, Wu Y-W. 2014. The role of the hypervariable C-terminal domain in Rab GTPases membrane targeting. *P Natl Acad Sci Usa* **111**:2572–7. doi:10.1073/pnas.1313655111
- Li P, Lees JA, Lusk CP, Reinisch KM. 2020. Cryo-EM reconstruction of a VPS13 fragment reveals a long groove to channel lipids between membranes. *J Cell Biology* **219**. doi:10.1083/jcb.202001161
- Liang C, Feng P, Ku B, Dotan I, Canaani D, Oh B-H, Jung JU. 2006. Autophagic and tumour suppressor activity of a novel Beclin1-binding protein UVRAG. *Nat Cell Biol* **8**:688–698. doi:10.1038/ncb1426
- Liang C, Lee J, Inn K-S, Gack MU, Li Q, Roberts EA, Vergne I, Deretic V, Feng P, Akazawa C, Jung JU. 2008. Beclin1-binding UVRAG targets the class C Vps complex to coordinate autophagosome maturation and endocytic trafficking. *Nat Cell Biol* **10**:776–787. doi:10.1038/ncb1740
- Lippé R, Miaczynska M, Rybin V, Runge A, Zerial M. 2001. Functional Synergy between Rab5 Effector Rabaptin-5 and Exchange Factor Rabex-5 When Physically Associated in a Complex. *Mol Biol Cell* **12**:2219–2228. doi:10.1091/mbc.12.7.2219

- Lőrincz P, Lakatos Z, Maruzs T, Szatmári Z, Kis V, Sass M. 2014. Atg6/UVRAG/Vps34-containing lipid kinase complex is required for receptor downregulation through endolysosomal degradation and epithelial polarity during *Drosophila* wing development. *Biomed Res Int* **2014**:851349. doi:10.1155/2014/851349
- Lowe M, Kreis TE. 1996. In Vivo Assembly of Coatamer, the COP-I Coat Precursor. *J Biol Chem* **271**:30725–30730. doi:10.1074/jbc.271.48.30725
- Lu J, He L, Behrends C, Araki M, Araki K, Wang QJ, Catanzaro JM, Friedman SL, Zong W-X, Fiel MI, Li M, Yue Z. 2014. NRBF2 regulates autophagy and prevents liver injury by modulating Atg14L-linked phosphatidylinositol-3 kinase III activity. *Nat Commun* **5**:3920. doi:10.1038/ncomms4920
- Lucas M, Gaspar AH, Pallara C, Rojas AL, Fernández-Recio J, Machner MP, Hierro A. 2014. Structural basis for the recruitment and activation of the Legionella phospholipase VipD by the host GTPase Rab5. *P Natl Acad Sci Usa* **111**:E3514-23. doi:10.1073/pnas.1405391111
- Ma M, Liu J-J, Li Y, Huang Y, Ta N, Chen Y, Fu H, Ye M-D, Ding Y, Huang W, Wang J, Dong M-Q, Yu L, Wang H-W. 2017. Cryo-EM structure and biochemical analysis reveal the basis of the functional difference between human PI3KC3-C1 and -C2. *Cell Res* **27**:989–1001. doi:10.1038/cr.2017.94
- Maeda S, Otomo C, Otomo T. 2019. The autophagic membrane tether ATG2A transfers lipids between membranes. *Elife* **8**:e45777. doi:10.7554/elife.45777
- Manni MM, Tiberti ML, Pagnotta S, Barelli H, Gautier R, Antony B. 2018. Acyl chain asymmetry and polyunsaturation of brain phospholipids facilitate membrane vesiculation without leakage. *Elife* **7**:e34394. doi:10.7554/elife.34394
- Mari M, Griffith J, Rieter E, Krishnappa L, Klionsky DJ, Reggiori F. 2010. An ATG9-containing compartment that functions in the early steps of autophagosome biogenesis. *J Cell Biology* **190**:1005–1022. doi:10.1083/jcb.200912089
- Marko M, Hsieh C, Schalek R, Frank J, Mannella C. 2007. Focused-ion-beam thinning of frozen-hydrated biological specimens for cryo-electron microscopy. *Nat Methods* **4**:215–217. doi:10.1038/nmeth1014
- Martinez J, Malireddi RKS, Lu Q, Cunha LD, Pelletier S, Gingras S, Orchard R, Guan J-L, Tan H, Peng J, Kanneganti T-D, Virgin HW, Green DR. 2015. Molecular characterization of LC3-associated phagocytosis reveals distinct roles for Rubicon, NOX2 and autophagy proteins. *Nat Cell Biol* **17**:893–906. doi:10.1038/ncb3192
- Masson GR, Burke JE, Ahn NG, Anand GS, Borchers C, Brier S, Bou-Assaf GM, Engen JR, Englander SW, Faber J, Garlish R, Griffin PR, Gross ML, Guttman M, Hamuro Y, Heck AJR, Houde D, Iacob RE, Jørgensen TJD, Kaltashov IA, Klinman JP,

- Konermann L, Man P, Mayne L, Pascal BD, Reichmann D, Skehel M, Snijder J, Strutzenberg TS, Underbakke ES, Wagner C, Wales TE, Walters BT, Weis DD, Wilson DJ, Wintrode PL, Zhang Z, Zheng J, Schriemer DC, Rand KD. 2019. Recommendations for performing, interpreting and reporting hydrogen deuterium exchange mass spectrometry (HDX-MS) experiments. *Nat Methods* **16**:595–602. doi:10.1038/s41592-019-0459-y
- Masson GR, Maslen SL, Williams RL. 2017. Analysis of phosphoinositide 3-kinase inhibitors by bottom-up electron-transfer dissociation hydrogen/deuterium exchange mass spectrometry. *Biochem J* **474**:1867–1877. doi:10.1042/bcj20170127
- Masson GR, Perisic O, Burke JE, Williams RL. 2015. The intrinsically disordered tails of PTEN and PTEN-L have distinct roles in regulating substrate specificity and membrane activity. *Biochem J* **473**:135–44. doi:10.1042/bj20150931
- Mastrorade DN. 2005. Automated electron microscope tomography using robust prediction of specimen movements. *J Struct Biol* **152**:36–51. doi:10.1016/j.jsb.2005.07.007
- Matsunaga K, Saitoh T, Tabata K, Omori H, Satoh T, Kurotori N, Maejima I, Shirahama-Noda K, Ichimura T, Isobe T, Akira S, Noda T, Yoshimori T. 2009. Two Beclin 1-binding proteins, ATG14L and Rubicon, reciprocally regulate autophagy at different stages. *Nat Cell Biol* **11**:385–396. doi:10.1038/ncb1846
- Matthew JB, Richards FM. 1983. The pH dependence of hydrogen exchange in proteins. *J Biological Chem* **258**:3039–44.
- Matthies D, Dalmás O, Borgnia MJ, Dominik PK, Merk A, Rao P, Reddy BG, Islam S, Bartesaghi A, Perozo E, Subramaniam S. 2016. Cryo-EM Structures of the Magnesium Channel CorA Reveal Symmetry Break upon Gating. *Cell* **164**:747–56. doi:10.1016/j.cell.2015.12.055
- Mayor S, Pagano RE. 2007. Pathways of clathrin-independent endocytosis. *Nat Rev Mol Cell Bio* **8**:603–612. doi:10.1038/nrm2216
- McBride HM, Rybin V, Murphy C, Giner A, Teasdale R, Zerial M. 1999. Oligomeric Complexes Link Rab5 Effectors with NSF and Drive Membrane Fusion via Interactions between EEA1 and Syntaxin 13. *Cell* **98**:377–386. doi:10.1016/s0092-8674(00)81966-2
- McDowell AW, Chang J-J, Freeman R, Lepault J, Walter CA, Dubochet J. 1983. Electron microscopy of frozen hydrated sections of vitreous ice and vitrified biological samples. *J Microsc-oxford* **131**:1–9. doi:10.1111/j.1365-2818.1983.tb04225.x
- McEwan DG, Popovic D, Gubas A, Terawaki S, Suzuki H, Stadel D, Coxon FP, Miranda de Stegmann D, Bhogaraju S, Maddi K, Kirchof A, Gatti E, Helfrich MH, Wakatsuki S, Behrends C, Pierre P, Dikic I. 2015. PLEKHM1 Regulates

References

- Autophagosome-Lysosome Fusion through HOPS Complex and LC3/GABARAP Proteins. *Mol Cell* **57**:39–54. doi:10.1016/j.molcel.2014.11.006
- McLaughlin S, Aderem A. 1995. The myristoyl-electrostatic switch: a modulator of reversible protein-membrane interactions. *Trends Biochem Sci* **20**:272–276. doi:10.1016/s0968-0004(00)89042-8
- Meer G van, Kroon AIPM de. 2011. Lipid map of the mammalian cell. *J Cell Sci* **124**:5–8. doi:10.1242/jcs.071233
- Meer G van, Voelker DR, Feigenson GW. 2008. Membrane lipids: where they are and how they behave. *Nat Rev Mol Cell Bio* **9**:112–124. doi:10.1038/nrm2330
- Mercer TJ, Gubas A, Tooze SA. 2018. A molecular perspective of mammalian autophagosome biogenesis. *J Biol Chem* **293**:5386–5395. doi:10.1074/jbc.r117.810366
- Merithew E, Hatherly S, Dumas JJ, Lawe DC, Heller-Harrison R, Lambright DG. 2001. Structural Plasticity of an Invariant Hydrophobic Triad in the Switch Regions of Rab GTPases Is a Determinant of Effector Recognition. *J Biol Chem* **276**:13982–13988. doi:10.1074/jbc.m009771200
- Miller S, Tavshanjian B, Oleksy A, Perisic O, Houseman BT, Shokat KM, Williams RL. 2010. Finding a fitting shoe for Cinderella: searching for an autophagy inhibitor. *Autophagy* **6**:805–7. doi:10.1126/science.1184429
- Mishra A, Eathiraj S, Corvera S, Lambright DG. 2010. Structural basis for Rab GTPase recognition and endosome tethering by the C2H2 zinc finger of Early Endosomal Autoantigen 1 (EEA1). *P Natl Acad Sci Usa* **107**:10866–71. doi:10.1073/pnas.1000843107
- Mizuno-Yamasaki E, Rivera-Molina F, Novick P. 2012. GTPase Networks in Membrane Traffic. *Biochemistry-us* **81**:637–659. doi:10.1146/annurev-biochem-052810-093700
- Mochizuki Y, Ohashi R, Kawamura T, Iwanari H, Kodama T, Naito M, Hamakubo T. 2012. Phosphatidylinositol 3-phosphatase myotubularin-related protein 6 (MTMR6) is regulated by small GTPase Rab1B in the early secretory and autophagic pathways. *J Biological Chem* **288**:1009–21. doi:10.1074/jbc.m112.395087
- Moreau K, Ravikumar B, Puri C, Rubinsztein DC. 2012. Arf6 promotes autophagosome formation via effects on phosphatidylinositol 4,5-bisphosphate and phospholipase D. *J Cell Biology* **196**:483–96. doi:10.1083/jcb.201110114
- Mott HR, Owen D. 2015. Structures of Ras superfamily effector complexes: What have we learnt in two decades? *Crit Rev Biochem Mol* **50**:85–133. doi:10.3109/10409238.2014.999191

- Muller MP, Peters H, Blumer J, Blankenfeldt W, Goody RS, Itzen A. 2010. The Legionella Effector Protein DrrA AMPylates the Membrane Traffic Regulator Rab1b. *Science* **329**:946–949. doi:10.1126/science.1192276
- Munson MJ, Allen GF, Toth R, Campbell DG, Lucocq JM, Ganley IG. 2015. mTOR activates the VPS34–UVRAG complex to regulate autolysosomal tubulation and cell survival. *Embo J* **34**:2272–2290. doi:10.15252/embj.201590992
- Murray JT, Panaretou C, Stenmark H, Miaczynska M, Backer JM. 2002. Role of Rab5 in the Recruitment of hVps34/p150 to the Early Endosome. *Traffic* **3**:416–427. doi:10.1034/j.1600-0854.2002.30605.x
- Nakamura S, Oba M, Suzuki M, Takahashi A, Yamamuro T, Fujiwara M, Ikenaka K, Minami S, Tabata N, Yamamoto K, Kubo S, Tokumura A, Akamatsu K, Miyazaki Y, Kawabata T, Hamasaki M, Fukui K, Sango K, Watanabe Y, Takabatake Y, Kitajima TS, Okada Y, Mochizuki H, Isaka Y, Antebi A, Yoshimori T. 2019. Suppression of autophagic activity by Rubicon is a signature of aging. *Nat Commun* **10**:847. doi:10.1038/s41467-019-08729-6
- Nakamura S, Yoshimori T. 2017. New insights into autophagosome–lysosome fusion. *J Cell Sci* **130**:jcs.196352. doi:10.1242/jcs.196352
- Nascimbeni AC, Giordano F, Dupont N, Grasso D, Vaccaro MI, Codogno P, Morel E. 2017. ER–plasma membrane contact sites contribute to autophagosome biogenesis by regulation of local PI3P synthesis. *Embo J* **36**:2018–2033. doi:10.15252/embj.201797006
- Nassar N, Horn G, Herrmann CA, Scherer A, McCormick F, Wittinghofer A. 1995. The 2.2 Å crystal structure of the Ras-binding domain of the serine/threonine kinase c-Raf1 in complex with Rap1A and a GTP analogue. *Nature* **375**:554–560. doi:10.1038/375554a0
- Newton AC, Koshland DE. 1989. High cooperativity, specificity, and multiplicity in the protein kinase C-lipid interaction. *J Biological Chem* **264**:14909–15.
- Nguyen N, Shteyn V, Melia TJ. 2017. Sensing Membrane Curvature in Macroautophagy. *J Mol Biol* **429**:457–472. doi:10.1016/j.jmb.2017.01.006
- Nguyen T, Cigler M, Lang K. 2018. Expanding the Genetic Code to Study Protein–Protein Interactions. *Angewandte Chemie Int Ed* **57**:14350–14361. doi:10.1002/anie.201805869
- Nicastro D. 2009. Chapter 1 Cryo-Electron Microscope Tomography to Study Axonemal Organization. *Methods Cell Biol* **91**:1–39. doi:10.1016/s0091-679x(08)91001-3
- Nicastro D, Schwartz C, Pierson J, Gaudette R, Porter ME, McIntosh JR. 2006. The Molecular Architecture of Axonemes Revealed by Cryoelectron Tomography. *Science* **313**:944–948. doi:10.1126/science.1128618

- Noda NN, Kobayashi T, Adachi W, Fujioka Y, Ohsumi Y, Inagaki F. 2012. Structure of the Novel C-terminal Domain of Vacuolar Protein Sorting 30/Autophagy-related Protein 6 and Its Specific Role in Autophagy*. *J Biological Chem* **287**:16256–16266. doi:10.1074/jbc.m112.348250
- Ohashi Y, Soler N, Ortegón MG, Zhang L, Kirsten ML, Perisic O, Masson GR, Burke JE, Jakobi AJ, Apostolakis AA, Johnson CM, Ohashi M, Ktistakis NT, Sachse C, Williams RL. 2016. Characterization of Atg38 and NRBF2, a fifth subunit of the autophagic Vps34/PIK3C3 complex. *Autophagy* **12**:1–16. doi:10.1080/15548627.2016.1226736
- Ohashi Y, Tremel S, Williams RL. 2018. VPS34 complexes from a structural perspective. *J Lipid Res* **60**:229–241. doi:10.1194/jlr.r089490
- Oppermann FS, Gnad F, Olsen JV, Hornberger R, Greff Z, Kéri G, Mann M, Daub H. 2009. Large-scale proteomics analysis of the human kinome. *Mol Cell Proteom* **8**:1751–64. doi:10.1074/mcp.m800588-mcp200
- Orsi A, Razi M, Dooley HC, Robinson D, Weston AE, Collinson LM, Tooze SA. 2012. Dynamic and transient interactions of ATG9 with autophagosomes, but not membrane integration, are required for autophagy. *Mol Biol Cell* **23**:1860–73. doi:10.1091/mbc.e11-09-0746
- Palmer CM, Löwe J. 2013. A cylindrical specimen holder for electron cryotomography. *Ultramicroscopy* **137**:20–9. doi:10.1016/j.ultramic.2013.10.016
- Pang SS, Bayly-Jones C, Radjainia M, Spicer BA, Law RHP, Hodel AW, Parsons ES, Ekkel SM, Conroy PJ, Ramm G, Venugopal H, Bird PI, Hoogenboom BW, Voskoboinik I, Gambin Y, Sierecki E, Dunstone MA, Whisstock JC. 2019. The cryo-EM structure of the acid activatable pore-forming immune effector Macrophage-expressed gene 1. *Nat Commun* **10**:4288. doi:10.1038/s41467-019-12279-2
- Pankiv S, Alemu EA, Brech A, Bruun J-A, Lamark T, Overvatn A, Bjørkøy G, Johansen T. 2010. FYCO1 is a Rab7 effector that binds to LC3 and PI3P to mediate microtubule plus end-directed vesicle transport. *J Cell Biology* **188**:253–69. doi:10.1083/jcb.200907015
- Park J-M, Jung CH, Seo M, Otto NM, Grunwald D, Kim KH, Moriarity B, Kim Y-M, Starker C, Nho RS, Voytas D, Kim D-H. 2016. The ULK1 complex mediates MTORC1 signaling to the autophagy initiation machinery via binding and phosphorylating ATG14. *Autophagy* **12**:547–564. doi:10.1080/15548627.2016.1140293
- Park J-M, Seo M, Jung CH, Grunwald D, Stone M, Otto NM, Toso E, Ahn Y, Kyba M, Griffin TJ, Higgins L, Kim D-H. 2018. ULK1 phosphorylates Ser30 of BECN1 in association with ATG14 to stimulate autophagy induction. *Autophagy* **14**:584–597. doi:10.1080/15548627.2017.1422851

- Parzych KR, Ariosa A, Mari M, Klionsky DJ. 2018. A newly characterized vacuolar serine carboxypeptidase, Atg42/Ybr139w, is required for normal vacuole function and the terminal steps of autophagy in the yeast *Saccharomyces cerevisiae*. *Mol Biol Cell* **29**:1089–1099. doi:10.1091/mbc.e17-08-0516
- Parzych KR, Klionsky DJ. 2013. An overview of autophagy: morphology, mechanism, and regulation. *Antioxid Redox Sign* **20**:460–73. doi:10.1089/ars.2013.5371
- Payraastre B, Missy K, Giuriato S, Bodin S, Plantavid M, Gratacap M-P. 2001. Phosphoinositides : key players in cell signalling, in time and space. *Cell Signal* **13**:377–387. doi:10.1016/s0898-6568(01)00158-9
- Pereira-Leal JB, Seabra MC. 2000. The mammalian Rab family of small GTPases: definition of family and subfamily sequence motifs suggests a mechanism for functional specificity in the Ras superfamily 1 Edited by M. Yaniv. *J Mol Biol* **301**:1077–1087. doi:10.1006/jmbi.2000.4010
- Perelman B, Dafni N, Naiman T, Eli D, Yaakov M, Feng TLY, Sinha S, Weber G, Khodaei S, Sancar A, Dotan I, Canaani D. 1997. Molecular Cloning of a Novel Human Gene Encoding a 63-kDa Protein and Its Sublocalization within the 11q13 Locus. *Genomics* **41**:397–405. doi:10.1006/geno.1997.4623
- Peter BJ, Kent HM, Mills IG, Vallis Y, Butler PJG, Evans PR, McMahon HT. 2004. BAR Domains as Sensors of Membrane Curvature: The Amphiphysin BAR Structure. *Science* **303**:495–499. doi:10.1126/science.1092586
- Pfeffer SR. 2013. Rab GTPase regulation of membrane identity. *Curr Opin Cell Biol* **25**:414–9. doi:10.1016/j.ceb.2013.04.002
- Pinot M, Vanni S, Pagnotta S, Lacas-Gervais S, Payet L-A, Ferreira T, Gautier R, Goud B, Antonny B, Barelli H. 2014. Lipid cell biology. Polyunsaturated phospholipids facilitate membrane deformation and fission by endocytic proteins. *Sci New York N Y* **345**:693–7. doi:10.1126/science.1255288
- Plutner H, Cox AD, Pind S, Khosravi-Far R, Bourne JR, Schwaninger R, Der CJ, Balch WE. 1991. Rab1b regulates vesicular transport between the endoplasmic reticulum and successive Golgi compartments. *J Cell Biology* **115**:31–43. doi:10.1083/jcb.115.1.31
- Pols MS, Brink C ten, Gosavi P, Oorschot V, Klumperman J. 2012. The HOPS proteins hVps41 and hVps39 are required for homotypic and heterotypic late endosome fusion. *Traffic Cph Den* **14**:219–32. doi:10.1111/tra.12027
- Poteryaev D, Datta S, Ackema K, Zerial M, Spang A. 2010. Identification of the switch in early-to-late endosome transition. *Cell* **141**:497–508. doi:10.1016/j.cell.2010.03.011

- Pranke IM, Morello V, Bigay J, Gibson K, Verbavatz J-M, Antonny B, Jackson CL. 2011. α -Synuclein and ALPS motifs are membrane curvature sensors whose contrasting chemistry mediates selective vesicle binding. *J Cell Biology* **194**:89–103. doi:10.1083/jcb.201011118
- Proikas-Cezanne T, Takacs Z, Donnes P, Kohlbacher O. 2015. WIPI proteins: essential PtdIns3P effectors at the nascent autophagosome. *J Cell Sci* **128**:207–217. doi:10.1242/jcs.146258
- Puente C, Hendrickson RC, Jiang X. 2016. Nutrient-regulated Phosphorylation of ATG13 Inhibits Starvation-induced Autophagy. *J Biological Chem* **291**:6026–35. doi:10.1074/jbc.m115.689646
- Pylypenko O, Hammich H, Yu I-M, Houdusse A. 2017. Rab GTPases and their interacting protein partners: Structural insights into Rab functional diversity. *Small Gtpases* **9**:22–48. doi:10.1080/21541248.2017.1336191
- Qu K, Glass B, Doležal M, Schur FKM, Murciano B, Rein A, Rumlová M, Ruml T, Kräusslich H-G, Briggs JAG. 2018. Structure and architecture of immature and mature murine leukemia virus capsids. *Proc National Acad Sci* **115**:E11751–E11760. doi:10.1073/pnas.1811580115
- Radermacher M. 2006. Electron Tomography 245–273. doi:10.1007/978-0-387-69008-7_9
- Radermacher M. 1988. Three-Dimensional reconstruction of single particles from random and nonrandom tilt series. *J Electron Microscop* **9**:359–394. doi:10.1002/jemt.1060090405
- Ramlal K, Palmer CM, Aylett CHS. 2018. A Local Agreement Filtering Algorithm for Transmission EM Reconstructions. *J Struct Biol* **205**:30–40. doi:10.1016/j.jsb.2018.11.011
- Ravikumar B, Imarisio S, Sarkar S, O’Kane CJ, Rubinsztein DC. 2008. Rab5 modulates aggregation and toxicity of mutant huntingtin through macroautophagy in cell and fly models of Huntington disease. *J Cell Sci* **121**:1649–60. doi:10.1242/jcs.025726
- Resolution Trends in the Electron Microscopy Data Bank EMDB
(https://www.ebi.ac.uk/pdbe/emdb/statistics_tom_res.html/)
- Rice WJ, Cheng A, Noble AJ, Eng ET, Kim LY, Carragher B, Potter CS. 2018. Routine determination of ice thickness for cryo-EM grids. *J Struct Biol* **204**:38–44. doi:10.1016/j.jsb.2018.06.007
- Ridley SH, Ktistakis N, Davidson K, Anderson KE, Manifava M, Ellson CD, Lipp P, Bootman M, Coadwell J, Nazarian A, Erdjument-Bromage H, Tempst P, Cooper MA, Thuring JW, Lim ZY, Holmes AB, Stephens LR, Hawkins PT. 2001. FENS-1

- and DFCP1 are FYVE domain-containing proteins with distinct functions in the endosomal and Golgi compartments. *J Cell Sci* **114**:3991–4000.
- Rosier DJD, Klug A. 1968. Reconstruction of Three Dimensional Structures from Electron Micrographs. *Nature* **217**:130–134. doi:10.1038/217130a0
- Rostislavleva K, Soler N, Ohashi Y, Zhang L, Pardon E, Burke JE, Masson GR, Johnson C, Steyaert J, Ktistakis NT, Williams RL. 2015. Structure and flexibility of the endosomal Vps34 complex reveals the basis of its function on membranes. *Science* **350**:aac7365. doi:10.1126/science.aac7365
- Russell RC, Tian Y, Yuan H, Park HW, Chang Y-Y, Kim J, Kim H, Neufeld TP, Dillin A, Guan K-L. 2013. ULK1 induces autophagy by phosphorylating Beclin-1 and activating VPS34 lipid kinase. *Nat Cell Biol* **15**:741–750. doi:10.1038/ncb2757
- Rutherford AC, Traer C, Wassmer T, Pattni K, Bujny MV, Carlton JG, Stenmark H, Cullen PJ. 2006. The mammalian phosphatidylinositol 3-phosphate 5-kinase (PIKfyve) regulates endosome-to-TGN retrograde transport. *J Cell Sci* **119**:3944–3957. doi:10.1242/jcs.03153
- Sabatini DD, Adesnik M. 2013. Christian de Duve: Explorer of the cell who discovered new organelles by using a centrifuge. *P Natl Acad Sci Usa* **110**:13234–5. doi:10.1073/pnas.1312084110
- Sasaki T, Takasuga S, Sasaki J, Kofuji S, Eguchi S, Yamazaki M, Suzuki A. 2009. Mammalian phosphoinositide kinases and phosphatases. *Prog Lipid Res* **48**:307–343. doi:10.1016/j.plipres.2009.06.001
- Saxton RA, Sabatini DM. 2017. mTOR Signaling in Growth, Metabolism, and Disease. *Cell* **168**:960–976. doi:10.1016/j.cell.2017.02.004
- Scheres SHW. 2012. RELION: implementation of a Bayesian approach to cryo-EM structure determination. *J Struct Biol* **180**:519–30. doi:10.1016/j.jsb.2012.09.006
- Schmid MF, Booth CR. 2007. Methods for aligning and for averaging 3D volumes with missing data. *J Struct Biol* **161**:243–8. doi:10.1016/j.jsb.2007.09.018
- Schur FK. 2019. Toward high-resolution in situ structural biology with cryo-electron tomography and subtomogram averaging. *Curr Opin Struc Biol* **58**:1–9. doi:10.1016/j.sbi.2019.03.018
- Seixas E, Barros M, Seabra MC, Barral DC. 2013. Rab and Arf Proteins in Genetic Diseases: Rab and Arf Proteins in Genetic Diseases. *Traffic* **14**:871–885. doi:10.1111/tra.12072
- Shen F, Seabra MC. 1996. Mechanism of Digeranylgeranylation of Rab Proteins. *J Biol Chem* **271**:3692–3698. doi:10.1074/jbc.271.7.3692

References

- Siempelkamp BD, Rathinaswamy MK, Jenkins ML, Burke JE. 2017. Molecular mechanism of activation of class IA phosphoinositide 3-kinases (PI3Ks) by membrane-localized HRas. *J Biol Chem* **292**:12256–12266. doi:10.1074/jbc.m117.789263
- Stack JH, Emr SD. 1994. Vps34p required for yeast vacuolar protein sorting is a multiple specificity kinase that exhibits both protein kinase and phosphatidylinositol-specific PI 3-kinase activities. *J Biological Chem* **269**:31552–62.
- Stein M-P, Feng Y, Cooper KL, Welford AM, Wandinger-Ness A. 2003. Human VPS34 and p150 are Rab7 Interacting Partners. *Traffic* **4**:754–771. doi:10.1034/j.1600-0854.2003.00133.x
- Stenmark H, Parton RG, Steele-Mortimer O, Lütcke A, Gruenberg J, Zerial M. 1994. Inhibition of rab5 GTPase activity stimulates membrane fusion in endocytosis. *Embo J* **13**:1287–1296. doi:10.1002/j.1460-2075.1994.tb06381.x
- Stenmark H. 2009. Rab GTPases as coordinators of vesicle traffic. *Nat Rev Mol Cell Bio* **10**:513–525. doi:10.1038/nrm2728
- Stjepanovic G, Baskaran S, Lin MG, Hurley JH. 2017. Vps34 Kinase Domain Dynamics Regulate the Autophagic PI 3-Kinase Complex. *Mol Cell* **67**:528-534.e3. doi:10.1016/j.molcel.2017.07.003
- Stroupe C, Collins KM, Fratti RA, Wickner W. 2006. Purification of active HOPS complex reveals its affinities for phosphoinositides and the SNARE Vam7p. *Embo J* **25**:1579–1589. doi:10.1038/sj.emboj.7601051
- Su H, Yang F, Wang Q, Shen Q, Huang J, Peng C, Zhang Y, Wan W, Wong CCL, Sun Q, Wang F, Zhou T, Liu W. 2017. VPS34 Acetylation Controls Its Lipid Kinase Activity and the Initiation of Canonical and Non-canonical Autophagy. *Mol Cell* **67**:907-921.e7. doi:10.1016/j.molcel.2017.07.024
- Sun Q, Fan W, Chen K, Ding X, Chen S, Zhong Q. 2008. Identification of Barkor as a mammalian autophagy-specific factor for Beclin 1 and class III phosphatidylinositol 3-kinase. *Proc National Acad Sci* **105**:19211–19216. doi:10.1073/pnas.0810452105
- Sun Q, Westphal W, Wong KN, Tan I, Zhong Q. 2010. Rubicon controls endosome maturation as a Rab7 effector. *P Natl Acad Sci Usa* **107**:19338–43. doi:10.1073/pnas.1010554107
- Suzuki K, Ohsumi Y. 2007. Molecular machinery of autophagosome formation in yeast, *Saccharomyces cerevisiae*. *Febs Lett* **581**:2156–2161. doi:10.1016/j.febslet.2007.01.096
- Tabata K, Matsunaga K, Sakane A, Sasaki T, Noda T, Yoshimori T. 2010. Rubicon and PLEKHM1 negatively regulate the endocytic/autophagic pathway via a

References

- novel Rab7-binding domain. *Mol Biol Cell* **21**:4162–72. doi:10.1091/mbc.e10-06-0495
- Takáts S, Piracs K, Nagy P, Varga Á, Kárpáti M, Hegedűs K, Kramer H, Kovács AL, Sass M, Juhász G. 2014. Interaction of the HOPS complex with Syntaxin 17 mediates autophagosome clearance in *Drosophila*. *Mol Biol Cell* **25**:1338–1354. doi:10.1091/mbc.e13-08-0449
- Tamura N, Mima J. 2014. Membrane-anchored human Rab GTPases directly mediate membrane tethering in vitro. *Biol Open* **3**:1108–15. doi:10.1242/bio.20149340
- Tan X, Thapa N, Choi S, Anderson RA. 2015. Emerging roles of PtdIns(4,5)P2-- beyond the plasma membrane. *J Cell Sci* **128**:4047–56. doi:10.1242/jcs.175208
- Tan X, Thapa N, Liao Y, Choi S, Anderson RA. 2016. PtdIns(4,5)P2 signaling regulates ATG14 and autophagy. *Proc National Acad Sci* **113**:10896–10901. doi:10.1073/pnas.1523145113
- Thumm M, Egner R, Koch B, Schlumpberger M, Straub M, Veenhuis M, Wolf DH. 1994. Isolation of autophagocytosis mutants of *Saccharomyces cerevisiae*. *Febs Lett* **349**:275–280. doi:10.1016/0014-5793(94)00672-5
- Tilley SJ, Orlova EV, Gilbert RJC, Andrew PW, Saibil HR. 2005. Structural Basis of Pore Formation by the Bacterial Toxin Pneumolysin. *Cell* **121**:247–256. doi:10.1016/j.cell.2005.02.033
- Touchot N, Chardin P, Tavitian A. 1987. Four additional members of the ras gene superfamily isolated by an oligonucleotide strategy: molecular cloning of YPT-related cDNAs from a rat brain library. *Proc National Acad Sci* **84**:8210–8214. doi:10.1073/pnas.84.23.8210
- Traut TW. 1994. Physiological concentrations of purines and pyrimidines. *Mol Cell Biochem* **140**:1–22. doi:10.1007/bf00928361
- Tsukada M, Ohsumi Y. 1993. Isolation and characterization of autophagy-defective mutants of *Saccharomyces cerevisiae*. *Febs Lett* **333**:169–174. doi:10.1016/0014-5793(93)80398-e
- Turoňová B, Schur FKM, Wan W, Briggs JAG. 2017. Efficient 3D-CTF correction for cryo-electron tomography using NovaCTF improves subtomogram averaging resolution to 3.4Å. *J Struct Biol* **199**:187–195. doi:10.1016/j.jsb.2017.07.007
- Vadas O, Burke JE, Zhang X, Berndt A, Williams RL. 2011. Structural Basis for Activation and Inhibition of Class I Phosphoinositide 3-Kinases. *Sci Signal* **4**:re2–re2. doi:10.1126/scisignal.2002165

References

- Valverde DP, Yu S, Boggavarapu V, Kumar N, Lees JA, Walz T, Reinisch KM, Melia TJ. 2019. ATG2 transports lipids to promote autophagosome biogenesis. *J Cell Biology* **218**:1787–1798. doi:10.1083/jcb.201811139
- Vance JE. 2015. Phospholipid Synthesis and Transport in Mammalian Cells. *Traffic* **16**:1–18. doi:10.1111/tra.12230
- Vanhaesebroeck B, Guillermet-Guibert J, Graupera M, Bilanges B. 2010. The emerging mechanisms of isoform-specific PI3K signalling. *Nat Rev Mol Cell Biology* **11**:329–41. doi:10.1038/nrm2882
- Vanni S, Hirose H, Barelli H, Antonny B, Gautier R. 2014. A sub-nanometre view of how membrane curvature and composition modulate lipid packing and protein recruitment. *Nat Commun* **5**:4916. doi:10.1038/ncomms5916
- Vanni S, Riccardi L, Palermo G, Vivo MD. 2019. Structure and Dynamics of the Acyl Chains in the Membrane Trafficking and Enzymatic Processing of Lipids. *Accounts Chem Res* **52**:3087–3096. doi:10.1021/acs.accounts.9b00134
- Vanni S, Vamparys L, Gautier R, Drin G, Etchebest C, Fuchs PFJ, Antonny B. 2013. Amphipathic Lipid Packing Sensor Motifs: Probing Bilayer Defects with Hydrophobic Residues. *Biophys J* **104**:575–584. doi:10.1016/j.bpj.2012.11.3837
- Vetter IR. 2014. Ras Superfamily Small G Proteins: Biology and Mechanisms 1 25–50. doi:10.1007/978-3-7091-1806-1_2
- Vicinanza M, D'Angelo G, Campli AD, Matteis MAD. 2008. Membrane traffic in the secretory pathway: Phosphoinositides as regulators of membrane trafficking in health and disease. *Cell Mol Life Sci* **65**:2833–2841. doi:10.1007/s00018-008-8353-2
- Wade RH. 1992. A brief look at imaging and contrast transfer. *Ultramicroscopy* **46**:145–156. doi:10.1016/0304-3991(92)90011-8
- Walker SA, Ktistakis NT. 2019. Autophagosome biogenesis machinery. *J Mol Biol.* doi:10.1016/j.jmb.2019.10.027
- Wallroth A, Haucke V. 2017. Phosphoinositide conversion in endocytosis and the endolysosomal system. *J Biological Chem* **293**:1526–1535. doi:10.1074/jbc.r117.000629
- Walz J, Typke D, Nitsch M, Koster AJ, Hegerl R, Baumeister W. 1997. Electron Tomography of Single Ice-Embedded Macromolecules: Three-Dimensional Alignment and Classification. *J Struct Biol* **120**:387–395. doi:10.1006/jsbi.1997.3934
- Wan W, Briggs JAG. 2016. Chapter Thirteen Cryo-Electron Tomography and Subtomogram Averaging. *Methods Enzymol* **579**:329–367. doi:10.1016/bs.mie.2016.04.014

- Wan W, Kolesnikova L, Clarke M, Koehler A, Noda T, Becker S, Briggs JAG. 2017. Structure and assembly of the Ebola virus nucleocapsid. *Nature* **551**:394–397. doi:10.1038/nature24490
- Wang J, Davis S, Menon S, Zhang J, Ding J, Cervantes S, Miller E, Jiang Y, Ferro-Novick S. 2015. Ypt1/Rab1 regulates Hrr25/CK1 δ kinase activity in ER-Golgi traffic and macroautophagy. *J Cell Biology* **210**:273–85. doi:10.1083/jcb.201408075
- Wang J, Menon S, Yamasaki A, Chou H-T, Walz T, Jiang Y, Ferro-Novick S. 2013. Ypt1 recruits the Atg1 kinase to the preautophagosomal structure. *P Natl Acad Sci Usa* **110**:9800–5. doi:10.1073/pnas.1302337110
- Webster CP, Smith EF, Bauer CS, Moller A, Hautbergue GM, Ferraiuolo L, Myszczyńska MA, Higginbottom A, Walsh MJ, Whitworth AJ, Kaspar BK, Meyer K, Shaw PJ, Grierson AJ, Vos KJD. 2016. The C9orf72 protein interacts with Rab1a and the ULK1 complex to regulate initiation of autophagy. *Embo J* **35**:1656–76. doi:10.15252/emboj.201694401
- Wei Y, Liu M, Li X, Liu J, Li H. 2018. Origin of the Autophagosome Membrane in Mammals. *Biomed Res Int* **2018**:1–9. doi:10.1155/2018/1012789
- Weidberg H, Shpilka T, Shvets E, Abada A, Shimron F, Elazar Z. 2011. LC3 and GATE-16 N Termini Mediate Membrane Fusion Processes Required for Autophagosome Biogenesis. *Dev Cell* **20**:444–454. doi:10.1016/j.devcel.2011.02.006
- Weiss GL, Kieninger A-K, Maldener I, Forchhammer K, Pilhofer M. 2019. Structure and Function of a Bacterial Gap Junction Analog. *Cell* **178**:374–384.e15. doi:10.1016/j.cell.2019.05.055
- Whited AM, Johs A. 2015. The interactions of peripheral membrane proteins with biological membranes. *Chem Phys Lipids* **192**:51–9. doi:10.1016/j.chemphyslip.2015.07.015
- Wijdeven RH, Janssen H, Nahidiazar L, Janssen L, Jalink K, Berlin I, Neefjes J. 2016. Cholesterol and ORP1L-mediated ER contact sites control autophagosome transport and fusion with the endocytic pathway. *Nat Commun* **7**:11808. doi:10.1038/ncomms11808
- Winkler H, Zhu P, Liu J, Ye F, Roux KH, Taylor KA. 2008. Tomographic subvolume alignment and subvolume classification applied to myosin V and SIV envelope spikes. *J Struct Biol* **165**:64–77. doi:10.1016/j.jsb.2008.10.004
- Winslow AR, Chen C-W, Corrochano S, Acevedo-Arozena A, Gordon DE, Peden AA, Lichtenberg M, Menzies FM, Ravikumar B, Imarisio S, Brown S, O’Kane CJ, Rubinsztein DC. 2010. α -Synuclein impairs macroautophagy: implications for Parkinson’s disease. *J Cell Biology* **190**:1023–37. doi:10.1083/jcb.201003122

References

- Wold MS, Lim J, Lachance V, Deng Z, Yue Z. 2016. ULK1-mediated phosphorylation of ATG14 promotes autophagy and is impaired in Huntington's disease models. *Mol Neurodegener* **11**:76. doi:10.1186/s13024-016-0141-0
- Wong S-W, Sil P, Martinez J. 2017. Rubicon: LC3-associated phagocytosis and beyond. *Febs J* **285**:1379–1388. doi:10.1111/febs.14354
- Woodward C, Simon I, Tschersan E. 1982. Hydrogen exchange and the dynamic structure of proteins. *Mol Cell Biochem* **48**:135–160. doi:10.1007/bf00421225
- Xie Z, Klionsky DJ. 2007. Autophagosome formation: core machinery and adaptations. *Nat Cell Biol* **9**:1102–1109. doi:10.1038/ncb1007-1102
- Yamamoto H, Kakuta S, Watanabe TM, Kitamura A, Sekito T, Kondo-Kakuta C, Ichikawa R, Kinjo M, Ohsumi Y. 2012. Atg9 vesicles are an important membrane source during early steps of autophagosome formation. *J Cell Biology* **198**:219–33. doi:10.1083/jcb.201202061
- Yasuda S, Morishita S, Fujita A, Nanao T, Wada N, Waguri S, Schiavo G, Fukuda M, Nakamura T. 2015. Mon1-Ccz1 activates Rab7 only on late endosomes and dissociates from the lysosome in mammalian cells. *J Cell Sci* **129**:329–40. doi:10.1242/jcs.178095
- Yoshida A, Hayashi H, Tanabe K, Fujita A. 2017. Segregation of phosphatidylinositol 4-phosphate and phosphatidylinositol 4,5-bisphosphate into distinct microdomains on the endosome membrane. *Biochim Biophys Acta* **1859**:1880–1890. doi:10.1016/j.bbamem.2017.06.014
- Young ARJ, Chan EYW, Hu XW, Köchl R, Crawshaw SG, High S, Hailey DW, Lippincott-Schwartz J, Tooze SA. 2006. Starvation and ULK1-dependent cycling of mammalian Atg9 between the TGN and endosomes. *J Cell Sci* **119**:3888–3900. doi:10.1242/jcs.03172
- Young LN, Goerdeler F, Hurley JH. 2019. Structural pathway for allosteric activation of the autophagic PI 3-kinase complex I. *P Natl Acad Sci Usa* **116**:21508–21513. doi:10.1073/pnas.1911612116
- Yuan H-X, Russell RC, Guan K-L. 2013. Regulation of PIK3C3/VPS34 complexes by MTOR in nutrient stress-induced autophagy. *Autophagy* **9**:1983–1995. doi:10.4161/auto.26058
- Zachari M, Ganley IG. 2017. The mammalian ULK1 complex and autophagy initiation. *Essays Biochem* **61**:585–596. doi:10.1042/ebc20170021
- Zerial M, McBride H. 2001. Rab proteins as membrane organizers. *Nat Rev Mol Cell Bio* **2**:107–117. doi:10.1038/35052055

References

- Zhang Z, Zhang T, Wang S, Gong Z, Tang C, Chen J, Ding J. 2014. Molecular mechanism for Rabex-5 GEF activation by Rabaptin-5. *Elife* **3**:e02687. doi:10.7554/elife.02687
- Zheng J-X, Li Y, Ding Y-H, Liu J-J, Zhang M-J, Dong M-Q, Wang H-W, Yu L. 2017. Architecture of the ATG2B-WDR45 complex and an aromatic Y/HF motif crucial for complex formation. *Autophagy* **13**:0. doi:10.1080/15548627.2017.1359381
- Zhong Y, Wang QJ, Li X, Yan Y, Backer JM, Chait BT, Heintz N, Yue Z. 2009. Distinct regulation of autophagic activity by ATG14L and Rubicon associated with Beclin 1-phosphatidylinositol-3-kinase complex. *Nat Cell Biol* **11**:468–476. doi:10.1038/ncb1854
- Zhu G, Zhai P, Liu J, Terzyan S, Li G, Zhang XC. 2004. Structural basis of Rab5-Rabaptin5 interaction in endocytosis. *Nat Struct Mol Biol* **11**:975–983. doi:10.1038/nsmb832
- Zivanov J, Nakane T, Forsberg BO, Kimanius D, Hagen WJ, Lindahl E, Scheres SH. 2018. New tools for automated high-resolution cryo-EM structure determination in RELION-3. *Elife* **7**:e42166. doi:10.7554/elife.42166
- Zoppino FCM, Militello RD, Slavin I, Álvarez C, Colombo MI. 2010. Autophagosome Formation Depends on the Small GTPase Rab1 and Functional ER Exit Sites. *Traffic* **11**:1246–1261. doi:10.1111/j.1600-0854.2010.01086.x